The clustering and number counts of galaxies

Busswell, Geoffrey Stuart

The Clustering and Number Counts of Galaxies

Geoffrey Stuart Busswell

A thesis submitted to the University of Durham
in accordance with the regulations for admission to the
Degree of Doctor of Philosophy.

University of Durham
2001

Acknowledgements

Well, that's it!! Seven years of University life at an end. It seems a long time ago now when my mum dropped me off at Warwick University as a young, innocent eighteen year old. So where do I begin? Well first of all I must thank my supervisor Tom Shanks for all the lively, and sometimes heated, discussions which have taught me so much - although I'm not quite sure what kind of example you were trying to set in Edinburgh that time, Tom? Thanks also to Dick Fong for his un-ending enthusiasm, Phil Outram for the youthful point-of-view, Nigel Metcalfe for to-the-point answers, Peter Draper for help with the STARLINK software and Adam Myers for... well, dragging me out to play pool (sorry Adam there was nothing astronomy related I could think of). In no particular order I would also like to take this opportunity to thank Peder Norberg, Fiona Hoyle, Henry McCracken, Kevin Pimbblet, Dave Gilbank, Nathan Courtney and Steve Moore for help with general astronomy and computing problems. Cheers Stelios for ensuring that I was rarely alone in the office during the last couple of months - no matter what time it was!

I must thank my family for all the support they have given me over the years. Mum and dad, from a very early age you have always, and continue, to encourage me to aim for the top. More than anything you have both led by example in that anything worth achieving takes some sacrifices. I'm very proud of you both. Thanks to my Uncle Peter for driving me from University to University, to both my sisters for always being there for me, and to my Nana and Grandad for fussing over me. Thanks also to my four year old brother, Stian. You won't understand what this is all about yet mate, but the thought of seeing you in a months time has made me fight on with this thesis in order to meet my deadline.

I've met some life-long friends in Durham and I will never forget my three years here. Ed, do you remember that first session of pool we ever played in the summer

of 1999? I still can't believe I lost the GradSoc ladder tournament in the final week of the year - how did that black stay in the jaws? And then I met the Porter one night at Howlands. Do you remember that evening, Alex? If I say the words "fluorescent arc" I think you and Ed will know what I mean. Then the motley crew of Jim, Hendrik, Chris, Sarah, Lee, Rosie, Natalie and Rich came on the scene. That year of 1999/2000 was just fantastic and there was some memorable evenings. What about that famous Van Mildert night, where the Ginger Magician was quicker out of the blocks than Maurice Greene, and we recorded the best ever result for the GradSoc A team of 8-1 and the beer leg? That was a demolition job of the highest order. And of the course there was that saturday night when I knocked up that wonderful, refreshing curry. Hendy, you were in a whole world of trouble - I never thought I'd see you cry! Jim, I'm proud to know that I introduced you to the wonder of hot indian food. You were hooked within weeks and Jermal still mentions you every time I go into Shaheen's. What about that "special" Aloo Gobi he served for us one evening? You were a broken man! And Chris - that effort in the Court... words fail me.

Jon and Jamie, thanks for making a difficult year at Cambridge a lot less difficult. I'd also like to thank all my mates that I met at Warwick University who introduced me to the wonders of a Real Ale. Mud, Bag, Lewis and Batta, I can't wait for our holiday next year. Hopefully we've all moved on slightly since our Benidorm escapade in 1994, but that was actually my last holiday with all my friends. That flick on in the sea though - the chances of that happening! And Batta, you know I'm gonna give you a hard lesson on the pool table over Christmas, although to be honest with you I'm still smarting from that 100-97 defeat when I was 15.

But finally, I must thank Linda who I have leaned on very heavily in the last few months. As well as love and support you have provided me with focus and I think this PhD would have gone on a whole lot longer without you.

Abstract: The Clustering and Number Counts of Galaxies

by **Geoffrey Stuart Busswell**

We present a Curtis Schmidt CCD survey of two strips of the sky overlapping with the NGC and SGC 2dFGRS fields. When this survey is used in conjunction with data from the APM Galaxy Survey, DUKST, 2dFGRS and 2MASS, we find that there is a hole in the SGC distribution of galaxies of 100°x60° in angular extent which extends to z$\sim$0.1. The magnitude of this galaxy number deficiency is 30% . The two-point correlation function for our CTIO data is calculated and we find that there is excess power in our SGC function with the break occurring on larger angular scales relative to that in the NGC. When we take into account the effect of the integral constraint we find that a power law form of the two-point correlation function extending beyond $\sim 100h^{-1}$Mpc cannot be ruled out, and we show that this kind of pure power law behaviour is an example of what might be needed to explain the hole we claim exists in the SGC distribution of galaxies. We also find evidence of bias from the fact that the galaxy number deficiency in the 2dF SGC n(z) is greater when more instrinsically luminous galaxies are sampled.

We also investigate the clustering properties of a sample of faint blue galaxies at z=1-2 and are able to use our CTIO clustering results in order to constrain the galaxy correlation length in the local Universe where we find that $r_0=4.7h^{-1}$Mpc. By parametrising the clustering evolution using the clustering growth parameter ϵ, we find that our faint blue galaxies are consistent with an $\epsilon=0.1$ model, which corresponds to a scenario where clustering is approximately fixed in proper co-ordinates.

Finally, we investigate whether the presence of dust in such faint blue galaxies could have an impact in the sub-mm wave-band. We show that by using either a $1/\lambda$ or Calzetti absorption law for the dust and re-distributing the evolved spiral galaxy ultraviolet (UV) radiation into the far infrared (FIR), we can account for all of the 'faint'($\leq$ 1mJy) 850μm galaxy counts and a significant proportion of the sub-mm extra-galactic background.

Contents

List of Figures

List of Tables

Preface

The Clustering and Number Counts of Galaxies

The work described in this thesis was undertaken between October 1998 and November 2001 whilst the author was a research student under the supervision of Prof. Tom Shanks and Dr. Dick Fong in the Department of Physics at the University of Durham. This work has not been submitted for any other degree at this (or any other) university.

The observations described in chapter 5 were taken by Dr. S. Croom of the AAO. All other content presented in chapters 2, 3, 4, 5 and 6 is the authors own work. Collaborators involved in this thesis are Prof. T. Shanks, Dr. R. Fong, Dr. N. Metcalfe, Dr. P.J. Outram & Mr. W.J. Frith.

Results from chapter 6 have appeared in the following paper:

- Busswell G. S. & Shanks T., 2001, MNRAS, 323, 67

Chapter 1 | *Introduction*

1.1 Preliminaries

Cosmology is entering a golden era. The next decade should provide answers to some of the most fundamental of questions about the Universe. Will the Universe expand forever? How old is the Universe? How much of it is composed of baryonic matter? Is the current Cold Dark Matter model (e.g. Davis et al 1985; White et al. 1987) of structure formation correct? The past 10 years has seen the fusion of exponential growth in computing power and immense progression of astronomical instrumentation culminating in the ongoing acquisition of enormous amounts of data characterising the local ($z<0.3$) Universe. Galaxy surveys are the natural way to map the visual distribution of matter in the Universe and such projects have already been performed via the Lick and APM Surveys (Shane & Virtanen 1967; Seldner et al. 1977; Maddox et al. 1990a), revealing complex large scale structure in the form of walls and filaments on scales $>10h^{-1}$Mpc.

In this introduction we first give an overview of two of the most powerful techniques in observational cosmology used to characterise the distribution of galaxies, galaxy number counts and the correlation function as a measure of the clustering of galaxies. We will see that these techniques, when used in conjunction with enormous amounts of data from a new generation of galaxy surveys, will provide tight constraints on models of structure formation for the simple reason that they will have to predict the correct number density and clustering properties of galaxies. Details will then be given of the galaxy surveys that are used in conjunction with the work in this thesis, namely the completed APM Galaxy Survey and the next generation projects of the 2-Degree Field Galaxy Red-Shift Survey (2dFGRS), the

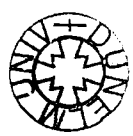

2-Micron All Sky Survey (2MASS) and the Sloan Digital Sky Survey (SDSS). We will then discuss the more distant Universe and we describe how clustering is predicted to evolve with red-shift in the context of the currently favoured biased Cold Dark Matter (CDM) models of structure formation. In chapter 6, we will see how the sub-mm or far infra-red end of the electromagnetic spectrum can be used as a diagnostic probe with which to view the distant Universe. This relatively new area of astronomy is one of the most promising ways to study the star-formation history of galaxies as well as the formation of and merging history of galaxies themselves. Finally, we outline the layout of this thesis and how our work ties in with the main topics of this introduction - galaxy number counts, galaxy clustering and sub-mm cosmology.

1.2 Bright Galaxy Number Counts

The counting of galaxies as a function of apparent magnitude is one of the most famous tools in observational cosmology. Ever since the 1920's when Hubble (1926) first plotted the number density of galaxies as a function of apparent magnitude, it has been known that tests of the homogeneity of the galaxy distribution could be performed using this simple method. Galaxy number counts have been shown to provide information on the number density of galaxies, both in the distant and local Universe (Shanks et al. 1984; Metcalfe et al. 1991), as well as constraints on galaxy evolution (Brown & Tinsley 1974) and the cosmological parameters q_0 and H_0 (Sandage 1961; Yoshii & Takahara 1988; Campos & Shanks 1997). This is because, from the cosmological principle, we expect the Universe to be homogenous and isotropic over a sufficiently large volume of space. If our magnitude limit is faint enough and our survey area big enough, then the number of galaxies we observe should be independent of where we look in the Universe. By understanding on exactly what scale this homogeneity occurs we can constrain the local normalisation of galaxies and use this as a foundation to model the luminosity and density evolution of the galaxy population as a function of red-shift.

However, despite a wealth of new data in the past fifty years due to advances

in astronomical instrumentation, the normalisation of galaxy count models still remains uncertain by as much as 50% (Jones et al. 1991). Since the 1950's, 14 major surveys of very large areas of sky have been performed from the three Schmidt telescopes at Palomar, Siding Springs and La Silla. Technological breakthroughs in the 1980's have meant that digitization of the resulting photographic plates from these surveys has been possible using facilities such as the Automated Plate Measuring Machine (Kibblewhite et al. 1984) at Cambridge, and COSMOS at Edinburgh (MacGillvray et al. 1984). However, despite these advances, the problem remains that there are significant photometric uncertainties in this photographic data and also errors in the calibration of zero points, mainly due to the non-linearity of the plates themselves. Ideally, we would like to be able to say that any observed differences in the bright galaxy counts from different surveys are real, due to the fact that one survey is probing a more dense region of space than the other. Although signficant advances have been made where the effect of significant large-scale structure appears to have been observed in bright number counts (Stevenson et al. 1986; Metcalfe et al. 1991), because of the uncertainties in the reduction of the plate data, and the resulting errors invoked in the normalisation of the counts, other expalanations such as strong evolution at low red-shift ($z<0.1$) (Maddox et al. 1990c) were unable to be ruled out.

CCD detectors have provided us with the means to acquire much more accurate photometry. Although surveys using CCD imaging have revolutionized our knowledge of the properties of faint galaxies (Hall & Mackay 1984; Metcalfe et al. 1995, 1996; Gardner et al 1993), the field of view of such surveys is typically far too small to enable meaningful statistics of bright galaxies to be extracted. Clearly what is needed is accurate bright galaxy count data, using CCD imaging, over large areas of sky and it is only in the last few years that the technology has been developed which makes this possible.

1.3 The Power Spectrum and Correlation Function

We have seen in the previous section how galaxy number counts can be a powerful way of analysing large-scale structure in the local Universe, due to deviations from a model of a homogeneous and isotropic galaxy distribution at bright magnitudes. In 1967 Shane & Wirtanen completed the most extensive and detailed map of the sky at Lick Observatory and one striking feature emerged from their work. Galaxies were not spread thinly and evenly over the sky, they were clustered, forming long sheets and filaments where the projected galaxy number density was very high. There were also regions on the sky where the galaxy number density was very low, known as voids. Peebles (1980) made huge advances in the understanding of the galaxy distribution via statistical studies using moments of the correlation function and finding that density inhomogeneities in the galaxy distribution exist on scales $>10h^{-1}$Mpc.

The most common form of the correlation function is the second order moment or two-point correlation function (see chapter 4 for detailed explanation) where the striking features are the smooth power law behaviour on scales <10-30h^{-1}Mpc before a characteristic "break" on scales $>\sim 20h^{-1}$Mpc where the slope gradually steepens with the clustering amplitude dropping sharply as the length scale increases. This "break" in the clustering amplitude can provide tight constraints on cosmological models of structure formation via the connection, using linear theory, of this very weak clustering in the galaxy distribution beyond the break in the correlation function, to perturbations in the Cosmic Microwave Background Radiation (CMBR) (Smoot et al. 1992). These tiny fluctuations in the CMBR (of order 1 part in 10^5) were frozen into the radiation field when decoupling of photons and matter occurred about 100,000 years after the "Big Bang". One possible explanation for the density inhomogeneities in the matter-radiation field before "de-coupling" occurred is that they are the result of quantum fluctuations in the matter-energy field (Hawking 1982) about 10^{-36}s after the Big Bang that were magnified during an expansion phase of the early Universe called inflation (Guth 1981).

During the last 20 years the standard CDM model has emerged as the leading candidate to explain the formation and evolution of structure in the Universe. The CDM model assumes that most of the mass in the Universe is in the form of slowly-moving, non-baryonic dark matter which has the major gravitational influence on the way structures form. After the "de-coupling" of the matter-radiation field at z$\sim$1000 small Gaussian inhomogeneities in the dark matter density field grow and merge with each other under the influence of gravity into huge rotating "halos". Baryonic matter then falls onto these rotating dark matter halos and is shocked, heated and eventually forms stars over a time-scale governed by how fast the gas can cool. The dark matter halos continue to merge over time due to gravity, building larger and larger aggregates of non-baryonic matter within which stars, and eventually galaxies, continue to form. This process of large structures being built up from the aggregation of many smaller structures is known as "hierarchical merging". It is therefore vital to be able to analyse statistically variations in the density distribution of matter as a function of red-shift in the Universe, and the fundamental statistical tool of interest is the power spectrum of the density fluctuations (Sugiyama 1995).

The power spectrum measures the amount of structure or "power" on a given length scale (see 8.3 in appendix). Also, the two-point correlation function is the Fourier transform of the power spectrum and therefore both the power spectrum and the two-point function are directly related and are both powerful tools with which to measure the clustering properties of galaxies. The shape and amplitude of the power spectrum and correlation function are predicted directly from the CDM model and contain information about the relative densities of the dark matter and baryons. One of the major weak points of the standard CDM model is that it was found from the galaxy surveys of the infra-red selected QDOT redshift survey (Efstathiou et al. 1990a; Saunders et al. 1991) and the Galaxy Surveys of APM & Lick (Maddox et al. 1990; Groth & Peebles 1977) that there was more power in the galaxy distribution on large scales by a factor of a few than standard CDM predicted. The CDM shape parameter, Γ, directly affects the power spectrum in

terms of the ratio of power on large scales to small scales and it was found that Γ had to be decreased from 0.5 in standard CDM to $\sim$0.25 (Efstathiou et al. 1992; Peacock & Dodds 1994) in order to be consistent with these new clustering results from large galaxy surveys. Low density Universes favour this new value of Γ=0.25 and this is one of the reasons that a variant of the standard CDM model called ΛCDM, where Ω_m=0.3 and Ω_Λ=0.7, is currently our best candidate for explaining structure in the Universe.

1.4 Galaxy Clustering from Astronomical Surveys

In the early 1990's the Lick Survey and the APM Survey were the two largest galaxy samples by some distance and were both exceptional achievements in terms of the technology of the time. This early work of Groth & Peebles (1977) and Maddox et al. (1990b) to characterise this large scale structure was based on 2-D maps of galaxies, e.g. the Lick (Shane & Wirtanen 1967; Seldner et al. 1977) and APM survey's where a model of the spatial correlation function must be used in order to de-project the calculated angular correlation function (Phillipps et al. 1978). Using the immense galaxy catalogues of Lick and APM it was possible to make a detailed analysis of the distribution and clustering properties of galaxies on huge cosmic scales $>>10h^{-1}$Mpc. The results of Maddox et al. were in contrast to the results of Groth & Peebles (1977) as Maddox et al. found much larger clustering amplitudes on scales $>10h^{-1}$ Mpc.

Although at first sight it may seem that 3-D information is highly desirable via galaxy red-shifts in order that the spatial correlation function can be calculated directly, red-shifts are particularly expensive in terms of telescope time. Due to this reason galaxy surveys with no red-shift information tend to be much larger than surveys with red-shifts and therefore the apparent disadvantage of 2-D galaxy co-ordinate information is compensated by the relatively low errors on the angular correlation function due to the large galaxy sample. This relatively expensive amount of telescope time to acquire red-shifts has meant a trade-off in past red-shift surveys between angular sky coverage and the red-shift depth reached. For exam-

ple, the ESO slice project (Vettolani et al. 1998) have reached fairly high red-shift ($z\sim0.2$), but the angular sky coverage is unsatisfactorily small ($\sim$23 deg^2). Results from this survey found significant deficiencies of galaxies at $z\sim0.06$, but because of the small survey areas it cannot be determined whether this is a common feature of the way galaxies cluster. On the other hand, red-shift surveys such as the Durham/UK Schmidt (DUKST) Survey (Ratcliffe et al. 1998a) covering 1500 deg^2 in the South Galactic Cap (SGC) have bright magnitude limits ($b_J \sim17$) and reach relatively low red-shift depths ($z\sim0.1$). Although significant large scale structure is observed in the DUKST galaxy number:red-shift distribution, because of the relatively shallow red-shift limit the survey is unable to probe magnitudes at which the cosmological principle is obeyed.

The next generation of red-shift surveys (see next section), made possible by the fusion of digital information storage capabilities and advanced astronomical instrumentation, will have huge angular sky coverage coupled with galaxy red-shift information and will be capable of making a much more detailed description of the cosmological principle. In the next five years these surveys, coupled with unprecedented knowledge of the power spectrum of density perturbations in the CMBR from the MAP satelite (Hu & Dodelson 2001), should enable us to determine all the cosmological parameters (H_0, q_0, Ω_m, Λ) to within a few percent and realise some of the most ambitious goals in the history of science.

1.5 Galaxy Surveys

1.5.1 APM Galaxy Survey

The APM Galaxy Survey (Maddox et al. 1990a) contains images of 20,000,000 sources brighter than b_J=22 and is still the largest galaxy survey to date by some distance. Major technological advances such as photographic emulsions, ever increasing computing power and the development of the SERC Automatic Plate Measuring (APM) machine in Cambridge made the ambitious APM project possible. The APM catalogue was constructed by scanning 185 contiguous high galactic lat-

itude plates ($\delta < -20$) taken from the UK Schmidt Telescope Unit (UKSTU) in Australia. Each plate covers a 6°x6° field culminating in a total APM area of a staggering 4300 deg^2 in the SGC. Over the full 4300 deg^2 area a uniform sample of 2 million galaxies was selected brighter than b_J=20.5, probing an effective depth of $\sim 600h^{-1}$ Mpc.

Two crucial results that emerged from the analysis of the APM Galaxy Survey was the steep slope of the galaxy number counts and the excess power on large scales found in the two-point angular correlation function relative to the predictions of the standard CDM model. The steep slope of these APM galaxy number counts in the magnitude range 16<b_J<19 was interpreted by Maddox et al. (1990c) as being the result of dramatic galaxy evolution at low red-shift. This evolution was inferred by the fact that a number counts model normalised to match the APM count at b_J=17 then under-predicts the data at b_J=20.5 by a factor of two. However, Metcalfe et al. (2001) have shown that that by normalising to the number count data at B=18 and using a Bruzual & Charlot Pure Luminosity Evolution (PLE) model they can get good fits to the B-band counts and red-shift distribution in the range 18<B<22.5 as well as accounting for very faint number count data at B=26. This relatively high normalisation to the number count data at B=18 then means that the model over-predicts data in the literature of galaxies at bright (B<17) magnitudes (Maddox et al. 1990a; Yasuda et al. 2001) by a factor of 1.5-2. A different explanation was therefore invoked (Metcalfe et al. 1996) where the deficiency of galaxies in the APM survey at bright magnitudes could be due to large scale structure in the galaxy distribution. This would seem surprising given the large 4300 deg^2 area of the APM survey, but results from the Durham/UKST redshift survey (Ratcliffe et al. 1998a) which also covers a large 1500 deg^2 area have supported this hypothesis.

This alternative "large scale structure" explanation may tie in with the second crucial result of the APM Galaxy survey. The excess power on large scales, relative to the standard CDM model, found in the angular two-point correlation would seem to support the fact that a hole in the galaxy distribution could exist

over such a large volume of the Universe. It has been suggested that this excess power on large scales could be due to artificial galaxy clustering induced by photometric errors (Fong et al. 1992) from the calibration of the APM plates. These photometric errors could also mean that the deficiency of galaxies seen at bright magnitudes, relative to the Metcalfe et al. models, in the APM counts are not as much as first thought. Perhaps these errors, in conjunction with the large scale structure explanation of Metcalfe et al., may together explain the large apparent hole in the galaxy distribution? The next generation of galaxy surveys should be able to accurately tell us the power on large scales of the correlation function as well as providing detailed 3-D maps of the galaxy distribution. We will then know once and for all if we do live in a particularly under-dense region of the Universe and if this was confirmed it would lay down challenging tests for the CDM model of structure formation.

1.5.2 2-Degree Field Galaxy Red-Shift Survey (2dFGRS)

The 2-Degree Field Galaxy Red-Shift Survey (2dFGRS) is an ambitious, ongoing, project which aims to measure the red-shifts of 250,000 galaxies in the North and South Galactic Caps. The survey has an extinction corrected magnitude limit of b_J=19.45 and the galaxies have been selected from both the Southern Galactic Cap APM Galaxy Survey and the Northern equatorial region, covering a total area of 2000 deg^2. The 2dFGRS has only been possible due to the 2dF instrument (Colless et al. 2001), one of the most complex pieces of astronomical instrumentation equipment ever built. The 2dF instrument is mounted on the 3.9 metre Anglo Australian Telescope and is capable of observing 400 sources simultaneously using optical fibres which are positioned by a very accurate robotic arm. The survey is on schedule to be completed by the end of 2001 with the status at the time of writing comprising 183,501 galaxies with unique spectroscopic red-shifts.

When finished, the project will sample a volume of space ten times larger than any other red-shift survey to date and the fact that 3-D information is available via the galaxy red-shifts means the spatial distribution and clustering of galaxies can

be directly quantified, imposing unprecedented constraints on cosmological models. Already, preliminary results are addressing fundamental questions about the power spectrum of galaxy clustering (Percival et al. 2001), although this analysis is currently confined to relatively large scales >100Mpc where red-shift space distortions (see chapter 4) do not have a big effect on the calculated power spectrum. Work is still in progress to quantify the effect of these distortions on smaller scales (Efstathiou in prep.) which may provide challenging tests for CDM. Other significant results from the ongoing 2dFGRS has been the analysis of the spatial two-point correlation function where Peacock et al. (2001) have found that $\Omega_0 = 0.3$ is favoured, and also the calculation of the galaxy luminosity function for different morphological types (Folkes et al. 1999). Perhaps the most relevent for our purposes is the preliminary result of Norberg et al. (priv. com.) who have found significant large scale structure in the SGC number:redshift distribution for z< 0.1. The large scale structure is characterised by two large holes in the galaxy distribution at z=0.08 and z=0.04 where the galaxy number is deficient relative to the models of Metcalfe et al. by about 30% . This would certainly seem to add weight to similar conclusions drawn from the DUKST survey results, also in the SGC, and provides support to the hypothesis that there is significant structure or power in the galaxy distribution on large scales.

1.5.3 2-Micron All Sky Survey (2MASS)

The 2MASS Galaxy Survey (Jarrett et al. 2001) aims to map the whole sky in the near infra-red between 1μm and 2μm in the H, J and K-bands using CCD-based photometry uniform to better than 10%. When finished at the end of 2001 the catalogue will contain more than 3,000,000 galaxies with K_s <14.5 and have high completeness to magnitude limits of J=15.0 and K_s=13.5. The basic aim of the project is to map in detail the distribution of galaxies and characterise large scale structure of the whole Universe out to z=0.2! The survey will also probe, at lower completeness, higher red-shifts of 0.3-0.4 allowing the calculation of galaxy counts using the location of all sources with z>0.2 in B-J-K_s colour space as a star/galaxy separator. Not only will most of the observed sources be newly discovered, but

2MASS will also be probing huge volumes of uncharted space at low galactic latitudes in the vicinity of the galactic plane where optical band surveys suffer from the problem of severe extinction due to huge amounts of dust and gas.

Early results from 2MASS have included an estimate of the K-band luminosity function using 4192 galaxies (Kochanek et al. 2001) where it was found that early and late-type galaxies had a similar shape Schecter function, with the early types having a slightly brighter M^* but being slightly less numerous. It has been shown that these luminosity functions accutately predict K-band number counts and red-shift distributions for K<18, but for fainter galaxies hierarchical merging and/or evolution is required as an ingredient in the model predictions. The survey has also discovered new galaxies and globular clusters towards the galactic plane (Hurt et al. 2000) which have previously been undetected due to huge amounts of dust, gas and stars in this region of the galaxy. The high detection rates of 1-2 galaxies deg^2 at K<12.1 (Jarrett et al. 2000) in the vicinity of the galactic plane indicates that 2MASS will uncover a large population of sources that will greatly enhance our knowledge of the galaxy distribution in the local Universe. One consequence of this will be a more accurate description of one of the most fundamental questions in physics and cosmology, the cosmological principle. After analysis of the galaxy distribution in the whole local Universe, we will know exactly on what scales the Universe looks homogeneous and isotropic.

1.5.4 Sloan Digital Sky Survey (SDSS)

While the 2dFGRS will certainly be the largest ever red-shift survey when finished, it will soon be complemented by the the Sloan Digital Sky Survey (SDSS), which, in turn, will become the largest galaxy survey in history. The SDSS (York et al. 2000) is a five year observational project (complete in 2005) which aims to map the positions and magnitudes of 100,000,000 celestial objects as well as measuring the red-shifts of 1,000,000 galaxies and 100,000 quasars. The completed survey will have mapped one quarter of the entire sky (π steradians) with accurate CCD photometry uniform over the entire catalogue to 2% and will observe in five passbands

u, g, r, i, z with magnitude limits of 22.3, 23.3, 23.1, 22.3, and 20.8 respectively. What really makes this project possible is the huge imaging array consisting of 30 2048 $\times$ 2048 Tektronix CCDs arranged in six columns and five rows with each row corresponding to one of the five filters. The vast majority of the sky coverage lies in the North Galactic Cap with the finished survey planned to contain a contiguous 10,000 deg^2 area at b>30° consisting of 45 overlapping great circle arcs. In the South Galactic Cap 3 strips will be observed - one in the equatorial region and two others north and south of this, covering a total area of $\sim$750 deg^2. The equatorial region is scheduled to be observed repeatedly in order to find variable sources and so, when co-added, flux limits will be reached that are about 2 magnitudes fainter than in the Northern region. The early release commissioning data which is used in this thesis contains two equitorial strips in the North and South Galactic Cap covering about 500 deg^2. The SDSS is, without doubt, *the* most ambitious astronomical project *ever* undertaken and the scientific community expects to answer fundamental questions about the evolution of the Universe.

Early results from the survey have come from the SDSS Commissioning Data which covers 230 and 210 deg^2 in the NGC and SGC equatorial regions respectively (Yasuda et al. 2001). The galaxy number counts in these regions agree well for B>17 but the SGC data shows no evidence of a galaxy deficiency at bright magnitudes which would seem to suggest that no significant evolution of the galaxy population is occurring for B<17. Thus, if the APM results were showing a large galaxy deficiency due to large scale structure in the SGC galaxy distribution then this hole certainly does not extend as far North as the SGC equatorial region. Interestingly, the NGC counts do show a galaxy deficiency at bright magnitudes but whereas for the APM counts this deficiency persists even at B=18, the SDSS NGC counts agree well with the Metcalfe et al. (2001) model at B=16.75.

The two-point angular correlation function has also been calculated for the NGC Commissioning data (Connolly et al. 2001). Good agreement is found with the APM $\omega(\theta)$ on scales <1° but there is slightly less power on larger angular scales, although still more then predicted by standard CDM. Gaztanaga (2001) has cor-

roborated this result, but also calculated the correlation function for the SDSS SGC data-set and found that this contains significantly *more* power on large scales than the APM and therefore also significantly more than predicted by standard CDM. However, these two-point correlation functions were bases on data-sets covering areas of 150 and 230 deg^2, roughly 2% of the expected total data, and it will be an exciting prospect as more and more of the SDSS observations are perfomed, from which clustering results can be analysed.

1.6 Evolution of the Correlation function

As we have seen variants of the standard CDM model are currently our best candidates for describing structure formation and evolution in the Universe. A crucial ingredient of these models is that a high fraction (80-95%) of the matter in the Universe is unsobservable, or dark matter, the nature of which is very uncertain. It is thought that galaxies, which trace the visual distribution of matter in the Universe, can only form in deep potential wells of dark matter halos - the so called high-peaks model (Baugh et al. 1998; Coles et al. 1998; Wechsker et al. 1998). This then means that galaxies are a "biased" tracer of the overall mass distrubution as they will appear, not only to be more clustered than the dark matter, but brighter galaxies will be more clustered than fainter ones. One of the goals of the surveys we have mentioned is to understand the nature of the details of the relationship between galaxies and the underlying mass distribution in the local Universe. But does this bias relationship remain constant with red-shift or evolve? Given that we still don't know an exact biasing prescription at zero red-shift it may seem ambitious to try and investigate a possible evolutionary trend.

However, technological advances have made it possible to obtain large samples of galaxies at high redshift ($z>1$) and analyse the clustering properties of these sources (McCracken et al. 2000; Roche et al. 1996; Williams et al. 1996). So, even though we may not understand exactly how biasing works, building a sample of high red-shift galaxies can tell us from an observational point of view how clustering of the visual matter in the Universe is evolving. This can't tell us directly how

dark matter halos cluster but, using cosmological simulations (Jenkins et al. 1998; Mo et al. 1998) which incorporate the physics of CDM, one can make predictions about the underlying mass distribution as a function of red-shift by constraining the galaxy clustering as a function of red-shift to match the observations. It has been found from the simulations that the correlation functions of galaxies and dark matter halo's do evolve very differently with red-shift with the bias factor being much larger at high ($z\sim$ 3) red-shift when large density fluctuations in the dark matter were very rare (Brainerd & Villumsen 1994: Bagla 1998b). One particular example of this high biasing at $z\sim$ 3 is the results of Steidel et al. (1996) who have found large amounts of galaxies using the Lyman-Break technique. It is thought that these Lyman-Break Galaxies (LBG's), which exhibit very strong clustering, only form in the very densest regions of dark matter halo's at $z\sim3$ and that they are the progenitors of the rich clusters we see today (Steidel et al. 1998a; Governato et al. 1998).

1.7 The Universe in the Sub-mm

This discussion involving LBG's brings us nicely to the final topic of this introduction, concerning the Universe as viewed in the sub-mm region of the electromagnetic spectrum. In the last few years, the Sub-millimetre Common-User Bolometer Array (SCUBA) camera (Holland et al. 1999) on the James Clerk Maxwell Telescope has transformed our knowledge of dusty galaxies in the distant Universe as a result of the discovery of a new population of luminous, dusty, infra-red galaxies (Smail et al. 1997; Ivison et al 1998). It has been proposed that these galaxies are at high red-shift ($z>1$) and that they are similar to IRAS ULIRGs (ultra-luminous infra-red galaxies), which appear to be starbursting/AGN galaxies containing large amounts of dust. The fact that LBG's must be intrinsically very luminous in order to be selected optically at $z\sim3$ means that it is natural to suggest a connection with the newly discovered sub-mm sources (Peacock et al. 2000) as is discussed briefly in the next section.

What is so special about the sub-mm wave-band though? Why has it uncover-

ing so many previously un-observed sources? The reason is that at high red-shift much star-formation is postulated to be hidden by dust meaning that, in the optical, sources tend to be heavily obscured. This dust absorbs radiation, primarily in the ultra-violet, which is then emitted at far infra-red wavelengths and therefore the sub-mm wave-band is particularly sensitive to high red-shift, luminous, dusty galaxies e.g. possibly LBG's. What is also quite unique about the sub-mm wave-band is that a galaxy can appear as bright at z=1 as at z=10 (Hughes & Dunlop 1999) due to the negative k-correction, which is a consequence of the thermal dust emission peak in distant, starbursting galaxies getting red-shifted into the FIR. This relatively insensitive dependence on red-shift means that we can study our Universe all the way back to very early times in order to try and understand how galaxies form and evolve.

The first sub-mm galaxy to be detected by SCUBA was SMM J02399-0136 (Ivison et al. 1998), which is a massive starburst/AGN at z=2.8 and the current situation is that the complete 850μm sample from all the various groups consists of well over 50 sources (Blain et al. 1999; Eales et al. 1999; Hughes et al. 1998; Holland et al. 1998; Barger et al. 1998; Smail et al. 1997). Optical and near infra-red (NIR) counterparts have been identified for about a third of the sources, although the reliability of these identifications varies greatly. This problem is due to the fact that the $\approx$ 15″ FWHM of the SCUBA beam results in $\pm$3 arcsecond positional errors on a sub-mm source, so there is a reasonable chance that several candidates could lie within these errors. Also, there is no guarantee that the true source will be detected down to the optical flux limit as, for example, many of the sources have been shown to be very red objects (Dey et al. 1999; Ivison et al. 2000; Smail et al. 2000) and therefore have not been found in optical searches for sub-mm sources.

What has proved extremely enlightening is that radio counterparts at 1.4GHz have now been identified for many of the sub-mm sources (Smail et al. 2000: Ivison et al. 2000) providing much more accurate angular positions ($<$ 1″ in some cases) and reasonably accurate photometric red-shifts. Various groups have obtained red-

shift distributions of sub-mm samples (Hughes et al. 1998; Barger et al. 1999a; Lilly et al. 1999; Smail et al. 2000) and they all derive results that are consistent with a mean red-shift in the range $1<z<3$. The fact that almost all of the sources are associated with mergers or interactions seems to confirm that the population of sources contributing at the 'bright' ($>$ 2mJy) sub-mm fluxes are similar to local IRAS ULIRG's, i.e. massive, starbursting/AGN galaxies which are extremely luminous in the far-infra-red. This hypothesis is strengthened further by the fact that the only two sub-mm sources (SMM J02399-0136 and SMM J14011+0252) with reliable red-shifts have been followed up with millimetre wave observations (Frayer et al. 1998, 1999), resulting in CO emission being detected at the red-shifts of both sources ($z=2.8$ and $z=2.6$), a characteristic indicator of large quantities of molecular gas present in IRAS galaxies.

1.8 Scientific Aims and Thesis Outline

The aim of this thesis is to quantify the galaxy distribution in the local and high red-shift ($z>0.5$) Universe as well as predicting the contribution that evolved spirals, or faint blue galaxies, could have to the sub-mm number counts and background. The thesis has 3 main parts - optical galaxy number counts (Chapters 2 and 3), galaxy clustering in the optical (Chapters 4 and 5) and galaxy number counts in the sub-mm (Chapter 6). Chapter 2 outlines our CTIO galaxy catalogue and explains how the data was collected, our reduction techniques and photometry checks. In Chapter 3, we present accurate CCD galaxy number counts over large volumes of space and attempt to constrain the structure and depth of any inhomogeneities in the NGC and SGC galaxy distributions using our galaxy sample in conjunction with the 2dFGRS (Norberg et al. 2001) the Durham/UKST Survey (Ratcliffe et al. 1998b) and publicly available 2MASS data. Our CTIO CCD data, covering large areas of sky in the NGC and SGC, provides the first *ever* opportunity to perform extensive checks of the bright ($B<17$) photometry of surveys like DUKST and the 2dFGRS in their SGC field. Any photometry zero-point errors found in these surveys could have profound implications regarding the nature of the local galaxy distribution.

In chapter 4 we use our CTIO galaxy samples to calculate the two-point correlation function in order to quantify the galaxy clustering in the North and South Galactic Caps. The fact that we have accurate CCD data over large areas of sky in both galactic caps is useful for two main reasons. Firstly, the accuracy of our photometry means that we are less likely to measure artificial clustering when we calculate the two-point correlation function, which is a particular headache for past surveys based on relatively inaccurate photographic magnitudes. Secondly, we can use our two data-sets, which are from the same telescope, to compare our correlation functions from the two galactic caps in order to see if there are any significant differences in the clustering properties of these galaxies. Chapter 5 is devoted to analysing the clustering properties of the faint optical B-band (B<26) galaxy population at z$\sim$1 using data obtained at the Isaac Newton Telescope in La Palma, Canary Islands. We have seen how the evolution of galaxy clustering with redshift is an important prediction from both observations and in the context of the currently favoured biased CDM model of structure formation. By calculating the two-point angular correlation functions for magnitude limits in the range 22<B<26 and combining this with our CTIO B-band observations we can track the evolution of the amplitude of the two point function in the large redshift range 0<z<2

Chapter 6 is devoted to the sub-mm or far-infra-red Universe. It seems that the bright sub-mm population may well be due to massive galaxies containing huge amounts of dust and gas. This dust is then heated by either radiation from stars or an Active Galactic Nucleus (AGN). What is not clear is the nature of the faint (< 2mJy) population. It has proved very difficult to perform any sort of cross-correlation analysis with the distant optical galaxy population e.g. Lyman Break Galaxies (Chapman et al. 2000), because in the majority of cases no optical counterpart to a faint sub-mm source even exists down to the photometric limit of optical telescopes. We will investigate the possibility that the faint sub-mm galaxy population could be due, at least in part, to normal star-forming spiral galaxies used in the models of Metcalfe et al. (2001). The crucial ingredient in these models is the small amounts of dust assumed in these spiral galaxies which absorbs starlight

in the ultra-violet and, due to the typically cold temperatures of 20-25K found for these galaxies, re-radiates this energy into the far-infra-red, which we detect here on Earth. In fact it has been claimed by Peacock et al. (2000) and Adelberger et al. (2000) that the Lyman Break Galaxy (LBG) population could not only contribute significantly to the faint sub-mm number counts, but could also account for a substantial proportion of the background at 850μm. This may indicate that ULIRG's cannot explain all of the sub-mm population and that the UV-selected galaxy population, which are predicted to be evolved spirals by the Bruzual & Charlot models used by Metcalfe et al. (2001), may in fact make a substantial contribution.

Finally, we summarise the findings of this thesis in chapter 7.

Chapter 2

Bright Galaxy Counts: Data Reduction

2.1 Introduction

In this chapter, we present details of our observations and data reduction in both the North and South Galactic Caps in section 2.2, before in section 2.3 briefly summarising the different techniques used to calculate source magnitudes. Section 2.4 describes our star/galaxy separation technique and section 2.5 outlines tests of our photometry accuracy and the galaxy completeness and stellar contamination of our data. Finally, in section 2.6 we summarize our findings.

2.2 Data Reduction

2.2.1 Observations

The observations were taken using the 0.6m Curtis Schmidt Telescope at CTIO, La Serena, Chile. We had two filters, Harris B and R, with magnitude limits of 20.5 and 19.5 respectively, and the imaging data was taken over 2 observing runs of 7 nights, each in excellent weather conditions. The North Galactic Cap (NGC) observations were taken from 8-14 April 1999 inclusive, when my co-observer was T.Shanks, and the data in the South Galactic Cap (SGC) from 17-23 October 2000 inclusive by myself and P.J. Outram. The CCD is a 2048x2048 24 micron chip with 2.3 arcsecond pixels, so that when the bias was subtracted this resulted in a 1.69 degree^2 field of view for each exposure.

In the NGC, we observed 3 main strips of sky in B and R at declinations of

0, -5 and -10 degrees, where the equatorial and -5 degree strips overlap with the 2dF Galaxy Redshift Survey (Colless et al. 2001). The strips were 1.3 degrees wide, which was dictated by the field of view of the telescope, and had an RA range from 9hrs. 45mins. up to 15hrs. The strips were joined at the ends by two smaller strips which were constant at declinations of 10hrs and 15 hrs. In total, this gave a potential 300 hundred square degrees of data in our B and R filters, assuming we had photometric conditions throughout all 7 nights.

In the SGC, we again observed in 3 main strips at constant declinations, this time at -28, -30 and -32, with the knowledge that this would completely overlap with the 2dFGRS fields. Figs. 2.1 and 2.2 show all the galaxies observed with B<=18 in our fields in the NGC and SGC respectively. The ends of the strips were at RA's of 21hrs. 40mins. and 03hrs. 15mins. Because the strips were much closer together than in the NGC, it was possible to connect the strips by simply doing single exposures every half hour of RA at declinations of -29 and -31 degrees. In addition to these three long strips of $\sim$ 100 square degrees each, we also observed a shorter strip at a declination of -45 degrees from an RA of 02hrs. to 02hrs. 45mins. giving an area of $\sim$ 15 square degrees. In total this gave us an imaging area in the SGC of 337 square degrees.

The format of our observations would be to take two standard star frames of suitable Landolt equatorial fields in each band at the beginning, the middle and the end of each night. We would then begin the observations in our chosen field by taking an exposure in the R band for 120 seconds and stop the tracking of the telescope for 1 min 18 seconds (when observing in the North, 1 min. 30 secs. in the South), so that the sky moved over by one quarter of the CCD chip. This 1 min 18 seconds was sufficient to let the CCD readout which took $\sim$ 45 seconds. An exposure of the same length of time would then be taken in the B filter, and so on. The result would be a series of frames at a constant declination in the sky where each frame overlapped its adjacent frames in the same filter by about half a chip. We would typically be able to cover about 90 mins. of RA (30 deg^2) using this method before the sky was too far over and we would then move the telescope

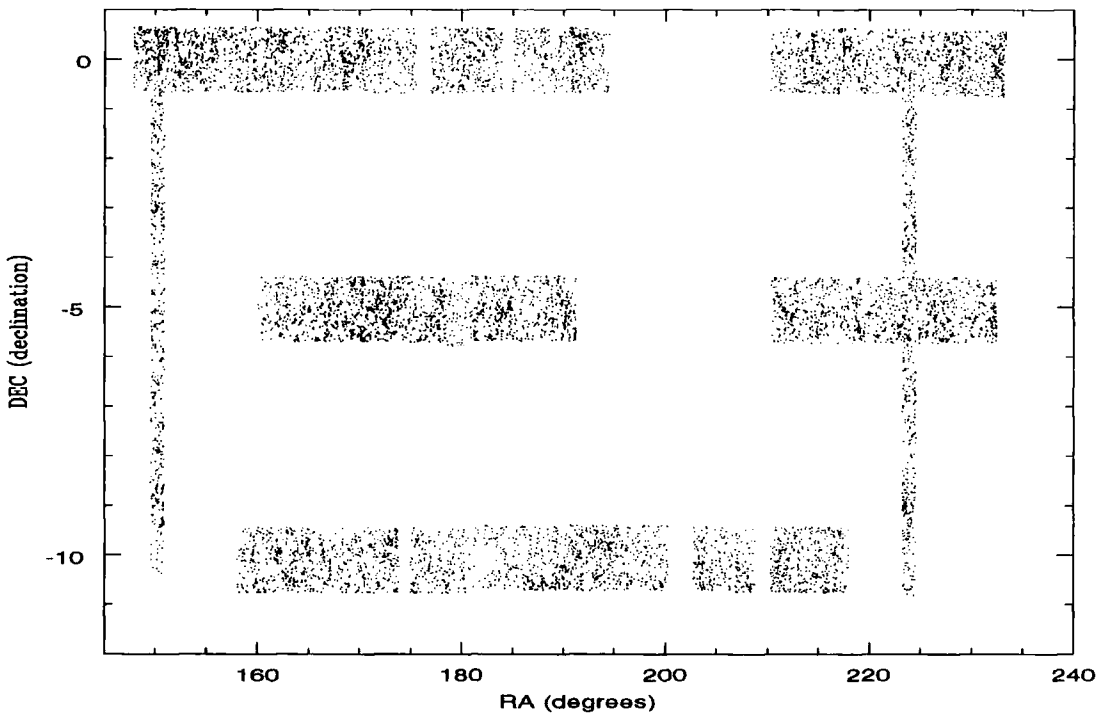

Figure 2.1: This plot illustrates the regions observed in the NGC with the galaxies that were observed with B$\leq$ 18 in photometric conditions shown by the dots. The strips at 0 and -5 degrees both overlap with areas of sky observed by the 2dFGRS team.

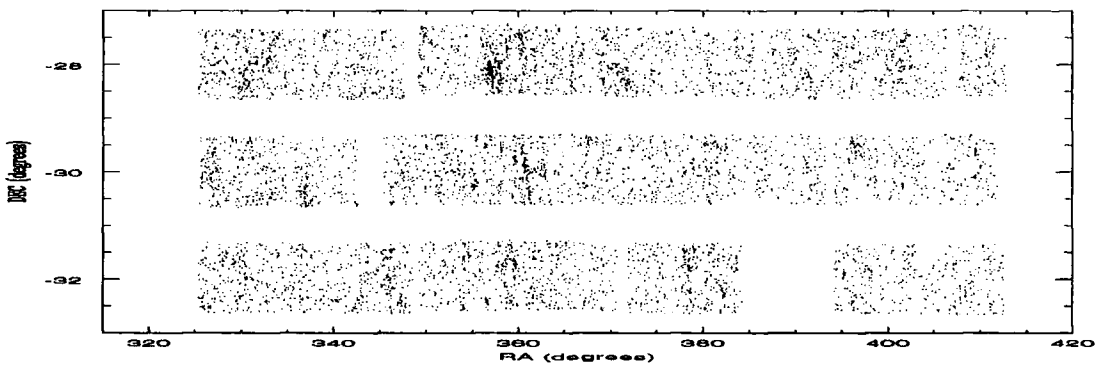

Figure 2.2: This plot illustrates the regions observed in the SGC by plotting all the galaxies observed with B$\leq$ 18 in photometric conditions, shown by the dots. All these strips overlap with 2dFGRS fields. There is also a further, smaller strip in the SGC which we observed, at a declination of -45 degrees, with an RA range between 2 hrs and 2hrs 45, that is not shown here.

and begin again. Fig. 2.3 shows a plot in pixel co-ordinates of a series of frames observed in the B band using the method described.

The bias was subtracted, images trimmed and bad pixels corrected using the IRAF quadproc package. Typically, five or six dawn and twilight flat field images were taken in each bandpass. A master flat field image was produced in each filter for each night by first using the imcombine routine to median together each of the dawn flats and evening flats separately. The resulting frames were then averaged to produce our B and R master flats for that night. By dividing the median-ed dawn and twilight flats we typically found a 1-2% gradient from top to bottom of the resulting frame, implying an error of about 0.005-0.01 to our galaxy photometry due to this effect. The frames for a particular night in each filter were then flat-fielded using the IRAF ccdproc package and the appropriate flat-field master frame.

2.2.2 Astrometry and Photometric Analysis

Since the pointing was done manually on the Curtis Schmidt Telescope and the sky co-ordinate information was just typed in, astrometry information could be in error on a frame by anything up to 0.5 degrees. This proved quite a problem and was solved by aligning and re-sampling each series of images in pixel x-y co-ordinates as has already been shown by Fig. 2.3. Accurate astrometry could then be achieved by manually calibrating the first frame in the series for each filter using GAIA, and then, by making use of the x-y pixel co-ordinate information now in the headers, all the frames in the series (typically $\sim$ 30) could be calibrated in an automated way. The RMS error on the astrometry for each frame was typically 0.4-0.5 pixels or about 1″. Finally, using the inverse of the linear transformations used to align the frames, the astrometry information in the re-sampled frames could then be copied back to the original, un-resampled data frames.

The fact that accurate sky coordinate information was then available for each frame meant the half-a-chip overlaps in each filter could be used to make a detailed

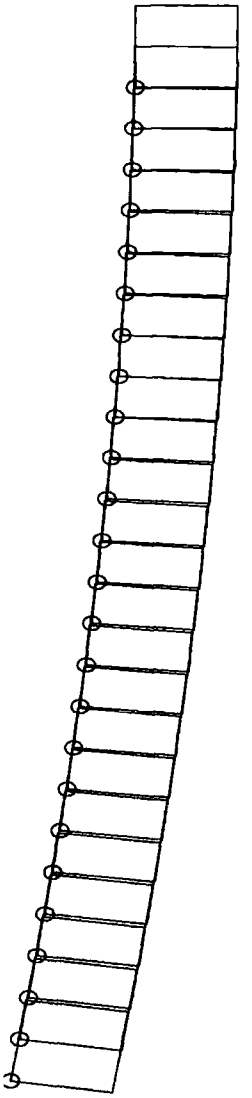

Figure 2.3: Here we show a sequence of 26 frames, plotted in pixel co-ordinates, which were observed in the B-band at a constant declination of -28 degrees. These frames were taken in the SGC during one of the sessions where we took a 120 second exposure in B, stopped the tracking for 1 min. 30 secs. to move to the next field, and then started the tracking again to observe in the R band. The figure illustrates how the resulting frames in a particular bandpass overlap by half a chip. The fact that these frames are observed at a declination of -28 degrees means that they do not trace the segment of a great circle on the sky, which is reflected in the curve that the circles trace out. The circles are drawn around the origin of each frame at the bottom, left-hand edge.

NGC field		SGC field	
night	photometric?	night	photometric?
1	yes	1	yes
2	partial	2	yes
3	partial	3	yes
4	yes	4	partial
5	partial	5	yes
6	yes	6	yes
7	yes	7	no

Table 2.1: By using the fact that the frames in each filter overlap adjacent frames by half a chip, we were able to analyse the photometric conditions for each night. This table shows a summary of this analysis from the two observing runs in the North and South Galactic Caps respectively. In total our survey areas taken in photometric conditions were 255 and 297 square degrees for the NGC and SGC respectively.

analysis of the photometric conditions throughout each night. The results of this photometric analysis is shown in Table 2.1. A night is deemed partially photometric if two or more adjacent frames show significant offsets (> 0.1 mag) from each other when performing best fits to the magnitude residuals of the stars. If a particular night was deemed to be "partially photometric" then none of the frames were used where > 0.1 magnitude offsets were found.

Our original strategy was to calculate a series of internal zero-points for a sequence of frames before calculating a global zero-point from the Landolt standard stars (described shortly). To calculate the internal zero-points for each frame we would use the magnitude offsets from the overlap analysis. Now a magnitude offset for frame n is defined as being the best fit to the magnitude residual for frames n and n-1. So, for example, the internal zero-point for frame n is equal to $\sum_{i=2}^{n} m_i$, where m_i is the magnitude offset for frame i. The idea was that any large scale gradient along the sequence could be removed by attempting to scale all the frames, using the offsets, to be consistent with frame 1. This would also take into account any airmass variations as well, which could change by 0.4 along the sequence. If

the conditions are photometric then one would expect the cumulative magnitude offset along the whole sequence to be equal to that expected from the total airmass variation. In fact, we found typical cumulative offsets of 0.3 in B and 0.26 in R, vastly in excess of the 0.08 magnitudes in B (0.05 in R) one would expect from airmass differentials alone. The reason for this was due to the master flat field frames, which tended to have fractionally more counts, on average, on the upper half of the chip than the lower half. After flat-fielding, this effect has a tiny effect on the stellar magnitudes for a single frame, making stars slightly brighter, on average, on the top half of the frame by $\sim$0.006 mags. However, because all frames for a particular night are flat-fielded using the same flat-field master frame, when calculating the cumulative magnitude offset along a sequence this small $\sim$0.006 mag error propagates in a monotonic way inducing a 0.22 mag. offset from the 1st frame to the last (assuming a typical value of 35 frames). Taking into consideration the expected airmass variation, inducing a further 0.08 mags. (in B) we were able to account for this large apparent gradient of 0.3 mags. in B and 0.26 mags. in R.

One approach would have been to follow the original strategy, but to calculate the induced magnitude offset along a sequence for each night's flat-field images, and accounting for this effect when correcting by the internal zero-points. We chose not to do this for two reasons. Firstly, a few sequences were not complete because frames were removed that showed large offsets. This meant that overlap information (and therefore internal zero-point information) was not then available for all frames in the sequence that were observed in photometric conditions. Secondly, we were worried that any errors in calculating a magnitude offset between two frames would then propagate along the sequence, affecting all subsequent internal zero-points. Given that the sequences were quite long, typically containing 35 frames, this was a distinct possibility. What we in fact decided to do was to scale each frame based on its airmass relative to the first frame in the sequence. From our previous approach we knew that, assuming photometric conditions, that the cumulative magnitude offset along the whole sequence of frames was consistent with the airmass variations after the flat-field problem had been taken into account. Since we enforced strict criteria on whether frames had been observed in photometric conditions, this

assumption was justified. This also meant that the calibration of each frame was completely independent of all the others in the sequence, eliminating the possibility of the propagation of magnitude offset errors. To take these airmass variations into account the frames were scaled according to the equations:

$$f_B = 10^{0.209(X_{1_B} - X_{n_B})/2.5} \tag{2.1}$$

$$f_R = 10^{0.108(X_{1_R} - X_{n_R})/2.5} \tag{2.2}$$

where X_{1_B}, X_{n_B} are the air-masses in the first and nth frames in a B filter sequence and X_{1_R}, X_{n_R} the corresponding air-masses for the R filter. f_B and f_R are the scale factors for the B and R filters respectively and the values 0.209 and 0.108 are the quoted airmass coefficients in B and R for the CTIO observatory. By using high-mass standard star frames in the B and R filters we obtained values for the airmass coefficients of 0.19 and 0.10 respectively, in good agreement with the quoted values.

2.2.3 Standard Stars and the Colour Equation

Once the internal zero-points had been calibrated a global zero-point for each sequence had to be calculated. We did this by using the B and R magnitudes of the Landolt (1992) standards stars from our standard star frames which were taken at the beginning, middle and the end of each night using the fields SA101, SA107, and SA110. Our standard star exposure times were 10 secs. in R and 20 secs. in B. The IRAF fitparams routine was then used to determine the best fit zero-point offsets (b_1 and r_1) and colour-term coefficients (b_3 and r_3) for each band in the equations:

$$m_b = B + b_1 + b_2 * X_b + b_3 * (B - R) \tag{2.3}$$

$$m_r = R + r_1 + r_2 * X_r + r_3 * (B - R) \tag{2.4}$$

where B and R are the Landolt standard star magnitudes, X_b and X_r are the air-masses of the standard star frame for the B and R bands respectively and m_b, m_r are the calculated magnitudes of the stars. The parameters b_2 and r_2 are equal to

0.209 and 0.108 respectively and are the quoted airmass coefficients for the CTIO observatory in our two passbands. Fig 2.4 shows such a fit for the B filter on night four where function (the m_b magnitude in this case) is plotted against residual, equal to B_{CTIO}-m_b, where B_{CTIO} is the observed B magnitude we measure using the source flux count . The crosses (+) indicate the used stars and the single "X" was a star not used in the fit because it was found not to be in the Landolt catalogue. This particular fit was performed for just the zero-point offset b_1 with b_2=0 and shows an rms scatter on the residual of 0.058 magnitudes, with the best fit for b_1=4.52. If we fit both b_1 and b_3 then we find an rms of 0.051 with b_1=4.44 and b_3=0.05. However, the error on the value of b_3, the colour-term coefficient, was equal to 0.04 and since this was comparable to b_3, which was itself small, we decided only to fit b_1 in the colour equation. Because of the same reasons we only fitted the R band zero-point offset, r_2 in equation 2.4. Since we did not use any colour terms in equations 2.3 and 2.4 all reduced magnitudes of our final sources will be in B and R_{kc}, as used by Landolt (1992). The mean of the b_1's and r_1's was calculated over all seven nights and our resulting colour equations were then:

$$m_b = B + 4.533(\pm 0.0053) + 0.209 * X_b \tag{2.5}$$

$$m_r = R + 4.203(\pm 0.0067) + 0.108 * X_r \tag{2.6}$$

In order that we could eventually use the SExtractor (Bertin et al. 1996) software on our data we decided to convert all our frames to NDF format. In order to work out the global zero-point for each sequence of frames we used the values of b_1 and r_1 from equations 2.5 and 2.6, but we had to take into account the fact that the IRAF fitparams routine converts all its source magnitudes to 1 second exposures. Since our exposures were 120 seconds this meant using an additive constant of 2.5log120 in our global zero-point calculation. Also, recall that our internal zero-points were determined so that all the frames were consistent with frame 1 of the sequence. Since our colour equations are determined at zero airmass we also need to take into account the additive constants $0.209X_{1_B}$ and $0.209X_{1_R}$ for the B and R bands respectively. Therefore, to determine the global zero-points, z_{G_B} and

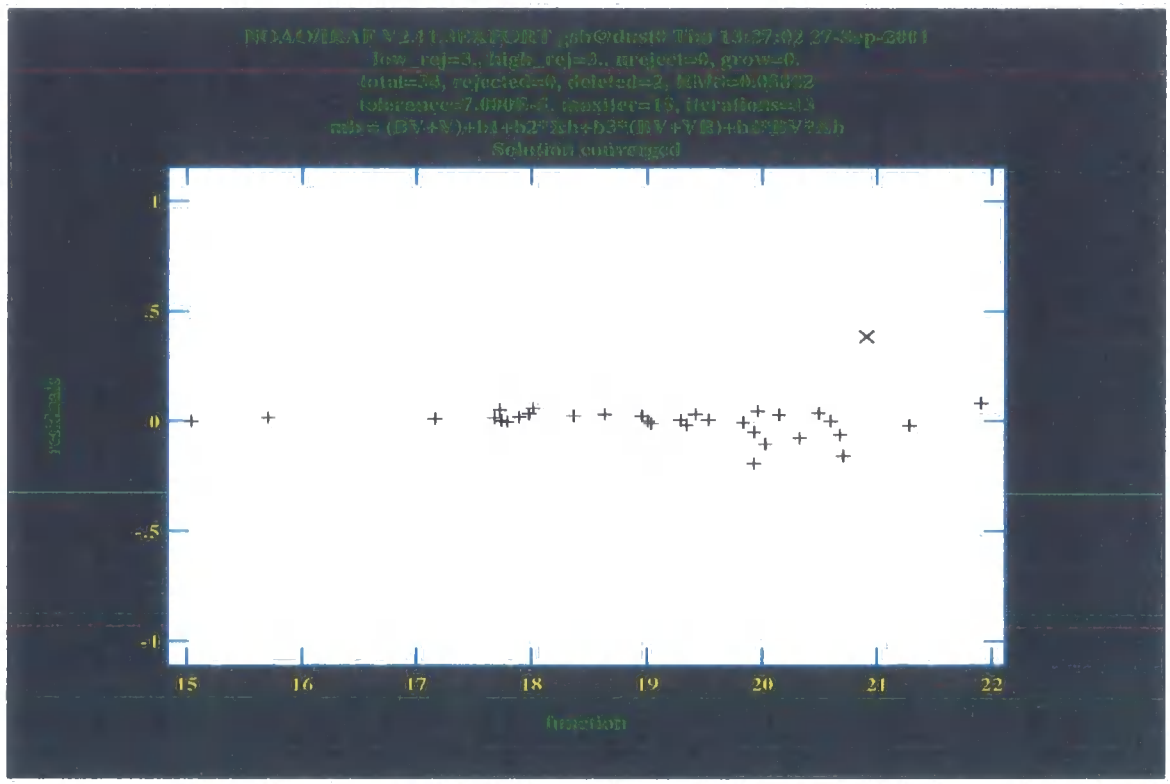

Figure 2.4: This plot shows an output from the IRAF fitparams routine, which was produced for our night four data from three Landolt (1992) standard star fields, SA101, SA107 and SA110. The crosses (+) signify standard stars and the single "X" was not included in the fit because it turned out not to be one of the Landolt stars. The m_b magnitude (labelled function) is plotted against residual, equal to B_{CTIO}-m_b where B_{CTIO} is our observed B magnitude determined straight from the source flux count. The fitparams routine finds the value for b_1 in equation 2.3 by minimizing the sum of the residuals. This particular fit has an rms scatter on the residual of 0.058 magnitudes.

z_{G_R}, in the B and R band filters for a sequence of frames we use the equations:

$$z_{G_B} = 25.0 - b_1 - 0.209X_{1_B} + 2.5log120 \tag{2.7}$$

$$z_{G_R} = 25.0 - r_1 - 0.108X_{1_R} + 2.5log120 \tag{2.8}$$

where the value 25.0 comes from the fact that the IRAF fitparams routine used this as its initial zero-point estimate when performing the best fit to the standard star fields. These global zero-points can then be used to obtain a magnitude in our B Landolt and R Kron-Cousins system, for each source from SExtractor via the usual flux-magnitude relation.

The sources were then extracted, sequence by sequence, and frame by frame in each sequence, using the SExtractor software package. The seeing stellar FWHM was first estimated for a particular frame with an initial call of SExtractor and then the objects were extracted with a second pass, making use of the calculated stellar FWHM. We used the MAG_BEST parameter in SExtractor for the source magnitudes (described in more detail in the next section) and since we had at least two observations of each source because of our frame overlaps, the mean of the two magnitudes was used in order to minimize errors in the photometry. A cosmic ray was defined as being a source which appeared on one frame but on neither of the adjacent frames and these would not be included in our source catalogue, but written to a cosmic ray file.

2.3 Magnitude Estimates

It is worthwhile devoting a small section to magnitude estimates, since there are distinct variations in how they are calculated in the astronomical community. For example, the SDSS commissioning data uses the photo software package, which uses a Petrosian magnitude, as opposed to our use of the SExtractor MAG_BEST parameter. If we are to understand any differences in the photometry from other surveys then it is essential to know about any systematics that arise from using

different magnitude estimators.

2.3.1 Aperture Magnitude

This is the simplest and most commonly used magnitude. The aperture flux is calculated by looping through the pixel list and asking whether a given pixel is closer to the object centre than the aperture radius. If so, the pixel value is added to the summed flux. The magnitude is then calculated via the usual relation:

$$m_{aper} = -2.5 log F_{aper} + c \tag{2.9}$$

where m_{aper} is the aperture magnitude, F_{aper} is the aperture flux and c is the zeropoint of the CCD frame.

2.3.2 Isophotal Magnitude

The flux is calculated by looping over the pixel list and asking whether a given pixel has a value greater than the surface brightness threshold. If so, the pixel value is added to the summed flux. With this method you are effectively defining a surface brightness contour on your source, within which defines the area over which you integrate your flux. The magnitude is again calculated via the usual relation:

$$m_{iso} = -2.5 log F_{iso} + c \tag{2.10}$$

where m_{iso} is the isophotal magnitude, F_{iso} is the isophotal flux and c is the zeropoint of the CCD frame.

Clearly these two methods will run into problems when trying to estimate the total magnitude of an object. Low surface brightness sources will be a problem for isophotal magnitudes, whereas a fixed aperture method can be poor at measuring both total flux of a star and an extended source such as an edge-on spiral galaxy. The SExtractor software uses two main total magnitude estimators, which can both be found in the parameter file default.param (see Bertin et al. 1996 for further explanation of the SExtractor software).

2.3.3 Adaptive Aperture Method

This is an extension of the technique used by Kron (1980) and Infante (1987). These authors found that an almost constant fraction of flux lies within a circular aperture of radius kr_1, assuming standard star and galaxy profiles convolved with gaussian seeing. r_1 is known as "the first moment" of the brightness distribution and is defined:

$$r_1 = \frac{\Sigma r I(r)}{\Sigma I(r)} \tag{2.11}$$

The extension of this method uses the fact that it also applies to an elliptical aperture, defined by principal axes of ekr_1 and kr_1/e, where e is the ellipticity of the ellipse. The values of r_1 and e are defined by the second moments of the ellipse. By using k=2.5, a fixed fraction of 6% of the total flux of the source is lost, corresponding to a mean offset of 0.06 mags. for galaxies and 0.03 for stars. The SExtractor software labels this magnitude MAG_KRON.

2.3.4 Corrected Isophotal Method

This method attempts to estimate the magnitude difference between an isophotal and a total magnitude and is labelled MAG_ISOCORR in the default.param file of SExtractor. If the source intensity profiles are assumed gaussian because of atmospheric blurring then the fraction of the total flux, η, measured within the isophote follows the relation (see Maddox et al. 1990b):

$$(1 - \frac{1}{\eta})ln(1 - \eta) = \frac{A.t}{I_{iso}} \tag{2.12}$$

where $\eta = \frac{I_{iso}}{I_{tot}}$, A is the area and t the threshold relating to this isophote. It is impossible to solve analytically for η, but a good approximation is given by:

$$\eta \approx 1 - 0.1961\frac{A.t}{I_{iso}} - 0.7512\left(\frac{A.t}{I_{iso}}\right)^2 \tag{2.13}$$

The estimation of the difference between the isophotal and total magnitude is then given by $2.5\log\eta$ and so:

$$m_{tot} = -2.5logF_{iso} + 2.5log\eta \tag{2.14}$$

The difference between the two methods is that the adaptive aperture method is more accurate for uncrowded fields, as it gives a better estimation of sources such as spheroidal galaxies, which have broad wings. However, it relies on no significant flux contamination from nearby sources within roughly 2 isophotal radii. The corrected isophotal magnitude, however, uses only 1 isophotal radii from the centroid source and therefore is better for crowded fields, but is inaccurate for extended galaxies. The SExtractor software uses the adaptive aperture method, MAG_KRON unless it suspects that a nearby source is biasing the magnitude estimate by more than 0.1, when it uses MAG_ISOCORR. The parameter MAG_BEST is assigned the appropriate value. MAG_BEST therefore takes advantage of the fact that MAG_KRON is more accurate, but recognises the problem of nearby sources for this estimate.

2.3.5 Petrosian Magnitude

The Petrosian magnitude (Shimasaku et al. 2001) is an aperture magnitude using the Petrosian radius. The Petrosian flux is therefore defined by the relation:

$$F_P = 2\pi \int_0^{kr_P} I(r) r dr \tag{2.15}$$

where r_P is the Petrosian radius. When the slope in the aperture flux divided by the aperture flux equals the Petrosian constant, η, the radius of the aperture flux is the Petrosian radius. The Petrosian radius is therefore defined to satisfy:

$$\eta = \frac{I(r_P)}{2\pi \int_0^{r_P} I(r) r dr / (\pi r_P^2)} \tag{2.16}$$

This magnitude is used by the SDSS team and the Petrosian radius is defined so that it is independent of the foreground reddening. Two parameters are required to specify the Petrosian flux, k and η. The Petrosian radius can also be made insensitive to seeing variations if a small value of η is chosen (<0.2). However, in order to achieve high signal-to-noise, $\eta \geq 0.2$ is desirable. With regard to the SDSS data, simulations were carried out to estimate the mean difference between

the Petrosian magnitude and the total magnitude for a galaxy sample consisting of a mix of morphologies. Typically, a mean offset of 0.03 magnitudes was found.

We decided to use the SExtractor software and adopted the MAG_BEST parameter to estimate the total magnitude. We use a Kron factor, k, equal to 2.5 and therefore we correct by 0.06 mags. for each galaxy.

2.4 Star/Galaxy Separation

The SExtractor software uses a tunable neural network which has been trained on realistic simulation images and has been shown to reliably separate galaxies from stars. The parameter CLASS_STAR is assigned a value for a particular source which varies between 0 (definitely a galaxy) and 1 (definitely a star). Once technical details of the CCD have been supplied, this parameter is essentially only dependent on the stellar FWHM of a particular frame, which varied over the two observing runs between 3.2" and 4.1". See Table 2.2 for estimates of the seeing for each night during the two observing runs. These values may seem large, given that a large proportion of our observing time was in photometric conditions, but this is entirely due to the pixel size of 2.3" dictated by the set-up of the Schmidt telescope. Shown in Fig. 2.5 and Fig. 2.6 are plots, over a 19.25 square degree area, of the SExtractor CLASS_STAR parameter vs. magnitude in both B and R respectively.

For B<18 and R<17 the SExtractor STAR_CLASS parameter is a good separator of stars and galaxies with 91% in B and 90% in R of sources either having CLASS_STAR >0.9 (a star) or CLASS_STAR <0.1 (a galaxy). The fact that we have two filters is useful in terms of the star/galaxy separation as we get four attempts instead of two (as we have overlaps in each filter) to classify a particular source. For sources that were not classed as stars or galaxies i.e. 0.1<CLASS_STAR<0.9 it is enlightening to plot how the sources were classified in the other filter. We have therefore isolated all sources that satisfied R<17 and 0.1<CLASS_STAR<0.9 in the R-band. Fig 2.8 shows a histogram of how these sources were classed as a function of magnitude in the B-band. Fig 2.7 shows the corresponding plot of

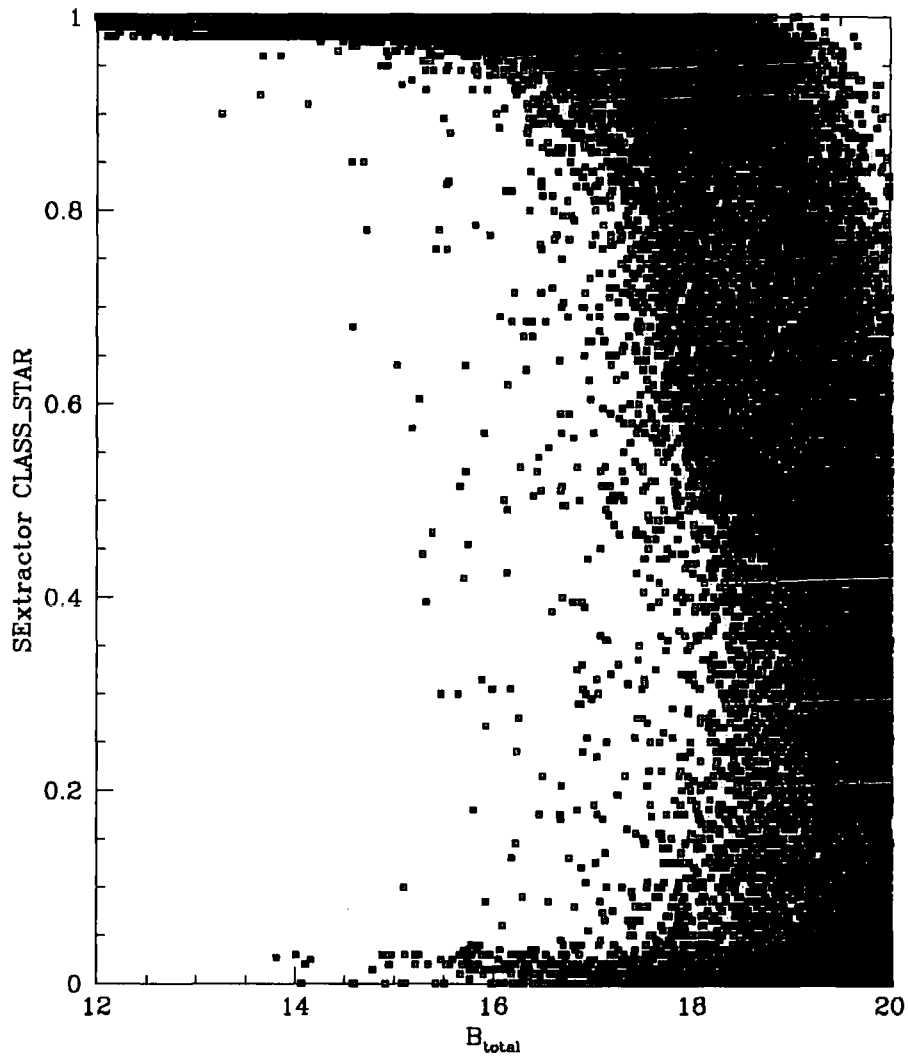

Figure 2.5: Here we show total B-band magnitude plotted against the SExtractor CLASS_STAR parameter. The plot contains 56217 objects taken from a sequence of frames covering 19.25 square degrees. The seperation is reliable up to about B=18, after which the software is unable to distinguish between a star and a galaxy. The objects in the region 12 <B< 18 and 0.1 <CLASS_STAR< 0.9 tend to be either merged objects or lie on a line of interpolated pixels, which are present on every frame.

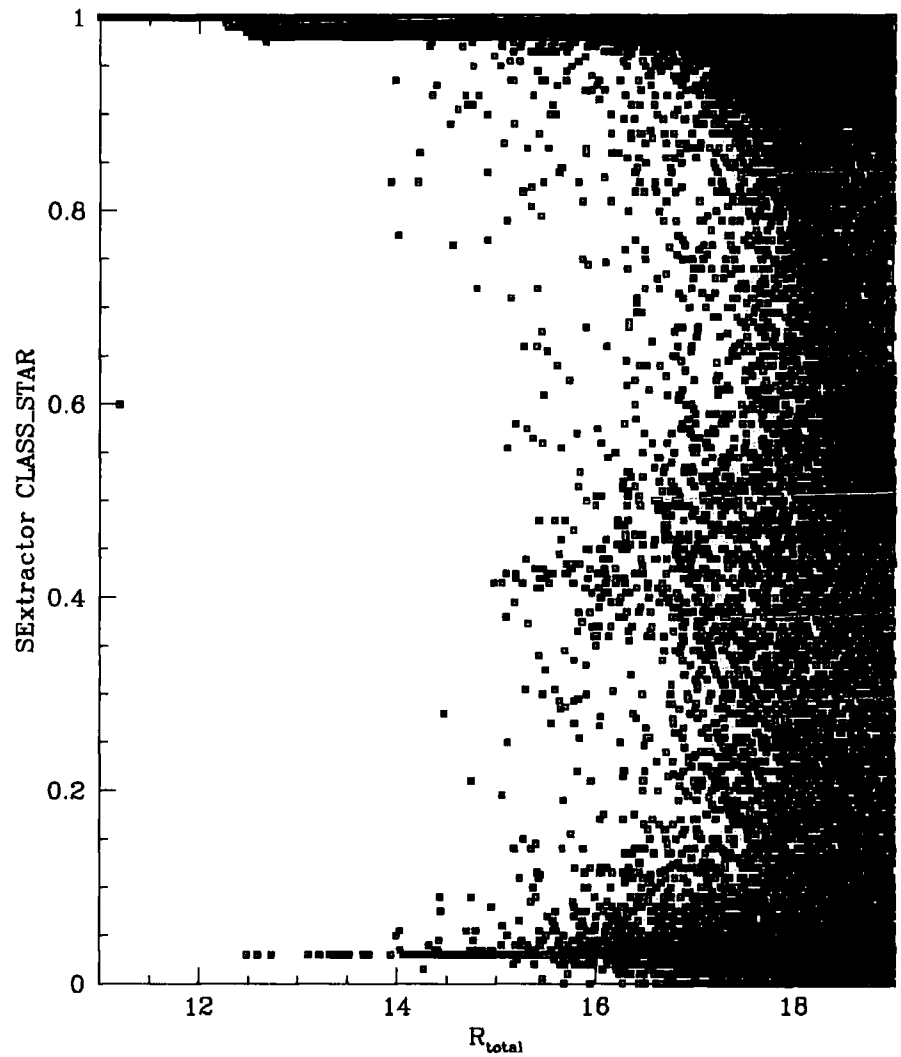

Figure 2.6: Here we show the same plot as in Fig. 2.5 except using the R filter. Our star/galaxy separation appears to be unreliable for sources with magnitudes fainter than R=17. The feature at R≈16 with 0.4<CLASS_STAR<0.5 is due to a column of interpolated pixels already mentioned in Fig. 2.5.

NGC field		SGC field	
night	mean stellar FWHM (″)	night	mean stellar FWHM(″)
1	3.2	1	3.8
2	3.8	2	3.3
3	3.7	3	3.7
4	3.3	4	4.0
5	3.9	5	3.3
6	3.4	6	3.5
7	3.3	7	N/A

Table 2.2: This table shows the mean stellar FWHM for each night during the two observing runs. The relatively large seeing values, even though a large proportion of our observing time was during photometric conditions, is due to the large pixel size of 2.3″ dictated by the instrumentation and geometry of the Curtis Schmidt telescope.

the source classification in the R filter, this time for all objects with B<18 and 0.1<CLASS_STAR<0.9.

In both figures it is clear that for most of the sources, where an object was classed in one filter in the range 0.1<CLASS_STAR<0.9, in the other filter the source was either classed as a star(>0.9) or a galaxy(<0.1). However, the proportion of sources that are classed as galaxies does vary when comparing Figs. 2.8 and 2.7. It appears that the CLASS_STAR parameter in the R filter is less reliable in terms of classifying sources correctly as galaxies. Of these 2,275 sources with CLASS_STAR<0.1 in the B band (Fig. 2.8), 75% of them have CLASS_STAR<0.5 in the R band. These 2,275 sources are 15% of the galaxies detected in the R band i.e. it seems that CLASS_STAR in the R band effectively "misses" 15% of the galaxies. On the other hand, Fig. 2.7 shows that in the B filter relatively few galaxies are missed (7%) that are detected in the R band. The percentage of stars "missed" by the CLASS_STAR parameter is 4% and 0.4 % in the B and R bands respectively. It appears that while the CLASS_STAR parameter in the B band is roughly twice as reliable as in the R band at classifying galaxies, it is 10 times less reliable at correctly classifying stars.

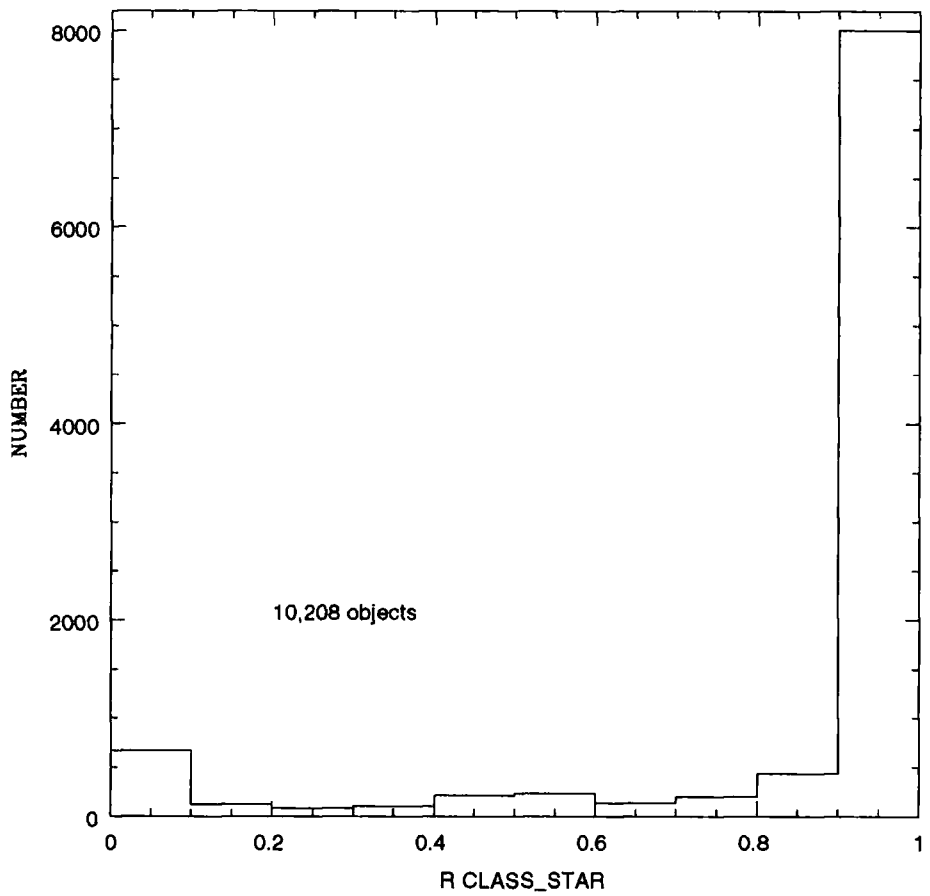

Figure 2.7: Here we show the CLASS_STAR parameter in the R filter for all sources that satisfy B<18 and 0.1<CLASS_STAR<0.9. The majority (80%) of these sources are classified as stars in the R band and the 700 classed as galaxies is roughly 7% of the number of sources already classed as galaxies in the B band i.e. CLASS_STAR in the B band has effectively "missed" 7% of the galaxies. The corresponding number for the "missed" stars is 4%.

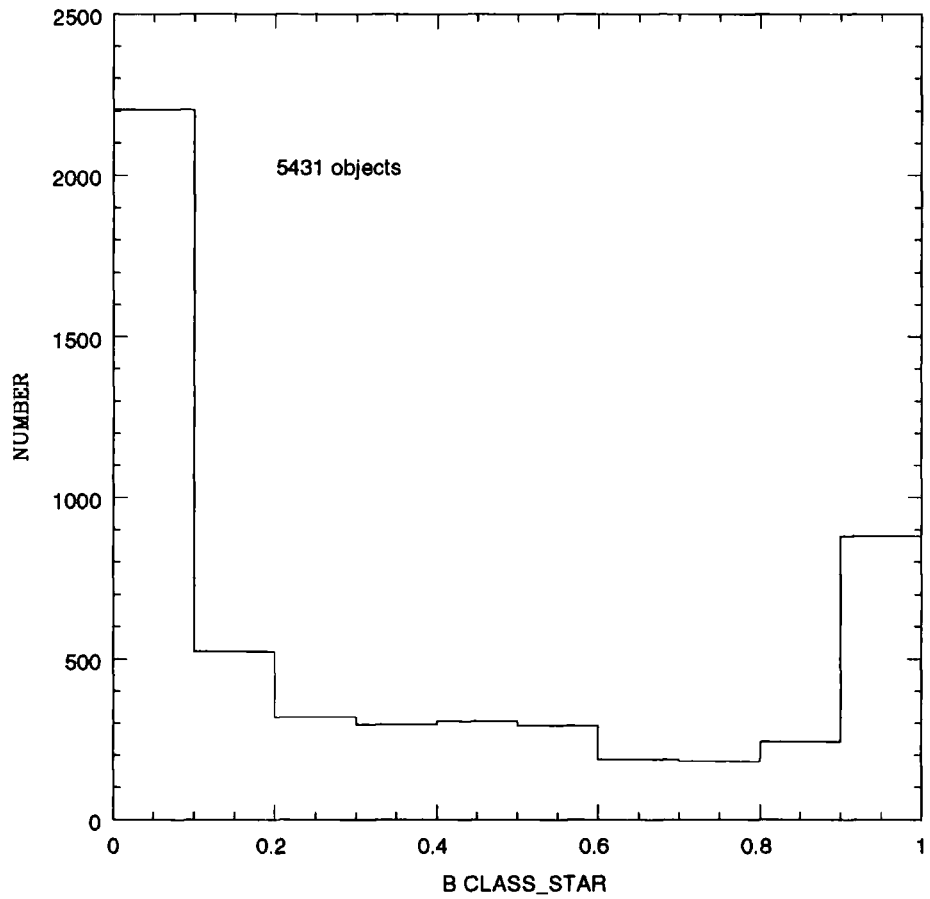

Figure 2.8: This plot shows how the B filter classes objects that satisfy R<17 and 0.1<CLASS_STAR< 0.9. Here we see a slightly different scenario to that shown in fig 2.7. Most of the these sources are classified as galaxies. The 2275 galaxies in this histogram is 15% of the total number already detected in the R band i.e. CLASS_STAR in the R band has effectively "missed" 15% of the galaxies. The corresponding number for the "missed" stars is 0.4%.

selection criterion	no. sources	no. gals	no. stars	star-star	star-gal	gal-gal
(a)	100	97	0	3	0	0
(b)	100	88	4	8	0	0
(c)	100	82	5	13	0	0

Table 2.3: This table shows results of eyeball tests of our NGC galaxy sample for stellar contamination. There are three selection criterion, a, b and c, which are dictated by our star/galaxy separation rule (see main text). (a) is for sources with CLASS_STAR<0.1 in B and R, (b) for CLASS_STAR<0.1 in B and CLASS_STAR<0.5 and (c) is for sources with CLASS_STAR<0.2 in R and CLASS_STAR<0.5 in B. The percentages of sources relative to the total number in the galaxy sample satisfying each selection criterion is 64% , 22% and 13% for (a), (b) and (c) respectively. Taking these relative proportions into account along with the number of stars and double stars found in our galaxy sample, this implies a 3x0.64+12x0.22+18x0.13=6.9% figure for our stellar contamination in both B and R.

There are two main reasons why the classification of a source seems to be "more certain" in a particular filter when the situation was unclear in the other filter. Firstly, there is a column of interpolated pixels on the lower portion of the chip. If a source falls in this region in one filter then it almost never does in the other filter due to the fact that the telescope has let the sky move over by a quarter of a chip and therefore the source is detected on a different set of pixels in the other filter. The second reason is due to cosmic rays. A cosmic ray can fall on or very near a source, meaning it gets blended with the star/galaxy (and is not written to the cosmic ray file), making it difficult for the software to ascertain the source morphology. In the other filter the cosmic ray is of course not present and the software is then able to ascertain the nature of the source. There are, however, close pairs of sources, that get blended by the SExtractor software, and on the vast majority of occasions the CLASS_STAR parameter lies in the 0.1<CLASS_STAR<0.9 range in both filters. On rare occasions, blended double stars, blended stars and galaxies and blended galaxies are classed as galaxies in both filters, which will be a source of stellar contamination to our galaxy sample. This unwanted blending is inevitable given the large pixel size of our CCD chip.

Using the information gained about the CLASS_STAR parameter in the two filters it is possible to define a more reliable star/galaxy separation. We choose to define our star/galaxy separation as a source having: (CLASS_STAR<0.1 in B AND CLASS_STAR<0.5 in R) OR (CLASS_STAR<0.2 in R AND CLASS_STAR<0.5 in B). We found, by using eyeball checks and comparing with external galaxy data, that making this galaxy criterion slightly stricter meant losing a large number of galaxies with the stellar contamination decreasing relatively little. On the other hand, relaxing the galaxy criterion meant gaining a few galaxies with the stellar contamination increasing by a relatively large amount. Therefore, the star/galaxy separation described gave the optimum ratio of galaxy to stellar numbers within the CLASS_STAR parameter space.

By choosing the star/galaxy criterion we have just described and effectively combining the information from each filter, we now expect to have minimized the errors on our source classification. However, eyeball checks were made of sources in each filter in the NGC in order to provide an alternative estimate of the stellar contamination in our galaxy sample. These eyeball checks were performed on 300 galaxies with B<18 and R<17 in the following way. We checked 100 sources that had CLASS_STAR<0.1 in B and R (criterion (a)). We also checked 100 sources that satisfied the criterion of CLASS_STAR<0.1 in B and CLASS_STAR<0.5 in R (criterion (b)) and a further 100 with CLASS_STAR<0.2 in R and CLASS_STAR<0.5 in B (criterion (c)), thereby complying with our chosen star/galaxy criterion. The results are shown in table 2.3. Galaxies that satisfy criterion (a) are 63% of the total number in our galaxy sample. The corresponding figures for criterion (b) and (c) are 22% and 14% respectively. Taking these relative proportions into account along with the number of stars and double stars found in our galaxy sample, this implies a 3x0.63+12x0.22+18x0.13=6.87% figure for our stellar contamination in both B and R. No attempt was made to estimate the galaxy completeness with this check (this was done with the external checks below), as because our sources are relatively bright, stars outnumber galaxies by ~10:1 and this would mean checking 3000 galaxies in order to reduce statistical noise to the levels in the stellar contam-

ination check.

It is now useful to be able to check our star/galaxy separation against other reliable external sources. The Sloan Digital Sky Survey Commissioning data (SDSS - Yasuda et al. 2001) and the Millennium Galaxy Catalogue (MGC) (Driver priv. com.) are ideal for this purpose. Our equatorial strip in the North Galactic Cap overlaps with a large region of sky ($\sim$ 90 square degrees) for which SDSS data is now publicly available. By comparing our sources with those in the SDSS catalogue in this region it is possible to estimate not only the stellar contamination, but also the galaxy completeness of our sample. Figs. 2.9 and 2.10 show these plots in the B and R bands respectively.

Fig. 2.9 shows, *at least*, a 90% galaxy completeness level in our B band for magnitudes brighter than B=18. The stellar contamination to our galaxy sample is, at most, 10% for the same magnitude range. We already know that our star/galaxy separation begins to break down for B>18 (see fig 2.5) and so we expect the galaxy completeness to decrease and the stellar contamination to increase here. Fig. 2.10 shows a similar trend with our R band data, except that the completeness begins to drop at R=16.5, but it is still equal to 84% for R=17. The stellar contamination shows a steady rise for R>16 and these two effects are again explained by the corresponding star/galaxy separation plot for the R filter in Fig 2.6.

We now do a similar check with the Millennium Galaxy Catalogue (MGC) in the B band, kindly supplied to us by Simon Driver. Fig. 2.11 shows a histogram of our galaxy completeness in 0.5 mag. bins and also the stellar contamination relative to the MGC. A better agreement is seen than with the SDSS data in Fig. 2.9 and we find that 100% of our source classifications agree for B<16. Even at B=18 we are still 93% complete with 5% stellar contamination. It should be noted that the MGC also used SExtractor for it's photometry and star/galaxy separation and therefore one would expect minimal systematic differences to be inherent between our galaxy catalogues.

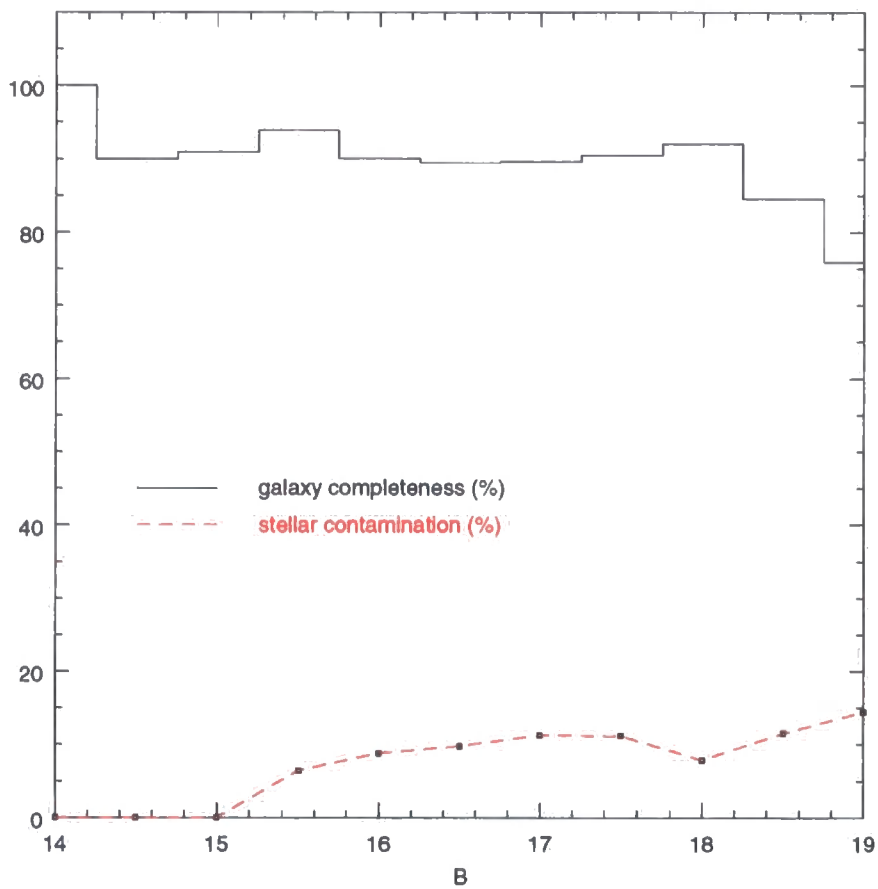

Figure 2.9: Here we show the completeness of our galaxy catalogue (the solid histogram) and the stellar contamination (the dotted line) relative to the SDSS data in the B band. The overlapping area totals 90 square degrees in our NGC equatorial strip.

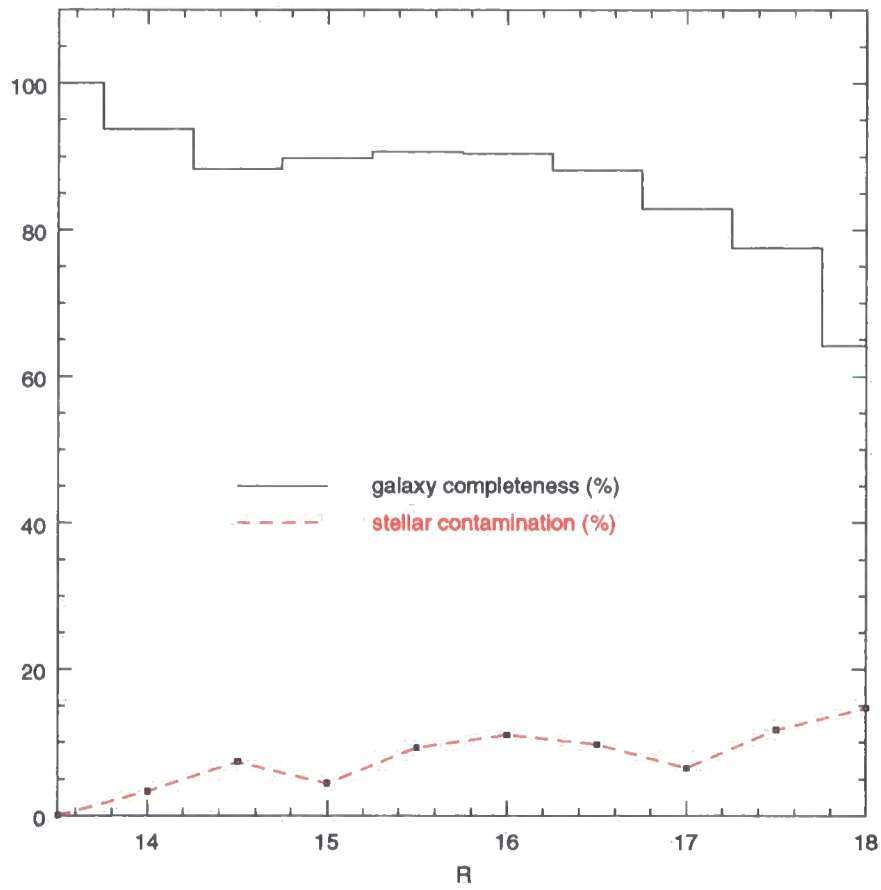

Figure 2.10: Here we show the completeness of our galaxy catalogue and the stellar contamination relative to the SDSS data in the R band. This comparison is performed over the same area described in fig 2.9.

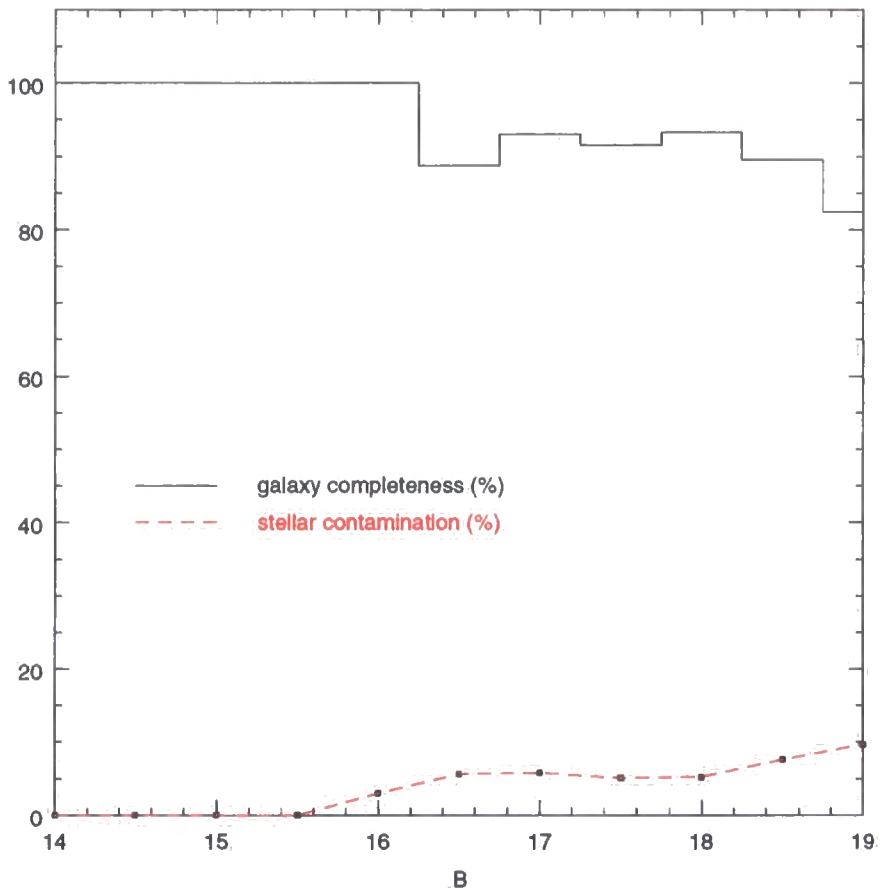

Figure 2.11: This plot shows our galaxy completeness (solid histogram) and stellar contamination (dotted line) compared to the MGC catalogue. In terms of the galaxy completeness we find perfect agreement for B<16 and at B=18 the corresponding figure is 93% with 5% stellar contamination. The overlapping area totals 32 square degrees in our NGC equatorial strip.

2.5 Photometry Comparisions

Now that we have our galaxy sample, it is important to check that our photometry is consistent with other very accurate CCD data-sets. First, in Fig. 2.12, we show a comparison with the MGC. As already mentioned, there is a 32 square degree overlap with our data in the North Galactic Cap, with 20,073 matching sources (stars and galaxies). The MGC photometry is also calculated using the MAG_BEST parameter in the SExtractor software and so we would expect good agreement. In this photometry comparison of all the sources, which will mostly be stars, there is excellent agreement in the 16<B<18 range with a mean offset of MGC-CTIO of 0.014 mags. The MGC go deeper than our survey and therefore the stellar photometry starts becoming unreliable due to saturation at a fainter magnitude limit than for us. The plot clearly shows where this occurs for B<16.0. Although the 1σ scatter on the residual is steadily increasing for B>18, due to our large pixel size, this rise is small and indicates we can still have confidence in our photometry - even at B=19.

Fig 2.13 shows the same comparison, but with just the matching galaxies from the two data-sets. The agreement is good, with negligible zero-point or scale errors. These 5,778 galaxies provide a very good check of our galaxy photometry in the B-band. Our magnitude errors can be seen to increase significantly for B fainter than 18th magnitude, as was the case with the stellar photometry comparison.

We can make a similar comparison with the SDSS data over the 90 square degree overlap region, using the g and r filters which need to be converted to our B Landolt band. The colour equation used in Yasuda et al. (2001) is:

$$B = g^\star + 0.482(g^\star - r^\star) + 0.169 \tag{2.17}$$

where $g^\star$ and $r^\star$ are in the AB magnitude system and the asterisks represent the fact that the SDSS photometry is preliminary. This relation has been derived from SDSS standard star work (Smith et al. 2001). By plotting B-$g^\star$ against $g^\star - r^\star$, shown in Fig 2.14 we can test this colour transformation for our galaxy sample. We in fact find the best fit line corresponds to the colour equation $B =$

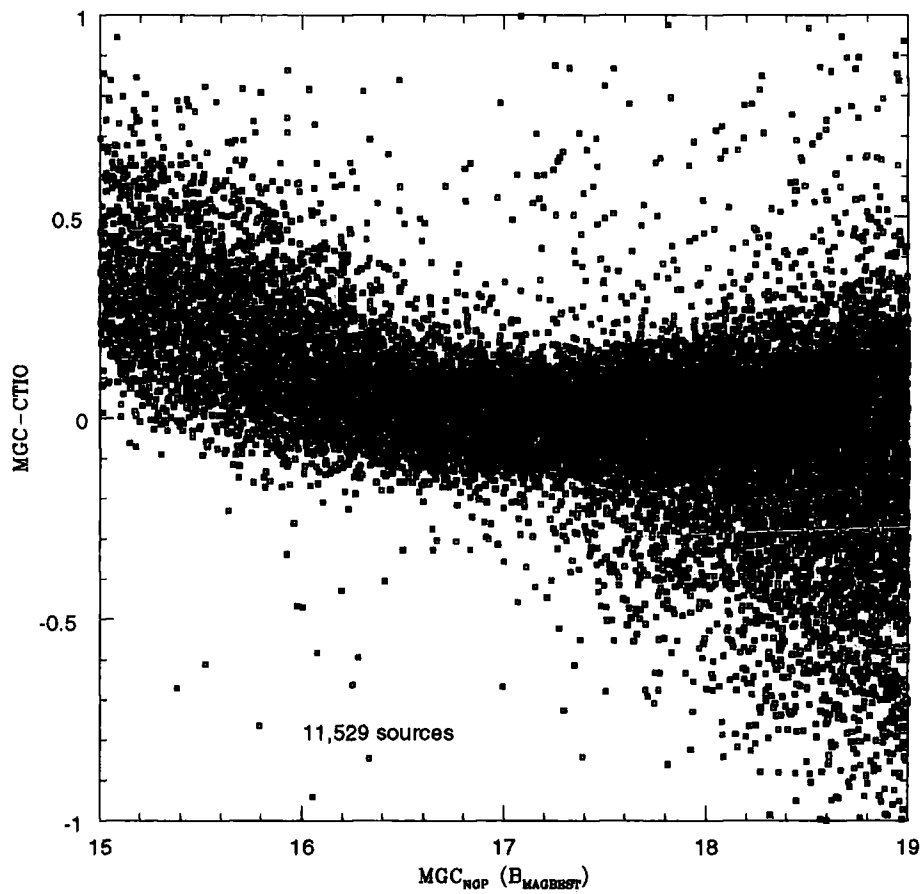

Figure 2.12: Our B-band CCD magnitudes are plotted against the difference between the MGC magnitudes and our magnitudes. The plot shows 11,529 matching sources (stars and galaxies) in an area of 32 square degrees in the North Galactic Cap. We find good agreement in the range 16<B<18 with a mean offset, MGC-CTIO=0.014 mags. The rms 1σ scatter around the value is 0.08 mags. For B>18 our photometry errors, due to our large pixel size and short exposure times, begin to increase and the effect can clearly be seen from the scatter in the residual. The problem of stellar saturation for the MGC catalogue is clearly visible for B< 16.

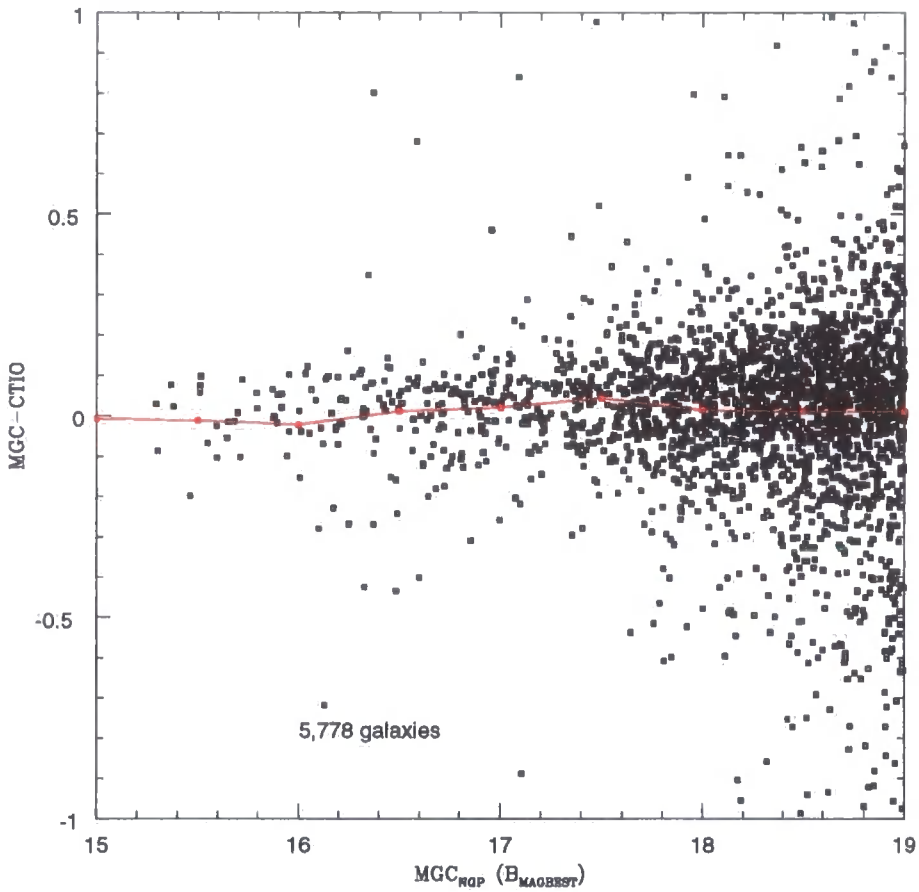

Figure 2.13: Our B-band CCD magnitudes are plotted against the residual of the MGC magnitudes and our magnitudes for galaxies common to both data-sets. The plot shows 5,778 galaxies and the black line connects the mean of the residual in each 0.5 magnitude bin. For B<18, we calculate a mean magnitude difference of MGC-CTIO=0.03 and a 1σ scatter of 0.1 about this value. For B>18, our photometry errors are observed to increase, which is unavoidable given the length of our exposures and size of our pixels. Note that galaxies present in the MGC catalogue with B<16 are not saturated on this plot due to the more extended nature of their intensity profile as compared to stars.

$g + 0.549(\pm 0.07) * (g^* - r^*) + 0.114$. The discrepancy between the colour terms, which is consistent with the ± 0.07 error, accounts for the 0.169-0.114=0.055 difference in the zero-point. In fact, if we insist on using the 0.482 colour term from Yasuda et al. (2001) then the zero-point difference (i.e. the average of the relation B-g*-0.482(g*-r*)-0.169 for all common galaxies between the SDSS and our CTIO survey) is less then 0.01 mag. The photometry system used for the SDSS data is new and the appropriate transformations to other band-passes are relatively poorly understood. This, combined with the fact that their photometry is still preliminary, could explain the discrepancy between the colour terms.

A comparison with the SDSS photometry, this time in the R Kron-Cousins pass-band, is shown in Fig. 2.15, where we have plotted the SDSS R_{kc} magnitude estimate against the magnitude difference SDSS(R_{kc})-CTIO(R_{kc}). The SDSS R_{kc} magnitude is calculated using the colour equation quoted in Blanton et al. (2001) of R_{GKC}=r*-0.05-0.089(g*-r*). A further correction is performed using the relation R_{GKC}-R_{kc}=0.08 (Shectman et al. 1996) in order to obtain an estimate of the SDSS R_{kc} magnitude. We find excellent agreement over the magnitude range shown in Fig. 2.15, with a mean zero-point difference of SDSS(R*kc*)-CTIO(R_{kc})=0.02($\pm$0.01).

We now show a further check of our galaxy R-band photometry in the NGC in Fig. 2.16 and also comparisons to our B and R data in the SGC, shown in Figs. 2.17 and 2.18 respectively. To do this we have used data from Metcalfe et al. (1998) of galaxies in the DARS GSA and GNB fields. Metcalfe et al. used the PDS microdensitometer at the Royal Greenwich Observatory to acquire accurate photometry for all the galaxies for which redshifts had been obtained in the DARS survey. This data is expected to show an intrinsic scatter of 0.06 mags. in both B and R. We plot the relevant magnitude against the magnitude difference between DARS and us in Figs. 2.16, 2.17 and 2.18 and find mean magnitude differences of -0.02$\pm$0.018, +0.02$\pm$0.02, and, -0.03$\pm$0.02 respectively. The 1σ standard deviations for the magnitude differences of 0.06, 0.1 and 0.1 are consistent with the intrinsic scatter of 0.06 expected from the DARS data, given that there are small photometry errors inherent within our data also.

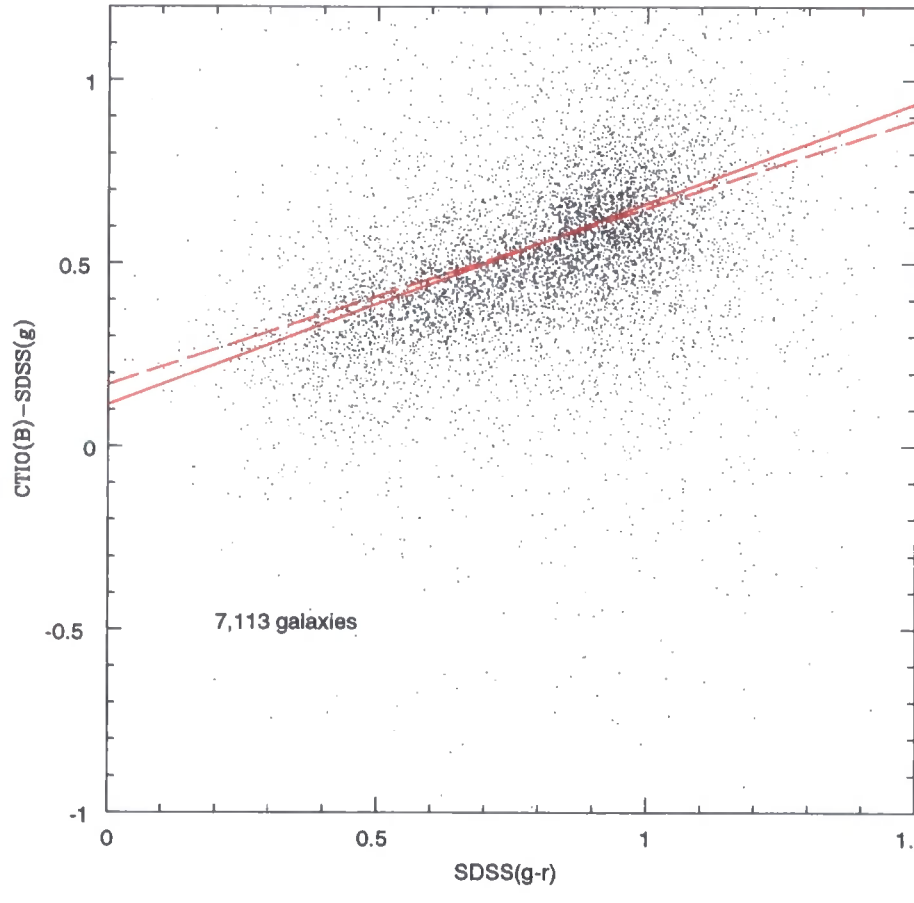

Figure 2.14: This plot shows the SDSS $(g^\star - r^\star)$ vs. CTIO(B)-SDSS($g^\star$) for 7,133 galaxies in the 90 deg^2 overlap region. The solid line shows the best fit to the data and corresponds to a colour equation of $B = g^\star + 0.549(\pm 0.07)(g^\star - r^\star) + 0.114$ as opposed to the relation $B = g^\star + 0.482(g^\star - r^\star) + 0.169$ (dashed line) quoted in Yasuda et al. (2001).

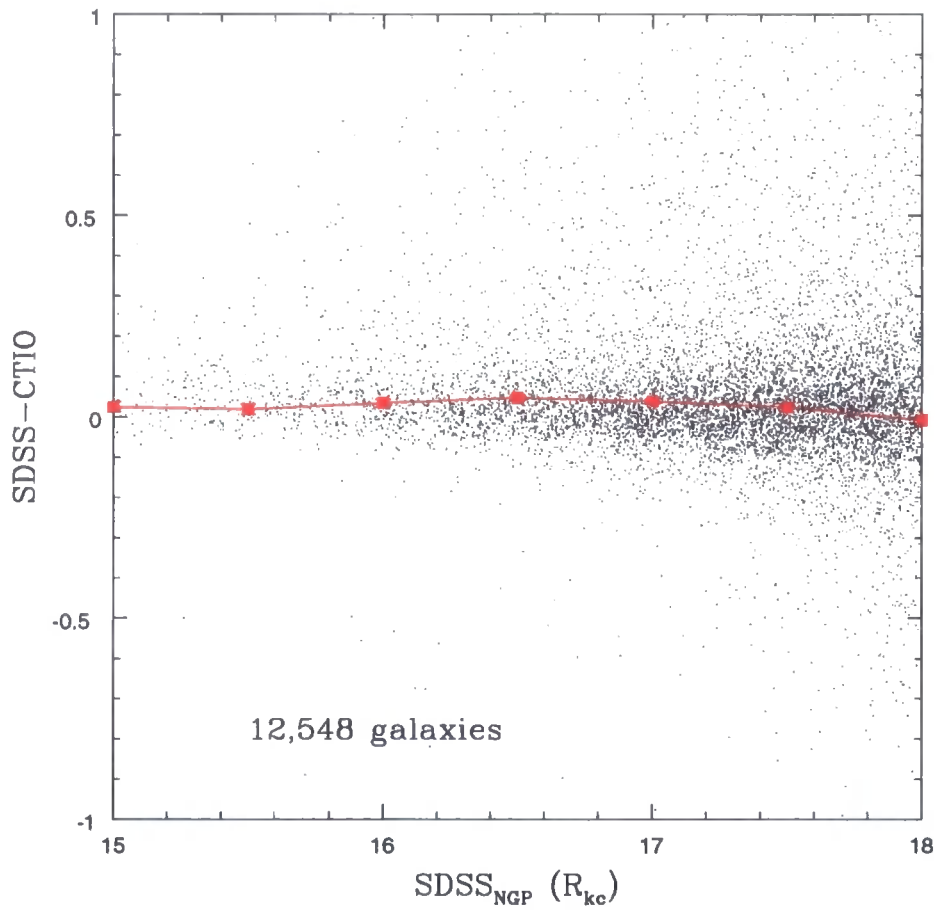

Figure 2.15: This plot shows a comparison with the SDSS photometry, but this time in our R Kron-Cousins pass-band. We have used the colour transformation, R_{GKC}=r*-0.05-0.089(g*-r*), quoted in Blanton et al. (2001) in order to transform to the R_{GKC} filter. The relation R_{GKC}-R_{kc}=0.08 is then used (Shectman et al. 1996) in order to obtain an SDSS magnitude estimate in our R Kron-Cousins filter. In this figure we have plotted the SDSS R_{kc} magnitude vs the quantity SDSS(R_{kc})-CTIO(R_{kc}) with the mean of the magnitude difference plotted in half magnitude bins. Excellent agreement is seen over the magnitude range shown with a mean zero-point difference of SDSS(R_{kc})-CTIO(R_{kc})=0.02($\pm$0.01)

2.6 Summary

In this chapter we have explained the procedures involved in our data reduction such as astrometry calibration, star/galaxy separation and source extraction. We also performed several checks of our photometry using data-sets such as the Sloan Digital Sky Survey, the Millennium Galaxy Catalogue and the Durham AAT Redshift Survey. A summary of the key points of our data reduction as well as the photometry comparisons of our NGC and SGC data in each of the filters, B and R, are presented below:

- Our final reduced galaxy sample covered 255 deg^2 and 297 deg^2 in the North and South Galactic Caps respectively. Our SGC data was entirely contained in the 2dF SGC strip, whereas about two-thirds of our NGC galaxy sample was contained in the NGC 2dF strip.

- Using the SDSS and MGC galaxy catalogues we found typical galaxy completeness levels in our catalogue of 90% and stellar contamination of 5-10% for B<18 and R<17.

- Photometry Comparisons:

  1. NGC B-band.

  (a) Millennium Galaxy Catalogue comparison over a 32 square degree area. Excellent agreement for both the star and galaxy comparison with a 1σ scatter of 0.08 and 0.1 respectively in the range 14<B<18. The accuracy of our photometry starts to deteriorate for B>18, but is still reliable at B=19 where the 1σ scatter is 0.18 mag. For B>19 the errors on our magnitudes increase markebly and this is inevitable due to our large pixel size and relatively short exposure times.

  (b) Sloan Digital Sky Survey. A 90 square degree comparison which showed a 0.05 mag. offset for galaxies. A possible explanation is the value of the colour term used in the transformation equation by the SDSS team to convert from g-r to the B band. We find a slightly higher colour term of 0.549, but if we

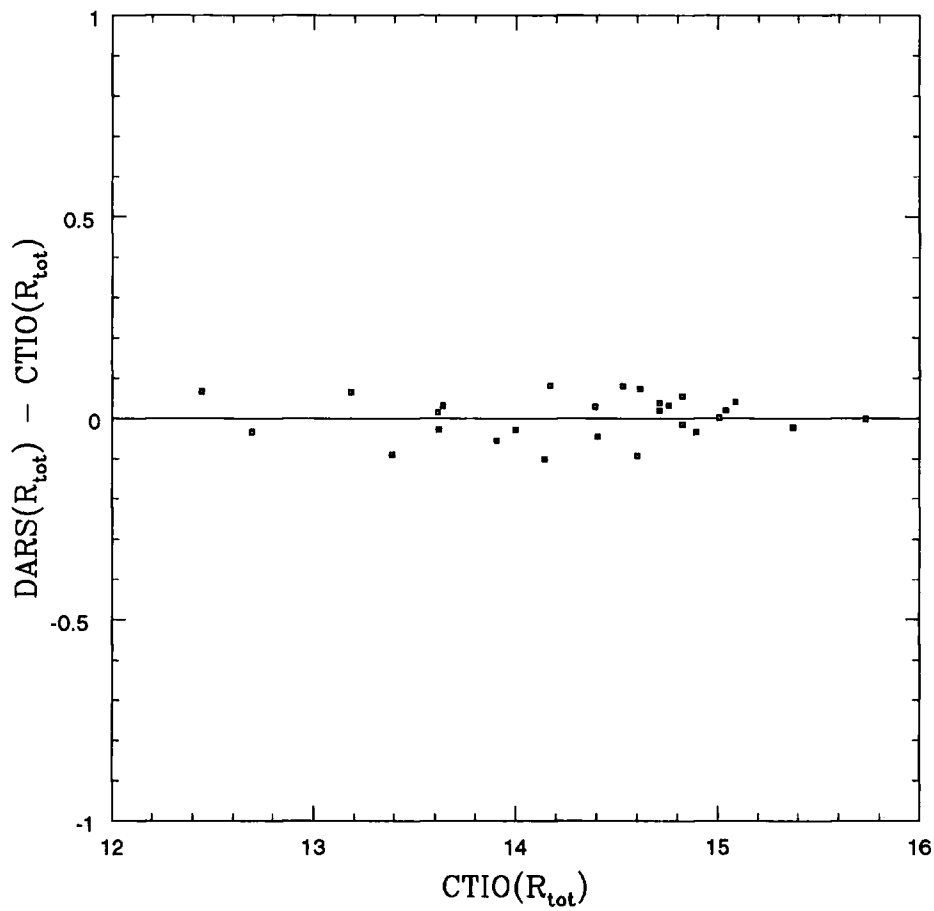

Figure 2.16: This DARS GNB field R-band comparison consists of 27 galaxies with the residual of the magnitudes all less than 0.1 with a mean offset, DARS-CTIO=-0.02$\pm$0.018 mag. The data shows a 1σ standard deviation of 0.06 mag, consistent with the errors quoted in Ratcliffe et al. (1998). The photometry of this DARS data was obtained using the PDS microdensitometer at the Royal Greenwich Observatory.

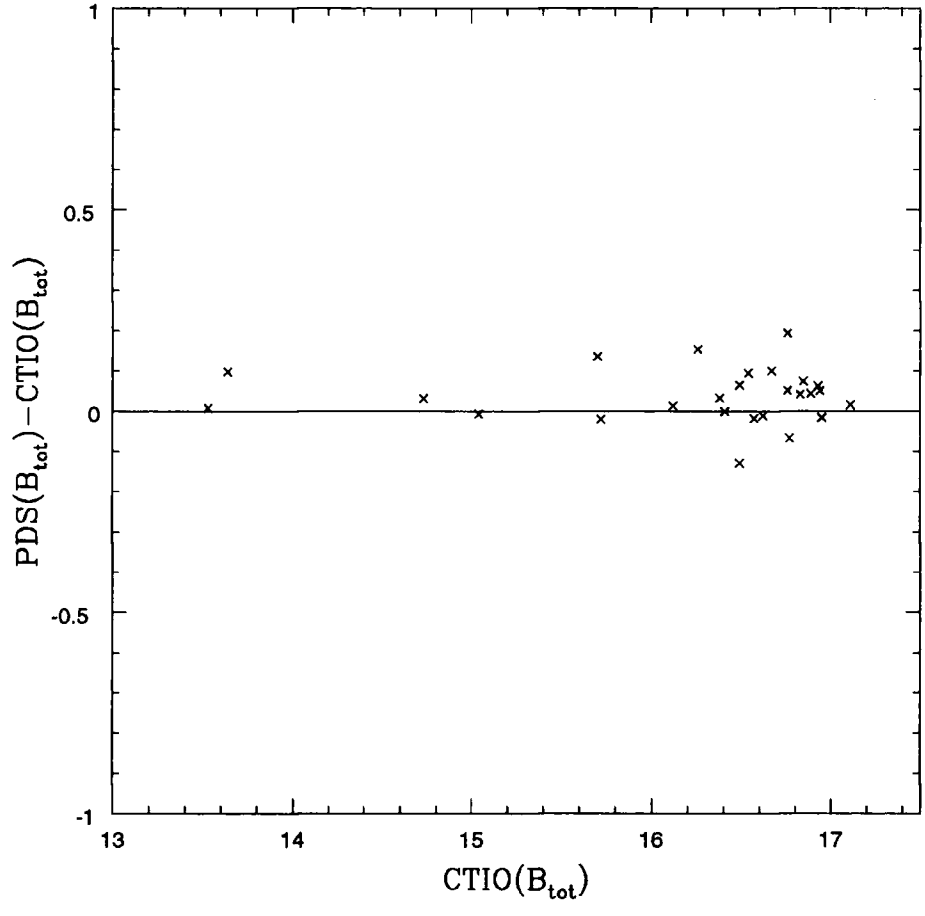

Figure 2.17: The DARS GSA field B-band comparison for our SGC data. This DARS GSA photometry was obtained using the PDS microdensitometer at the Royal Greenwich Observatory (Ratcliffe et al. 1998). We find a mean magnitude offset of 0.02 ± 0.02 and a 1σ rms scatter of 0.1 for the 27 galaxies used in the comparison

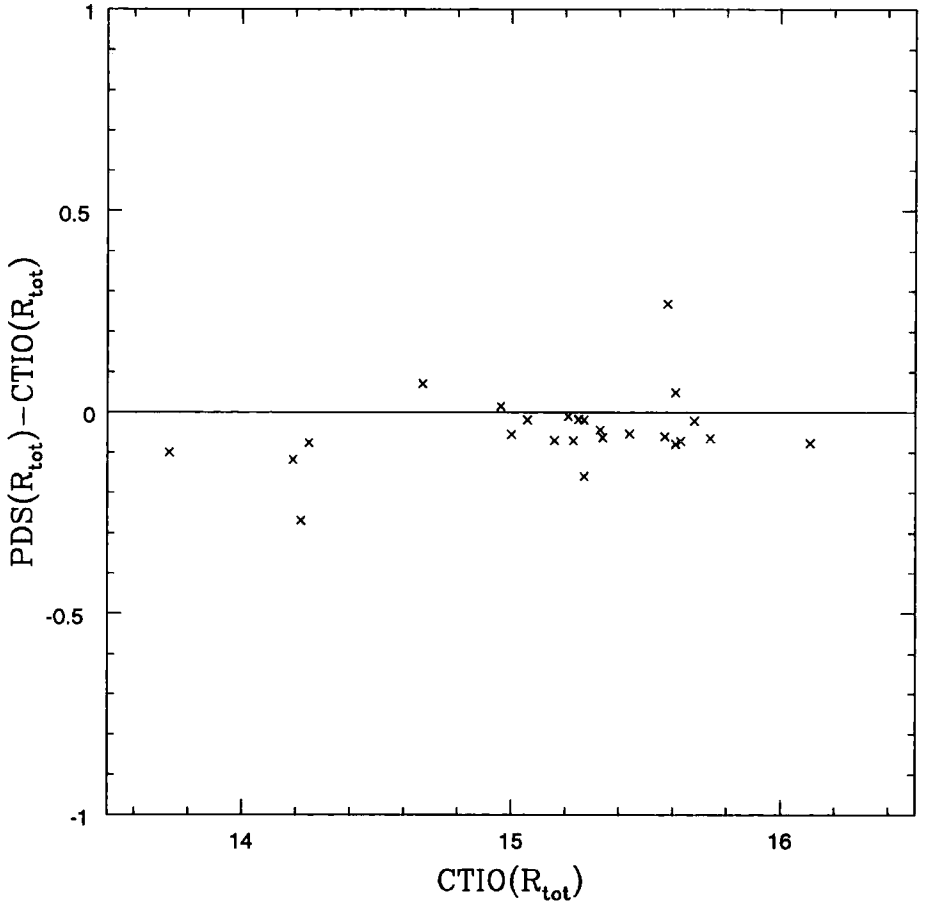

Figure 2.18: The DARS GSA field R-band comparison for our SGC data. This DARS GSA photometry was obtained using the PDS microdensitometer at the Royal Greenwich Observatory (Ratcliffe et al. 1998). We find a mean magnitude offset of -0.04$\pm$0.02 and a 1σ rms scatter of 0.1 for the 27 galaxies used in the comparison.

insist on using their 0.482 colour term when finding the best fit colour transformation then we recover the zero-point of the SDSS team to within 0.01 mag.

2. NGC, R band.

(a) Sloan Digital Sky Survey. We find good agreement with a $0.02(\pm 0.01)$ zero-point difference and an rms scatter of 0.1 mag. between our data and that of the SDSS R_{kc} magnitude estimates.

(b) DARS GNB data. Using photometry obtained using the PDS microdensitometer at the Royal Greenwich Observatory (Ratcliffe et al. 1998) we found a -0.02 mag offset with a 0.06 rms scatter for the 27 galaxies used in the comparison.

3. SGC, B band.

DARS GSA data. Again using the PDS calibrated DARS data, this time from the GSA field with 27 matching galaxies, we found a +0.02 offset, with an rms scatter of 0.1.

4. SGC, R band.

Using the same galaxies as in the B band, SGC comparison, we find a -0.03 magnitude offset and an rms scatter of 0.1.

Chapter 3

Bright Galaxy Counts: Results and Modelling

3.1 Introduction

In the last chapter we outlined the reduction of our CTIO, Curtis Schmidt data covering ~550 deg^2 in the Landolt B and R band-passes. We also performed scale and zero-point checks of our photometry as well as estimates of the completeness of our galaxy sample and the contamination from stars. In this chapter we first present our resulting galaxy number counts in each filter for the NGC and SGC fields covering 255 and 297 deg^2 respectively. We also present B-band star counts for our NGC and SGC fields. In section 3.3 we explain the galaxy number count model of Metcalfe et al. (2001), which we use to predict the expected number of galaxies in the Universe as a function of apparent magnitude, as well as number:redshift distributions for a given apparent magnitude limit. In section 3.4 this model will then be used, in conjunction with data from the APM Bright Galaxy Catalogue (APMBGC), the Durham/UK Schmidt Redshift Survey (DUKST), the 2-Degree Field Galaxy Redshift Survey (2dFGRS), and the 2-Micron All Sky Survey (2MASS), to investigate the existence of a possible "hole" in the local distribution of galaxies in the SGC. In section 3.5 we discuss the results of this modelling before summarizing in section 3.6.

3.2 CTIO Number Counts

Figs 3.1 and 3.2 show our galaxy number counts in the B and R bands respectively, which are both corrected for galactic extinction using the Schlegel et al. (1998) dust maps. Our B-band number counts in the NGC agree very well, firstly with

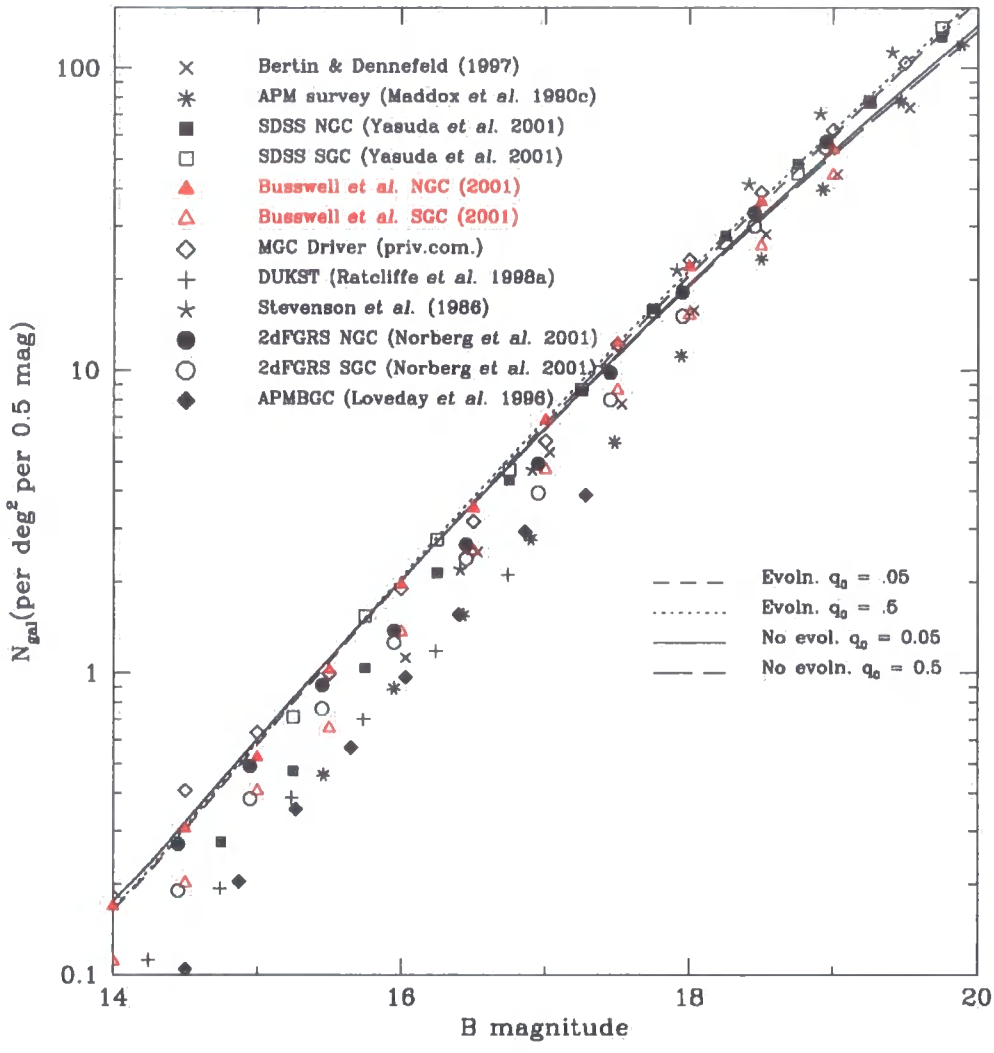

Figure 3.1: Our B band galaxy number counts. The filled and unfilled triangles show our number counts in the North and South Galactic Caps respectively. The filled and unfilled squares show the SDSS Commissioning Data in the Northern and Southern equatorial strips (Yasuda et al. 2001), the circles the 2dFGRS data, the diamonds the Millenium Galaxy Catalogue (Driver priv. com.) results, the x's the data of Bertin & Dennefield (1997) and the star-like symbols show the data of Stevenson et al. (1986) and the APM counts (Maddox et al. 1990c). The crosses show the Durham/UKST data of Ratcliffe et al. (1998) and the filled diamonds the APM bright galaxy data (for B<16.6 - at B>16.6 the filled diamonds illustrate the APM-Stromlo counts) of Loveday et al. (1996). The curves are Pure Luminosity Evolution (PLE) models of Metcalfe et al. (2001) and they are explained further in section 3.3. See text for details of dust corrections.

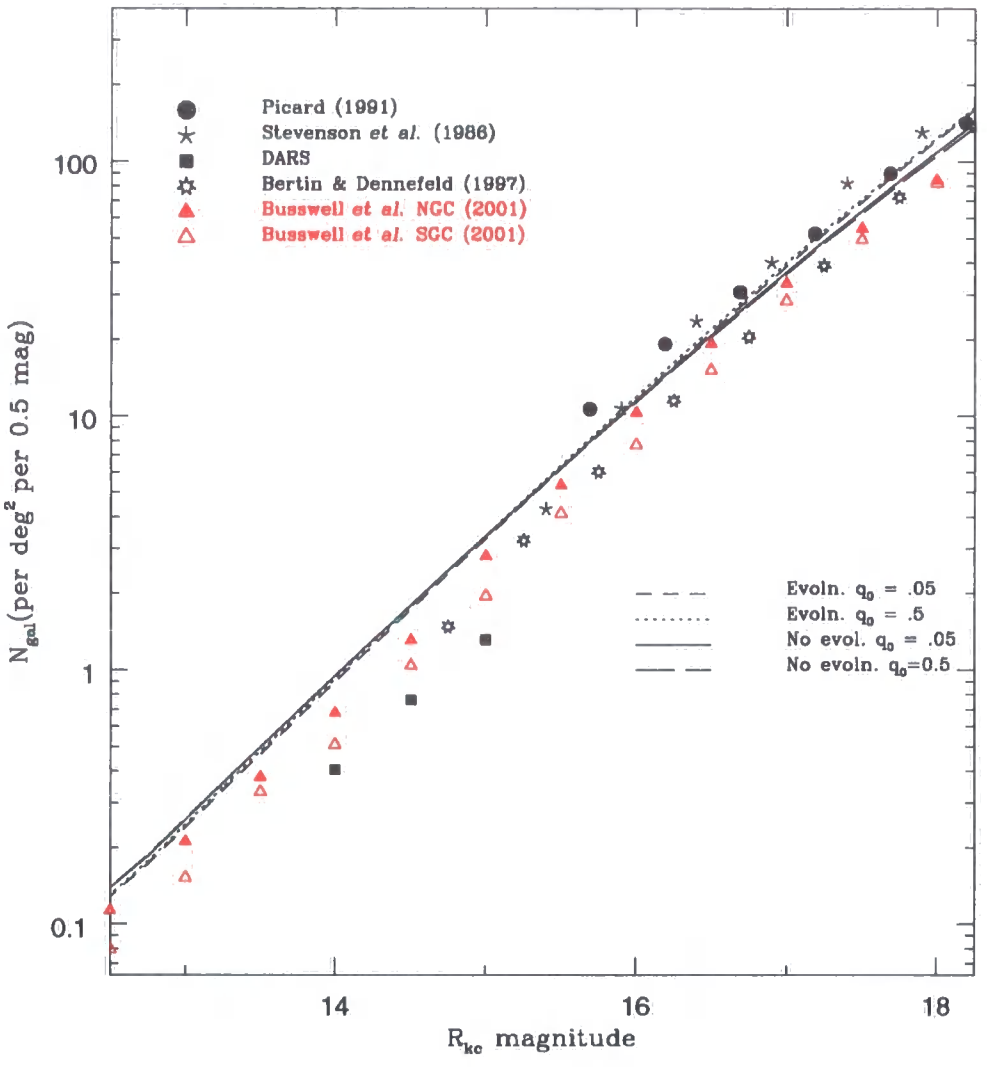

Figure 3.2: Our R band galaxy number counts. The filled and unfilled triangles show our number counts in the North and South Galactic Caps respectively. The filled circles show the data of Picard (1991), the skeleton stars that of Stevenson et al.(1986), the filled squares are the DARS data (Metcalfe et al. 1998) and the open stars show the data of Bertin & Dennefield (1997). The curves are Pure Luminosity Evolution (PLE) models of Metcalfe et al. (2001) which assume the presence of dust in late type spiral galaxies. The models are explained further in section 3.3. See text for details of dust extinction corrections.

	N_{gal}^{NGC}deg^{-2}0.5mag^{-1}	N_{gal}^{SGC}deg^{-2}0.5mag^{-1}	N-S discrepancy (%)
12.25-12.75	0.031	0.017	45.2
12.75-13.25	0.047	0.024	48.9
13.25-13.75	0.066	0.067	-1.5
13.75-14.25	0.168	0.111	33.9
14.25-14.75	0.305	0.201	34.1
14.75-15.25	0.524	0.406	22.5
15.25-15.75	1.021	0.655	35.8
15.75-16.25	1.959	1.367	30.2
16.25-16.75	3.508	2.535	27.7
16.75-17.25	6.855	4.714	31.2
17.25-17.75	12.353	8.619	30.2
17.75-18.25	22.059	15.283	30.7
18.25-18.75	36.047	25.779	28.5
18.75-19.25	53.604	44.353	17.3
19.25-19.75	59.521	76.012	-27.7

Table 3.1: Here we show our dust-corrected B-band number counts in half magnitude intervals for our NGC and SGC fields. We have also shown the number discrepancy (as a percentage) of the SGC data relative to the NGC data.

the SDSS data in the magnitude range 16.5 <B< 18.5 and also with the MGC for 15.5 <B< 18.5. It should be noted that all three data sets were taken in overlapping regions of sky - a 32 and 90 deg^2 overlap with the MGC and SDSS data respectively in the NGC. Our CTIO data also overlaps with 163 deg^2 of the 2dFGRS in the NGC and 297 deg^2 in the SGC. Our SGC number counts agree extremely well the 2dFGRS, which is important given the large overlap, but our NGC data is showing significantly more galaxies than that of the 2dF team. This could be due to real differences in the galaxy number density between the current 740 deg^2 2dF field and our 297 deg^2 field, or due to zero-point/scale differences in the galaxy photometry (see section 4.4.1).

The shape and normalisation of our NGC number counts also agrees remarkably

	N_{gal}^{NGC}deg^{-2}0.5mag^{-1}	N_{gal}^{SGC}deg^{-2}0.5mag^{-1}	N-S discrepancy (%)
11.25-11.75	0.019	0.020	-0.5
11.75-12.25	0.094	0.043	54.3
12.25-12.75	0.113	0.079	30.1
12.75-13.25	0.211	0.152	28.0
13.25-13.75	0.379	0.331	12.7
13.75-14.25	0.676	0.509	24.7
14.25-14.75	1.309	1.036	20.9
14.75-15.25	2.810	1.956	30.4
15.25-15.75	5.315	4.136	22.2
15.75-16.25	10.294	7.683	25.4
16.25-16.75	19.157	15.078	21.3
16.75-17.25	33.120	28.317	14.5
17.25-17.75	54.423	49.305	9.4
17.75-18.25	84.271	82.154	2.5
18.25-18.75	113.543	124.624	-9.8

Table 3.2: Here we show our dust-corrected R-band number counts in half magnitude intervals for our NGC and SGC fields. We have also shown the number discrepancy (as a percentage) of the SGC data relative to the NGC data.

well with the no-evolution predictions of the low-q_0 model (see section 4.3 for model details) from B=18 to as bright as B=14. The shape of our B-band number counts in the SGC agrees well with our NGC data set, but the striking difference is that of the normalisation, which is calculated in each 0.5 magnitude interval in Table 3.1 We a find an average 30.7% deficiency in galaxy numbers for our southern data compared to the north in the magnitude range 14<B<18. At B=19 this normalisation discrepancy has dropped to 17.3% , although it should be noted that our galaxy incompleteness is a factor in this magnitude bin (see Fig. 2.9). The 2dF number counts also show a north-south difference, but only 20% in galaxy numbers at B=18, with this difference virtually zero at B=19. The survey area of our SGC data was a subset of the 4300 deg^2 sky covered by the APM galaxy catalogue and our SGC number counts agree very well with the APM counts despite the order of

magnitude less of sky coverage on our part. Our SGC number counts also agree well with the CCD data of Bertin & Dennefeld (1997), who cover 62 and 83 square degrees at high declinations ($|\delta| > 40°$ in the North and South Galactic Caps respectively. Our CTIO counts, the 2dFGRS and MGC counts and those of Yasuda et al. have all been corrected for dust using the Schlegel et al. (1998) extinction maps. The APM and DUKST counts and those of Bertin & Dennefield are not corrected for dust and the reason for this was that the vast majority of all these observations were in the SGP where it was orginally thought dust extinction was negligible. In fact Schlegel et al. predict values of 0.03 in the B-band at the SGP and an average of 0.08 over the whole SGC.

Our R-band galaxy counts show a similar trend in the normalisation difference, where the number discrepancies of the SGC counts relative to those in the NGC are tabulated in Table 3.2. The average percentage discrepancy is 22.2% in the 13<R<17 range, and again this normalisation difference drops for fainter magnitudes. At R=18 there is only a 2.5% discrepancy in the galaxy numbers, although galaxy incompleteness is again a factor (see Fig. 2.10). The shape of both the data sets in the 13<R<17 range is consistent with the no-evolution models, but there is a slight normalisation discrepancy in that all the data sets show less galaxies compared to the models for R< 15.5. There is a noticeable dip in both our number counts compared to the models between about R=13.5 and R=15.5 and there is good agreement with Bertin & Dennefield, as in the B filter. Our data lies substantially below that of Picard et al. (1991), who cover 386 square degrees in both the NGC and SGC. In Fig. 3.1 our CTIO number counts have been corrected for dust using the Schlegel et al. (1998) extinction maps but none of the other data sets were de-reddened when originally published. This is because, either it was originally thought that a particular data-set suffered from negligible extinction, as in the case of the Stevenson points in the SGC, or the reddening correction was not known due to the absence of any accurate dust maps at the time of publication eg. Picard (1991).

Fig 3.3 shows our star number counts from regions of sky in the SGC and NGC

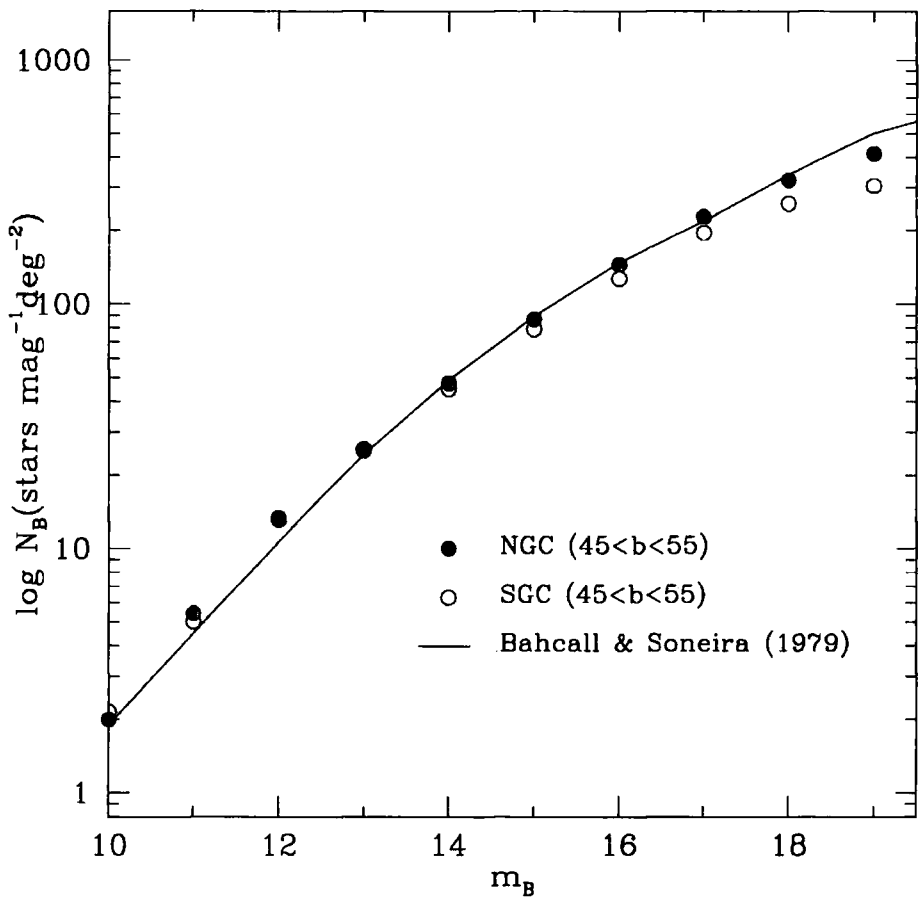

Figure 3.3: Our B band star counts. The filled circles show the NGC data which was observed in the galactic latitude range 45° <b<55° and galactic longitude range 242° <l<3°. This data covers 145 deg^2 of sky and therefore 57% of our entire NGC dataset. The open circles show the SGC data with -45>b>-55, which corresponded to a longitude range of 216° <l<30° and covered 62 deg^2. All these observations have been corrected for dust using the Schlegel et al. (1998) extinction maps. The solid curve shows a model from Bahcall & Soneira (1980), which predicts the differential star counts in the B band at b=50° and is averaged over all longitudes. Our observations at b=50° cover a large range of galactic longitude in both the NGC and SGC enabling good coverage of the bulge and disk of our galaxy and are therefore suitable for comparison with the model curve. The NGC and SGC data show good agreement with the model for B<18 and B<17 respectively. We know that the errors on our B band photometry increase markedly for B>18 and we cite this as the reason for the observed differences in this magnitude range. The SGC data covers only 62 deg^2 - a relatively small angular sky coverage.

that satisfied the criterion of the galactic latitude being in the range $45° < |b| < 55°$. This corresponded to 145 and 62 deg^2 for the NGC and SGC respectively. The solid line shows a model taken from Bahcall & Soneira (1979), which predicts the star counts averaged over all longitudes at a constant latitude b=50°. The NGC and SGC data show good agreement for B<18 and B<17 respectively and the under-prediction of the model at faint magnitudes could be due to the large errors on our photometry for B>18. Also, our plotted star counts in the SGC only covers 62 deg^2- a relatively small area.

3.3 The Galaxy Count Model

In this section we outline the Pure Luminosity Evolution (PLE) model of Metcalfe et al. (2001) which we have used in Figs 3.1 and 3.2. This is a simple model that assumes no density evolution of the galaxy population, but instead a morphological dependent luminosity evolution using the predictions of Bruzual & Charlot (1993). Although this evolution is essential for the faint (B>20) galaxy population, in order that these models do not under-predict the data by an order of magnitude (see Metcalfe et al. 2001 for a detailed description of faint galaxy number counts), it is virtually negligible in the redshift range of 0<z<0.15 where our CTIO data is probing. We split the model into 3 parts, which are described below.

3.3.1 Cosmological Relations

We know that the further away a particular galaxy is from the us the fainter it should appear. The luminosity distance d_L in Mpc's is defined in a relativistic Universe by the Friedman relation:

$$d_L(z) = \frac{c}{H_0 q_0^2}(q_0 z + (q_0 - 1)[(1 + 2q_0 z)^{\frac{1}{2}} - 1]) \tag{3.1}$$

where z is the redshift of the observed source, c is the speed of light and q_0, H_0 are the deceleration parameter and Hubble constant respectively. Note that in the limit $z \to 0$, d_L follows a Newtonian inverse square law model. The luminosity distance, d_L can then be used to calculate the absolute magnitude, M, of a galaxy as a function

of z and the apparent magnitude m, via the relation:

$$M(m,z) = m - k(z) - E(z) - 5log\left(\frac{d_L}{1\text{x}10^{-5}\text{Mpc}}\right) \tag{3.2}$$

where K(z) and E(z) are the k-correction and evolution correction respectively. The k-correction, k(z) is an empirically-derived correction to account for the alteration in frequency due to cosmological reddening of a galaxy's spectrum. This reddening shifts higher energy parts of the spectrum into the observed passband as compared to a galaxy observed at redshift zero. The k-corrections and evolution corrections, often written as (k+e)(z), are predicted by the Bruzual & Charlot (1993) models. These models correct for the fact that a particular filter is sampling bluer and bluer parts of the galaxy SED as one probes higher redshifts (the k-correction) and also that a galaxy is intrinsically brighter at higher redshift (the evolution correction). In fact, because we are modelling the local Universe the evolution correction is a tiny fraction of the k-correction at the low redshifts ($z<0.15$) we are probing. We adopt H_0=100 kms^{-1}Mpc^{-1} and q_0=0.05 for the rest of this section, but our results are relatively independent of our choice of these values because we are measuring distances in the local Universe. We define one further relation, the co-moving cosmological volume element differentiated with respect to redshift (subsequently written as $\frac{dV}{dz}$):

$$\frac{dV}{dz} = \frac{4\pi c d_L^2}{H_0(1+z)^3(1+2q_0z)^{\frac{1}{2}}} \tag{3.3}$$

where d_L is the luminosity distance defined in equation 3.1.

3.3.2 The Luminosity Function

The Luminosity Function, ϕ (Schechter 1976), describes the number of galaxies per unit magnitude per unit volume:

$$N(M,z)dMdz = \phi(M)dM\frac{dV}{dz}dz \tag{3.4}$$

where N(M,z) is the number of galaxies in the magnitude interval M to M+dM and in the redshift interval z to z+dz.

	E/SO	Sab	Sbc	Scd	Sdm
$\phi^\star$	$7.42\text{x}10^{-3}$	$3.70\text{x}10^{-3}$	$4.96\text{x}10^{-3}$	$2.18\text{x}10^{-3}$	$1.09\text{x}10^{-3}$
α	-0.7	-0.7	-1.1	-1.5	-1.5
$M^\star_B$	-19.35	-19.38	19.72	19.87	19.88
B-R	1.59	1.38	1.16	0.84	0.75

Table 3.3: The B-band Schechter parameters used in the Metcalfe et al. (2001) model assuming H_0=100kms^{-1}Mpc^{-1}. The Hubble classification is used to indicate the morphological type in the first row. The B-R colour is a function of galaxy type and is used to obtain the corresponding R-band Schechter parameters.

The functional form of the Luminosity Function using absolute magnitudes is:

$$\phi(M)dM = 0.92\phi^\star exp[-0.92(\alpha+1)(M-M^\star) - exp[-0.92(M-M^\star)]]dM \quad (3.5)$$

where M* defines the characteristic magnitude, $\phi^\star$, the normalisation and α the faint end slope. The values of these parameters are dependent on the morphological type and we use the B-band model of Metcalfe et al. (2001) shown in Table 3.3.

An important ingredient of the model is the inclusion of internal dust extinction, with $A_\lambda \propto 1/\lambda$ (Metcalfe et al 1996; Campos & Shanks 1997) for late-type spiral galaxies, allowing a good fit to the B-band number:redshift distribution at high redshift. Again, this is not relevant for our purposes of the optical bright galaxy population but we will see in Chapter 6 how this dust can have important consequences in terms of the nature of the newly discovered high redshift sub-mm population.

3.3.3 Number Count and N(z) Predictions

It is then straight-forward to calculate number:magnitude and n(z) predictions given the model described in 3.3.1 and 3.3.2. The galaxy normalisation is assumed not change as a function of redshift and so the galaxy number count as a function of apparent magnitude, n(m), in a particular passband can be obtained by an integral over redshift:

$$n(m)dm = \int_0^{\infty} \phi[M(m,z)] \frac{dV}{dz} dmdz \tag{3.6}$$

where M(m,z) is calculated from equation 3.2. The n(z) relation can be written in a similar way except the integration is performed over the all possible absolute magnitudes so that:

$$n(z)dz = \int_{M=-\infty}^{M=\infty} \phi[M(m,z)] \frac{dV}{dz} dzdM \tag{3.7}$$

3.4 A "Local hole" in the Universe?

In Section 3.2 we presented out CTIO number counts in the NGC and SGC in Figs 3.1 and 3.2. . It is clear from our data that there is a large number discrepancy of galaxies in the magnitude range 14<B<18 of 30.7% in the SGC relative to the NGC. The APM Galaxy Survey found similar number counts as a function of magnitude, but in a much bigger 4300 deg^2 in the SGC, although due to the known problems of errors in photographic photometry it is not clear the size of this under-density found by the APM survey over such a huge volume of space is real. We will attempt to address in this section, using data from the APM Galaxy Bright Galaxy Catalogue (Loveday et al. 1996), the DUKST (Ratcliffe et al. 1998b), the 2dFGRS (Cole priv. com.) and publicly available 2MASS photometry, the question of the depth and angular size of this "hole" in the local distribution of galaxies in the SGC.

3.4.1 The APM Bright Galaxy Photometry Correction

In order to investigate the APM photometry at bright magnitudes we have used our CTIO SGC data (our un-dust-corrected magnitudes), covering 297 deg^2, to check the accuracy of the publicly available APM Bright Galaxy Catalogue (APMBGC). This data reaches a magnitude limit of b_J=16.44 and so to reach slightly fainter magnitudes we have also used the publicly available photometry from the APM-Stromlo Redshift Survey (APMSRS), where the magnitude limit is b_J=17.15. We have converted our CTIO data to the b_J magnitude system using both our B Landolt and R Kron-Cousins data, in conjunction with the colour equation from Pimbblet

et al. (2001):

$$b_J = B - 0.17(B - R) \tag{3.8}$$

Fig. 3.4 shows this comparison with the b_J mag. plotted vs the mag. difference APM-CTIO. In our 297 deg^2 survey area we find 629 matching galaxies with the APMBGC, which are of course brighter than b_J=16.44 and 96 matching galaxies with the APMSRS brighter than b_J=17.15. Note that the APMSRS has a sampling rate of 1/20 over the full 4300 deg^2 APM area and so we therefore expect to find 20 times more matched galaxies with the APMBGC than for the APMSRS in a given mag. interval. This low sampling rate is clearly illustrated in Fig. 3.4, where the number of matched galaxies drops sharply as one moves to fainter magnitudes than b_J=16.44, the magnitude limit of the APMBGC. We find a mean zero-point difference of APM-CTIO=0.313$\pm$0.01 mag. The difference is quite large and we will see in the discussion section what this 0.313 mag. correction could mean in terms of the implications for a hole in the SGC distribution of galaxies.

3.4.2 The Durham/UKST Photometry Correction

In this section we use our CTIO CCD photometry to check the accuracy of the Durham/UKST photometry. The DUKST redshift survey covers 1500 deg^2 in 4 strips and our CTIO SGC data overlaps with one of these 4 strips. The angular size of the survey is 20°x75° in the SGC to a limiting apparent magnitude of b_J=16.86. The catalogue consists of ~2500 galaxy redshifts and therefore by comparing the model of Metcalfe et al. with the DUKST n(z) distribution, and taking into account any zero-point discrepancies with our CCD data, we can probe a larger area (1500 deg^2) in the SGC than the 2dFGRS can (~300 deg^2 at present). Although the DUKST will probe lower redshifts, the larger area will mean tighter constraints on the size and angular extent of the SGC deficiency in the galaxy distribution.

The DUKST galaxies were selected from the Edinburgh/Durham Southern Galaxy Catalogue (EDSGC: Collins, Heydon-Dumbleton & MacGillivray 1988; Collins, Nichol & Lumsden 1992). Ratcliffe et al. (1998) applied small corrections to the

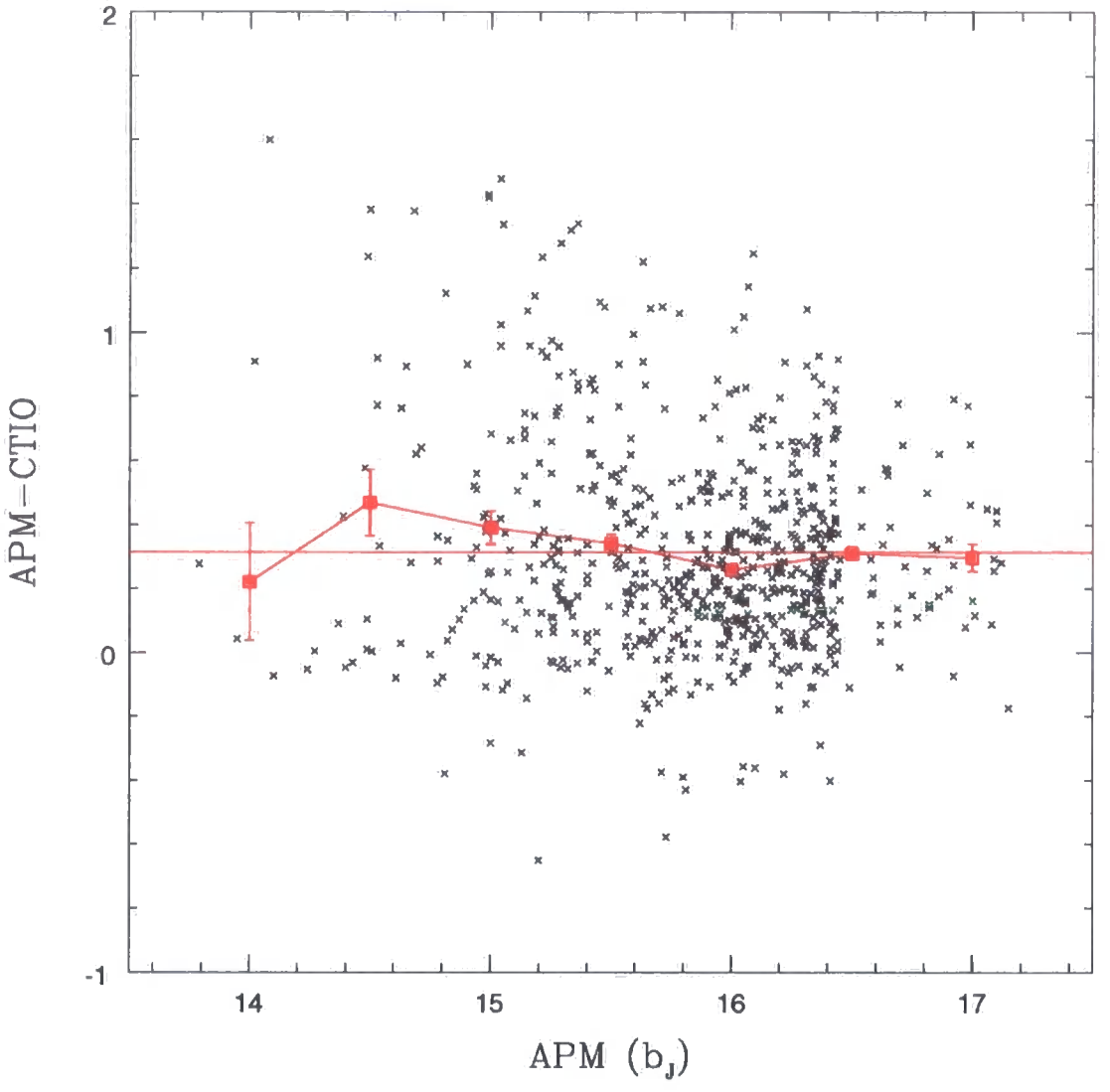

Figure 3.4: Comparison with the APMBGC and APMSRS galaxy photometry. Here we plot APM mag(b_J) vs APM(b_J)-CTIO(b_J) for all the APMBGC and APMSRS galaxies contained in our 297 deg^2 area The dotted line shows the mean of the residual in 0.5 mag. bins and the solid line shows the mean zero-point offset over all our measured magnitudes which we calculate to be 0.313 ± 0.01. The low sampling rate of the APMSRS is clearly illustrated, as the number of matched galaxies drops sharply as one moves to fainter magnitudes than b_J=16.44, the magnitude limit of the APMBGC.

EDSGC b_J magnitudes in each of the 60 fields in an attempt to put them on the same zero-point scale of the APM catalogue. These corrections were calculated from results of Dalton et al. (1995) with the mean correction over all 60 fields, $< b_J^{APM} - b_J^{EDSGC} >$=-0.05$\pm$0.11 mag. It should also be pointed out that the zero-point corrections were performed at $b_J \sim$19.5 as the APM is expected to give reliable photometry here. If this mean offset is to be believed in the magnitude range of the DUKST ($b_J < 17$), one is assuming there is no scale error in either the APM or EDSGC photometry.

Our CTIO SGC fields overlap with 28 of the 60 EDSGC fields and therefore we can make extensive tests of a large fraction of the DUKST photometry using our accurate CCD photometry. We have plotted DUKST b_J mag. versus DUKST(b_J)-CTIO(b_J) for all 28 fields in Figs. 3.5 and 3.6. To convert to the DUKST b_J magnitude system we use our B Landolt R Kron-Cousins photometry in conjunction with equation 3.8 (Pimbblet et al. 2001). Although the DUKST photometry was corrected in order to be consistent with the zero-point of the APM, it is clear that there are discrepancies compared to our accurate CCD data. These zero-point differences are extremely field dependent with field 411, for example, in agreement with our data, but field 471 showing a 0.5 mag. offset. In Fig. 3.7 we plot all the galaxies from each of the 28 fields in order to determine a mean zero-point offset. The dotted line shows the mean zero-point offset binned in half magnitude intervals and the solid line shows the mean zero-point offset over all magnitudes which we calculate to be 0.310. In fact the mean offset between the EDSGC photometry and the APM data at b_J=19.5 is 0.07 for the 28 fields which overlap with our CTIO data as opposed to 0.05 for all 60 fields. This means that we find a 0.31-0.07=0.24 zero-point offset between our CCD photometry and the corrected EDSGC photometry used for the DUKST survey.

This mean zero-point offset between our CTIO CCD data and that of the DUKST may seem surprising given that the DUKST photometry has already been corrected/brightened by an average value of 0.05 mag. in order that it is consistent with the APM data at b_J=19.5 However, as we have already mentioned, any scale

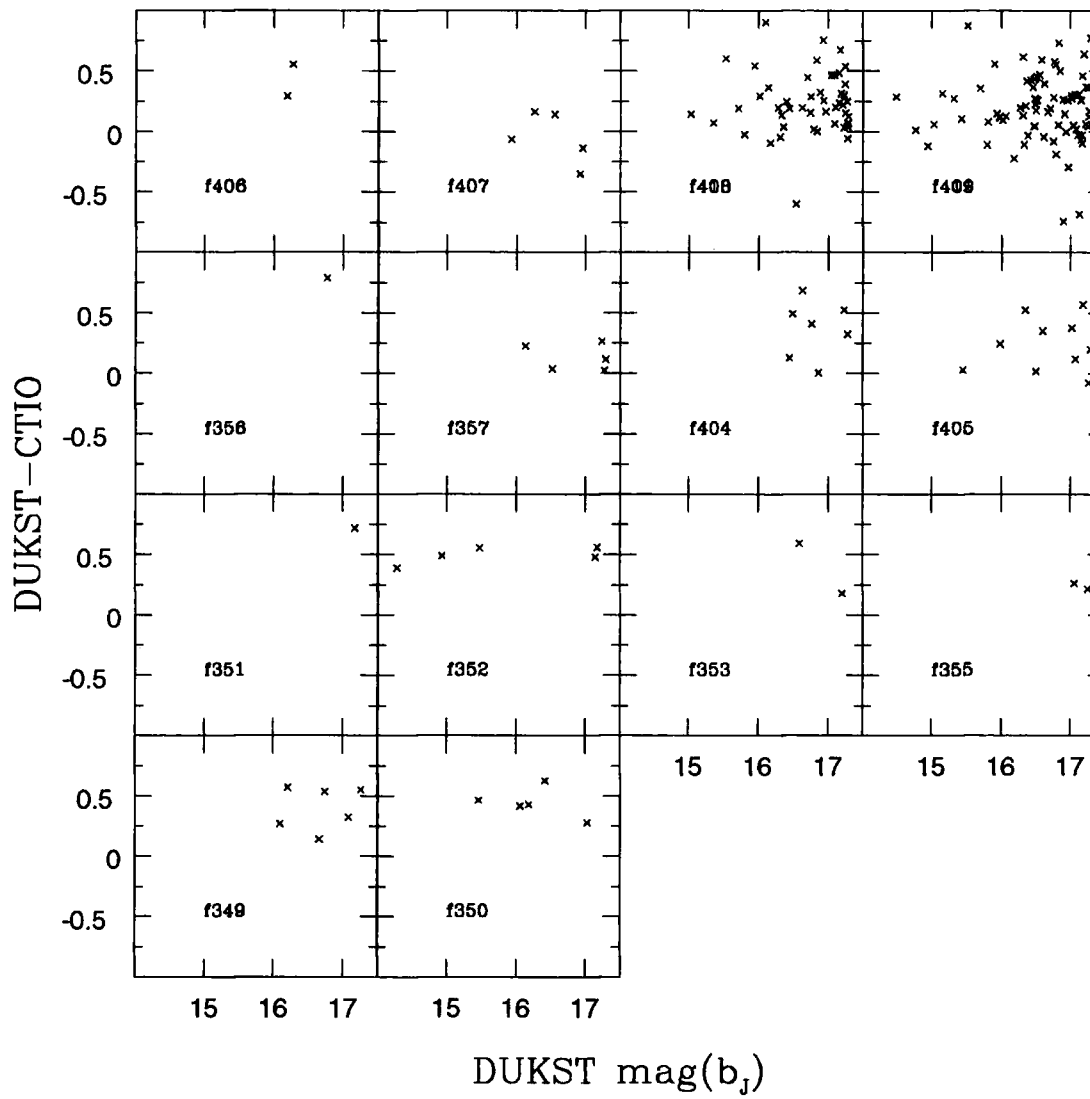

Figure 3.5: Here we show the first 14 of the 28 fields where our CTIO SGC fields overlap with those of the Durham/UKST Redshift Survey (see Ratcliffe et al. 1998a for details of each field such as coordinates). Although the DUKST photometry was corrected in order that it was consistent with the APM Galaxy Survey, it is clear that there are discrepancies relative to our CCD data. These discrepancies appear to vary significantly from field to field, although there are only a handful of galaxies in all but two of them.

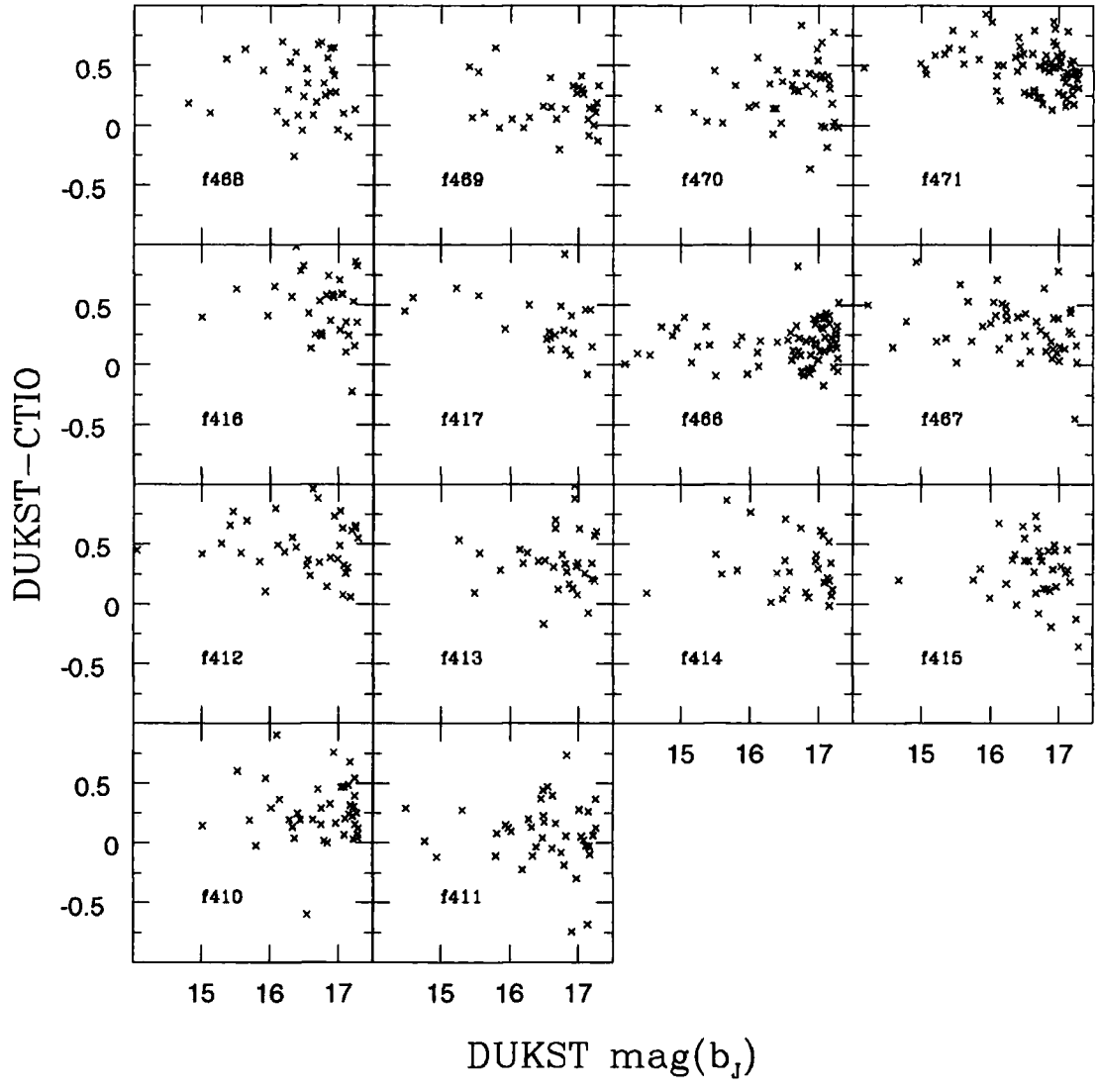

Figure 3.6: Here we show the second 14 of the 28 fields where our CTIO SGC fields overlap with those of the Durham/UKST Redshift Survey (see Ratcliffe et al. 1998 for details of each field such as co-ordinates). The DUKST photometry was corrected in order that it was consistent with the APM Galaxy Survey, however it is clear that there are discrepancies relative to our CCD data. These discrepancies appear to vary significantly from field to field. For example, we see good agreement in field 411 (labelled f411), but f471 shows a 0.5 mag zero-point discrepancy.

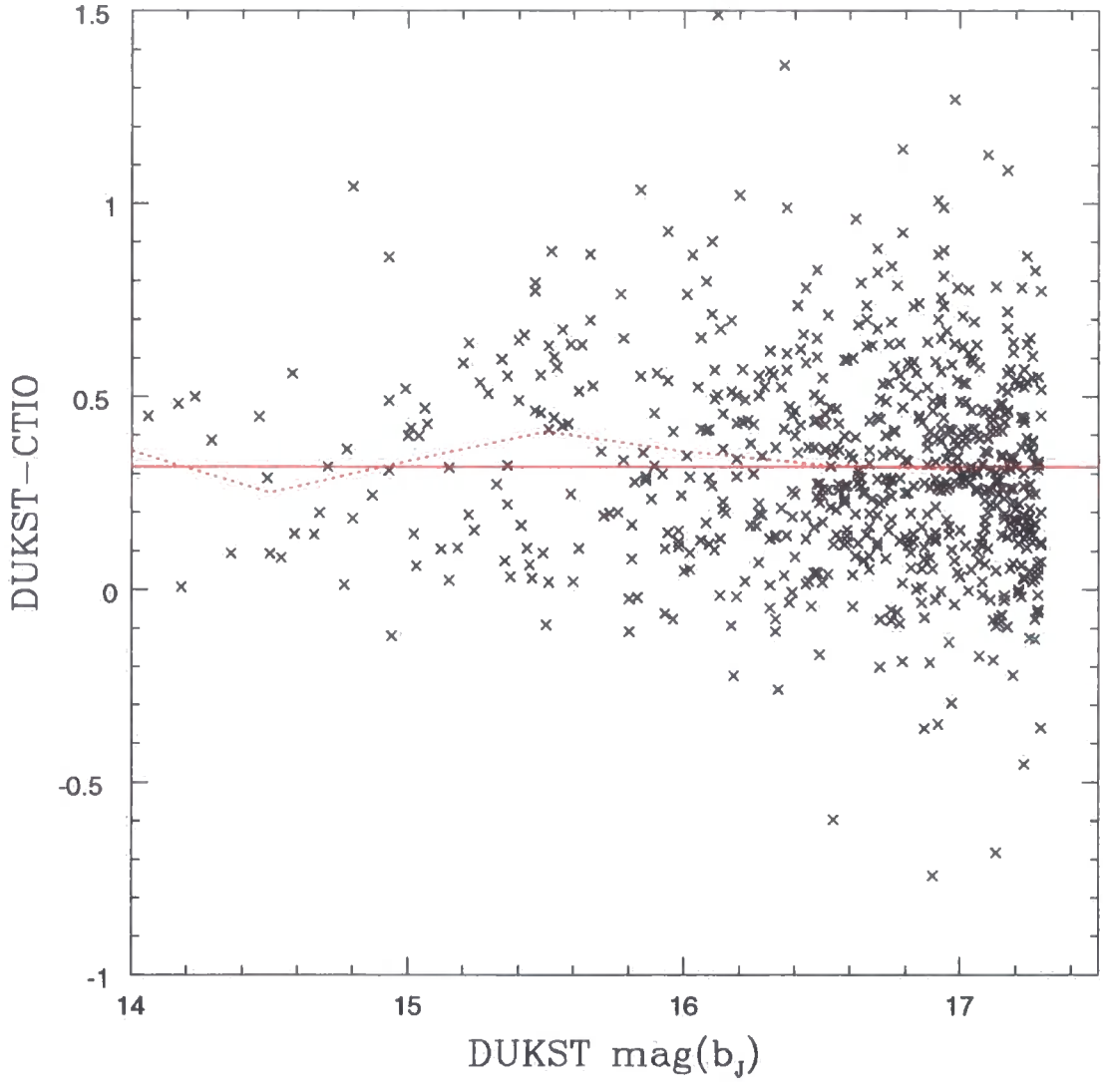

Figure 3.7: Here we plot EDGSC mag(b_J) vs EDGSC(b_J)-CTIO(b_J) for all the galaxies from each of the 28 fields displayed in Figs 3.5 and 3.6. The dotted line shows the mean of the residual in 0.5 mag. bins and the solid line shows the mean zero-point offset over all magnitudes which we calculate to be 0.310. In fact the mean offset between the EDSGC photometry and the APM data at b_J=19.5 is 0.07 ± 0.11 for these 28 fields which overlap with our CTIO data as opposed to 0.05 for all 60 fields. This means that we find a 0.31-0.07=0.24 ± 0.012 zero-point offset between our CCD photometry and the corrected EDSGC photometry used for the DUKST survey.

errors inherent in the APM or the DUKST could mean that this 0.05 correction may not apply at b_J <17. Scale errors are a well-known headache in photographic plate photometry and indeed fields 471 and 417 in Fig. 3.6 show clear evidence of this problem. Our checks of the 2dFGRS photometry (based on the original APM data) showed up no significant scale error in the magnitude range 16<b_J <19.5 and therefore we claim that the problem lies with the EDSGC photometry used for the DUKST survey. A scale error of order 0.1 mag/mag in the range 17< b_J <19.5 would explain the 0.24 mag. discrepancy with our CCD data which we have found to be accurate to a few hundredths of a magnitude at B<17 from checks performed in chapter 2.

3.4.3 The Durham/UKST N(z) Distribution

The zero-point discrepancy between the DUKST photographic plate photometry and that of our CCD based data has important consequences in terms of the DUKST number counts and n(z) distributions. We have used the "best sample" from Ratcliffe et al. (1998) using the uncorrected EDSGC photometry, taking into account the magnitude limits and completeness corrections of each of the 60 fields, in order to re-construct the DUKST n(z) distribution shown in Fig. 3.8. The average magnitude limit for the DUKST "best sample" over all 60 fields is b_J=16.86 and the dotted line shows the n(z) predicted using the Ratcliffe et al. (1998a) luminosity function parameters. This has been calculated using Ratcliffe's "best sample" magnitude limit, first brightened by 0.05 to take account of the DUKST photometry relative to that of the EDSGC at b_J=19.5, and secondly 0.2 mag is added in order to convert to the B Landolt system. We therefore use $B_{lim} = 16.86 - 0.05 + 0.2 = 17.01$. In fact this curve is equivalent to correcting all of the DUKST magnitudes by 0.24 mag. *and* the $M_\star$ value in the luminosity function by the same amount as the two effects cancel each other out. The dashed line shows a prediction except with the 0.24 mag. photometry correction applied to the magnitude limit, giving $B_{lim} = 17.01 - 0.24 = 16.77$, but with no alterations to the original value of the M* of Ratcliffe et al. (1998b).

Fig. 3.9 again shows the DUKST n(z) distribution but this time with predictions using the luminosity functions of Metcalfe et al. (2001) and Norberg et al. (2001). The b_J luminosity function of Norberg et al. (long dashed curve) has been calculated using 110,500 galaxies from the 2dFGRS at z=0, taking account of evolution, the distribution of magnitude measurement errors and small corrections for incompleteness within the 2dF catalogue. We have used their published values of $M^{\star}_{b_J}$=-19.66 ($M^{\star}_{B}$=-19.46) and $\alpha = -1.21$. A $\phi^{\star}$=2.6x10^{-2}Mpc^{-3} was chosen so that the predicted galaxy number count from the Norberg et al. luminosity function matched that of the Metcalfe et al. model at B=19.5. The magnitude limit was chosen to be $B_{lim} = 17.01$ i.e. the value of the DUKST survey without our CTIO photometry correction applied. This has been calculated using the "best sample" magnitude limit, first brightened by 0.05 to take account of the DUKST photometry relative to that of the EDSGC at b_J=19.5, and secondly 0.2 mag is added in order to convert to the B Landolt system. We therefore use $B_{lim} = 16.86-0.05+0.2 = 17.01$. We have also shown a prediction from the luminosity function of Metcalfe et al. (2001) using a magnitude limit of B_{lim}=17.01 (dotted curve) and the CTIO corrected magnitude limit of B_{lim}=16.77 (short dashed curve).

The predictions from the two luminosity functions agree reasonably well for z<0.05 but the Metcalfe et al. model predicts slightly more galaxies at higher redshift. However, both models clearly over-predict the DUKST n(z) at all redshifts. This clear deficiency of galaxies was originally considered surprising by Ratcliffe et al. given the DUKST covers 1500 deg^2 but it was thought that, because of the relatively low magnitude limit of b_J=16.86 and shallow redshift depths, that significant large scale structure at low redshift could explain this. By taking into account the zero-point correction of 0.240 and using the Metcalfe et al. model with B_{lim} =17.01-0.240=16.77, we find that this apparent underdensity of galaxies is not as large as first thought. Even so the corrected Metcalfe et al. model still over-predicts the n(z) distribution at virtually all redshifts and so we draw a similar conclusion to that of Ratcliffe et al. in that, even after our photometry correction is applied, significant large scale structure is still observed in the DUKST n(z) distribution. The dashed line in Fig. 3.9 illustrates this model which shows that

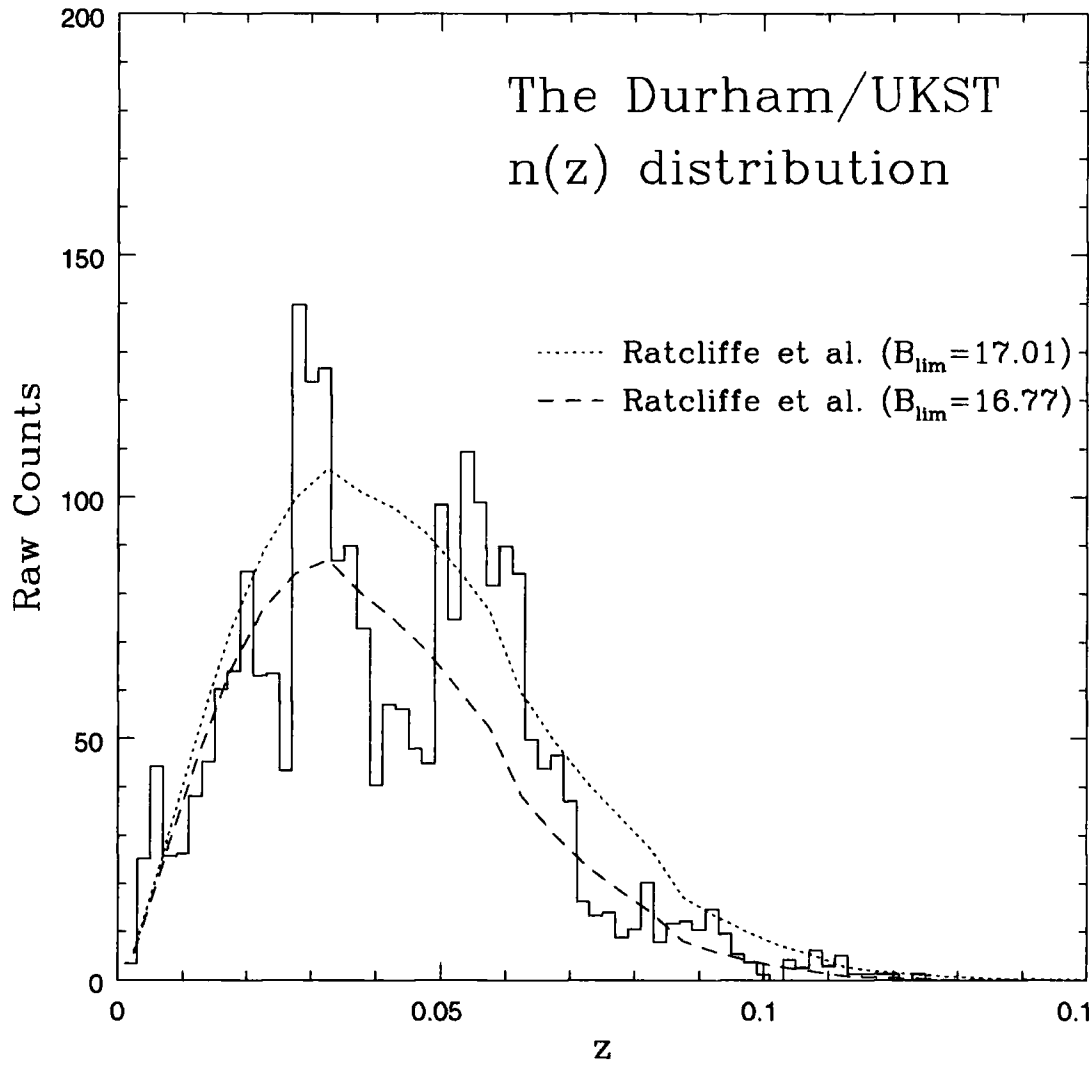

Figure 3.8: The plot shows the DUKST n(z) distribution, which has been constructed using the "best sample" from Ratcliffe et al. (1998) with the corresponding magnitude limits and completeness corrections for the raw EDSGC photometry in all 60 fields. The average magnitude limit of the 60 fields, taking into account the photometry correction applied by Ratcliffe et al. is b_J=16.86-0.05=16.81. The dotted line shows the prediction using the original luminosity function of Ratcliffe et al. (1998a) calculated from the data itself using the appropriate B Landolt magnitude limit of 16.86-0.05+0.20=17.01. The dashed line shows a prediction except with the 0.24 mag. photometry correction applied to the magnitude limit, giving $B_{lim} = 17.01 - 0.24 = 16.77$.

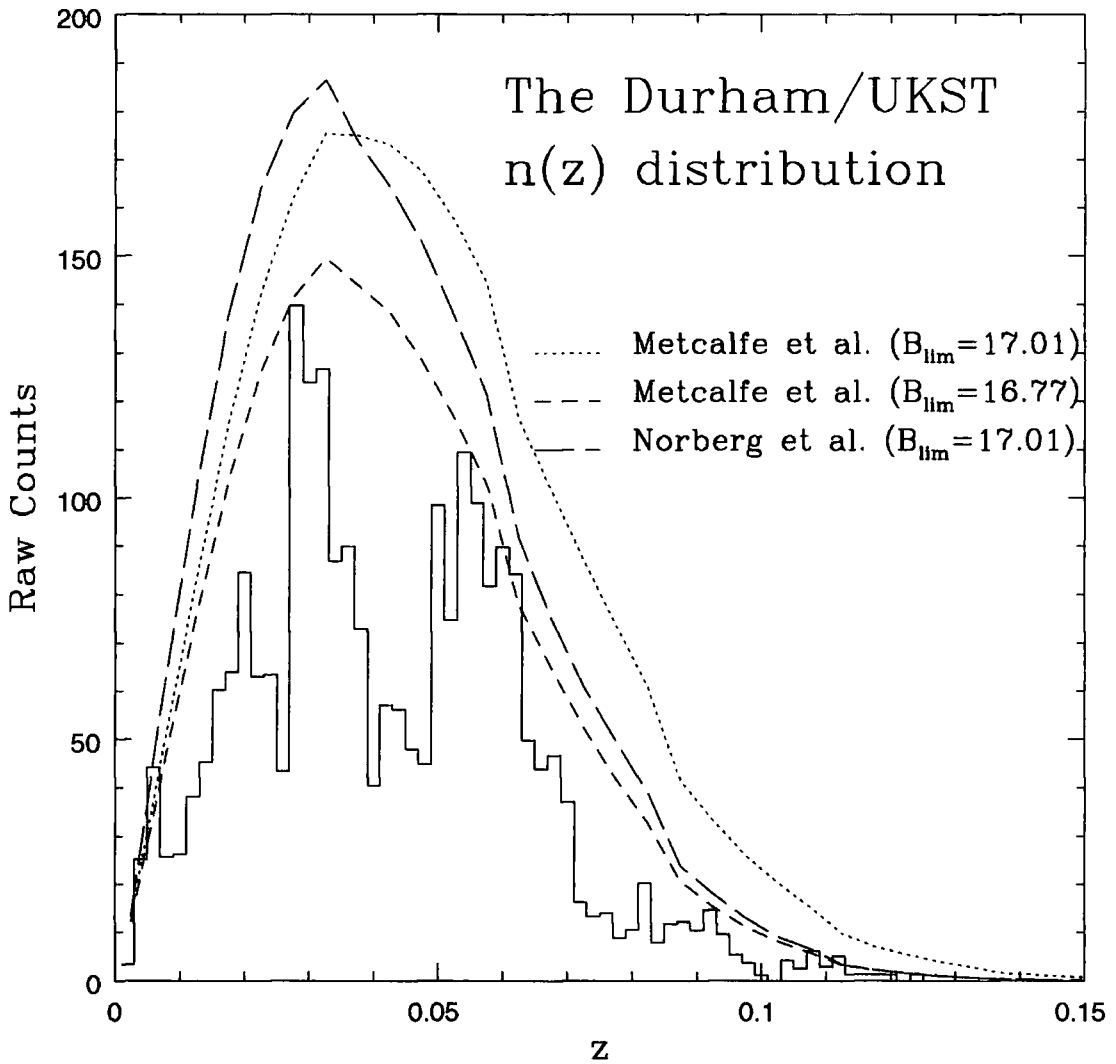

Figure 3.9: The DUKST n(z) distribution compared to predictions from other luminosity functions. The dotted line shows a prediction using the luminosity function of Metcalfe et al. (2001) calculated using the appropriate B Landolt magnitude limit of 16.86-0.05+0.20=17.01. The long dashed line shows a prediction from the new 2dFGRS luminosity function using the same magnitude limit (see text for more details of this luminosity function). Finally, the short dashed curve again shows a prediction using the luminosity function of Metcalfe et al. (2001) but calculated for the magnitude limit B_{lim}=16.77, which takes into account the 0.240 zero-point discrepancy found between our CTIO CCD data and the DUKST photographic photometry.

the deficiency of galaxies relative to the Metcalfe et al. model is still apparent until at least z=0.1 Relative to this photometry-corrected Metcalfe et al. model the DUKST n(z) distribution shows 4 clear holes in the galaxy distribution in the redshift ranges $0.005<z<0.025$, $0.03<z<0.055$, $0.06<z<0.09$ and $0.09<z<0.11$ with number discrepency percentages of ~40% , 45% , 50% and 60% respectively. In Section 3.5 we will analyse these apparent under-densities in more detail in conjunction with the results from the 2dFGRS n(z) distribution which we discuss in Section 3.4.4.

3.4.4 Photometry Checks of the 2dFGRS

As described in Chapter 2, our 297 deg^2 SGC field is a complete subset of the southern 2dFGRS region. Therefore, providing our photometry is consistent with that of the 2dF, their SGC n(z) distribution can help us understand the exact nature of the apparent under-density observed relative to the galaxy count model of Metcalfe et al. (2001). Furthermore, for $b_J > 17$, the 2dFGRS photometry has a zero-point that has changed slightly from the original APM data due to re-calibration with external CCD magnitudes. In the SGC this zero-point difference is very small, APM-2dFGRS=0.02, and so any comparisons of our CTIO data with the 2dFGRS magnitudes will also be good checks of the original APM photometry for $b_J > 17$. In the NGC this zero-point difference is APM-2dFGRS=0.08 (Cole priv. com.). In order to check how our photometry compares with that of the 2dFGRS we have matched all galaxies from the two surveys within a 3.5″ radius. As in Section 3.4.1, we use both our B Landolt and R Kron-Cousins galaxy photometry in conjunction with the colour equation from Pimbblet et al. (2001) in order to convert to the 2dFGRS b_J filter. Figs. 3.10 and 3.11 show these comparisons for the NGC and SGC regions respectively. Note that in the NGC only ~2/3 of our fields overlap with those of the 2dFGRS as opposed to 100% in the SGC explaining the factor of ~1.5 difference in the number of matching galaxies.

We have plotted the 2dF b_J magnitude against the magnitude difference 2dF-CTIO for each field with the mean of the residual illustrated by the squares in

each half magnitude bin. The 2dF galaxy photometry is of course based on that of the APM Galaxy Survey (Maddox et al. 1990a) with rms errors on the source magnitudes of 0.2-0.25, and this can be seen via the large scatter around the mean in each magnitude bin. We have shown in Chapter 2 that our CCD photometry is much more accurate than this with rms errors of 0.1 mag. at B=18 and 0.05 mag. at B=16, and therefore we expect any zero-point and scale errors between the two surveys to be contained within the photographic 2dF data. The NGC comparison in Fig. 3.10 shows clear evidence of both a zero-point and scale error. We find good agreement at b_J=16 but the scale error induces a maximum zero-point error of 0.13 at B=18 with a mean correction of 0.1 mag. for b_J >16. For the SGC field in Fig. 3.11 we find a much better agreement with no appreciable scale error and the mean of the residuals agreeing to within 0.05 over the whole magnitude range shown.

3.4.5 The 2dFGRS N(z) Distributions

This good photometry agreement in the SGC field between us and the 2dFGRS means that we are able to use the 2dF SGC n(z) distribution in conjunction with the galaxy count model of Metcalfe et al. (2001) described in 4.3, to perform a consistent analysis of the observed deficiency of galaxies in the SGC as a function of redshift. We can also make the appropriate zero-point correction in the NGC so we are then consistent with the 2dF photometry in order to investigate the 2dF NGC n(z) distribution.

We show these n(z) distributions in Figs. 3.12 and 3.13 which we have kindly been provided with by S.M. Cole. The mean magnitude limit of the 2dF photographic plates is b_J=19.35 and b_J=19.40 in the NGC and SGC respectively. Both n(z) distributions were normalised to 200 galaxies when we received the files for reasons that are not known, and so we have used the 2dF number counts at the appropriate magnitude limits in order to normalise the n(z) distributions. In Fig. 3.12 we have plotted 3 model curves, 2 of which use the Metcalfe et al. (2001) luminosity function (long dashed and solid curves) and a third which uses the lumi-

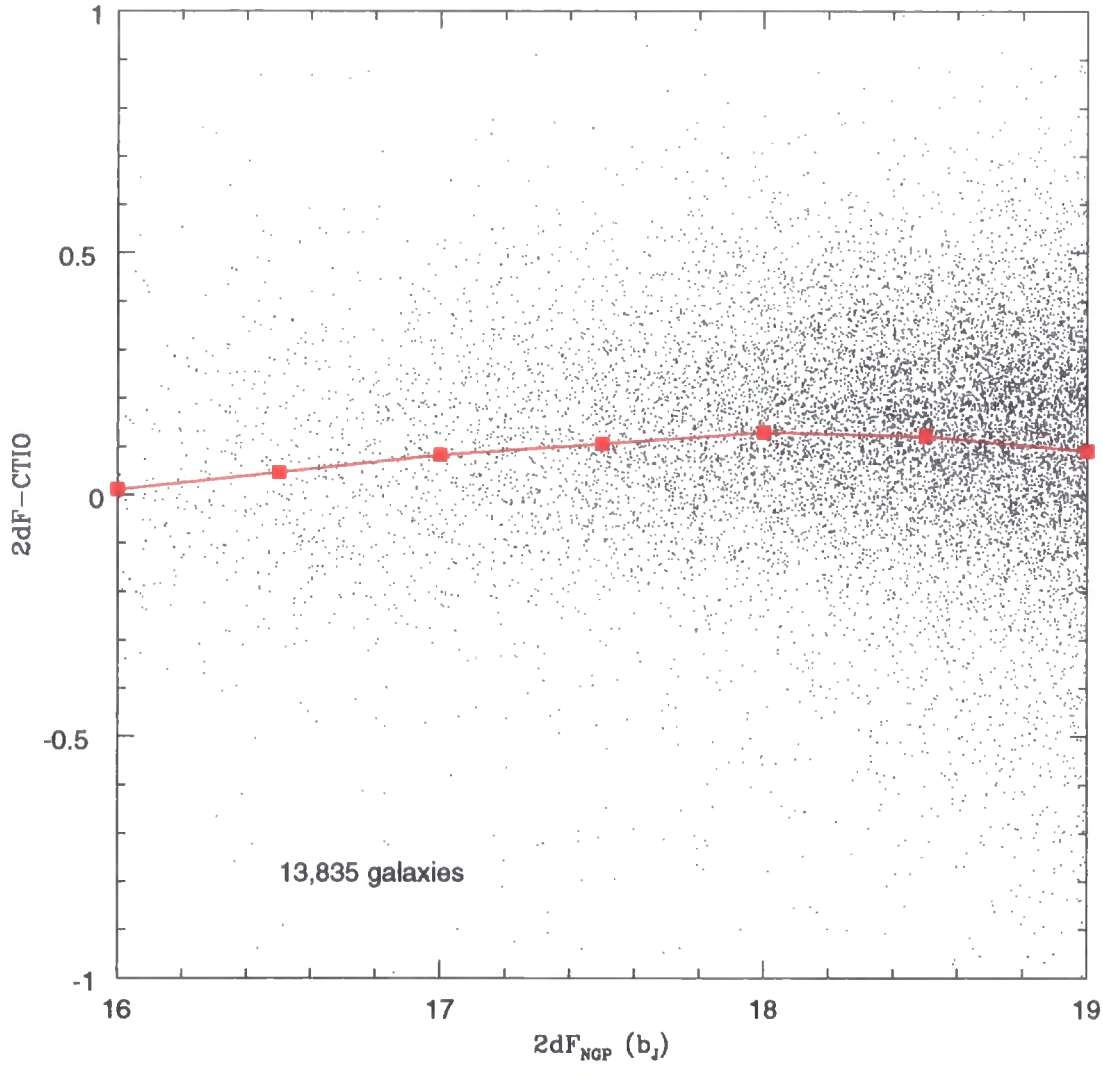

Figure 3.10: This plot shows 13,835 matching galaxies in the NGC from our CTIO survey and that of the 2dFGRS. We have plotted the 2dF b_J magnitude against the difference in magnitudes from the surveys, 2dF-CTIO, with the mean of this difference plotted in half magnitude bins. We converted the CTIO data to the 2dF b_J magnitude system using both our B Landolt and R Kron-Cousins band-passes in conjunction with the colour equation b_J=B-0.17(B-R) from Pimbblet et al. (2001). One can see a clear zero-point and scale error over the magnitude range shown with the zero-point difference peaking at 0.13 mag. when b_J=18. For $b_J > 16.0$ the mean correction is 0.1 ± 0.005 mag.

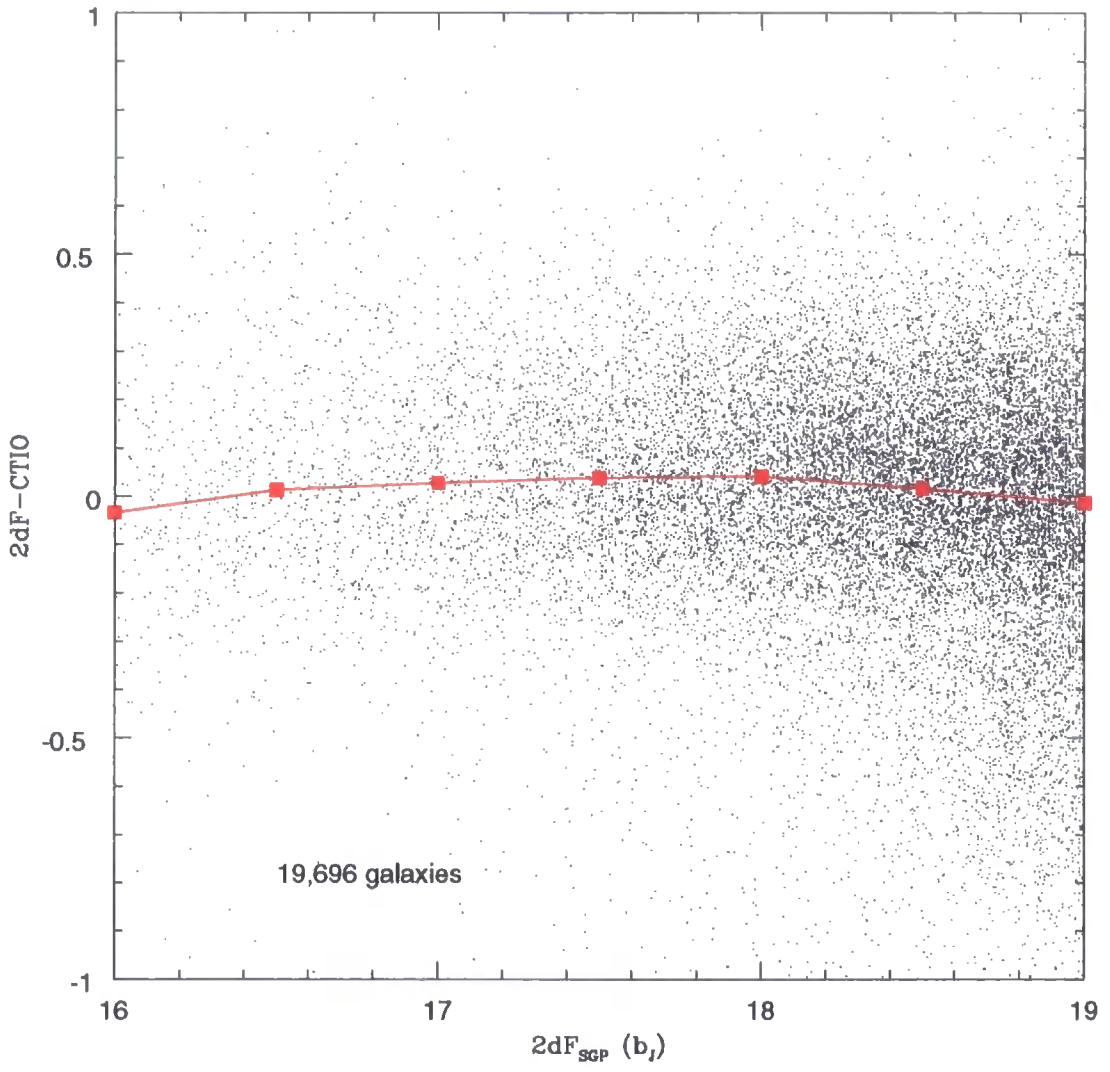

Figure 3.11: This plot shows 19,696 matching galaxies in the SGC from our CTIO survey and that of the 2dFGRS. We have plotted the 2dF b_J magnitude against the difference in magnitudes from the surveys, 2dF-CTIO, with the mean of this difference plotted in half magnitude bins. We converted the CTIO B-band data to the 2dF b_J magnitude system using both our B Landolt and R Kron-Cousins bandpasses in conjunction with the colour equation b_J=B-0.17(B-R) from Pimbblet et al. (2001). The agreement in the SGC is good with the mean of the magnitude difference $< 0.05 \pm 0.004$ mag. over the whole magnitude range shown.

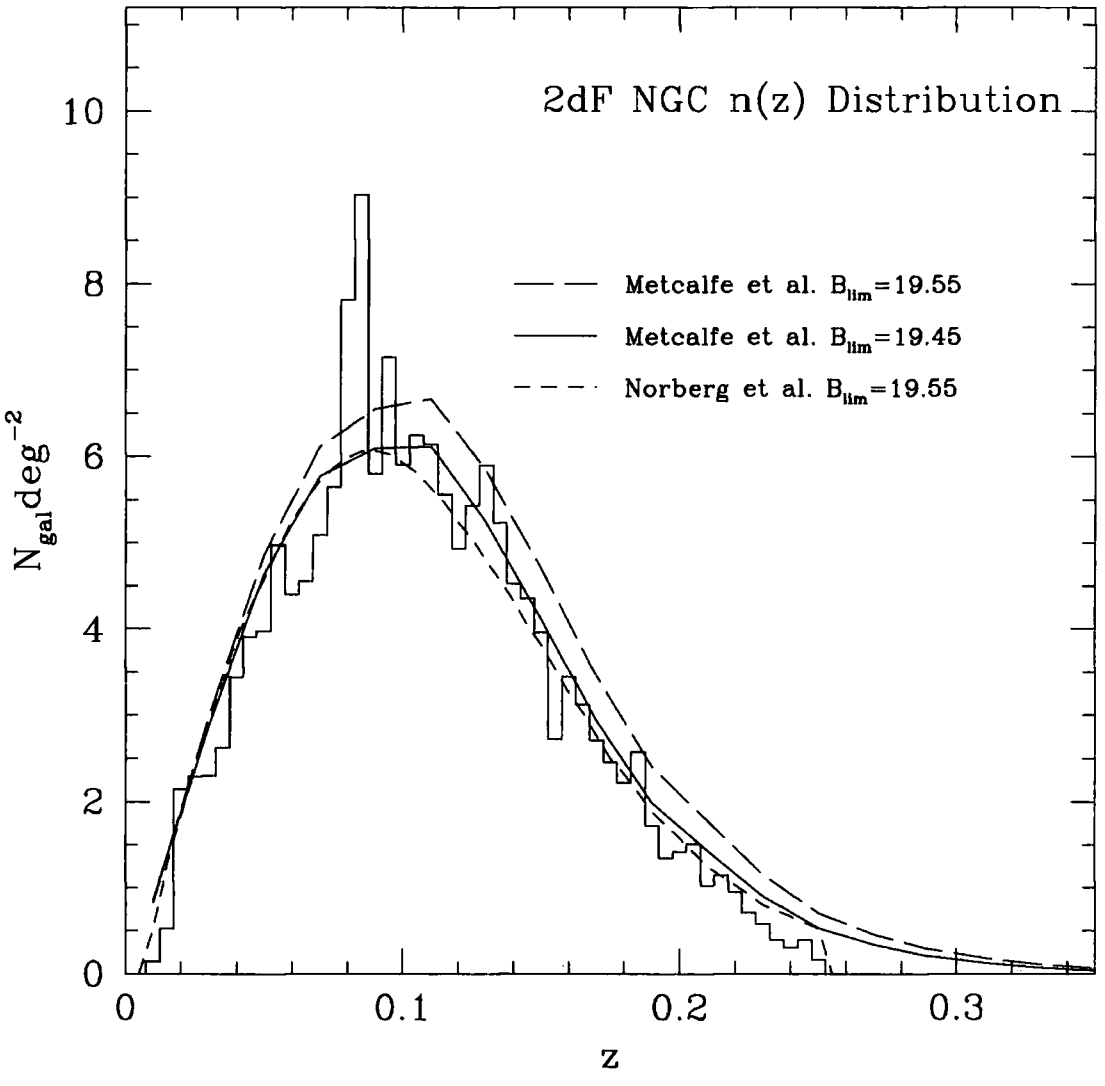

Figure 3.12: Here we show the n(z) distribution from the 2dFGRS in their NGC field along with two galaxy number count predictions using the luminosity function of Metcalfe et al. (2001) (solid and long dashed lines). We also show a prediction using the 2dF luminosity function (Norberg et al. 2001) (short dashed line). The mean magnitude limit of the APM-based photographic plates in the NGC is b_J=19.35 and so, assuming B-b_J=0.20 mag, we adopt a magnitude limit, m_{lim} of B=19.55 using each of the Norberg et al. and Metcalfe et al. models. The second prediction of the Metcalfe et al. model uses a magnitude limit corrected brighter by 0.1 mag. to B=19.45 in accordance with the zero-point difference we found between the 2dF NGC photometry and that of our CTIO data.

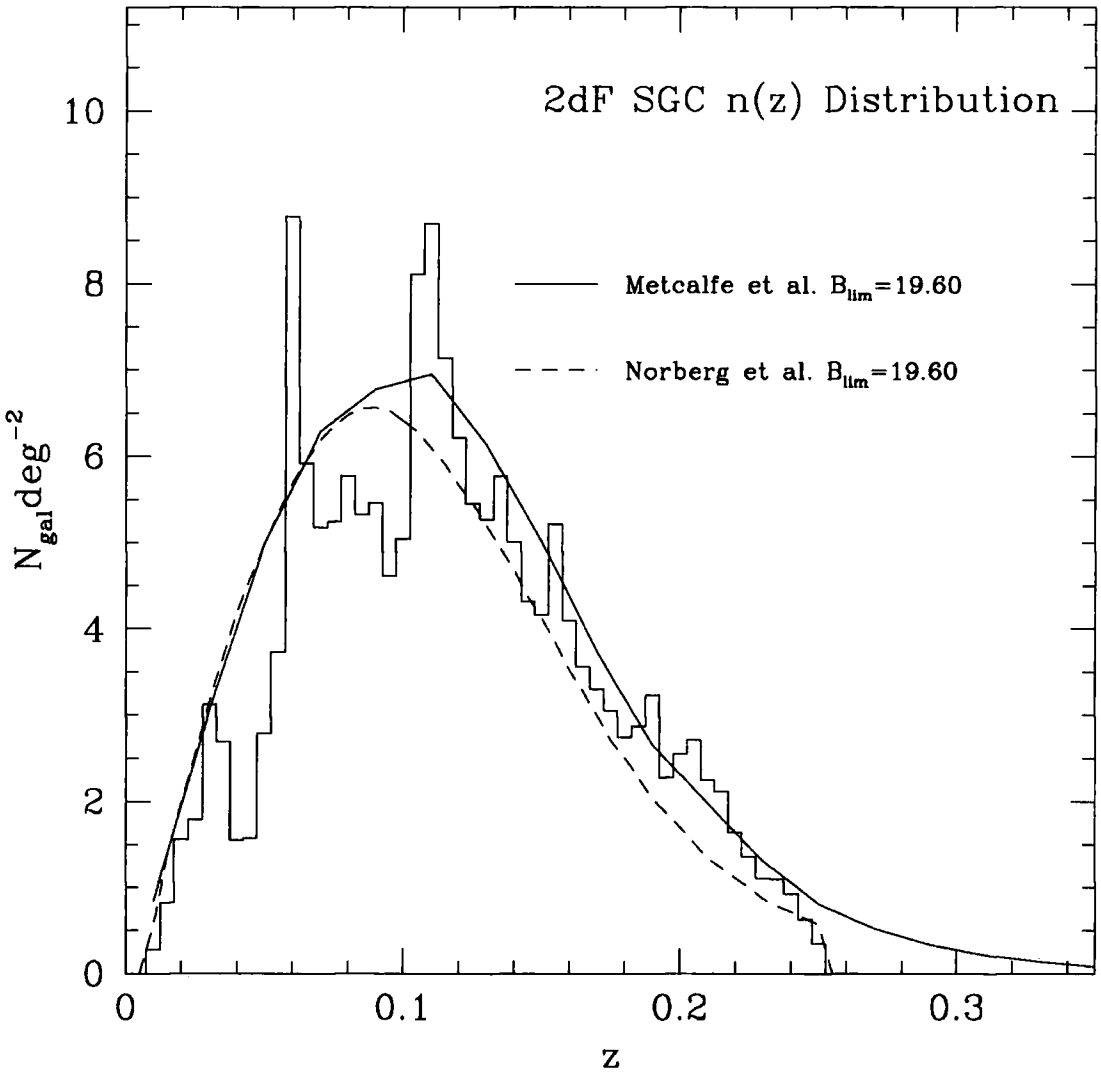

Figure 3.13: Here we show the n(z) distribution from the 2dFGRS in their SGC field and predictions using the luminosity functions of Metcalfe et al. (2001) (solid line) and Norberg et al. (2001) (dashed line). There are two clear "holes" in the 2dF SGC galaxy distribution in the ranges $0.03<z<0.06$, with an under-density of $\sim$35-40% , and $0.07<z<0.1$ where the galaxy density deficiency is $\sim$25% . The mean magnitude limit of the photographic plates in the SGC is b_J=19.40 and so, assuming B-b_J=0.20, we adopted a magnitude limit, m_{lim} of B=19.60 when computing the n(z) predictions.

nosity function of Norberg et al. (2001) (short dashed curve) described in section 3.4.2. The long dashed and short dashed curves were both calculated using the appropriate mean magnitude limit, B_{lim}=19.55, of the APM-based plates in the NGC (assuming B-b_J=0.2). We only show the Norberg et al. model at B_{lim}=19.55, since any photometry correction would be also applied to the Norberg et al. $M_\star$; this would leave the n(z) unchanged.

The models agree at low redshift but the Metcalfe et al. model significantly over-predicts the data, particularly at the higher redshifts plotted. The solid curve, however, takes into account our zero-point correction derived in the previous section, equal to 0.1 for b_J >16, and we therefore use a magnitude limit, B_{lim}=19.55-0.1=19.45. This model now shows excellent agreement with the observed data and it is interesting that this zero-point correction is vital in order that the Metcalfe et al. model does not over-predict the data. This excellent agreement of the data with the Metcalfe et al. and Norberg et al. models at all redshifts, indicates that the galaxy distribution appears to be fairly uniform in the 2dF NGC field with no evidence for any huge under-densities as we saw for the DUKST field.

Fig. 3.13 shows the 2dF SGC n(z) distribution along with two model predictions using the Metcalfe et al. luminosity function (solid curve) and that of Norberg et al. (dashed curve). Our photometry comparison with the 2dF SGC data in the previous section showed up no significant zero-point error and so we used the appropriate magnitude limit of B_{lim}=19.60 for each model. The main result of these model comparions so far has been that the Metcalfe et al. model predicts more galaxies at higher redshift and this case is no different, but the Metcalfe et al. model shows a slightly better agreement with the data than the Norberg et al. model which under-predicts the data for z>0.14. The most striking feature of the plot however is the two clear "holes" in the galaxy distribution in the ranges 0.03<z<0.0525, with an under-density of ~35-40% , and 0.06<z<0.1 where the density deficiency is ~25% . We refer the reader to the discussion section for a more detailed analysis of these holes in the galaxy distribution.

3.4.6 Luminosity Function Comparisons

Before moving on to the next section where we use the publicly available 2MASS data to analyse the local galaxy distribution, we provide a brief comparison of the luminosity functions of Metcalfe et al. (2001) and those from the DUKST (Ratcliffe et al. 1998a) and 2dFGRS (Norberg et al. 2001). We use our photometry corrections to appropriately alter the derived M*'s for these surveys to give a value of $M^{\star}_{corr}$, using corrections of 0.24 and 0.10 for the DUKST and 2dF NGC respectively and the results are shown in Table 3.4. The $M^{\star}_{corr}$ values are also dust corrected, using extinction values of 0.16 and 0.08 in the NGC and SGC. The Metcalfe et al. (2001) M* is consistent with observations at the South Galactic Pole where the dust correction in the B-band is predicted to be 0.02 mag by Schlegel et al.

Our DUKST photometry correction of 0.24 mag. (in addition to a 0.08 mag. correction for dust in the SGC) now means that $M^{\star}_{corr}$ is extremely bright relative to the other surveys. However, Ratcliffe et al. also calculated an error convolved luminosity function estimate, shown in Table 3.4 as DUKST(convolved). This DUKST (convolved) $M^{\star}_{corr}$ value coupled with the larger value of α means that the discrepancy with the other luminosity functions is not nearly so large. The DUKST photometry correction derived in this chapter only applies over one of the 4 strips observed by Ratcliffe et al. as that is the region where our data was taken in the SGC. We have assumed that our correction applies over the entire DUKST survey and this may not necessarily be the case, providing a possible explanation of why the DUKST (convolved) $M^{\star}_{corr}$ value is still too bright relative to other surveys.

The corrections applied by us now means that the values of $M^{\star}_{corr}$ for the 2dF NGC and SGC luminosity functions, coupled with the corresponding values of the α parameters, do not now agree as well as they did. The photometry difference of 0.1 mag. between our data and the 2dFGRS NGC data has been given support by the fact that Norberg et al. (2001) have found that SDSS galaxies in the NGC equatorial field are, on average, 0.058 mag. brighter than those in the 2dFGRS NGC field. The differences between the luminosity functions certainly needs

	α	$M^{\star}(b_J)$	$M^{\star}_{corr}(b_J)$
2dFGRS NGC	-1.135	-19.609	-19.709
2dFGRS SGC	-1.278	-19.732	-19.732
DUKST	-1.14	-19.72	-20.04
DUKST (convolved)	-1.04	-19.68	-20.00
Metcalfe et al. (2001)	-1.16	-19.56	-19.58

Table 3.4: Shown are luminosity function parameters α and $M^{\star}$ from 3 authors, assuming h_0=100kms^{-1}Mpc^{-1}. The $M^{\star}_{corr}$ values are dust corrected by us, assuming average values of 0.16 in the NGC and 0.08 in the SGC, as well as taking into account the zero-point differences of 0.1 and 0.24 for the 2dF NGC and DUKST surveys respectively relative to our CTIO data.

further investigation but it is not something we will pursue in this thesis.

3.4.7 The 2MASS View of the Local Universe

To further investigate the angular extent of a possible "hole" in the SGC galaxy distribution we have used the publicly available 2MASS K-band data. By taking 5° declination slices in the NGC and SGC with RA ranges similar to that of the 2dF regions, and plotting galaxy number counts in the K-band, it was possible not only to investigate the angular size of the "local hole" in the SGC but also any north-south asymmetry. Twelve declination slices of data, each of $\sim 300-400$ deg^2, were analysed totalling $\sim$ 4500 deg^2 from the two Galactic Caps and a schematic diagram of these fields relative to other observational survey areas in shown in Fig. 3.19.

Fig. 3.14 shows the 6 declination slices in both the NGC and SGC, where the K-band number counts have been plotted with the Euclidean slope subtracted. The solid line shows the prediction from the model of Metcalfe et al. where the number density of galaxies is constant as a function of redshift. The dotted and dashed predictions are variable $\phi^{\star}$ models calculated using the number-redshift distributions from the 2dFGRS in the NGC and SGC respectively. The value of $\phi^{\star}$ as a function of redshift for the SGC is determined for z<0.16 by multiplying the usual Metcalfe

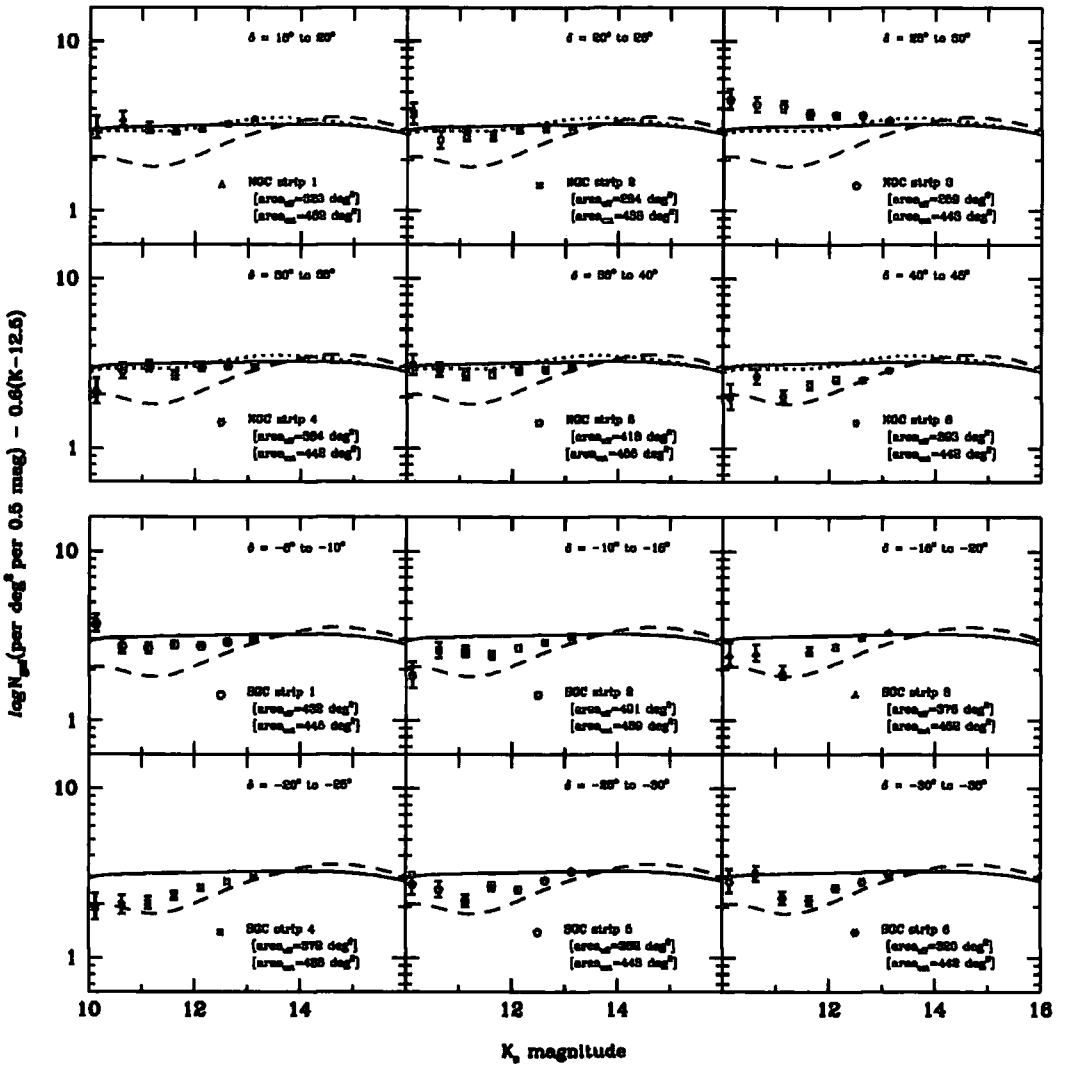

Figure 3.14: This plot shows the K-band number counts taken in 6 5° declination slices in both the NGC and SGC, with the extracted and effective (ie. gaps in the data subtracted) areas indicated. The solid line is a homogeneous model and the dotted and dashed lines are predictions using the NGC and SGC 2dF number-redshift distributions (see text for details). The SGC slices show under-densities in 5 of the 6 slices corresponding to the declination range -35° $< \delta <$ -10° and indicating that any "local hole" does not extend to the southern equatorial region. The southern SDSS number counts shown in Fig. 3.1 support this hypothesis. The declination slices in the NGC do not show any deficiency of galaxies in the range 15° $< \delta <$ 40° and agree well with the homogeneous model. The over-density of strip 3 is probably due to the Coma cluster.

et al. (2001) value by the factor $N_{data}(z)/N_{model}(z)$ (which is plotted in the lower panel of Fig. 3.15). $N_{data}(z)$ is the number of galaxies at a particular value of z in Fig. 3.13 and $N_{model}(z)$ is the prediction of the Metcalfe et al. model. For $z \geq 0.16$ the usual Metcalfe et al. (2001) $\phi^{\star}$ is used. The dotted curve is calculated in a similar way using the model and data curves in Fig. 3.12, but using the Metcalfe et al. prediction which has been calculated using the photometry corrected magnitude limit of B=19.45. What is very striking from these K-band counts is the angular extent of the galaxy deficiency in the SGC. Four of the six declination slices over the range $-35° < \delta < -15°$ in the SGC show clear under-densities for K<13 of 25-30% . Even the $-15° < \delta < -10°$ slice shows a slight under-density and as we start to probe the equatorial region with the $-10° < \delta < -5°$ slice we see the counts agreeing with the Metcalfe et al. model.

All the K-band declination slices in Fig. 3.14 show the data matching the homogeneous model for K>13.5, indicating a characteristic distance scale of 100-200 Mpc, above which we can rely on the cosmological principle. However, for the equivalent magnitude bin of B=17.5 in fig 3.17 we still find a clear galaxy number density discrepancy of 30% for our CTIO SGC data. Indeed, even as faint as B=18.5, our data shows this normalisation problem relative to the models and it is only in the B=19.0 bin that we see signs our NGC and SGC data will eventually obey the cosmological principle. Our field areas are very accurate and our photometry and galaxy completeness extremely good for B<18, so we are confident that the north-south asymmetry in our data is real. This normalisation difference is supported by the 2dF number counts plotted in Fig. 3.17 and the north-south number discrepancy agrees almost exactly with our number difference for B<18 after the zero-point corrections we derived in section 4.4.1 have been applied. These 2dF counts do seem to show that our galaxy completeness is a factor for B>18 as their north-south number difference is significantly smaller than ours for these magnitudes. We know that there are $\sim$10% uncertainties in the calculations of the 2MASS areas (as we don't have the full 2MASS mask) and therefore we cite this as the possible reason for the disagreement of our B-band counts and the K-band number counts in the 2dF SGC fields at K=14 (B=18) relative to the Metcalfe et

al. (2001) model. It will be interesting to see whether future results of the ongoing SDSS and 2MASS surveys will show up persistent variations in galaxy numbers from fields of a few hundred square degrees at B=18.

The K-band counts in the NGC indicate no deficiency of galaxies relative to the homogeneous model for 5 of the 6 declination slices covering the range $15< \delta <40$ and the over-density found in strip 3 is due to the Coma cluster. It is only close to the North Galactic Pole in strip 6 at $\delta = 45°$ where we see a significant under-density. It is clear that there is a definite north-south asymmetry regarding the galaxy number density, with the SGC strips of s4, s5 and s6 (see Fig. 3.19) showing similar, but slightly less, galaxy deficiencies than found from our SGC CTIO data or the predictions of the dashed line, computed from the 2dF SGC n(z). As already mentioned there is a 10% normalisation uncertainty in computing the declination slices of K-band number counts which probably explains this. As we move towards the SDSS southern equatorial field and pass through strips s1, s2 and s3 the under-densities become less pronounced until the s1 strip shows no appreciable galaxy deficiency in agreement with the SDSS SGC B-band number counts. Purely on the basis of these 2MASS results then, we argue that the angular extent of the hole in the SGC galaxy distribution extends from at least δ=-10° to δ=-35° and in the RA direction from 320° to 70°. The magnitude of the 2MASS galaxy deficiency in this region is 25-30% .

3.5 Discussion

We have attempted to analyse the depth and angular size of the apparent "hole" in the SGC galaxy distribution using data from the APM, 2dFGRS, DUKST and 2MASS surveys. One of the major discoveries of the work in this chapter has been the large galaxy-number deficiency relative to the Metcalfe et al. model in the DUKST and 2dF n(z) distributions. In fact there are distinct similarities between the two n(z) distributions which we attempt to quantify in Fig. 3.15. There are two panels in these histogram plots where the upper panel shows galaxy number deficiency vs redshift and the lower panel shows N_{gal}/N_{model} again vs redshift. We

define the galaxy number deficiency in % as:

$$D_g(z) = 100\frac{(N_{model}(z) - N_{data}(z))}{N_{model}(z)} \tag{3.9}$$

where N_{model} is the number of galaxies predicted using the Metcalfe et al. (2001) luminosity function and N_{data} is the number of galaxies from the appropriate survey data. In each panel predictions for the DUKST survey are shown by the solid lines and those of the 2dFGRS by the dashed line. In the upper panel the 4 holes found in the DUKST n(z) distribution are clearly illustrated by the 4 peaks in the solid histogram with the 2 peaks of the dashed histogram showing the under-densities found in the 2dF SGC n(z).

The similarity between the 2dF and DUKST n(z) distributions is quite striking. The two under-densities seen in the 2dF SGC n(z) in the redshift ranges $0<z<0.0525$ and $0.06<z<0.1$ are also clear features in the DUKST n(z). In fact, the galaxy discrepancy in the range $0<z<0.0525$ for the two surveys is almost the same magnitude in size with the histograms showing a very similar shape. The second under-density in the 2dF SGC n(z) is less pronounced than its DUKST counterpart, but they still cover very similar redshift ranges. The rise in the galaxy number density between the two 2dF SGC under-densities is also seen in the case of the DUKST survey. Given that the 2dF SGC field is entirely contained within the areas of sky observed for the DUKST survey we claim that the the similarities we have described in the two n(z) distributions are both artifacts of the *same* features in the galaxy distribution. Since the DUKST observes a larger 1500 deg^2 region than the 2dFGRS (who have redshifts for galaxies covering $\sim$300 deg^2 in the SGC at present) it could be that there is significant large scale structure observed by DUKST that is not seen by the 2dFGRS explaining the larger and more numerous galaxy number discrepancies in the DUKST n(z) distribution.

But there is evidence for an alternative explanation. Over the entire redshift range shown in the lower panel of Fig. 3.15, the DUKST survey shows significantly larger galaxy number discrepancies relative to the Metcalfe et al. model, except

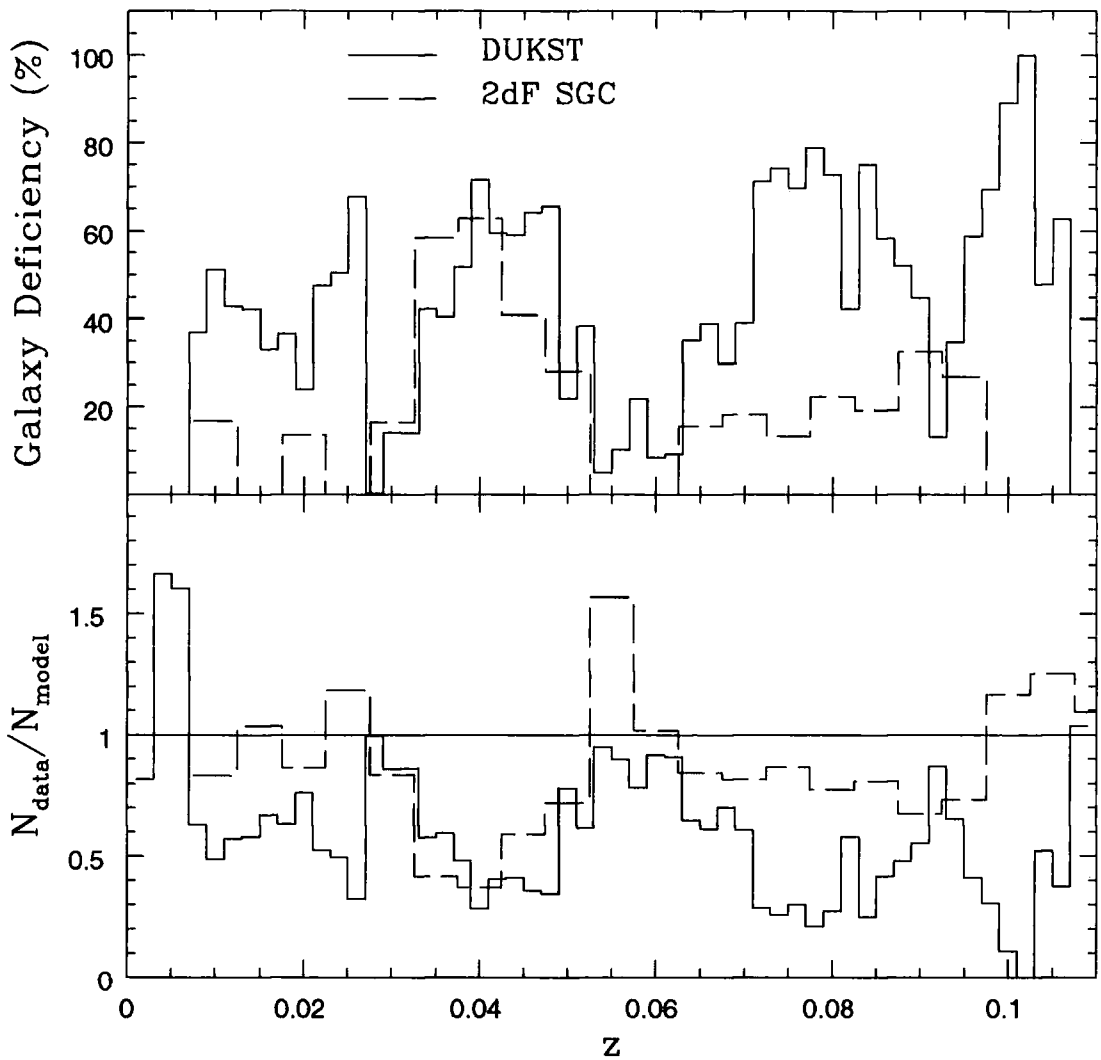

Figure 3.15: In the upper panel we show the galaxy number deficiency in the DUKST (solid line) and 2dF SGC (dashed line) n(z) distributions plotted as a function of redshift. We have calculated this using the histograms in Figs. 3.9 and 3.13 relative to the appropriate prediction using the Metcalfe et al. (2001) luminosity function. We define the galaxy deficiency (in %), $D_g(z)=100(N_{model}(z)-N_{data}(z))/N_{model}(z)$ where N_{data} is the number of galaxies from the appropriate survey data and N_{model} is the number predicted from the model of Metcalfe et al. The lower panel illustrates the ratio of the quantity N_{data}/N_{model} for the DUKST and 2dF SGC fields, also as a function of redshift.

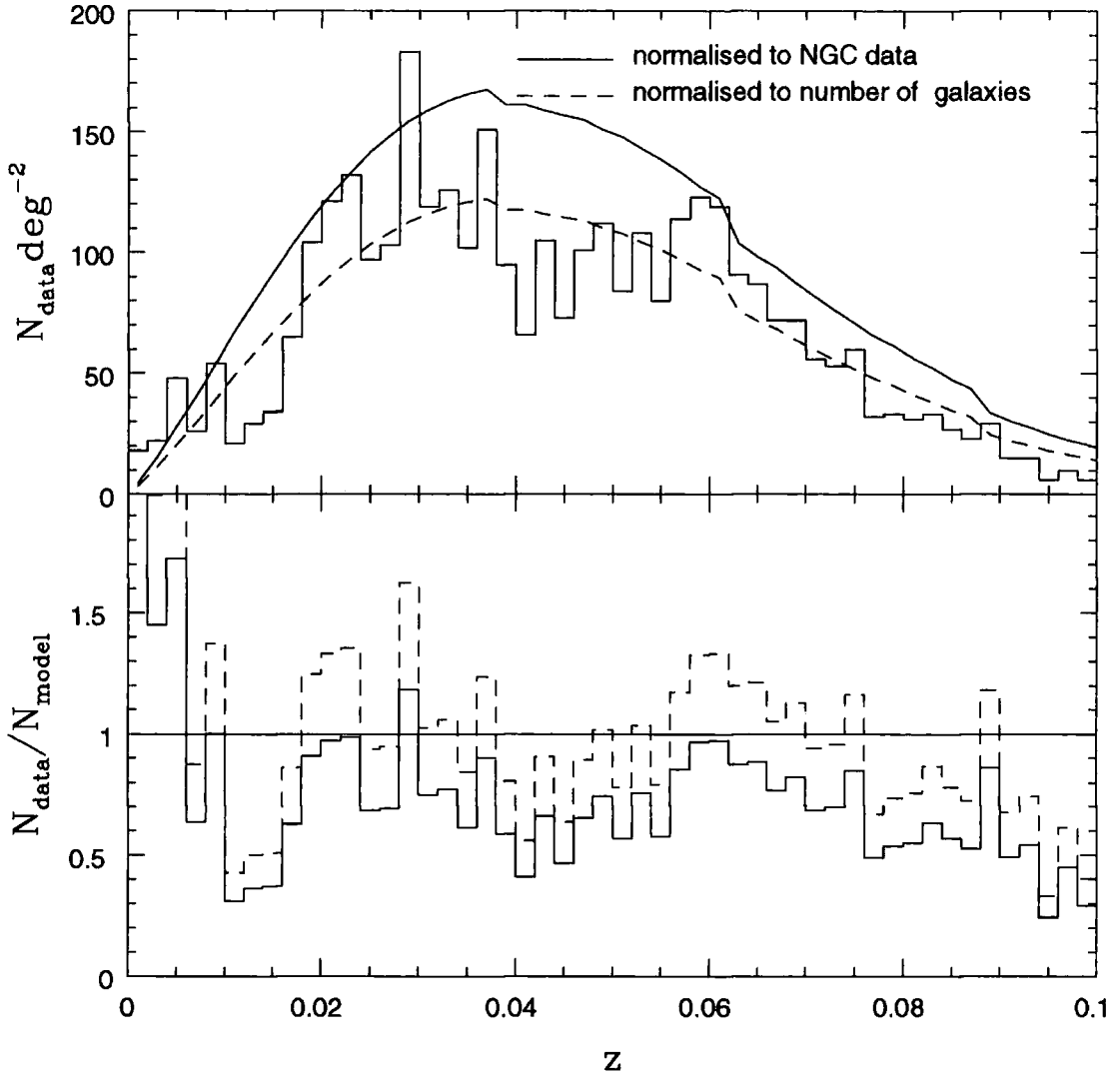

Figure 3.16: In the upper panel the histogram shows the 2dFSGC n(z) distribution with an imposed magnitude limit of B=17.01. The dashed curve shows a prediction from the luminosity function of Metcalfe et al. (2001), where we have normalised to the total number of galaxies predicted by the histogram. The solid curve show the same model but using the normal $\phi^{\star}$ values of Metcalfe et al., which we know is consistent with our NGC data at B=17. In the lower panel we have plotted N_{data}/N_{model} (as in Fig. 3.15), for each of these models.

for a tiny region of redshift space centered at z=0.04. We have seen that galaxies can be biased tracers of the overall mass distribution and that instrinsically more luminous galaxies are predicted to show stronger clustering properties, with regions of very high and low galaxy number densities. We suspect that the SGC might be under-dense and therefore the fact that the DUKST samples intrinsically brighter galaxies than the 2dF over all redshifts shown in Fig. 3.15, may mean that we are seeing the effects of bias.

Since this clearly needs further investigation, we have imposed the DUKST magnitude limit of b_J=16.81 (B=17.01) on the 2dFGRS SGC data. The results are shown in Fig. 3.16. In the upper panel we have included two model predictions using the luminosity function of Metcalfe et al. (2001), each with a magnitude limit of 17.01. The dashed curve is normalised to the total number of galaxies predicted from the histogram and the solid curve uses the normal $\phi^\star$ values of Metcalfe et al., which we know is consistent with our NGC data at B=17. In the lower panel we have plotted N_{data}/N_{model} for each of these models as a function of redshift. The solid histogram is similar to the long-dashed histogram in the lower panel of Fig. 3.15, except this time with the brighter magnitude limit imposed on the 2dFGRS data. The effect of this is to exclude galaxies that are, instrinsically, relatively faint. It is very interesting that we now see that the solid histogram in the lower panel of Fig. 3.16 shows larger galaxy number disrepancies over all redshifts than the long-dashed histogram in Fig. 3.15. This is entirely due to the different galaxy selection criterion we have used via the two magnitude limits of B=17.01 and B=19.60, and is clear evidence that the intrinsically brighter galaxies are clustered more strongly in accordance with the notion of bias.

Fig. 3.17 shows selected number count data with the appropriate zero-point corrections of 0.10 mag. to the 2dFGRS NGC data (for b_J >16.0), 0.24 mag. to that of the DUKST and 0.31 mag. to the APMBGC data. The DUKST corrected data is now significantly altered, but the counts are still much lower than the q_0=0.05 evolution model (solid curve) as we expect from Fig. 3.9. We have also made a small dust correction to the APM and APMBGC data shown in Fig. 3.17. A stan-

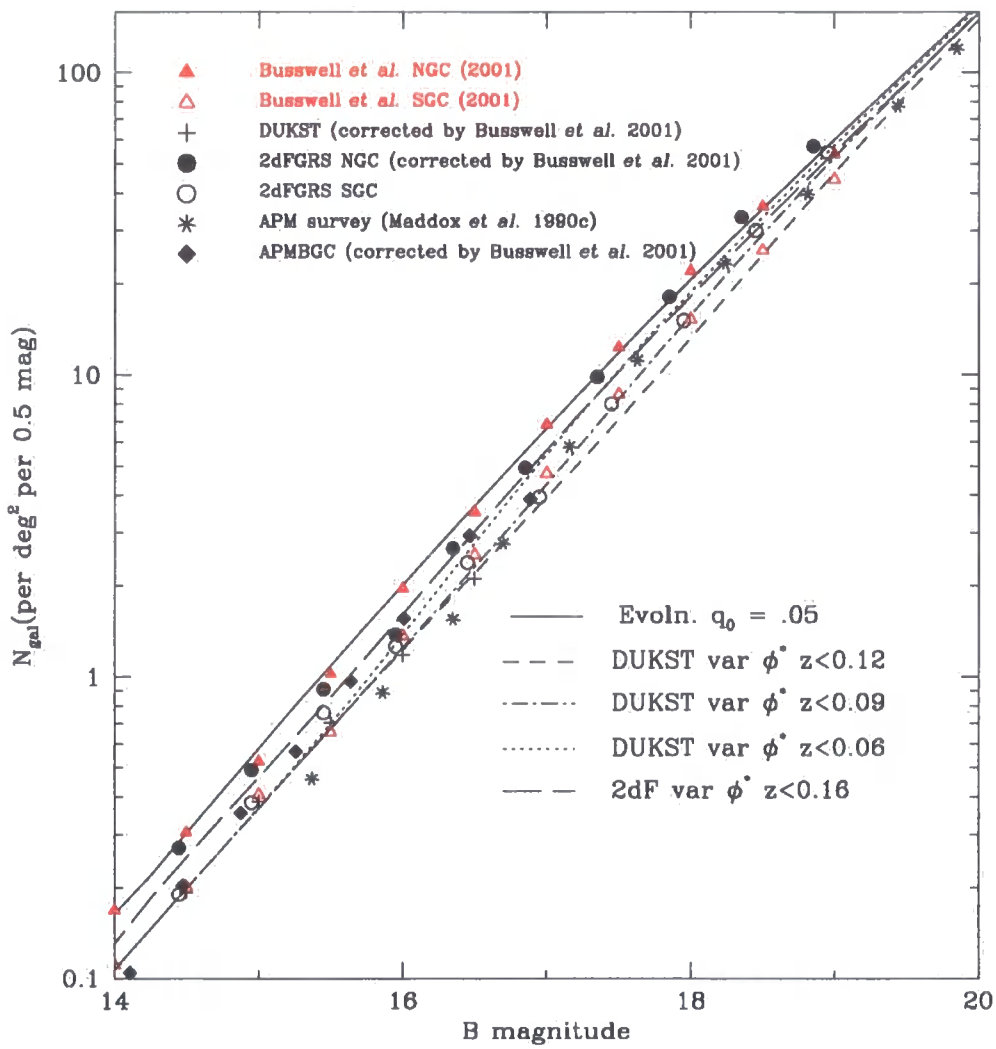

Figure 3.17: Here we show a similar plot to Fig 3.1, but we impose the 0.31, 0.24, 0.10 photometry corrections derived for the APMBGC, DUKST and 2dF NGC data (for $b_J > 16.0$) respectively. There is also a small 0.08 mag dust correction applied to the APM and APMBGC data (see text for details). We have also plotted 4 variable ϕ^* models shown by the short dashed, dot-dashed, dotted and long-dashed curves, where the value of ϕ^* is a function of redshift (see text for detailed expanation).

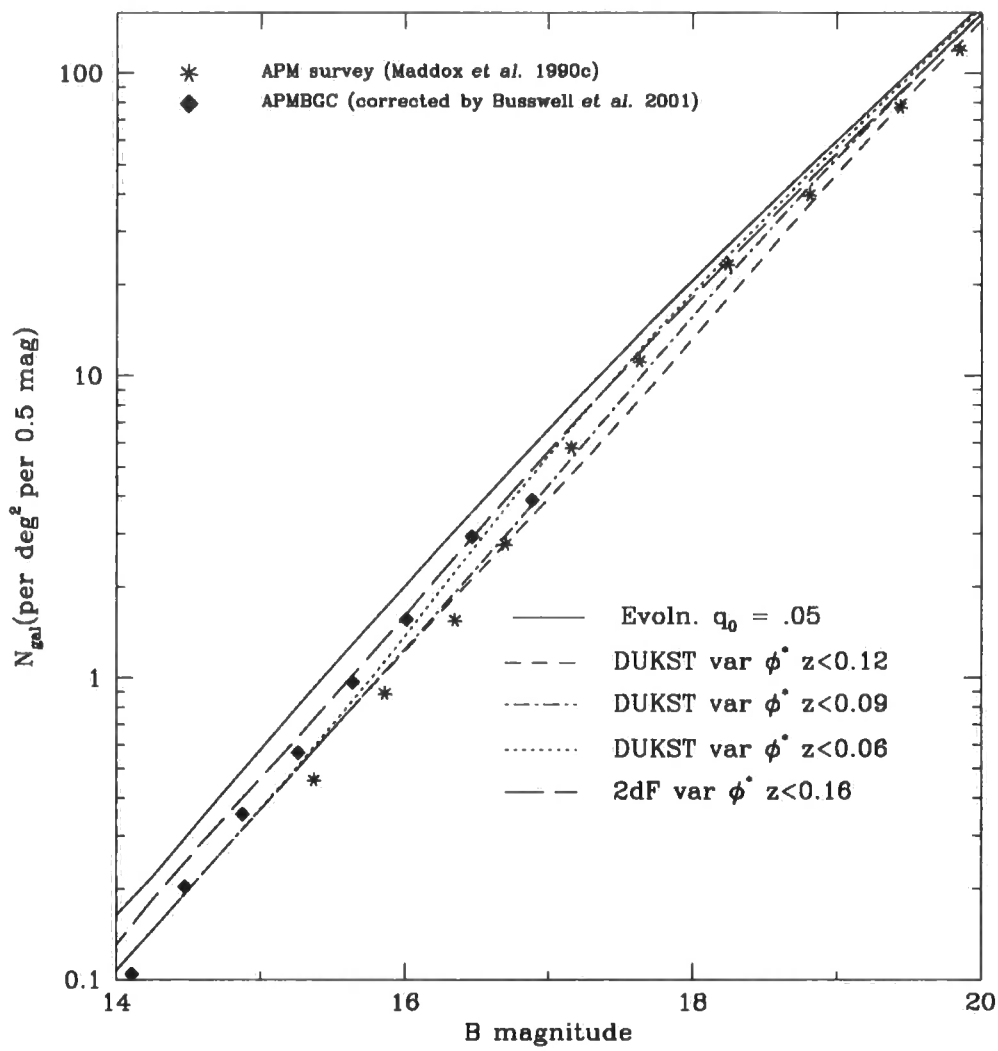

Figure 3.18: This plot is the same as 3.17 except, for clarity, we have plotted just the APM number counts of Maddox et al. (1990c) and the counts of the APM Bright Galaxy Catalogue (Loveday et al. 1996), in addition to the 4 variable ϕ^* models. Both these data sets cover a huge 4300 deg^2 area in the SGC.

dard A_B=C(cosec$b$-1) extinction law was originally assumed by Maddox et al. for the APM photometry, which corresponds to A_B=0 at the poles and a maximum A_B ~0.03 at $b = 50°$, averaging ~ 0.01 mag over the whole APM area. The Schlegel et al. (1998) dust maps, which are used to correct the 2dF counts and our own CTIO data, predict 0.02-0.03 mag. of extinction, even at the poles, and our average CTIO dust correction was 0.08 in the SGC. We have therefore corrected the APM counts and the APMBGC data by an additional 0.08 mag (so the total correction is 0.08 mag. for the APM counts and 0.39 mag. for the APMBGC data). The original APM counts now show no galaxy number deficiency for B>18, but still indicates a large local hole at brighter magnitudes over a huge 4300 deg^2 area.

The 2dF data shown in Fig 3.17 shows excellent agreement with our CTIO data in both galactic caps. The 0.1 zero-point correction we have applied to the 2dF NGC data now means that their north-south difference agrees with ours almost exactly for B<18. This agreement with our data in each galactic cap is interesting given the larger angular areas of 740 deg^2 and 1094 deg^2 of the 2dFGRS NGC and SGC fields respectively. Therefore it would seem that our survey areas of 242 deg^2 and 297 deg^2 are fairly typical samples of the galaxy distribution in these regions of the Universe.

Fig. 3.17 also shows 4 variable $\phi^\star$ models shown by the short dashed, dot-dashed, dotted, and long-dashed curves where the value of $\phi^\star$ is a function of redshift instead of the usual constant value defined from the Metcalfe et al. (2001) B-band luminosity function. For the 2dF model the curve is calculated in the same way as for the dashed curve in Fig. 3.14 i.e. the $\phi^\star$ is determined for z<0.16 by multiplying the usual Metcalfe et al. (2001) value by the factor $N_{data}(z)/N_{model}(z)$. For z≥0.16 the usual Metcalfe et al. (2001) $\phi^\star$ is used. The 3 DUKST models are calculated in a similar way using the values of $N_{data}(z)/N_{model}(z)$ plotted in Fig. 3.9. The only difference between them is that a variable $\phi^\star$ is used over different redshift ranges; z<0.12, z<0.09 and z<0.06.

The motivation behind these variable $\phi^\star$ models is to see what sort of structure

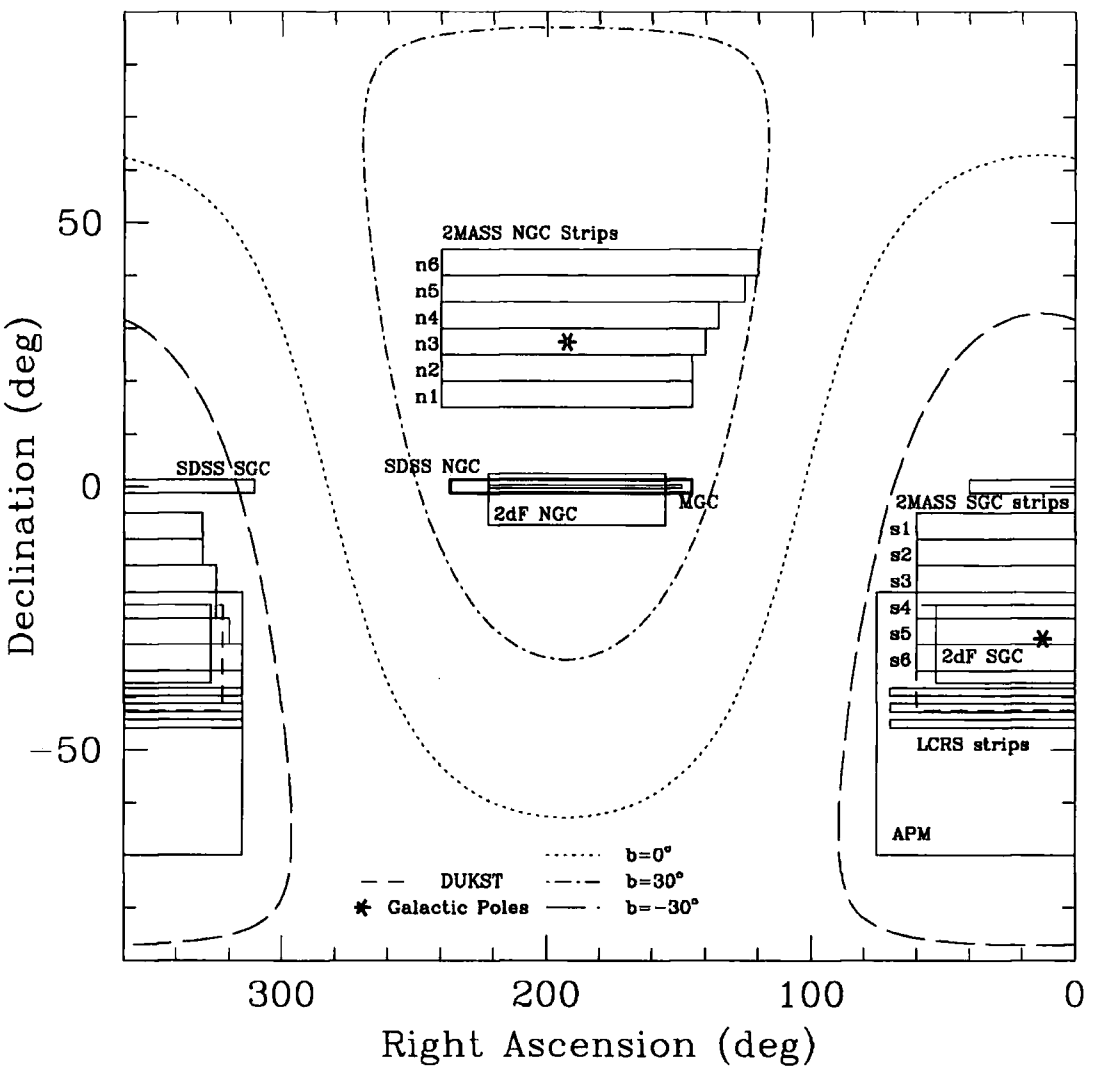

Figure 3.19: A plot showing the various regions on the sky observed in different astronomical surveys. Shown on this plot are the regions of sky observed by the SDSS, 2dFGRS, MGC, DUKST and APM surveys. All the surveys have been labelled next to the appropriate survey areas except the DUKST region (the dotted line) which is labelled in the lower region of the plot. We have also plotted constant lines of galactic latitude at b=0°, 30° and -30° and a point to show each galactic pole at b=90° and -90°. Our own CTIO data has not been plotted here because of clarity, but see Figs 2.1 and 2.2 for illustrations of the exact locations of our fields.

in the galaxy distribution the APM counts and the APMBGC counts (corrected using our derived value of 0.31 mag.) are consistent with. Therefore, for clarity, we have plotted just the APM and APMBGC counts as well as the 4 variable $\phi^{\star}$ models in Fig. 3.18. Recall that we have reliable checks, using our CTIO galaxy sample, of the photometry of the original APM data for B>17 and for the APM-BGC (combined with the APM-Stromlo data) for B<17.

The DUKST z<0.12 model under-predicts the number of galaxies relative to the APM data in the magnitude range 16.75<B<18.75 indicating that these observations are not consistent with the DUKST n(z) out to z=0.12. Recall that the DUKST n(z) showed 4 distinct holes in the galaxy distribution with the 3rd hole in the redshift range 0.06<z<0.09 and the 4th hole in the redshift range 0.09<z<0.11. The DUKST z<0.09 and z<0.06 models were constructed in order to see the effect on the predicted number counts, assuming that just the first 2 and then the first 3 of these holes actually exists. The DUKST z<0.09 model agrees well with the APM data for B>17, but is inconsistent with the APMBGC data, as is the DUKST z<0.06 model. The 2dF variable $\phi^{\star}$ model includes the effect of the two holes in the galaxy distribution seen in the 2dF SGC n(z). Although the variable $\phi^{\star}$ is used in this model for z<0.16, these holes are both at z<0.1. If we ignore the original APM counts for B<17 (where we have no reliable photometry checks) then this 2dF model provides the best fit to the APMBGC data at B<17 and the original APM counts at B>17. However, one must be aware that the effect of using a brighter magnitude limit of B=17.01 for the 2dFGRS SGC data, is to make the holes in the galaxy distribution appear much larger, in better agreement with those seen in the DUKST survey. The conclusion of these variable $\phi^{\star}$ models is that the APM and APMBGC (corrected) counts are most consistent with there being a galaxy number discrepancy for z<0.1, which is of order 30% .

Fig. 3.19 shows that the APM, 2dF SGC and DUKST survey areas all overlap with the s4, s5 and s6 2MASS strips where we know there is a significant under-density of 25-30% , similar to the 30% number deficiency found to be consistent with the APM and APMBGC data. The DUKST field then extends further south to

δ=-43° and the APM area even further to δ=-70°. Taken together with our 2MASS results this implies a hole in the SGC galaxy distribution of 100°x60°, which extends to z=0.1. This corresponds to a huge volume of space of $\sim$3x10^{6}Mpc^3 and implies significant power on large scales of $\sim$100-200Mpc.

To illustrate how excess power on larger scales increases the chances of finding a 30% galaxy deficiency over the kind of volumes we are claiming, we have used the 3-D analogue of equation 45.6 in Peebles (1980). By assuming a power law form of the spatial two-point correlation function (see Chapter 4 for a definition of the spatial two-point correlation function) out to a given scale length, we can calculate the probability of finding a given number deficiency of galaxies over a volume of space defined by a sphere of radius $150h^{-1}$Mpc. In this simplified scenario, the fluctuation in galaxy number over the expected galaxy number can be written as:

$$\frac{< (N-\bar{N})^2 >^{\frac{1}{2}}}{\bar{N}} = \frac{\left(1 + \frac{4\pi\bar{N}}{V}\int_0^{r_s} \xi(r) r^2 dr\right)^{\frac{1}{2}}}{\bar{N}^{\frac{1}{2}}} \tag{3.10}$$

where $\xi(r)$ is the two-point spatial function and V is the volume of the sphere over which a particular survey is sampling. If we write $\frac{<(N-\bar{N})^2>^{\frac{1}{2}}}{\bar{N}} = \frac{\delta N}{\bar{N}}$ and assume $\xi(r) = (r/r_0)^{-1.8}$ then it can be shown that:

$$\frac{\delta N}{\bar{N}} = \left(\frac{1}{\bar{N}} + \frac{3}{r_s^3}\left[\frac{r_0^{1.8} r_{cut}^{1.2}}{1.2}\right]\right)^{\frac{1}{2}} \tag{3.11}$$

where we assume the galaxy correlation length in proper coordinates, r_0=5.0h^{-1}Mpc, r_{cut} in Mpc is the length scale at which we assume the power law form of the correlation function extends to, r_s=150h^{-1}Mpc and is the radius of the sphere defining our volume, $\bar{N}$ is the expected number of galaxies in this volume and $\delta N/\bar{N}$ is the expected fluctuation in the galaxy number. We assume two cases, each corresponding to a different value of r_{cut}. In the first case r_{cut}=10h^{-1}Mpc. If we set $\bar{N}$=$(4\pi r_s^3 \bar{n})/3$, where we assume $\bar{n}$=0.01 which is the mean galaxy density in units of h^3Mpc^{-3}, then we find that $\delta N/\bar{N}$=0.016. This corresponds to an expected galaxy number fluctuation over our sphere of radius $150h^{-1}$Mpc of 1.6% and therefore means that finding a galaxy number deficiency of 30% over our sphere is a 18.75σ result!

However, if we assume our second case where r_{cut}=150Mpc then we find an expected galaxy number fluctation of 8% . This is a 3.75σ result and so, although unlikely, is much more probable than a 18.75σ result. What we have illustrated though is that more power on large scales does increase the chances of finding larger fluctuations in galaxy numbers over a given volume of space. The question is, how much power is there in the two-point correlation function on large scales?

3.6 Conclusions

In this chapter we first presented the resulting galaxy counts from our CTIO Curtis Schmidt data. The large deficiency of galaxies seen in the SGC motivated us to investigate the possible existence of a large "hole" in the SGC galaxy distribution. Using our CTIO data, covering 300 deg^2 in the SGC, we were able to make the first ever detailed checks of the bright (B<17) galaxy photometry in the DUKST and APM surveys which has crucial implications for the existence of a local hole in the distribution of galaxies. We also performed photometric checks of the 2dFGRS photometry and used the publicly available 2MASS data to investigate the angular size of this apparent hole in the SGC. Our conclusions are:

- Our B-band galaxy counts in the NGC agree extremely well with the model of Metcalfe et al. (2001) but our SGC counts shows a significant galaxy deficiency, a mean 30.7% in the magnitude range 14<B<18.5.

- Good agreement is found for our NGC data with the SDSS and MGC number counts in the magnitude interval 16.5<B<18.5 and likewise for our SGC galaxy counts with the data of Bertin & Dennefield and the APM survey in the range 16.5<B<19.

- We compared our CCD galaxy catalogue to that of the 2dFGRS in the NGC and SGC. In the NGC we find good agreement of the zero-point at b_J=16 but our galaxies are, on average, 0.13 mag. brighter at b_J=18 implying a scale error of 0.065 mag/mag. We find a mean zero-point difference of 0.1 mag. in the range 16<b_J<18. In the SGC we find no zero-point or scale errors.

- After applying this 0.1 mag. zero-point correction to the 2dF NGC photometry we then find excellent agreement in both galactic caps between our CTIO data and the 2dFGRS, who's zero-point corrected results also imply a 30% normalisation difference between the NGC and SGC galaxy counts at B=18.

- After comparing our CTIO photometry to both the DUKST and APMBGC data we found that our galaxies were, on average, brighter by 0.24 mag. and 0.31 mag. respectively.

- Our R-band galaxy counts show a normalisation difference for the NGC and SGC data of ~22.2% in the range 13<R<17.

- The 2dF and DUKST n(z) distributions show striking common structure with regard to 2 "holes" in the galaxy distribution in the redshift ranges 0.03<z<0.05 and 0.06<z<0.09, with number discrepancy percentages of 35-50% , 25-60% respectively.

- The DUKST survey finds significantly larger galaxy number discrepancies over virtually all redshifts than the 2dF survey in the SGC. We claim that this is evidence that galaxies are biased tracers of the underlying mass distribution.

- Our 2MASS counts indicate a hole in the SGC galaxy distribution extending from at least δ=-10° to δ=-35° and in the RA direction from 320° to 70°. The magnitude of the K-band galaxy deficiency in this region is 25-30%

- Using variable $\phi^{\star}$ models based on the structure seen in the DUKST and 2dFGRS n(z)'s we claim that the galaxy count data is consistent with there being a hole in the SGC galaxy distribution over the whole 4300 deg^2 APM area, which extends out to z=0.1.

- Taking together the conclusions using the 2MASS and our variable $\phi^{\star}$ models we conclude that there is a galaxy number deficiency of 30% over a huge angular area of 100°x60° in the SGC. The evidence is that this hole extends out to z=0.1 or $300h^{-1}$Mpc.

- We show, using a simple model, that significant power is required in the two-point correlation function on very large scales if there is to be any reasonable chance of the existence of such a large hole in the galaxy distribution.

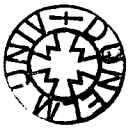

Chapter 4

Galaxy Clustering in the NGC and SGC

In the last chapter we used our CTIO data to calculate galaxy number counts in the NGC and SGC as well as making photometric checks of other galaxy catalogues. Our data, covering large areas of sky in the NGC and SGC, provided the *first ever* chance to make detailed checks of the bright ($b_J < 17$) galaxy data of the Durham/UKST survey and that of the APM-based 2dFGRS SGC field using our accurate CCD photometry. This enabled us to gain crucial information about the nature of the galaxy count and red-shift distributions over huge areas of sky in the local, $z < 0.2$, Universe. In this chapter we make further use of our CTIO CCD data to investigate further the form of the galaxy distribution, by analysing the clustering of galaxies in the NGC and SGC using the two-point correlation function. We will first introduce and explain the correlation function in Section 4.1 as a tool with which to analyse the clustering properties of galaxies. We will review the estimator methods of the two-point correlation function in Section 4.2 and then present galaxy clustering results from our CTIO, Curtis Schmidt data in Section 4.3. In section 4.4 we will discuss systematic biases that could effect our correlation functions and the implications of our results when coupled with the galaxy number count analysis from the previous chapter is discussed is Section 4.5. Our conclusions are presented in Section 4.6.

4.1 History

The correlation function is probably the most well-known tool that is used to quantify the clustering of a galaxy distribution from an astronomical data-set. The most common form of the correlation function is the two-point correlation function

(Peebles 1980), defined as:

$$\delta P_{ij} = \bar{n}\delta V_{ij}[1 + \xi(x)] \tag{4.1}$$

where $\bar{n}$ is the mean number of objects in the data-set. If a random member of the data-set, galaxy i, is selected then δP is the probability of finding a second member, galaxy j, within a volume δV_{ij} at a distance x from galaxy i. So, if $\xi(x) > 0$ then we have a clustered distribution as we have more chance of finding a second galaxy, given a first galaxy, within a distance x than if the galaxy distribution were random. Therefore, $\xi(x)$ is a measure of this excess probability. Conversely, if $\xi(x) < 0$ then we would have an anti-clustered distribution, and if $\xi(x) = 0$ then our equation reduces to $\delta P_{ij} = \bar{n}\delta V_{ij}$, which would correspond to a random distribution.

The two-point correlation function in this form is used to analyse the 3D distribution of galaxies in the Universe, but the projected or angular two-point correlation function (Groth & Peebles 1977) is also a very powerful tool and is the most useful for our purposes, since we do not have red-shifts for our galaxies. This is defined in a similar way to the spatial function:

$$\delta P_{ij} = \bar{N}\delta\Omega_{ij}[1 + \omega(\theta)] \tag{4.2}$$

where $\bar{N}$ is the mean number of galaxies per steradian. Here δP_{ij} is the probability of finding a galaxy j within solid angle $\delta\Omega_{ij}$ at an angular distance of θ from galaxy i.

The two-point correlation function is a second moment of the galaxy distribution, exactly like the standard deviation is a second moment of the distribution of a random variable. The standard deviation measures the width or spread of the distribution of a random variable, but it cannot give a complete description unless the distribution is Gaussian. In this special case, just the first and second order moments or the mean and standard deviation will completely describe your random sample. In general then, you will need higher order moments to quantify your distribution. The same is true of the correlation function. The two-point correlation function *can* therefore give you a complete description of the galaxy distribution,

provided the density fluctuations are Gaussian. Although this may seem an extreme assumption, the reason the two-point correlation function is such a powerful tool is that most current models of the early Universe invoke an "inflation" phase (Bardeen et al. 1983) which predict that very early density fluctuations in the Universe *were* gaussian after inflation. These gaussian density fluctuations about 10^{-34}s after the Big Bang can then be linked to the galaxy distribution on large (r>10Mpc) scales by linear purturbation theory meaning the two-point correlation function can give us a complete description of large-scale structure on scales >10Mpc. On small scales linear theory can not be assumed as density fluctuations dot not evolve independently of each other but are strongly coupled to each other by the presence, for example, of the gravitational potential well of a large structure like a galaxy cluster. In order to quantify structure on small scales higher order moments of the galaxy distribution may be needed. Even on large scales higher order moments are important as we expect them to be zero, assuming the fluctuations in the very early Universe were gaussian. For example, the three-point correlation function (or the third order moment) is defined as

$$\delta P_{ijk} = \bar{N}\delta\Omega_{ji}\delta\Omega_{ki}[1 + \omega(\theta_{ij}) + \omega(\theta_{jk}) + \omega(\theta_{ki}) + z(\theta_{ij}, \theta_{jk}, \theta_{ki})] \qquad (4.3)$$

where δP_{ijk} is the probability of finding, given a galaxy i, a second galaxy j and a third galaxy k within solid angles Ω_{ji} and Ω_{ki} at angular distances θ_{ij} and θ_{ki} respectively, where galaxies j and k are seperated by angle θ_{jk}.

Because $\omega(\theta)$ is a projected correlation function, it measures the clustering of *all* the galaxies along the line of sight. This effect can be reduced by taking magnitude slices, but even then these galaxies may still cover a large red-shift range. It is impossible to measure directly the spatial clustering of galaxies without knowledge of the 3D spatial distribution of the galaxy sample for which red-shift data is required. Even with galaxy distance information, there is still the "Finger of God" problem (Ratcliffe et al. 1998c). This is a particular problem in the relatively local Universe where an estimate of a red-shift can be in error, due to the fact that it is calculated from the measured recession velocity of the galaxy which can often contain a large

peculiar velocity component.

Despite this obvious limitation of the angular correlation function in terms of its 2-D information, its power lies in its simplicity and ease of computation. An angular correlation function will typically contain information from a much larger galaxy sample than that of a spatial correlation function due to the fact that obtaining red-shifts for galaxies is fairly expensive on telescope time. Obtaining photometry however is relatively less expensive - typically the spectroscopic limit for a telescope is 3 or 4 magnitudes brighter than the photometric limit. This larger sample of galaxies means that errors on the clustering amplitude are relatively small compared to the spatial correlation function.

The functional form of the two-point angular correlation function, $\omega(\theta)$, has been empirically found to be:

$$\omega(\theta) = A_\omega \theta^{-\delta} \tag{4.4}$$

on scales $\lesssim 1^\circ$ for large surveys, where A_ω is a normalisation coefficient and normally defined to be the clustering amplitude at 1 degree. Varying values of δ can be found in the literature and they lie in the range $0.55< \delta <0.8$ (Maddox et al. 1990; Ratcliffe et al. 1998b; Connolly et al. 2001). Note that A_ω is expected to decrease as the magnitude limit of a survey gets fainter according to Limber's equation (see section 5.3) and so the exact value of A_ω depends on the magnitude range of one's galaxy sample.

On scales $\gtrsim 1^\circ$ there is a characteristic break in the correlation function where δ gradually increases as θ increases (see Fig. 4.2 or Fig. 5 in Groth & Peebles 1977). The angular scale on which this break occurs, which is a function of the depth of the survey, implies a characteristic clustering length. Historically this "break" and large scale clustering amplitudes in general have proved difficult to measure accurately because of two main reasons. For small area, deep surveys eg. the Hubble Deep Field (Williams et al. 1996) there is the significant problem of the so-called integral

constraint. The integral constraint is a systematic effect induced by the fact that the mean galaxy density has to be estimated from the data itself, and which biases $\omega(\theta)$ low on all scales. For very large areas like the APM survey (a 4300 deg^2 field) this effect is negligible and the amplitude clustering bias is a negligible fraction of the intrinsic clustering signal. Our NGC and SGC data cover 243 and 297 deg^2 respectively, and we show in the next section that these areas are large enough for the integral constraint to be a very small fraction of our clustering amplitudes on all angular scales.

The second main source of error in determining the angular scale of the break in $\omega(\theta)$ is large scale gradients in the data. This is particularly problematic in large surveys because of the fact that small zero-point errors between CCD's/plates can propagate through the data. For example, a small zero-point error between two CCD's with the same exposure time, that cover the same area, will mean that one CCD will appear to detect more galaxies for a given magnitude limit. These density variations due to small zero-point errors in a survey add an artificial clustering signal to the correlation function and are a particular problem for large photographic surveys eg. the APM Galaxy Survey. The problem of large scale gradients has been controlled more successfully with the advent of CCD technology. Because of the linearity of CCD chips, zero-points can be calibrated extremely accurately suppressing this propagation effect over large areas. Our CCD data, covering large regions of sky in the North and South Galactic Caps is therefore an ideal source of information with which to analyse the clustering of galaxies.

4.2 The Calculation of the Two-Point Correlation Function

4.2.1 Estimators

As already explained, the two-point correlation is a measure of the excess probability of finding, given a galaxy i, a second galaxy j within solid angle $\delta\Omega$ at

angle θ from galaxy i. In order to estimate this "excess probability" one needs to compare the galaxy sample with a distribution of sources populated randomly and homogeneously within the survey area, where by definition $\omega(\theta) = 0$. If our random distribution has number density $\bar{n_R}$ per steradian, then the total random pair count, RR(θ) is given by:

$$RR(\theta) = 2\bar{n}_R^2 \sum_{i}^{N_R} \sum_{j>i}^{N_R} \delta\Omega_i \delta\Omega j \tag{4.5}$$

where N_R is the total number of random sources in the sample and the factor of 2 is to account for the fact that only values of j are used which satisfy the condition j>i. Similarly, we can calculate the total pair count, as a function of θ of the galaxy sample. Our galaxy sample will, in general, have $\omega(\theta) \neq 0$ and therefore we can write the total data pair count as:

$$DD(\theta) = 2\bar{n}_D^2(1 + \omega(\theta)) \sum_{i}^{N_D} \sum_{j>i}^{N_D} \delta\Omega_i \delta\Omega j \tag{4.6}$$

where $\bar{n_D}$ is the number density of the data (or galaxies) per steradian and N_D is the total number of galaxies. One can then obtain an estimate of the the angular correlation function by dividing equation 4.6 and 4.5 and re-arranging to obtain:

$$\omega(\theta) = \frac{DD(\theta)}{RR(\theta)} \left(\frac{\bar{n}_R}{\bar{n}_D}\right)^2 - 1 \tag{4.7}$$

This particular estimator is said to estimate the true galaxy number density to first order. Other estimators of the two-point correlation function also exist, where the number density is estimated to second order. These second order estimators have been shown, in general, to be less susceptible to biases when using small survey areas (Hamilton 1993). In our calculations we have used three estimators. The first is called the standard estimator (see Peebles 1980) and is a first order estimator of the number density and given by:

$$\omega(\theta) = \frac{DD(\theta)}{DR(\theta)} \frac{\bar{n}_R}{\bar{n}_D} - 1 \tag{4.8}$$

Secondly, the method of Hamilton (1993), which is a second-order measure of the galaxy number density:

$$\omega(\theta) = \frac{DD(\theta)RR(\theta)}{DR(\theta)^2} - 1 \tag{4.9}$$

The third is the method of Landy & Szalay (1993), which is also a second order estimator of $\bar{n_D}$ and given by

$$\omega(\theta) = \frac{DD(\theta) - 2DR(\theta)\left(\frac{\bar{n}_R}{\bar{n}_D}\right) + RR(\theta)\left(\frac{\bar{n}_R}{\bar{n}_D}\right)^2}{RR(\theta)\left(\frac{\bar{n_R}}{\bar{n_D}}\right)^2} \tag{4.10}$$

where the DD, DR and RR terms are the data-data, data-random and random-random pair counts and are defined in an analogous way to equations 4.6 and 4.5.

4.2.2 The Random Catalogue

When we generated the random sample of galaxies which we use to calculate our correlation function we had to make sure these random sources were distributed uniformly over exactly the same regions of sky as our data. Our strategy was as follows. First an artificial box around the entire data-set in question was constructed. For example, for our CTIO NGC data, the box was defined so a region was contained within constant lines of Right Ascension at 9hrs 30mins and 15hrs 00mins and constant lines of Declination at +1° and -11°. Random numbers were generated between 0 and 1 using the Numerical Recipes in Fortran (Press et al. 1989) RAN3 routine from which the outputs was linearly transformed to produce numbers in the required Declination range of -11°< δ <+1°. These numbers were then converted to radians before taking the arcsine of each of them. The reason for doing this is that when a random sample of sources in the (RA(α),Dec(δ)) coordinate system is projected onto a spherical surface, like the one assumed with our region around the NGC data, one finds that the galaxy density monotonically decreases as a function of $|\delta|$ according to a $\sin^{-1}\delta$ law, where δ is the declination of the source. Then, a second set of random numbers is generated in radians in the chosen RA range of our box. Each RA coordinate is assigned to one of the Dec co-ordinates so that we had a set of (α,δ) co-ordinates where the source density varies with δ according to this arcsin dependence. Each source is then compared to every one of the ~800 frames in our NGC data-set and our code calculates whether these source co-ordinates are

contained in regions of sky observed by us. Our SGC random sample was calculated in the same way but the box was defined by a region contained within constant Right Ascensions at 21hrs and 04hrs and Declinations in the range -46°< δ <-26°.

Also, we could not ignore the fact that the observations were carried out over a large region of sky when calculating the angle, θ, subtended by a pair of sources. For very small fields one can simply use Pythagoras' Theorem to calculate θ from the difference in the RA and DEC angles:

$$\theta_{ij}^2 = (\theta_{RA_i} - \theta_{RA_j})^2 cos(\theta_{DEC_i}) cos(\theta_{DEC_j}) + (\theta_{DEC_i} - \theta_{DEC_j})^2 \qquad (4.11)$$

where θ_{RA_i} is the RA of source i, etc.

However, for large fields, this becomes a very poor approximation due to the curved geometry of the spherical celestial sphere. By using spherical polar coordinates one can show that:

$$cos(\theta) = sin(\theta_{DEC_i}) sin(\theta_{DEC_j}) + cos(\theta_{DEC_i}) cos(\theta_{DEC_j}) cos(\theta_{RA_i} - \theta_{RA_j}) \qquad (4.12)$$

and this is the equation we used to calculate the angle subtended by a pair of sources in our fields.

4.3 Results

4.3.1 Galaxy Clustering Results from the NGC and SGC

We have calculated the two-point angular correlation function for our data-sets in both the North and South Galactic Caps using the standard estimator and the estimators of Hamilton and Landy & Szalay, with $\bar{n_R} = 10\bar{n_D}$. Fig. 4.1 shows the results of these calculations for our NGC data in the magnitude range 17<B<18. We find that the calculated clustering amplitudes of the Hamilton and Landy & Szalay estimators agree to within 0.2% in the range log(θ) >-1.8 and only at very

small angles are there slight deviations. The standard estimator shows good agreement with the other two for $\log(\theta) < 0$ but on larger scales it over-estimates the clustering amplitude of our data. The good agreement of the estimators is to be expected since our survey areas of 255 and 297 square degrees for the NGC and SGC respectively are relatively large and therefore minimize any biasing effects when estimating the mean density of galaxies over our fields. The small differences in the estimators in the range $\log(\theta) < -1.8$ are simply due to poor statistics as our bright galaxy data are not able to accurately sample clustering on angular scales this small. For $\log(\theta) > 0.6$ edge effects become significant as these clustering angles are comparable to the dimensions of our strips.

Shown in Figs 4.2 and 4.3 are the clustering amplitudes plotted as a function of $\log(\theta)$ for the NGC & SGC and "combined" (NGC plus SGC) data-sets respectively. These plots show the estimator of Landy & Szalay (1993) using bins of $\log(\theta) = 0.2$. We have shown magnitude slices of 17<B<18 and 18<B<19 in each figure with best fit lines using a simple least square method. The results of these fits are shown in table 4.1. The 17<B<18 slice for the NGC data in Fig. 4.2 shows a slope of -0.749 in the range -2.2<logθ <0 with the characteristic break in the correlation function occuring at about 1 degree. The 18<B<19 slice shows a slope of -0.726 in the range -2.2<logθ<-0.2 with the break occurring at about 0.6 degrees. In the SGC we find slopes of -0.756 and -0.741 with the breaks occurring at 4 and 1.6 degrees for the 17<B<18 and 18<B<19 magnitude slices respectively. We also note that on small scales where $\log\theta < -1.8$ our data appears to depart from the simple power law behaviour and shows a steeper slope. This may be a real effect, but the errors on our data-points are beginning to increase and therefore it is difficult to draw any definitive conclusions.

Note that the errors, $\delta\omega(\theta)$, on all the correlation function plots in this chapter are Poisson and calculated using the equation:

$$\delta\omega(\theta) = \frac{\omega(\theta) + 1}{\sqrt{DD(\theta)}} \tag{4.13}$$

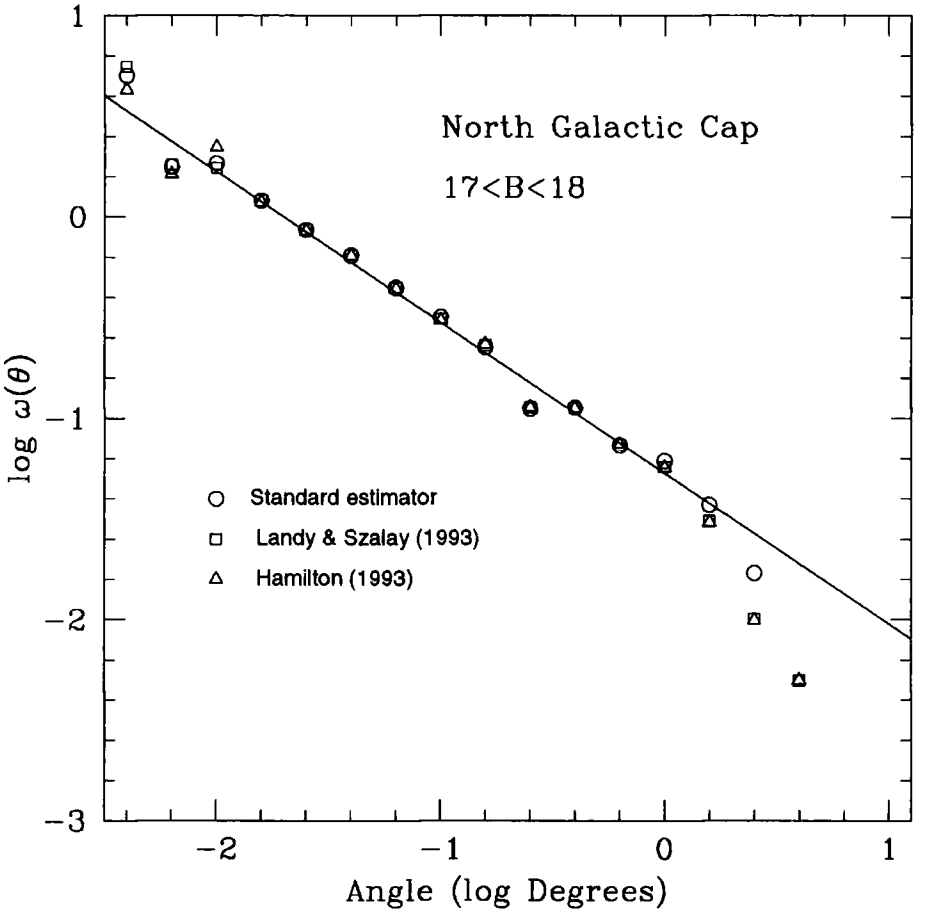

Figure 4.1: The correlation function of our NGC data in the magnitude range 17<B<18 is shown using the Standard estimator, and those of Hamilton and Landy & Szalay. Excellent agreement is found for -1.8<log(θ) <0 but the Standard estimator tends to over-estimate the clustering amplitude of our data relative to the other two for large ($\theta > 1°$) angles.

where $DD(\theta)$ is the number of galaxy-galaxy pairs as a function of θ as defined in equation 4.6. In fact Poisson errors are expected to underestimate the true error (Connolly et al. 2001) since the data points in each angular bin are highly correlated (see Scranton et al. 2001 for a detailed discussion of this effect).

The "combined" data-set was calculated assuming no clustering between galaxies in the NGC and SGC, which is a good assumption since any such signal would be on much larger scales than 10°, the upper limit of our angle axis in fig 4.3. We calculated the angular correlation function for the "combined" data-set using two different methods. The first method was to normalise to the total galaxy number count of the NGC and SGC and therefore sum the pair counts DD, DR and RR before using the Landy & Szalay estimator. The other method normalised to the NGC and SGC number counts separately, effectively taking the mean of the the two clustering amplitudes in corresponding magnitude bins. Now, because the galaxy number count for the NGC data is significantly larger than that of the SGC (~30% in the magnitude range 14<B<18 - see chapter 4) this will begin to make a difference between the estimates for large angles. The total-count normalised estimate will biased be towards that of the NGC $\omega(\theta)$ (relative to the mean of the NGC and SGC $\omega(\theta)$'s) because the larger number of galaxies means that the total NGC+SGC DD pair count will consist of $1.3^2 = 1.69$ times as many NGC pairs as SGC pairs. This therefore results in a lower $\omega(\theta)$ for large angles than that obtained by normalising to the NGC and SGC because the NGC has lower clustering amplitudes for the corresponding magnitude bin than the SGC. The difference between the two estimates is negligible except for very large angles ($\theta > 4°$) and so our conclusions are essentially independent of which method we choose. Note that we have not applied an integral constraint correction (see Section 4.4.1).

The higher clustering amplitudes for the brighter magnitude slice is expected because of two reasons. Firstly, a given angular scale corresponds to a larger spatial separation when probing deeper into the Universe and this causes the observations to be shifted to the left (ie larger angles) as the magnitude limit is increased. Secondly, there are more galaxies when probing larger volumes, inducing a larger

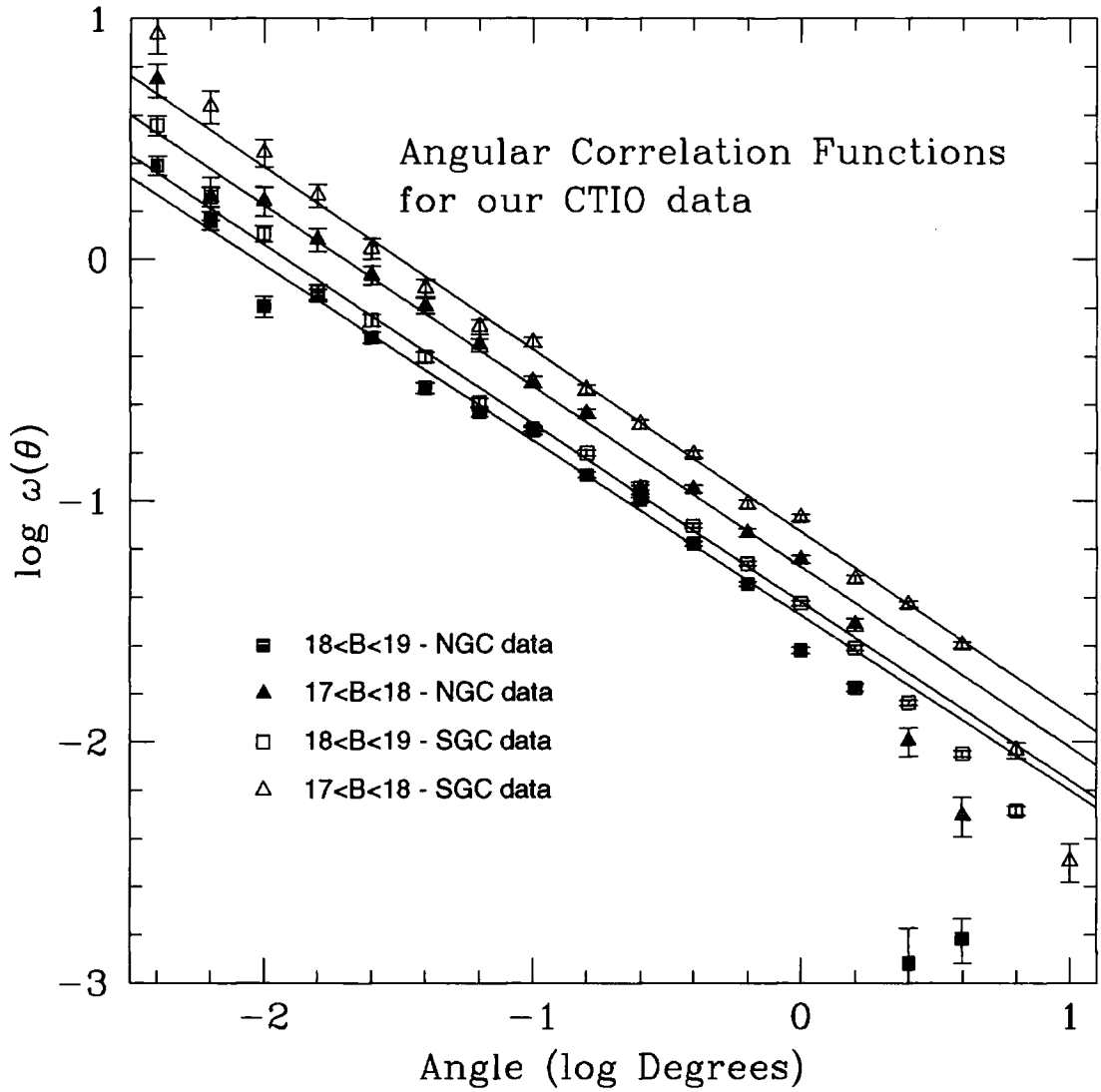

Figure 4.2: The B-band angular correlation functions for our CTIO data. This plot shows magnitude slices in the range 17<B<18 and 18<B<19 for our NGC and SGC data. The filled squares and triangles show the faint and bright magnitude slices respectively for the NGC and the unfilled triangles the corresponding slices in the SGC. Our clustering amplitudes for the SGC data are higher than the corresponding magnitude slices in the NGC with the clustering excess being more pronounced, at 40% , for the brighter magnitude slice as opposed to 14% for the 18<B<19 slice. No integral constraint correction has been applied to this data - see Section 4.4.1 for more details.

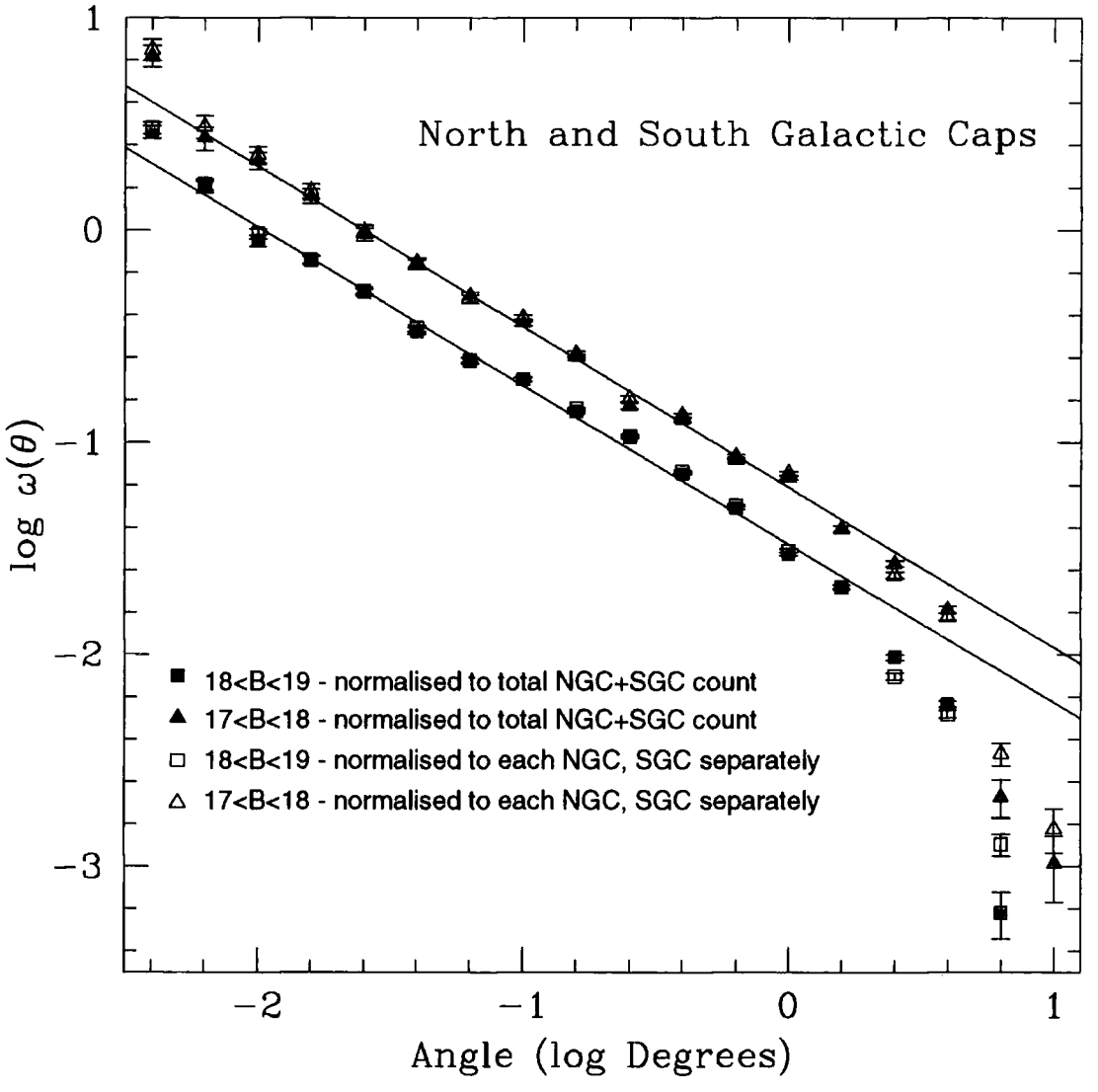

Figure 4.3: The B-band angular correlation function for the NGC and SGC "combined" data set. We assumed no clustering between galaxies in opposing galactic caps as any such signal would be on angular scales much larger than we show in this plot. The "combined" correlation function was calculated in two ways: the first way was to normalise to the total galaxy number count from the NGC+SGC (shown by the filled symbols) before calculating $\omega(\theta)$ and the second way was to normalise to the NGC and SGC seperately (the unfilled symbols), effectively taking a mean of the two clustering amplitudes. It can be seen that the difference between the two methods is negligible except at very large scales ($\theta > 4°$)

data-set	B	$\log(A_\omega)$	δ	$\sim\theta_{break}$
NGC	17-18	-1.272	0.749	1.3
	18-19	-1.474	0.726	0.8
SGC	17-18	-1.126	0.755	4.0
	18-19	-1.418	0.741	1.6
combined	17-18	-1.212	0.757	3.2
	18-19	-1.481	0.747	1.6

Table 4.1: Best fit values of $\log(A_\omega)$, δ for the NGC, SGC and "combined" samples along with an estimate by eye of the value of $\log_{10}(\theta_{break})$ where the characteristic break in the correlation function occurs.

projection effect which reduces the galaxy clustering signal. This has the effect of moving the observations downwards to lower clustering amplitudes for the same angular separation as the magnitude limit becomes fainter.

4.3.2 Scaling Tests and Comparisons

We can model this scaling represented by shifts in $\log(\theta)$ and $\omega(\theta)$, not only of our data in difference magnitude slices, but also between our data in a given magnitude interval and that of other authors (eg. Groth & Peebles 1977; Maddox et al. 1990; Connolly et al. 2001) by using the relativistic version of Limber's equation (Phillipps et al. 1978). Because $\omega(\theta)$ is a projected version of the spatial correlation function $\xi(r)$ one can calculate $\omega(\theta)$ using Limber's equation by integrating $\xi(r)$ along all possible lines-of-sight, where each pair of "lines of sight" subtend an angle θ. When performing this integration one needs to make assumptions about the functional form of $\xi(r)$ and the selection function of the particular data sample, which may contain evolutionary effects. Our procedure was to optimize the parameters of $\xi(r)$ so that when the integration was performed a good fit to the $\omega(\theta)$ of the particular data-set was found. We decided to scale everything to the depth of the Lick survey and so the calculated parameters for $\xi(r)$ were then used to perform the integration of Limber's equation again, except with the magnitude range and selection functions changed to those of the Lick survey. This results in a second $\omega(\theta)$, corresponding to a "Lick-scaled" version of the data-set $\omega(\theta)$ in question.

The translational shift between the two curves is then calculated and applied to the appropriate observations. The relativistic version of Limber's equation, as found in Phillipps et al. (1978), is:

$$\bar{N}^2[1+\omega(\theta)] = \int_0^\infty dz_1 f^2(z_1) g(z_1) \phi(z_1) \int_0^\infty dz_2 f^2(z_2) g(z_2) n(z_2) \phi(z_2) [1+\xi(r,z)] \tag{4.14}$$

The radial distance r of a source is

$$r^2 = f^2(z)\theta^2 + g^2(z)y^2 \tag{4.15}$$

and z is defined as

$$z = 0.5(z_1 + z_2), y = z_1 - z_2 \tag{4.16}$$

f(z) is the relativistic angular diameter distance written as:

$$f(z) = \frac{cq_0^2(1+z)^2}{H_0} q_0 z + (q_0 - 1)[(2q_0 z + 1)^{1/2} - 1] \tag{4.17}$$

and g(z) is the derivative of proper distance with respect to z defined as:

$$g(z) = \frac{c}{H_0(1+z)^2(2q_0+1)^{1/2}} \tag{4.18}$$

$\phi(z)$ is the probability of selecting a galaxy at red-shift z with absolute magnitude M, and is defined from a model of the galaxy luminosity function. The mean number density of galaxies in a survey $\bar{N}$ can thus be written as:

$$\bar{N} = \int_0^\infty dz f^2(z) g(z) n(z) \phi(z) \tag{4.19}$$

So, given an expression for $\xi(r,z)$ and a model for $\phi(z,M)$, equation 4.14 predicts $\omega(\theta)$ by integrating over all possible line-of-sight distances z_1 and z_2. We assume a two-power law fit to the spatial correlation function (Groth & Peebles 1977; Maddox et al. 1990; Connolly et al. 2001) of $\xi(r) = (r/r_0)^\gamma$ for r<r_1 and $\xi(r) \propto r^{-3}$ for r>r_1, where r_1 corresponds to the break feature we have described and r_0 the characteristic clustering length. We have used the galaxy luminosity function of Metcalfe et al. (2001) when performing these calculations, which is

data-set	B range	r_0 (Mpc)	γ	r_1 (Mpc)
NGC	17-18	4.5 ± 0.1	1.71 ± 0.01	10 ± 2
	18-19	4.9 ± 0.1	1.68 ± 0.02	10 ± 3
SGC	17-18	5.3 ± 0.1	1.72 ± 0.02	33 ± 2
	18-19	5.1 ± 0.1	1.72 ± 0.01	34 ± 2

Table 4.2: The best fit values of r_0, γ and r_1 for the NGC and SGC spatial functions using Limber's equation to de-project our angular correlation functions. r_0 is the characteristic clustering length, δ is the slope and r_1 is the scale, in proper co-ordinates, where the break in the spatial function occurs.

known to fit the bright B-band number counts (Metcalfe et al. 1996) and n(z) distribution (Campos 1996). The values of $M^\star$, $\phi^\star$ and α for the different galaxy types is shown in Table 3.3.

Figs. 4.4 and 4.5 show the results of the scaling tests described using equation 4.14. The resulting best fit values for the parameters r_0, r_1 and γ when we perform these scaling tests, assuming a double power law form for the spatial correlation function, are shown in Table 4.2. Both Figs 4.4 and 4.5 illustrate that our magnitude slices for the NGC and SGC show excellent agreement with each other after being scaled to a Lick depth of B=18.6 (equiv. to b_j=18.4 used in Maddox et al. 1990). Our NGC data agree well with the APM on small scales of $\log(\theta) < -1.5$ but, because of our slightly higher values of δ, show slightly lower clustering amplitudes than predicted from the Lick and APM data in the range $-1.5<\log(\theta)<0$. The characteristic "break" in $\omega(\theta)$ occurs at smaller scales for our NGC data ($\sim 1°$) than for the Lick and APM data ($\sim 1.6°$), but we find a similar shape to our correlation functions as Lick on large scales $> 1°$, although our amplitudes are slightly lower. This is in contrast to the APM data which shows a much gentler turnover after the break at $\theta = 1.6°$ than both us and Groth & Peebles. Fig 4.5 shows excellent agreement of our SGC correlation functions with that of the Lick and APM data on intermediate scales of $-1.8<\log(\theta)<0.0$. On larger scales, the "break" in the correlation functions of our data occurs at $\theta \sim 2°$ and our SGC points lie roughly equidistant between the points of the Lick and APM surveys for $\log(\theta) > 0.3$.

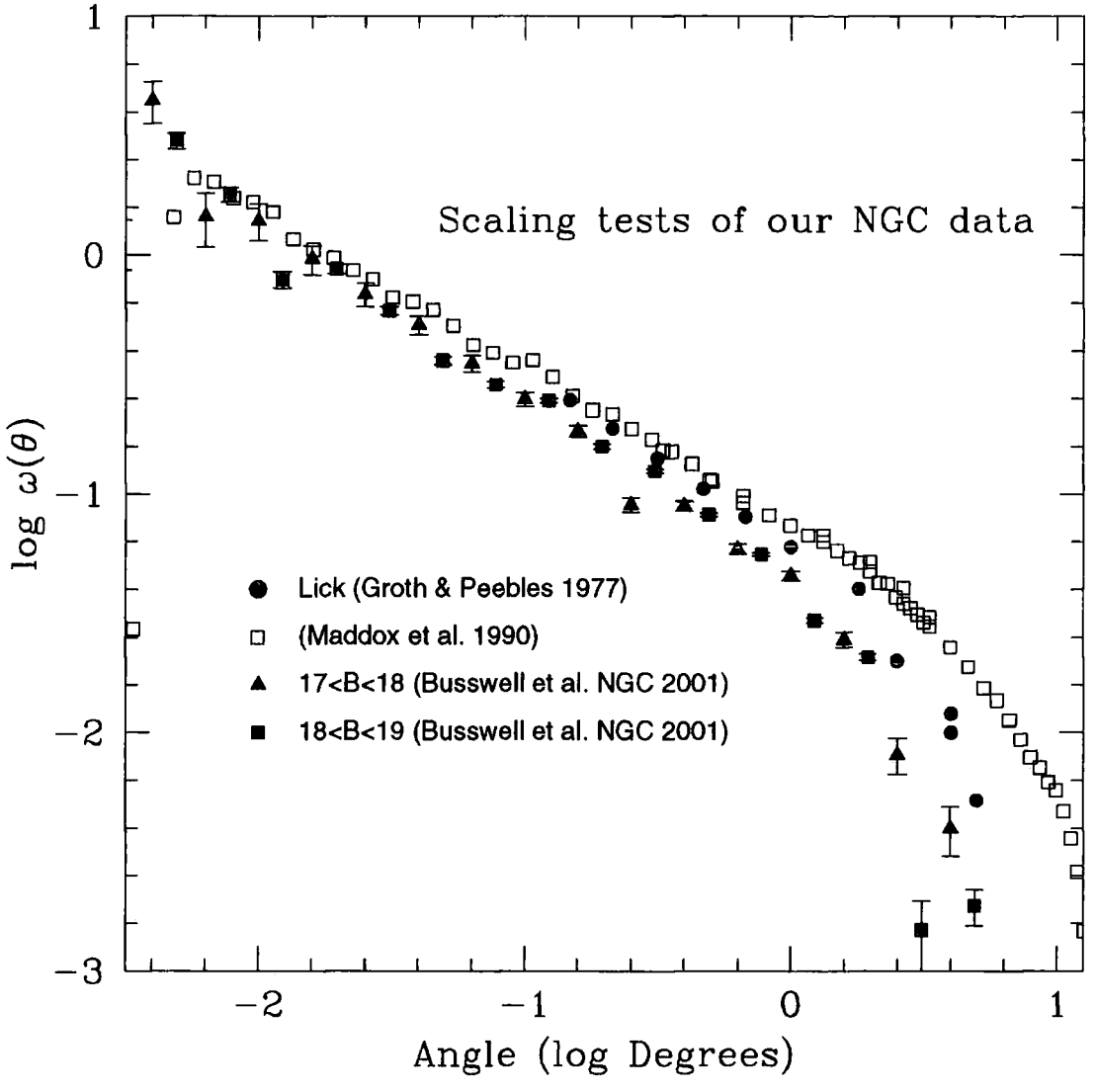

Figure 4.4: This plot shows the data of various surveys scaled to the Lick Depth using Limber's Formula. The Lick Depth was taken to lie at a magnitude limit of 18.6 or b_J=18.4 (see Maddox et al. 1990). The solid circles show the Lick data of Groth & Peebles, the open squares that of the APM survey (Maddox et al. 1990 and the filled triangles and squares that of our NGC CTIO data in magnitude ranges of 17<B<18 and 18<B<19 respectively.

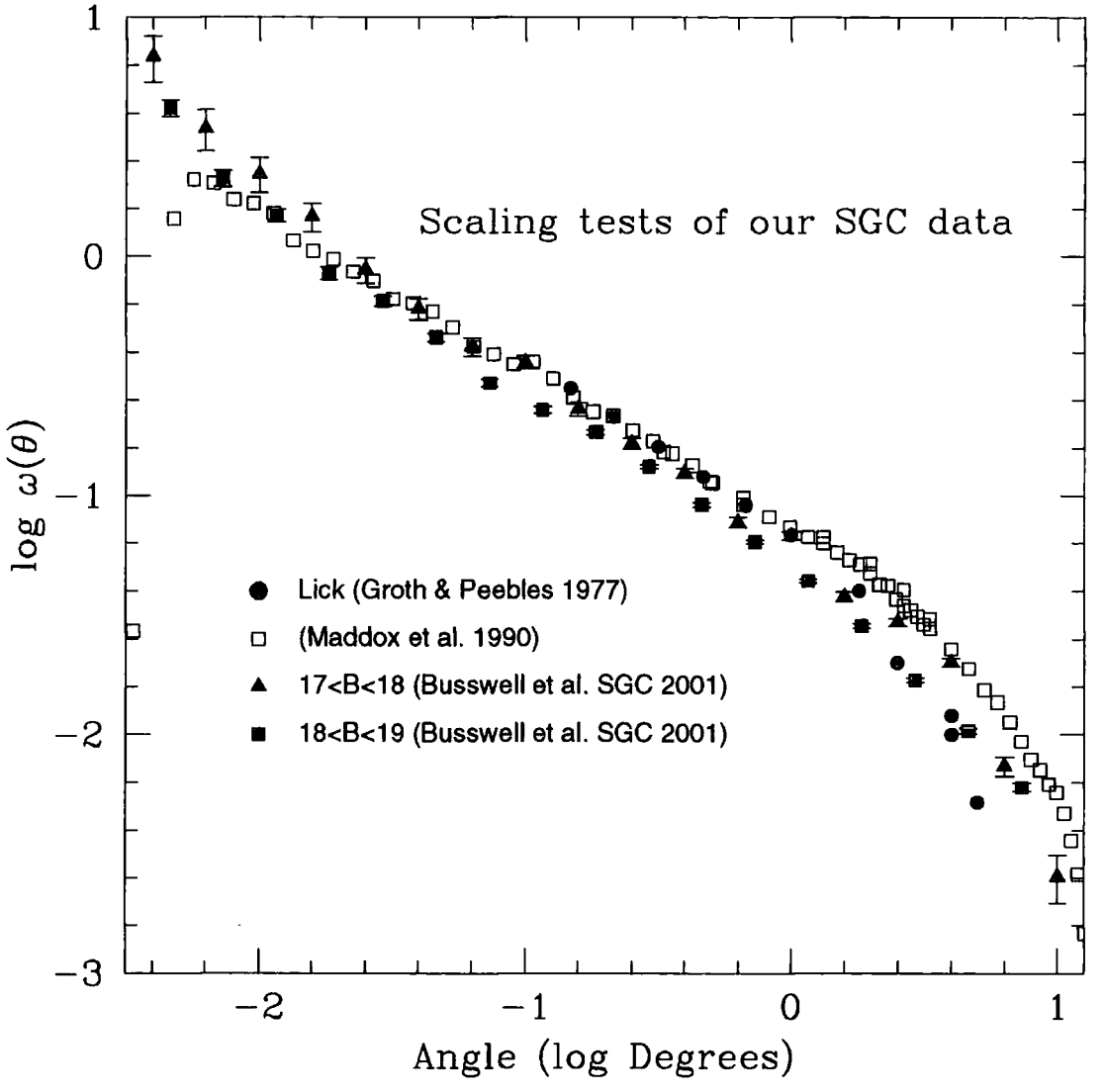

Figure 4.5: Here we show the same plot as in Fig. 4.4, but with our *SGC* CTIO data, again shown in magnitude slices of 17<B<18 and 18<B<19 with filled triangles and squares respectively. The Lick Depth was taken to lie at a magnitude limit of 18.6 or b_J=18.4 (see Maddox et al. 1990). The solid circles show the Lick data of Groth & Peebles and the open squares that of the APM survey (Maddox et al. 1990).

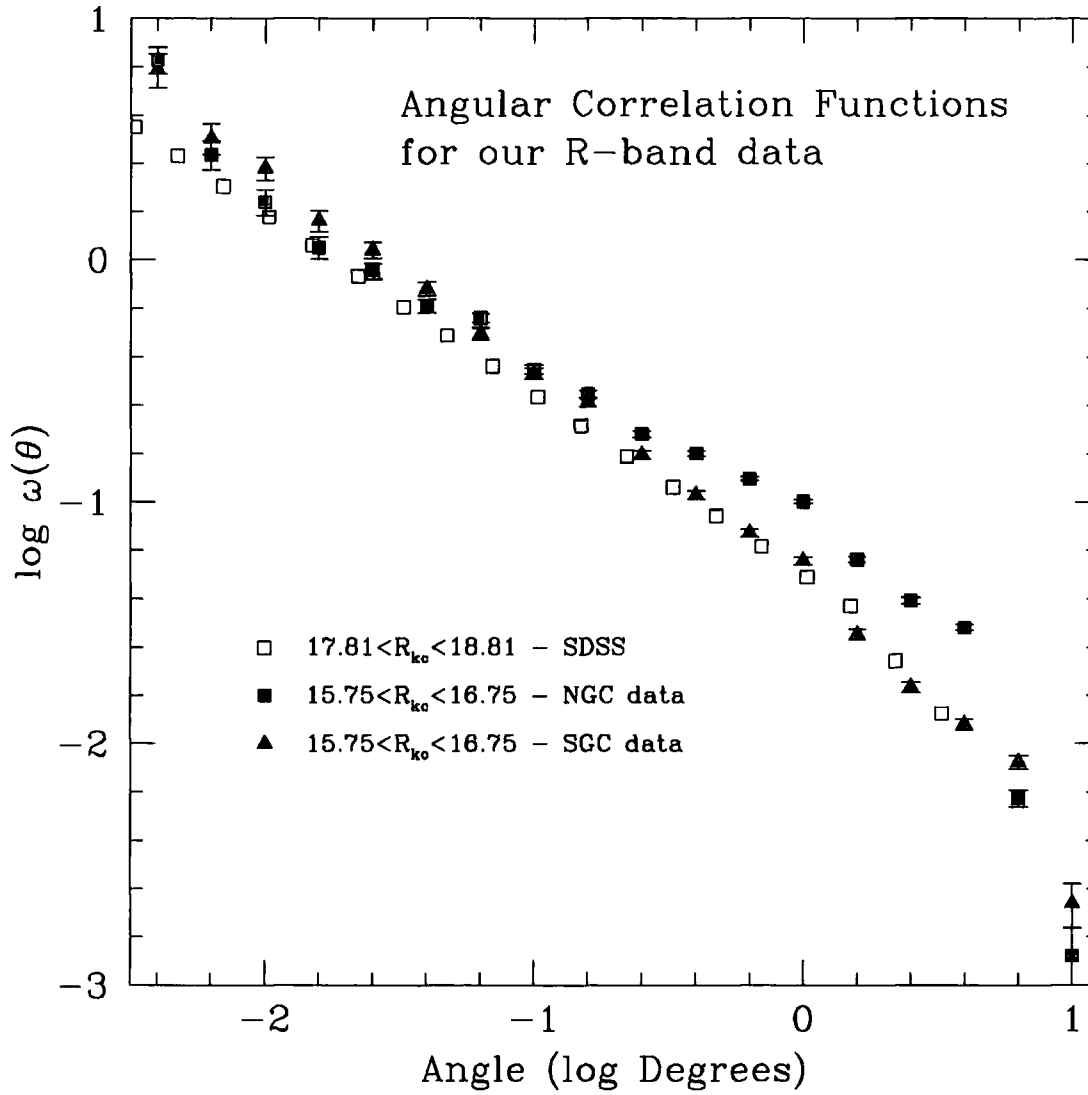

Figure 4.6: Here we show our R-band correlation functions for the NGC and SGC and that of the SDSS scaled to our depth of R_{kc}=16.75. The filled squares and triangles show our NGC and SGC R-band data respectively in the magnitude range 15.75<R_{kc} <16.75 with the open squares that of the SDSS data in the range 18< $r^{\star}$ <19 from Connolly et al. (2001). Note that the SDSS points for θ <1° have been plotted in accordance with the power law quoted in Connolly et al. i.e. that are not the actual data points. We have converted the Sloan $r^{\star}$ filter to that of the R_{GKC} filter using the transformation in Blanton et al. (2001). A further 0.08 magnitude offset (Shectman et al. 1996) is then applied in order to change to our R_{kc} band. Our data generally shows good agreement with that of the SDSS with the NGC data showing more power on large scales of θ >0.3°.

data-set	R range	r_0 (Mpc)	γ	r_1 (Mpc)
NGC	15.75-16.75	6.0 ± 0.1	1.68 ± 0.02	25 ± 2
SGC	15.75-16.75	5.7 ± 0.1	1.77 ± 0.02	31 ± 2

Table 4.3: The best fit values of r_0, γ and r_1 for our R-band NGC and SGC spatial correlation functions using Limber's equation to de-project our angular functions. r_0 is the characteristic clustering length, γ is the slope and r_1 is the scale, in proper co-ordinates, where the break in the spatial function occurs.

Fig. 4.6 shows our NGC and SGC R-band correlation functions and that of the SDSS (Connolly et al 2001) $18< r^* <19$ magnitude slice scaled to the depth of our survey. We have converted to our R_{kc} filter using the transformation quoted in Blanton et al. (2001) of R_{GKC}=r*-0.05-0.089(g*-r*). By assuming the quoted mean colour of g*-r*=0.7 and using a 0.08 magnitude offset to convert between R_{GKC} and R_{kc} (Shectman et al. 1996) we calculate a magnitude difference of r*-R_{kc}=0.19. The mean colour of our galaxy samples is B-R=1.25 and so we calculated our angular R-band correlation functions in the magnitude range $15.75<R_{kc}<16.75$ in order to be consistent with our 17<B<18 magnitude slices. Our NGC clustering amplitudes agree with the SDSS at small angles of θ <0.1°, but predict slightly more power on larger scales of θ >0.3°.

Our SGC data shows the opposite effect with excellent agreement on large scales but predicting slightly more power for θ <0.03°. There is a disagreement between the clustering amplitudes of our NGC and SGC fields on scales of θ >1° and this is probably due to large scale cosmic variance in the galaxy distrubution. On small scales of $\log(\theta) < -1.8$ our correlation functions depart from the fitted power laws and this may be due to the fact that our errors are relatively large here. However, it is interesting that Connolly et al. (2001) found a similar behaviour for the SDSS data, but drew similar conclusions to us because of the size of their errors. Only 2% of the SDSS data has so far been publicly released, but as the survey continues the errors will decrease and it will be possible to determine whether this behaviour on small angular scales is a real artifact of galaxy clustering.

We have de-projected our R-band angular correlation functions using the method already described except that we use the R-band luminosity function parameters of Metcalfe et al. (2001). The results are shown in Table 4.3. We find the break in the correlation function occuring on slightly larger scales of 31 Mpc as compared to the NGC value of 25 Mpc. However these differing values of the break for the NGC and SGC fields are much closer than for our B-band results. We also find fairly high values of r_0, 6.0 and 5.7 Mpc, relative to our B-band results. The SDSS team have derived a value of r_0=6.1 Mpc for their NGC angular correlation function, in excellent agreement with our NGC value of 6.0. There is a significant overlap between the NGC survey fields of us and the SDSS of 92 deg^2 and so this good agreement suggests that we are measuring real clustering in the galaxy distribution and are subject to minimal systematic biases in our angular correlation functions.

4.4 Systematic Biases

In Section 4.3 we showed that our clustering results in the B-band were consistent with the scaling trend expected by Limber's equation (equation 4.14) for the magnitude slices 17<B<18 and 18<B<19. This indicates that we can believe that our results are measuring real clustering in the galaxy distribution rather then clustering induced by systematic effects such as the integral constraint and large-scale gradients. Nevertheless we estimate the effect of possible systematics in order to be absolutely confident that the biases they induce are a small fraction of the actual clustering signal we have measured in our data.

4.4.1 The Integral Constraint

The integral constraint is a source of error that one must consider when calculating the correlation function. Our fields are relatively large and therefore we do not expect this well-known biasing effect to have a significant effect on our results. The integral constraint is quantified using the relation:

$$C = \frac{1}{\Omega} \int \int \omega(\theta) d\Omega_1 d\Omega_2 \tag{4.20}$$

where C is the integral constraint and θ is the angle subtended by the two solid angles $d\Omega_1$ and $d\Omega_2$. If we assume a power law form for $\omega(\theta)$ with $\delta = 0.8$ then we can calculate C for both our NGC and SGC data. We find that C_{NGC}=0.128A_ω and C_{SGC}=0.120A_ω. In fact these derived values of the integral constraint are probably upper limits because we have assumed the power law form of the correlation function extends to all angular scales. We will see in the discussion section that when these integral constraint values are applied to our measured two-point angular correlation functions, it does have an effect on angular scales of $\theta > 1°$.

4.4.2 Large Scale Gradients

As has been mentioned, large-scale gradients are always a problem for wide-area surveys even though we have the increased accuracy of CCD photometry, meaning high accuracy of our frame zero-points. We can investigate the possibility of a large scale gradient within our data by estimating the zero-point errors of our frames and invoking a random walk scenario along one of our sequences. For example, a typical sequence consists of 30 frames with constant declination and right ascensions varying such that they overlap each other by half a chip (see chapter 2 for details of data reduction). We estimate the typical error on our frame zero-points by comparing unsaturated stars on the overlap regions of the frames. A best fit zero-point offset is calculated for each pair of overlapping frames in the sequence and the mean of these offsets is typically ~0.005 mags. In a random walk scenario the cumulative zero-point error of the nth frame relative to the 1st frame will be $\sim 0.005\sqrt{n}$ mags. Assuming n=30 this gives 0.027 mags. In terms of flux/photon counts this corresponds to $10^{0.027/2.5} = 1.025$ implying a 2.52% gradient from the first frame to the 30th frame. The reason we estimate the large scale gradient only within a typical sequence of frames is that each sequence is calibrated independently of any other sequence from the standard star frames using our colour equations (equations 2.5 and 2.6).

We can also estimate the possible existence of a large scale gradient by using external CCD photometry from the MGC (Driver et al. - priv. com.). We have shown our galaxy photometry to be in good agreement with that of the MGC in terms of a global zero-point offset (Fig. 2.13). However, in terms of a large scale gradient it is the variation of the localised zero-point difference that is important, as this can create artificial density variations over the survey and therefore the presence of spurious clustering measurements. In Fig 4.7 we have plotted the Right Ascension of our NGC equatorial strip against the magnitude residual between our CTIO data and the MGC for all galaxies with B<18. Virtually all of the large discrepancies in terms of the residuals are where we are too bright and this is because of blending problems with our data due to our large pixel size, ie. the magnitude of two blended sources is measured by us as opposed to a single source in the MGC. The best fit line shown as a function of Right Ascension (binned in multiples of 10 degrees) uses a simple least squares fit. The maximum and minimum values of the residual fit from the RA binning are 0.04834 and 0.02778 for RA=190 and RA=160 respectively. This is a magnitude difference of 0.0206 or a gradient of 1.91%, in good agreement with the value estimated using the simple random walk model.

If we assume that this 2% gradient varies uniformly across our sequence of frames such that the zero-point difference moves from -1% on the first frame to +1% on the 30th frame then the effect can be estimated in terms of a bias in $\omega(\theta)$. An illustration of this simple model is shown in Fig. 4.8. We then use the Standard estimator defined as:

$$\omega(\theta) = \frac{DD}{DR}\frac{\bar{n}_R}{\bar{n}_D} - 1 \tag{4.21}$$

We have chosen our co-ordinate system such that $\bar{n}_R$=$\bar{n}_D$, $\rho_D(x) = (1 + x/100)$ and $\rho_R(x) = 1$. We know that DD$\sim \int dx\rho_D^2$ and DR$\sim \int dx\rho_D\rho_R$ and so:

$$\begin{aligned} \omega(\theta) &= \frac{\int_{x=-1}^{x=1} dx\rho_D^2}{\int_{x=-1}^{x=1} dx\rho_D\rho_R} - 1 \\ &= \frac{\int_{x=-1}^{x=1} dx(1 + x/100)^2}{\int_{x=-1}^{x=1} dx(1 + x/100)} - 1 \end{aligned} \tag{4.22}$$

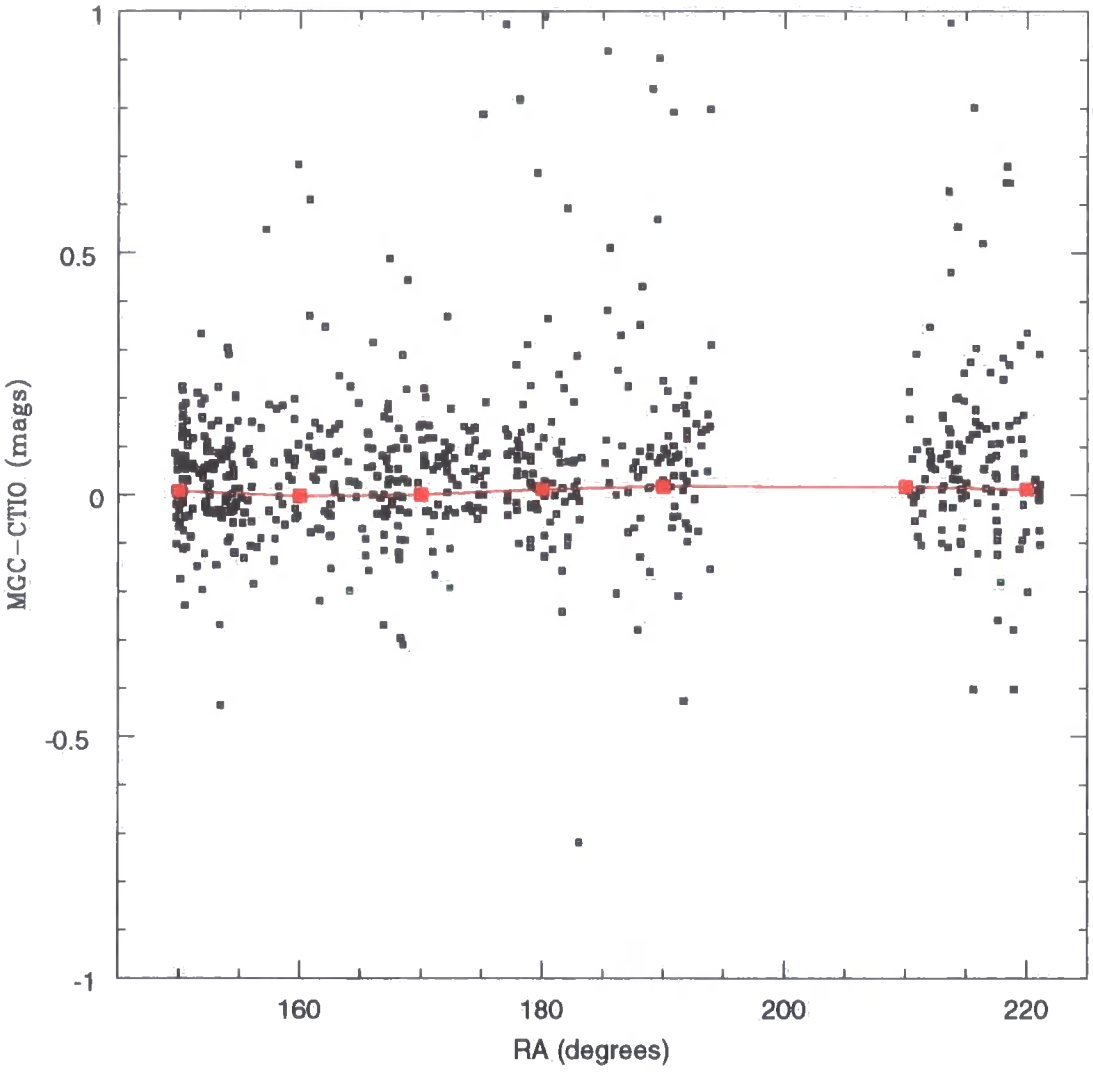

Figure 4.7: This plot consists of galaxies with B<18 which are in common to the MGC and our CTIO survey in the NGC equatorial region, covering 32 deg^2. We have plotted Right Ascension against residual (B(MGC)-B(CTIO)) in order to identify any large scale gradients inherent in our data. The maximum and minimum values of the residual are 0.0483 and 0.0278 in the RA=190 and RA=160 bins respectively. This is a 0.021 mag difference and implies a possible large-scale gradient of 1.91% .

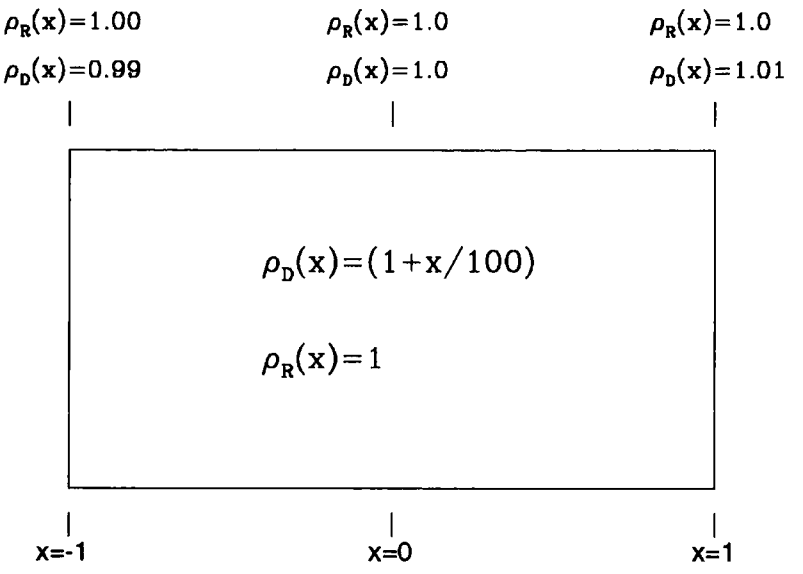

Figure 4.8: Here we illustrate a simple model of a 2% density gradient over one of our CCD sequences. We have freedom to choose our own co-ordinates and so we assume that the start and end of the field of view is at x=-1 and x=1 respectively. The data is then modelled as a function of the angle x by the simple law $\rho(x) = (1 + x/100)$ which correctly represents the relative 2% density gradient between x=-1 and x=1. The random sources are assumed to have $\rho = 1$ everywhere. See text for details of the calculation of $\omega(\theta)$.

$$= \frac{[x + x^2/100 + x^3/30000]^1_{-1}}{2} - 1$$
$$= 1/30000$$

(4.23)

We have obtained a value of $\omega(\theta)$=3x10^{-5} which is a tiny fraction of our clustering amplitudes on all measured angular scales and therefore we claim that large-scale gradients will not be a significant effect for our CTIO clustering results.

4.4.3 Reddening

Reddening effects can also bias the correlation function. If accurate dust corrections are not used then one is effectively inducing zero-point errors into their photometry and therefore the correlation function will be biased high for reasons already described in the previous section. Advances in the last few years means that current surveys have the advantage of accurate galactic dust extinction maps, eg. Schlegel et al. (1998), as opposed to using inaccurate theoretical models as in the case of the Lick and APM surveys for example. However, there are still uncertainties of 16% (Schlegel et al. 1998) in the magnitude extinction corrections of Schlegel dust map and we need to estimate exactly how this will bias our correlation functions. Dust corrections are, on average, larger for our NGC field than for the SGC, where the galactic latitudes are lower. This is illustrated in Figs 4.9 and 4.10, where we have plotted Right Ascension vs the extinction estimate from Schlegel et al. (1998) in our Landolt B band. For RA<200°, at galactic latitudes of b$\sim$ 60° in Fig. 4.9, the average extinction correction estimate is $\sim$ 0.16 mags. in B (divide by 1.61 to get corresponding correction in R). However, for RA>200° the galactic latitudes of our observations are much lower, around b=40°, and the corresponding extinction corrections much higher. In fact at RA$\sim$230° these corrections are as high as 0.8 mags, although this over a very small range of RA's. If we assume a zero-point error is induced as a result of the 16% error on the average 0.16 mag. dust correction in the B-band then we find this zero-point error to be 0.16*0.16=0.0256 mag. This corresponds to a gradient of 2.4% and, using the method of the last section will bias our $\omega(\theta)$ NGC B-band clustering amplitudes high by 4.7x10^{-5} (1.8x10^{-5} in the R-band). These biasing effects are a small fraction of our clustering amplitudes on

all our measured angular scales our B and R bands.

The galactic dust corrections in our B-band SGC data are, on average, much smaller (a mean of $\sim$ 0.08 mags.) and shown by Fig 4.10. We are probing high galactic latitudes of 60°-70° in our SGC field explaining the much lower extinction corrections. There is a another "spike" at RA=40° (shown at RA=400° in the figure) but, this again covers a small range of RA values and therefore we follow same argument as for the NGC, instead using the mean B-band extinction of 0.08 mags. We find a 1.2% gradient implying our B-band clustering amplitudes could be biased high by $1.2\text{x}10^{-5}$ in the SGC. The corresponding number for the R-band is $4.5\text{x}10^{-6}$ and, as in the NGC, we argue that this a very small fraction of our clustering amplitudes on all measured angular scales.

4.4.4 Stellar Contamination

A further bias to the correlation function will be introduced by stellar contamination within a galaxy sample. Although stars can be clustered eg a globular cluster, field galaxy stars on the whole tend to be unclustered (Bahcall & Soneira 1980) and therefore the correlation function for a pure stellar sample is approximately equal to zero. Assuming that a set of observations are not over a large range of galactic latitudes, stars within a galaxy sample will tend to suppress the intrinsic galaxy clustering amplitude and this effect can be quantified in the following way. For a catalogue which contains N_{obj} sources with N_s of these being unclustered stars the actual amplitude of the correlation function for the (N_{obj}-N_s) galaxies is suppressed by a factor $(N_{obj} - N_s)^2/N_{obj}^2$. If we set $N_s = f_s N_{obj}$ we can write:

$$A_\omega = \frac{A_\omega^s}{(1 - f_s)^2} \tag{4.24}$$

where A_ω is the intrinsic clustering amplitude of the galaxies in the sample, A_ω^s is the suppressed amplitude due to the stellar contamination and f_s is the fraction of stars within the catalogue. We know from chapter 2 that our stellar contamination is a fairly constant value of $\sim 5 - 10\%$ for B>15 (R>14) (see Figs. 2.9, 2.10 and 2.11) and so we assume a value of 7.5% for this calculation. We then find that our

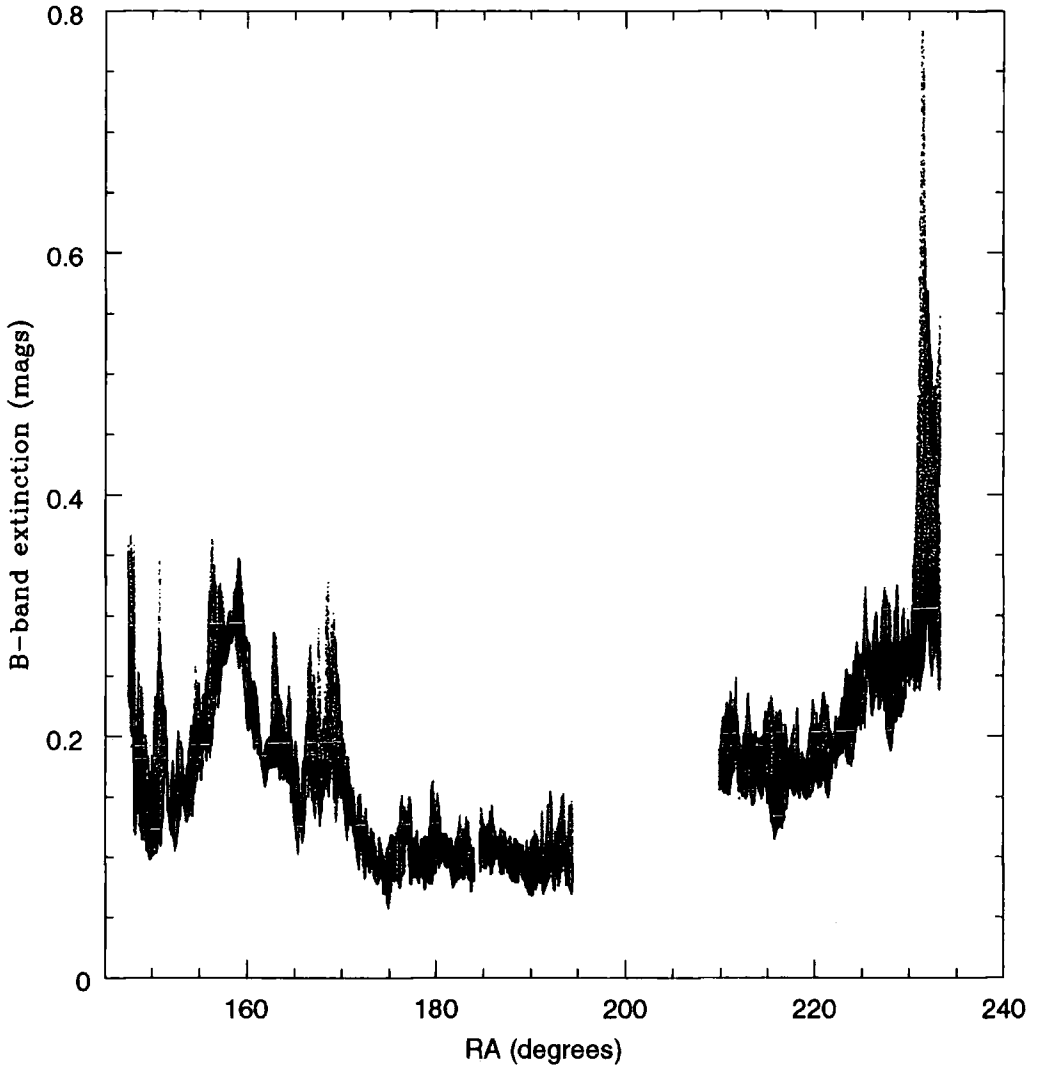

Figure 4.9: This plot shows the Right Ascension of our B-band NGC data plotted against the dust extinction correction in mags. predicted by the Schlegel et al. (1998) dust models. For RA's$<$ 200° the average extinction correction is$\sim$0.15, but for the higher RA's where we are probing relatively low galactic latitudes of b=40° this the dust correction is much larger. At RA$\sim$230° there is a huge spike where we have to correct by 0.8 mags. due to dust. The R-band corrections are not as large as in the B-band and can be obtained by dividing the B-band extinction correction by 1.6.

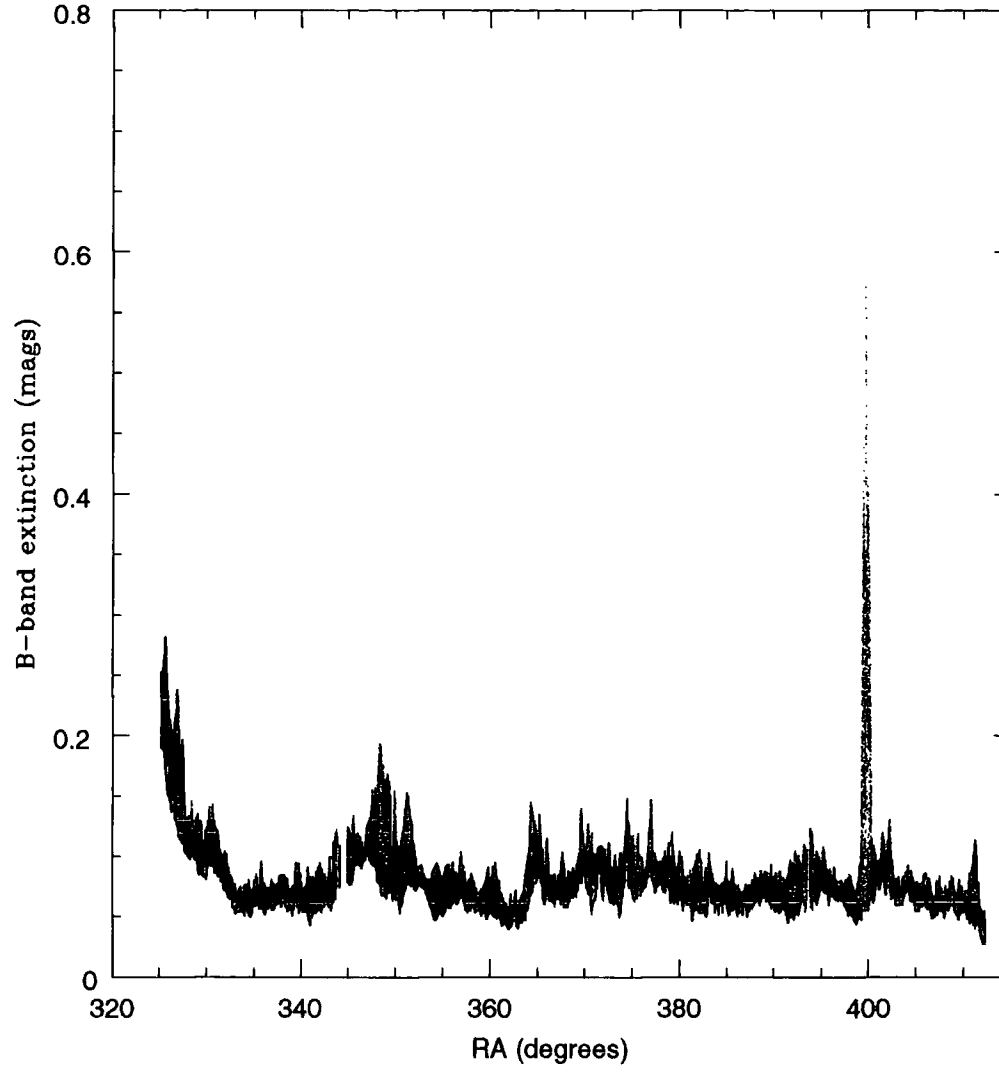

Figure 4.10: This plot shows the Right Ascension of our B-band SGC data, with a constant declination of -30°, plotted against the dust extinction correction in magnitudes predicted using the Schlegel et al. (1998) dust model. We have added 360 to all RA's< 100° to illustrate the continuous nature of our strip. These dust corrections are, on average, much smaller (a mean of $\sim$ 0.08 mags.) than for our NGC data due to the fact we are probing high galactic latitudes of |b|=60-70°. At RA$\sim$40° (400° in the plot) there is a spike where we have to correct by 0.58 mags. due to dust, but this is in stark contrast to the surrounding regions where the extinction correction is $\sim$ 0.06 mags. The R-band corrections are not as large as in the B-band and can be obtained by dividing the B-band extinction correction by a factor of 1.6.

Survey	CTIO NGC	CTIO SGC	DUKST	DARS/SAAO	APM
r_0	4.7	5.2	5.1	4.7	5.7
γ	1.695	1.72	1.59	1.8	1.65

Table 4.4: Comparison of our B-band spatial correlation function parameters, r_0 and γ, with other survey results.

Survey	CTIO NGC	CTIO SGC	LCRS	SDSS
r_0	6.0	5.7	5.0	6.1
γ	1.68	1.77	1.79	1.72

Table 4.5: Comparison of our R-band spatial correlation function parameters, r_0 and γ, with other survey results.

measured clustering amplitude is ~86% of the true value on all angular scales. This is a small, but non-negligible effect and we discuss this in the next section.

4.5 Discussion

In Tables 4.4 and 4.5 we show the results of our best-fit B and R-band spatial correlation function parameters compared to those derived from other surveys. Our B-band results are consistent with results from the surveys shown which show typical values of r_0 ~$5.0h^{-1}$Mpc and $\gamma = 1.7$, except for results of the APM Galaxy Survey. However, the model Maddox et al. use to derive this value assumes significant galaxy evolution at low redshift, an assumption which is not used by any of the other authors. Baugh et al. (1996) have independently derived values of r_0=$4.5h^{-1}$Mpc and γ=1.7 by numerically inverting the APM angular correlation assuming no evolution at low redshift. Our R-band results show excellent agreement with those of the SDSS in terms of the value of the galaxy correlation length, r_0 ~$6.0h^{-1}$, which is relatively high compared to the B-band results shown in Table 4.4.

The best-fit parameters for our de-projected B-band angular correlation functions were shown in Table 4.2, where we found values for the slope of the spatial

function to all be in good agreement at $\gamma \sim 1.70$. However, differences between the NGC and SGC fields were found in terms of the parameters r_0, the characteristic clustering length, and r_1, the distance scale at which the break occurs. Although the difference in the values of r_0 were not large, a mean of $4.7h^{-1}$Mpc in the NGC compared to $5.2h^{-1}$Mpc in the SGC, the best fit values of the break length scale, r_0, were significantly different. It should be noted that the nature of our scaling method meant that the values of best fit spatial correlation function parameters had to be determined by eye and so a certain amount of subjectivity is inherent within the quoted values. The errors on our derived parameters were computed by using our best-fit values and then varying each parameter individually until it was obvious that the model no longer gave a good approximation to the data. However, it is clear that the huge difference in the values of the break between the NGC and SGC, a mean of 10 Mpc compared to 33.5 Mpc, is greatly in excess of our quoted errors.

The slightly higher characteristic clustering lengths found in the SGC combined with these vastly different values of r_1 mean that we measure higher clustering amplitudes on all angular scales in the SGC relative to the NGC. However, we found in the previous section that our clustering amplitudes could be suppressed by about 10% or so due to stellar contamination. It is possible that stellar contamination could be a bigger problem in the NGC because in this field we observed at lower galactic latitudes than in the SGC. Therefore our SGC clustering amplitudes would then be suppressed less and this may explain these slightly high values of r_0 relative to the NGC. This effect, even if true, could still not explain the large differences in the values of the break as any amplitude suppression due to stellar contamination would still not change the angular scale on which the break occurs in each field.

In Section 4.4.1 we derived values for the integral constraint with values, $C_{NGC} = 0.128A_\omega$ and $C_{SGC} = 0.120A_\omega$. In Fig. 4.11 we show that correcting for the effect of the integral constraint does make a small difference for $\theta > 1°$. Plotted are the two $17<B<18$ two-point functions that were shown in Fig. 4.3, where the appropriate value of the integral constraint has been added to the clustering amplitudes in each

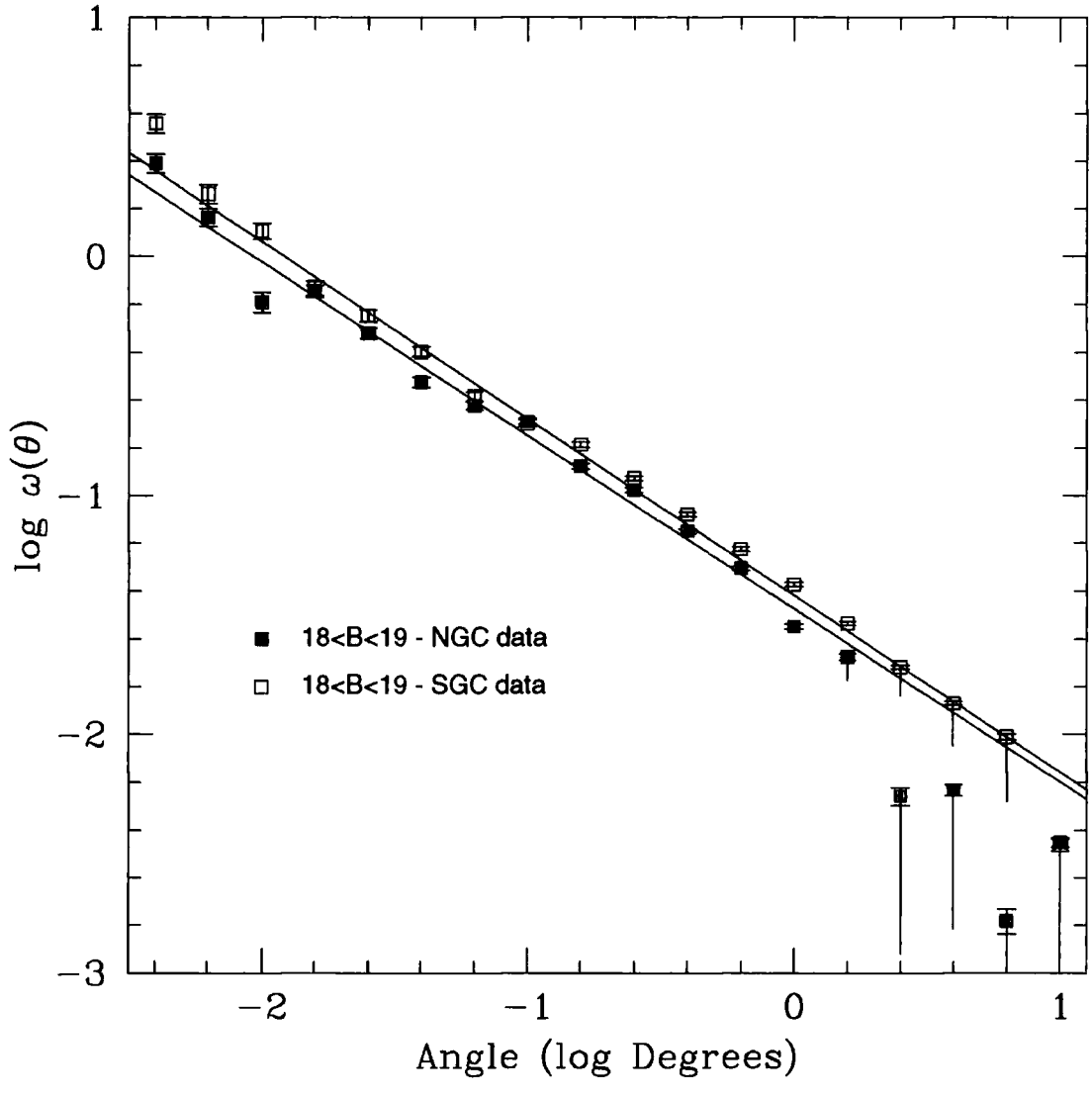

Figure 4.11: The effect of applying the integral constraint to our correlation functions. Here we show the same two 17<B<18 angular correlation functions and best fit lines that were plotted in Fig. 4.3, except we have corrected for the effect of the integral constraint. This makes a small difference on scales of $\theta > 1°$. We have illustrated this by drawing a line from each point to the co-ordinates of the point when the integral constraint had not been applied.

angular bin. We have also drawn a line from each point to the co-ordinates of that point when the effect of the integral constraint had not been included. This correction has no effect on any of the values of δ and r_0 we have calculated in this chapter and our B-band SGC correlation functions still show significantly more power on scales of $\theta > 1°$ than those in the NGC. The crucial point though is the values of the break, r_1.

We saw in Chapter 3 how one way of helping to explain the huge $3x10^6 h^{-3}Mpc^3$ hole in the SGC distribution of galaxies, was if the power law form of the correlation function extended out to very large scales of $150h^{-1}$Mpc. It is clear that although there does seem to be evidence for a break in the NGC correlation function our results in the NGC and SGC can definitely not rule out such a power law form over *all* our measured angular scales i.e. conistent with there being no break in the angular correlation function. This is certainly true for our SGC correlation function plotted in Fig. 4.11 which shows no evidence for a break at all.

The APM Galaxy Survey covers a huge angular area of 4300 deg^2 and the angular two-point correlation function calculated from the galaxy sample of Maddox et al. does show clear evidence for a break on scales of $\theta \sim 1°$, which is unaffected by the integral constraint. However, we have seen in Chapter 3 how there are large errors of 0.2-0.3 mag. inherent in photographic plate photometry and it could be these errors have had a systematic effect on the clustering amplitudes which is not yet understood.

It could also be that higher order moments such as the three-point correlation function are needed to help explain the huge hole in the SGC galaxy distribution. We have seen that the two-point function can only give a complete description of large scale structure if density fluctuations in the galaxy distribution are Gaussian, which may not be the case. Results from the completed SDSS will be able to throw light on exactly how much power there is on very large scales of 100-200h^{-1}Mpc, which could help us understand why there is such a large hole, over such a huge volume of space, in the SGC galaxy distribution.

4.6 Conclusions

In this chapter we have introduced the two-point correlation function as a tool for quantifying galaxy clustering and large scale structure in the Universe. We calculated the two-point function for our NGC and SGC data in the two pass-bands, B and R, and also performed scaling tests and investigated possible systematic effects and biases that could be inherent within our calculations. Our conclusions are as follows:

- Our angular correlation functions follow a power law behaviour with slopes of $\delta \sim 0.70$ in the angular range $-1.8 < \log(\theta) < 0$, but depart from this trend at smaller and larger angular scales where steeper slopes are observed.

- We find systematically lower clustering amplitudes on all angular scales in our B-band NGC correlation functions relative to the SGC.

- When we de-project our B-bands angular functions we find characteristic clustering lengths of $r_0 = 4.7h^{-1}$Mpc and $r_0 = 5.2h^{-1}$Mpc for our NGC and SGC fields respectively . We also find that the characteristic break occurs on much smaller spatial scales for the NGC ($10h^{-1}$Mpc) than the SGC ($33.5h^{-1}$Mpc).

- Our SGC data is therefore showing significant large scale power on angular scales of $\theta > 2°$ or length scales of $r > 30h^{-1}$ Mpc relative to our NGC data.

- We also de-projected our angular R-band correlation functions assuming a model for the spatial function. We found $r_0 = 6.0$, $\gamma = 1.68$ in the NGC and $r_0 = 5.7$, $\gamma = 1.77$ in the SGC, in good agreement with r_0 found by the SDSS team. Our slightly higher value of r_0 found in the NGC compared to the SGC was the opposite trend to that found in our B-band data.

- For these R-band results there was only tentative evidence of the break in the correlation function occuring on larger scales for the SGC - a value of $r_1 \sim 31h^{-1}$Mpc compared to $r_1 \sim 25h^{-1}$Mpc in the NGC.

- We scaled the correlation function of the SDSS to the depth of our survey and found good agreement on small scales of $\theta < 0.1°$ for both our NGC and SGC

functions, with our NGC angular function predicting slightly more power on larger scales.

- Scaling tests were made to our correlation functions for the different magnitude slices and we found that our data followed the expected increase in clustering amplitudes as the magnitude limit was brightened. This indicates that we are measuring real clustering in the galaxy distribution, rather than that due to systematic errors.

- Analysis of possible systematic biases to our correlation function was performed. We found that stellar contamination could depress our clustering amplitudes by 10% or so and that the integral constraint does have a small effect on angular scales of $\theta > 1^{\circ}$

- When we correct for the effect of the integral constraint, although it is small, we cannot rule out a pure power form for the correlation function, particularly in the SGC, over all our measured angular scales. This may help to explain the huge hole in the SGC galaxy distribution we described in Chapter 3.

Chapter 5

The Clustering of Faint Blue Galaxies

5.1 Introduction

In the last chapter we introduced the two-point angular correlation function, $\omega(\theta)$, as a tool to analyse the clustering of galaxies. We explained the standard methods of calculating the two-point correlation function along with systematic errors that one must consider, before estimating $\omega(\theta)$ for our CTIO bright galaxy data. In this chapter we use the tools outlined in the last chapter to analyse the clustering of galaxies, but this time for a much fainter galaxy sample using data reduced by Scott Croom of the AAO, enabling us to analyse the clustering of the faint, B<26, galaxy population. In the context of the Metcalfe et al. (2001) models we have used in this thesis, these galaxies are predicted to be evolved spirals. This assumed evolution using the models of Bruzual & Charlot (1993) is essential in terms of fitting faint (B>22) B-band number counts and provides a possible solution to the famous "faint blue galaxy problem" (Colless et al. 1993; Metcalfe et al. 1996), where non-evolving models were originally found to under-predict the faint B-band number counts by an order of magnitude (Shanks et al. 1984).

The original purpose of this data, taken on the Isaac Newton Telescope (INT) in La Palma, was to analyse the environments of QSO's out to z$\sim$ 1 (Croom et al. 2001), but because of the high quality galaxy photometry obtained it was decided that this would also be an ideal opportunity to analyse the clustering of these "faint blue galaxies". The one crucial difference to the data analysed in this chapter is that we are probing relatively high median redshifts of z$\sim$2 as opposed to z$\sim$0.1 in

our CTIO catalogue. This means, with the 11.2'x22.6' dimensions of each our CCD chips, we are only probing scales of $\sim 7h^{-1}$Mpc.

In the next section we briefly describe the data reduction performed by Scott Croom before describing the astrometry corrections applied by us in section 5.3 and the calculation of the integral constraint in section 5.4. In section 5.5 we present our clustering results for each of our fields as well as comparing to model predictions and other data in the literature. Section 5.6 gives a brief summary of the models we use and we discuss our findings as well as summarise systematic effects which could effect our results in section 5.7. Finally, we conclude in section 5.8.

5.2 Observations and Data Reduction

The data was taken in May 1998 using the Wide-Field Camera (WFC) on the 2.5m INT at the Observatorio del Roque de los Muchachos on La Palma. The WFC consists of a mosaic of 4 thinned EEV CCD's each with 2048x4100 pixels. Each CCD is 11.2'x22.6' meaning a total field of view of 0.28 deg^2. The pixel gain of the CCDs is 2.9e$^-$ADU^{-1} with a read noise of 12 e$^-$pixel^{-1} and their quantum efficiency in the B band is 80%. A total of 9 fields were observed using the KPNO B filter, which we denote as B_{ccd}, with exposure times of 5x1200s. The F864-1 field was observed for only 4x1200s as a result of an auto-guider failure. Details of these observations are shown in table 5.1.

Standard Fields from Landolt (1992) were observed each night and the fields were picked so that appropriate standard stars were captured on each of the 4 CCD chips in the same exposure. The used Landolt fields were SA104, SA110, SA111, SA112 and SA113 and a number of these fields were observed at a range of air-masses from which an airmass extinction coefficient of X_B=0.25 mag. was determined, in agreement with the standard La Palma value. All 3 nights were found to be photometric and the determined colour equation was:

$$B_{ccd} = B - 0.123(B - V) \tag{5.1}$$

Field name	RA (B1950)	DEC (B1950)	FWHM (arcsec.)	Exp. time (sec.)	effective air-mass	zero-point
SA57	13 06 54.8	+29 34 44	1.55″	5x1200	1.01	32.256
F864-2	13 41 30.9	-00 03 20	2.21″	5x1200	1.42	32.153
CFHT-2	16 42 54.4	+40 01 32	2.00″	5x1200	1.09	32.236
F855	10 44 12.1	-00 04 55	1.16″	5x1200	1.43	32.149
UK-deep	13 32 53.2	+38 14 04	0.96″	5x1200	1.09	32.235
QNZ4	15 19 53.6	+02 49 33	1.22″	5x1200	1.36	32.167
F861	12 40 19.9	-00 13 58	1.32″	5x1200	1.25	32.196
F864-1	13 41 10.9	+00 08 40	1.35″	4x1200	1.56	32.119
CFHT-1	16 43 18.2	+41 03 32	0.92″	5x1200	1.12	32.227

Table 5.1: Details of the observations taken with the WFC on the INT in La Palma. Nine fields were observed in total and each exposure produced ~40,000 sources from all 4 CCD chips.

where B and V are in the standard Johnson system and the RMS error on the fit is 0.012. Zero-points were also measured for each CCD on each night but no significant zero-point offsets were found between either different CCD's or different nights.

The 5x1200 sec. exposures in each field were offset from each other by 2-3″ and each set of 5 CCD exposures were combined together separately ie at the end of the reduction there was a file containing sources for each of the 4 CCD's in the mosaic. The combining procedure for each set of exposures was to register the 5 CCD frames to the same reference frame and then median combine them to remove the cosmic rays. This median frame was not used for the final photometry as the sky noise is generally higher than for an averaged frame. Instead the median frame was re-registered back to each of the original data frame and the data frames were divided by this median. The resultant image is then median filtered and divided by itself to produce a final mask of the cosmic rays which were blanked out during the final averaging combination if the registered data frames.

The galaxy catalogues for each of the 4 CCD's in the mosaic was created using

the SExtractor software of Bertin & Arnouts (1996). The software was run twice for each CCD. The first pass was to estimate the stellar full-width at half-maximum (FWHM) of the point-spread function (PSF) as the star/classification parameter (CLASS_STAR) in SExtractor is very strongly dependent on this value (see chapter 3 for more details). During this pass all saturated stars were also found and an image mask was created so that all large, bright sources would be absent from the final source catalogue.. The second pass of SExtractor extracted all the sources using a low threshold (1σ above sky) and a limit of ≥ 5 connected pixels.

5.3 Astrometry Corrections

We have outlined the reduction procedure for this B-band INT data. In order to calculate the two-point correlation function there were two main things we had to consider. The first was whether to attempt to combine the CCD's and calculate the correlation function using cross-pairs from all 4 chips. It was eventually decided that we would not do this, but instead calculate $\omega(\theta)$ for each individual chip and then take the mean. Although this means that we do not have information regarding the cross chip source pairs, this is compensated by the fact that we will not have any spurious clustering induced due to gradient effects over all 4 CCD's. The second problem was an astrometry issue and is the subject of this section.

Due to the refractive optics of the WFC on the INT, there is a radial distortion effect across the 4 CCD's, relative to the optical axis of the telescope. This results in a particular source appearing to lie further from the optical axis than it actually does. Fig. 5.1, taken from the WFC web-page illustrates this. The differential effect across any of the CCD's is, at most, 10″ near the field edges and this is something that could bias a correlation function since 10″ is a reasonable fraction of the dimension of a particular CCD. The radial distortion takes the form:

$$r_{true} = k_1 r + k_3 r^3 + k_5 r^5 \tag{5.2}$$

where r_{true} is the actual radial distance from the optical axis and r is the measured distance. The quoted values for the INT are k_1=24.7 arcsec/mm and k3=-

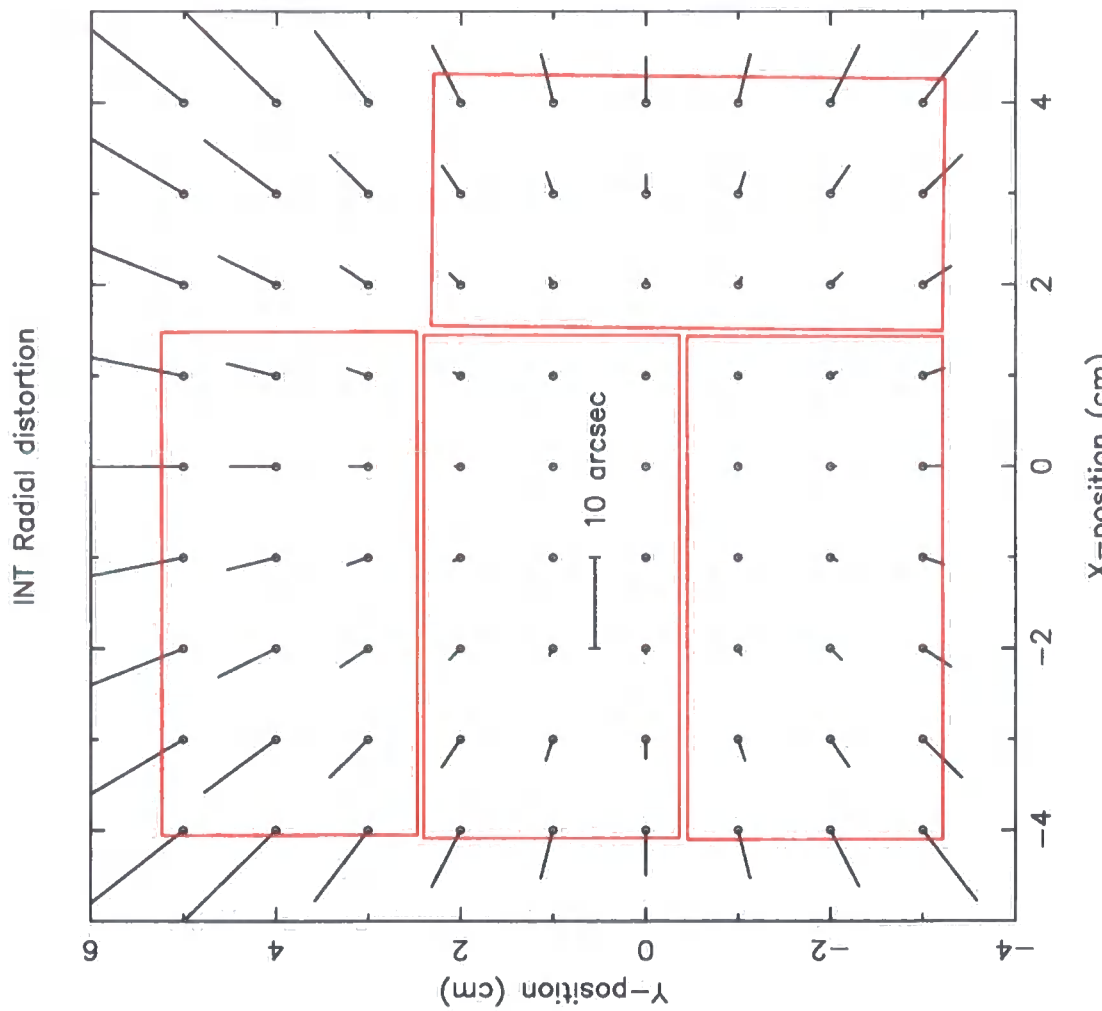

Figure 5.1: Due to the refractive optics of the WFC on the INT, there is a radial distortion effect across the 4 CCD's, relative to the optical axis of the telescope, which is illustrated here. This results in a particular source appearing to lie further from the optical axis than it actually does and the differential effect across any of the CCD's is, at most, 10″ near the field edges

$9.202\text{x}10^{-5}$ arcsec/mm^3. If we neglect the higher order k5 term and re-arrange equation 5.2 into a more convenient form we obtain:

$$r_{true} = r'(1 + (k_3/k_1)^3 r'^2) \tag{5.3}$$

where r$'$ is a more convenient form for the measured distance expressed in units of k_1. The value of k_3/k_1^3 in these units is $-7.59\text{x}10^{-9}$ arcsec^{-3}.

In order to take this distortion into account all CCD coordinates had to be transformed so their (x,y) pixel coordinates were relative to the optical axis. These linear transformations are well defined for each CCD as the chips are fixed via bolts to the baseplate. The transformations for CCD1 are as follows:

$$x_c = x_1 - 0.0010013y_1 + 335.94 \tag{5.4}$$

$$y_c = 0.00058901x_1 + y_1 - 3041.67 \tag{5.5}$$

where x_c and y_c are the (x,y) co-ordinates relative the rotator center, which lies along the optical axis. The transformations for CCD's 2, 3 and 4 are defined using similar notation such that:

$$x_c = -0.010272x_2 + 0.99992y_2 - 1699.16 \tag{5.6}$$

$$y_c = -1.0003x_2 - 0.010663y_2 - 3197.05 \tag{5.7}$$

$$x_c = 1.0003x_3 - 0.0023903y_3 - 3874.52 \tag{5.8}$$

$$y_c = 0.0024865x_3 + 1.0003y_3 - 3007.07 \tag{5.9}$$

$$x_c = x_4 - 1778.0 \tag{5.10}$$

$$y_c = y_4 - 3029.0 \tag{5.11}$$

The positions of the CCD chips along with the location of the rotator centre is shown by Fig. 5.2. Once the coordinates were defined relative to the rotator center then the actual position (x_{true},y_{true}) could be calculated using the equations:

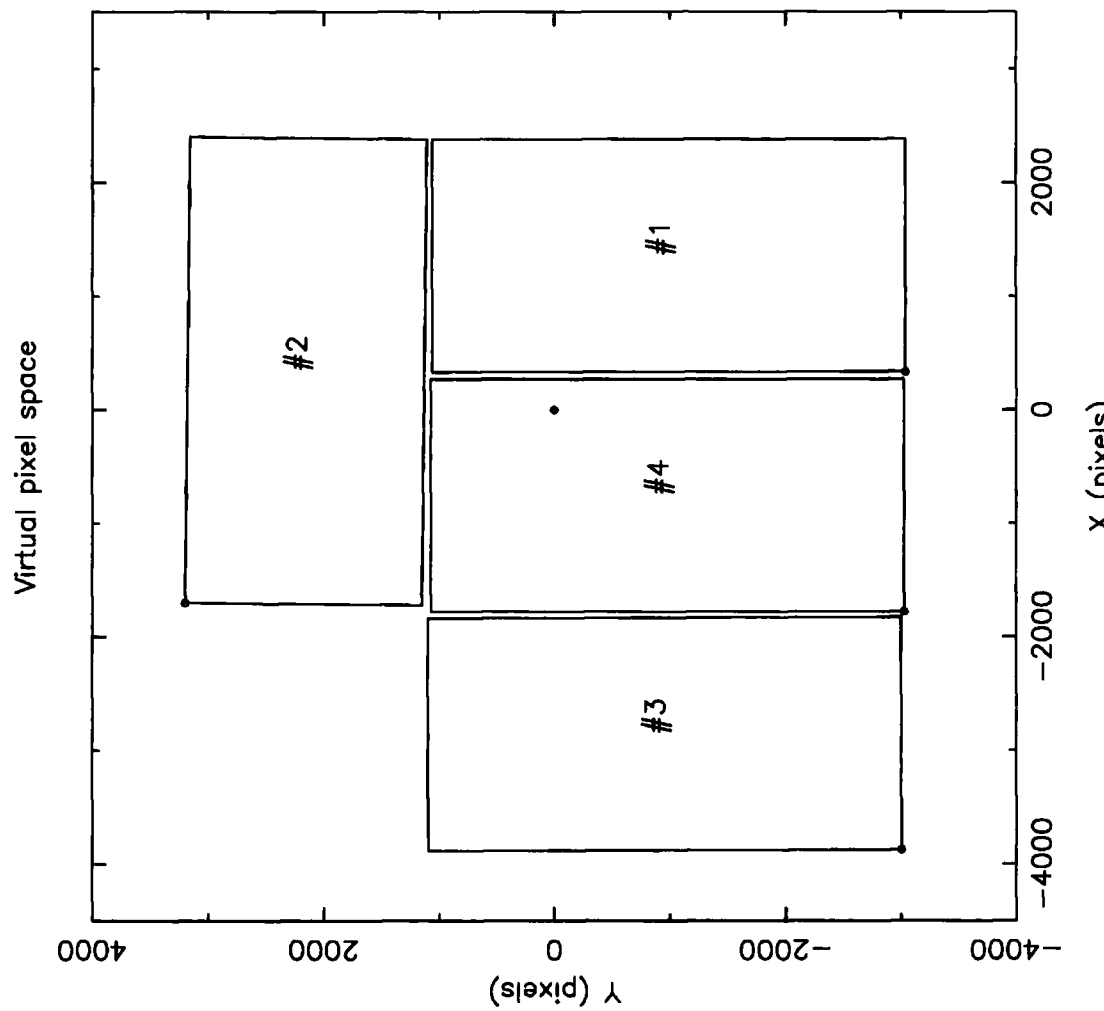

Figure 5.2: Here we show the geometry of the 4 CCD chips relative to each other on the WFC, along with the rotator centre shown by the solid dot which is located within CCD4. The equations which transform from CCD co-ordinates to those relative to the rotator centre are described in the main text.

$$x_{true} = \left(\frac{r_{true}^2 (x_c/y_c)^2}{1+(x_c/y_c)^2}\right)^{1/2} \quad (5.12)$$

$$y_{true} = \left(\frac{r_{true}^2}{1+(x_c/y_c)^2}\right)^{1/2} \quad (5.13)$$

where r_{true} is defined in equation 5.2. Obviously x_{true}, y_{true} and r_{true} obey Pythagoras's Theorem. Not only do the co-ordinates of each observed galaxy have to be altered using this astrometry correction but the masked areas of the CCD's must be as well. This is so that we can use a random sample of galaxies which populate exactly the same areas of each CCD as the actual observed data in order that we can then calculate the two-point correlation function using the data and random samples in a consistent manner.

5.4 The Integral Constraint

The integral constraint, which was described in chapter 4, is a bias which reduces the observed clustering signal in the correlation function due to the fact that the mean density of the field in question is estimated from the data itself. This bias is particularly important when dealing with relatively small fields, which is certainly the case for each our CCD's, with each chip covering 11.2'x22.6'.

The integral constraint can be calculated by the equation:

$$C_{int} = \frac{1}{\Omega^2} \int\int \omega(\theta) d\Omega_1 d\Omega_2 \quad (5.14)$$

where θ is the angular separation of each galaxy pair, Ω the field of view of the CCD (~ 0.07 deg^2) and $d\Omega_1$, $d\Omega_2$ the solid angle subtended by each pair. When we assume a power law correlation function of $\omega(\theta) = \theta^{-0.8}$, in order to be consistent with other workers, we find that $C_{int}=(6.5\pm0.1)A_\omega$, depending on the size of the masked regions on each CCD. The integral constraint biases the amplitude of the correlation function low by a constant translational amount on all angular scales and therefore we fit our measured clustering amplitudes as a function of angular separation to an expression of the form:

$$\begin{aligned} \omega(\theta) &= A_\omega \theta^{-0.8} - C_{int} \\ &= A_\omega(\theta^{-0.8} - 6.5) \end{aligned} \tag{5.15}$$

where A_ω is the amplitude of $\omega(\theta)$ at 1°.

5.5 Results

We have 4 chips for each of the 9 fields and in order to calculate the correlation function for each field we use each CCD and take the mean of the 4 calculated $\omega(\theta)$'s. Fig. 5.3 shows the results of this procedure using the F864-2 field for all galaxies with B<26. The triangles in the 4 panels show the observed two-point correlation function for each CCD, plotted as a function of $\log(\theta)$. The filled squares in each angular bin are the mean of the clustering amplitudes from all 4 CCD's and these are plotted in each panel in order that the scatter around the mean can be seen for each chip. The errors on all the triangular points are the 1σ scatter of the clustering amplitudes over all 4 CCD's in the corresponding angular bins and therefore the errors on the square points are half of these values due to the fact that 4 fields have been averaged. The model curve is the same in each panel and is a simple best fit of equation 5.15 to the square points. In this case we find that A_ω=3.34x10^{-4} $deg^{0.8}$.

We follow the same procedure for each of the 9 fields, calculating the two-point correlation function for 5 samples of galaxies defined by the magnitude limits B=26, B=25, B=24, B=23 and B=22 and the results are shown in Figs. 5.4, 5.5, 5.6, 5.7 and 5.8 respectively. The figure panels show the results of our clustering analysis for each of the 9 fields. The model curves in each panel are the best fits to the data of equation 5.15 and the optimum value of A_ω is shown. The errors are calculated in the way described for the F864-2 field ie. using the 1σ scatter of the data from all 4 chips. The fact that we have 9 fields is useful in terms of minimizing errors so that a very accurate resultant correlation function can be computed for each galaxy sample. This is done by taking the mean in each angular bin over all the fields for each of the 5 galaxy samples and the results are shown in Figs. 5.9, 5.10, 5.11, 5.12

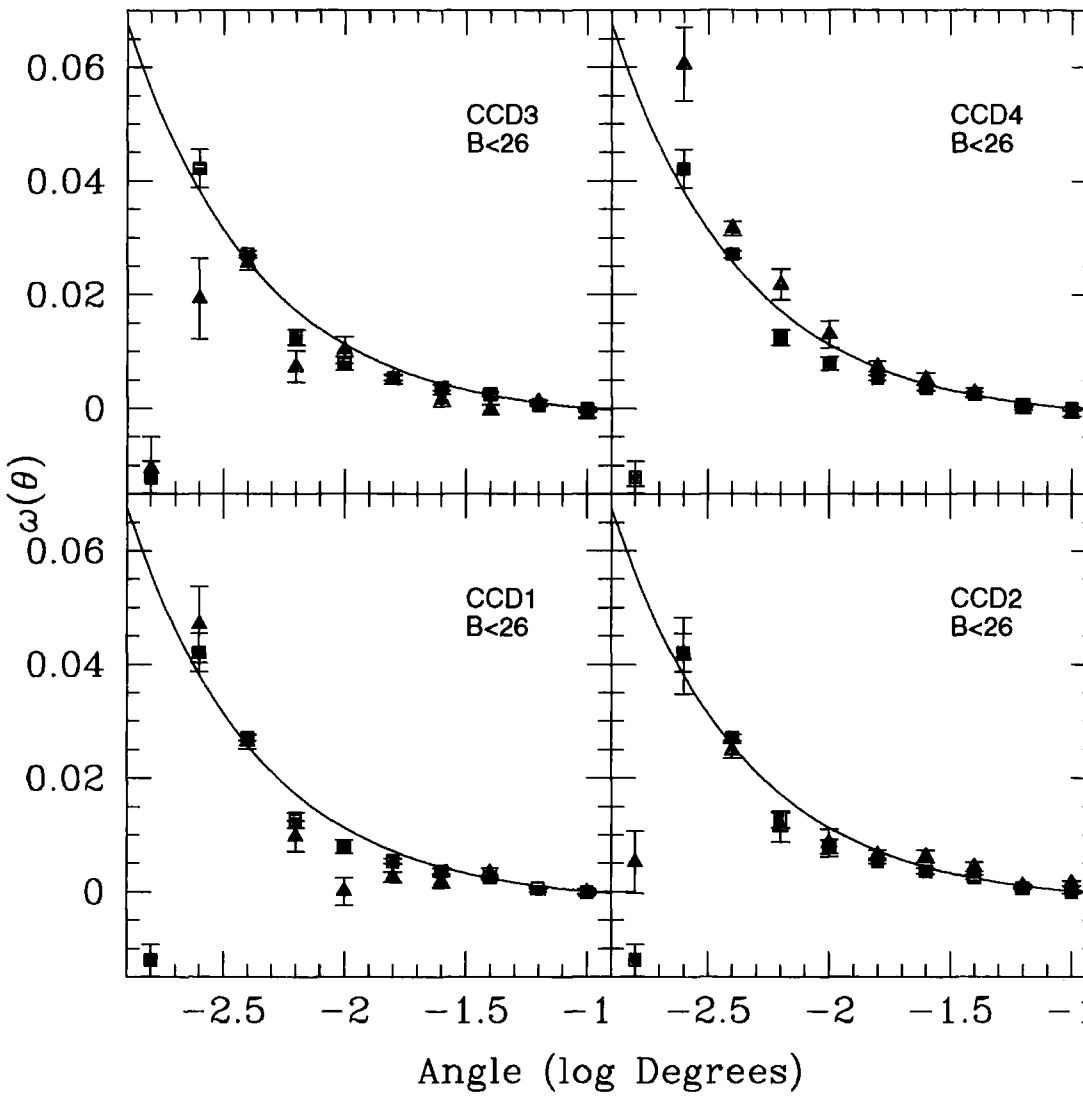

Figure 5.3: Here, the filled triangles show the two-point correlation functions of the F864-2 field from each of the 4 CCD chips using the B<26 galaxy sample. The filled squares are the mean of the clustering amplitudes in each angular bin using all 4 CCD's and these are plotted in each panel in order that the scatter around this mean can be seen for each chip. The errors on all the triangular points are the 1σ scatter of the clustering amplitudes about the mean in each angular bin and therefore the errors on the square points are half of these values due to the fact that 4 fields have been averaged. The model curve is the same in each panel and is a simple best fit of equation 5.15 to the square points. In this case we find that A_ω=3.34x10^{-4} deg$^{0.8}$.

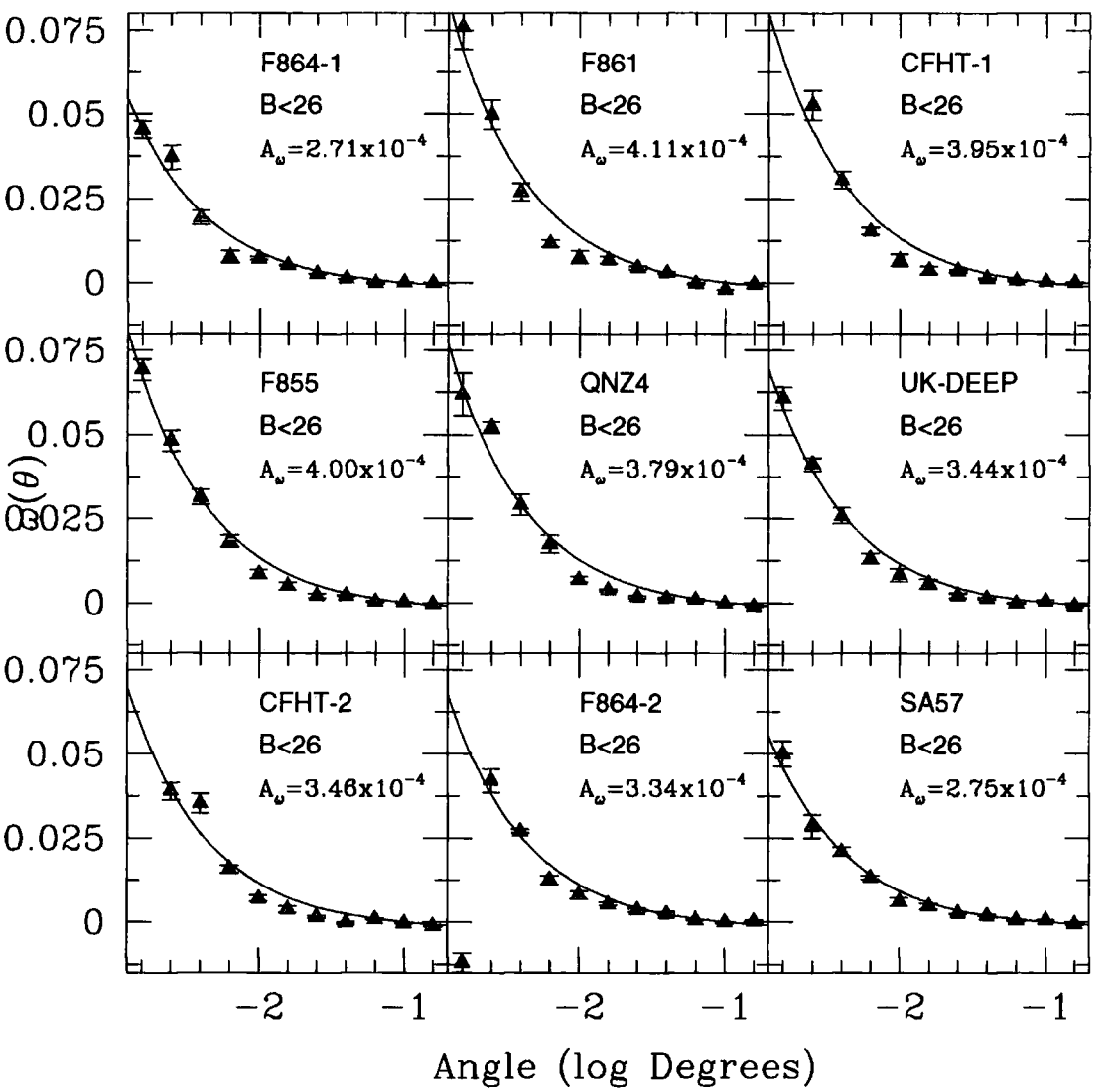

Figure 5.4: This plot shows the two point correlation function for each of the 9 fields using the B<26 galaxy sample. The errors are calculated using the 1σ scatter of the data from all 4 chips in each field and the model curves in each panel are the best fits to the data of equation 5.15. The resulting optimum value of A_ω is shown for each field.

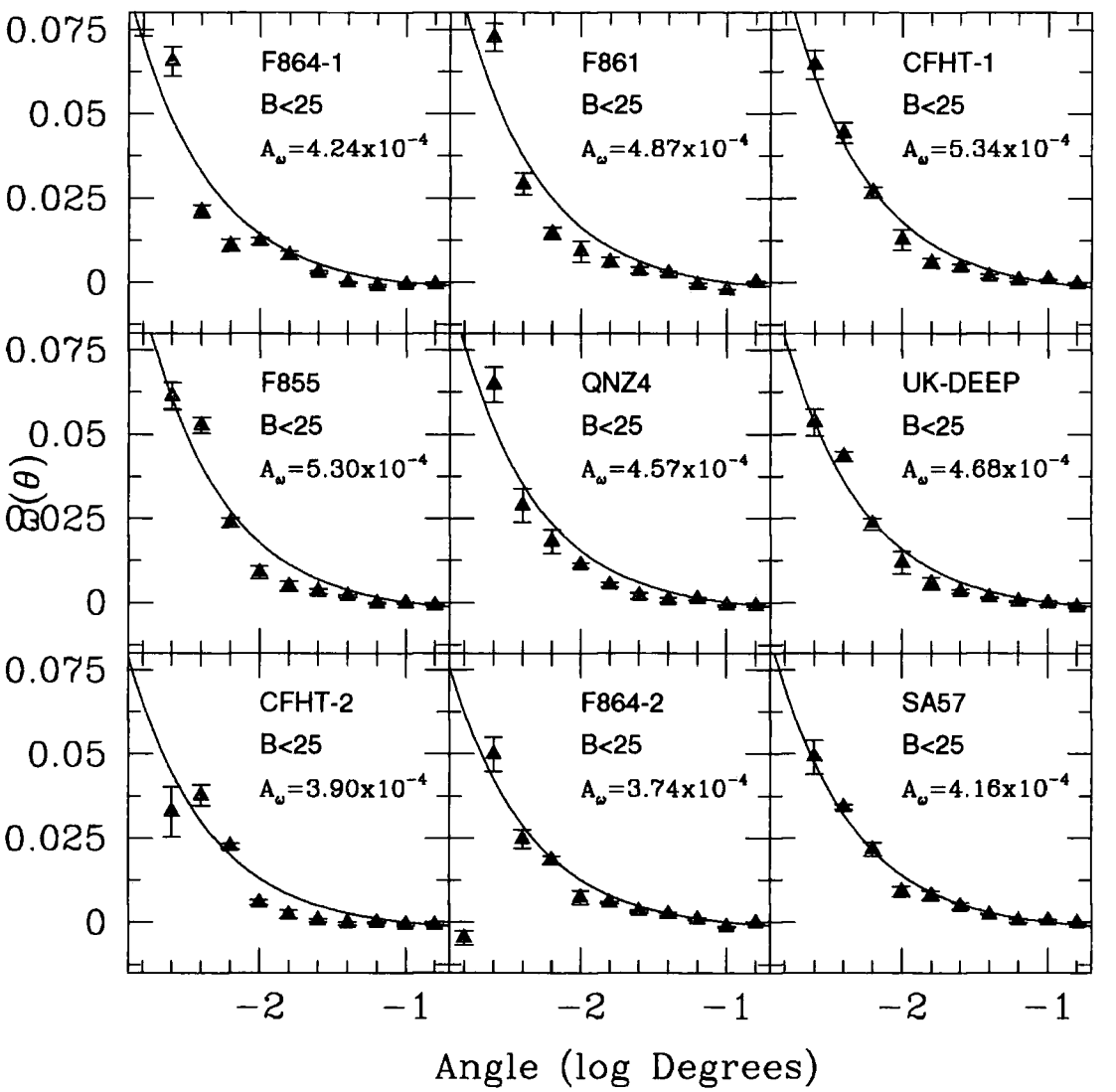

Figure 5.5: This plot shows the two point correlation function for each of the 9 fields using the B<25 galaxy sample. The errors are calculated using the 1σ scatter of the data from all 4 chips in each field and the model curves in each panel are the best fits to the data of equation 5.15. The resulting optimum value of A_ω is shown for each field.

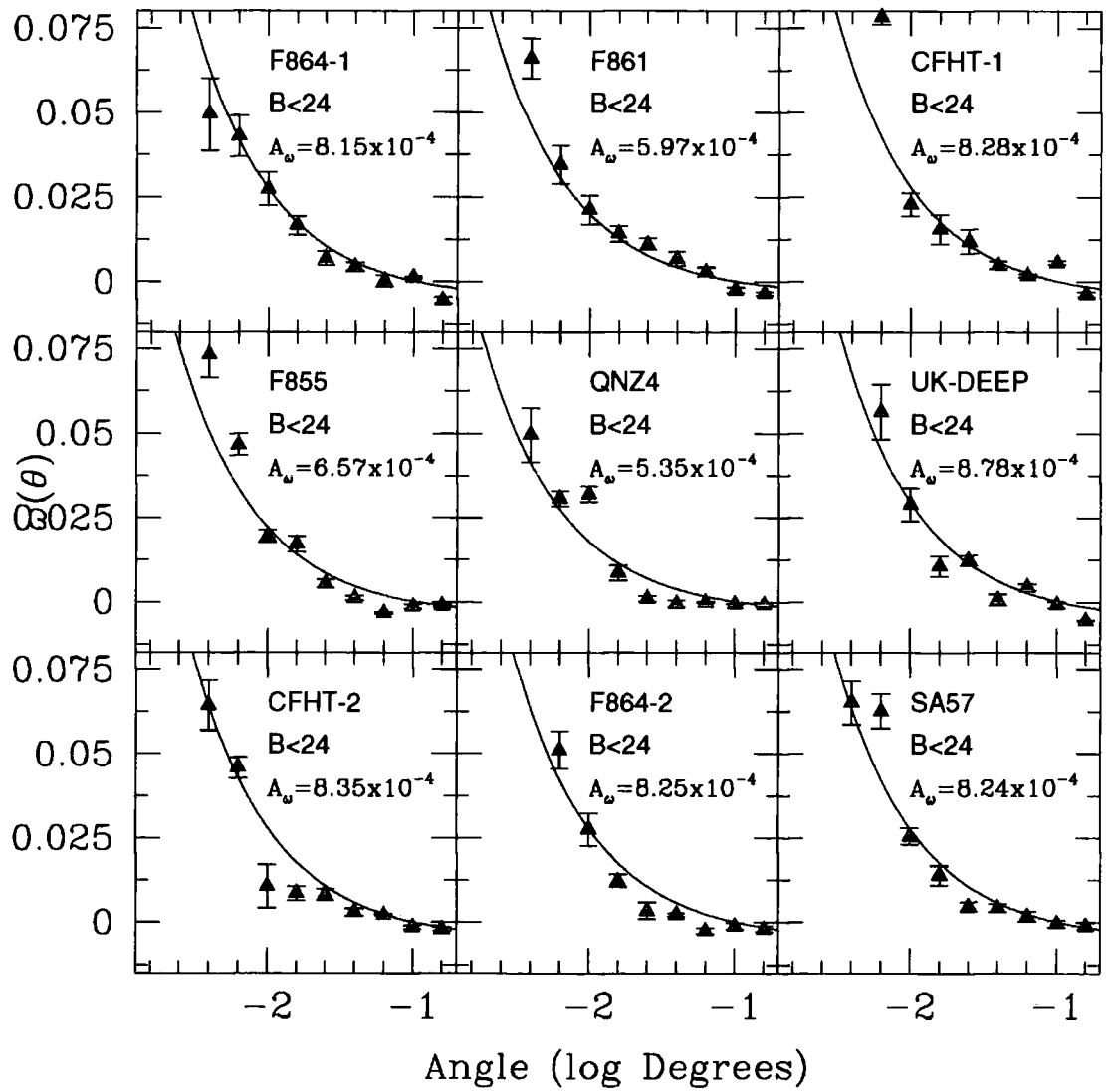

Figure 5.6: This plot shows the two point correlation function for each of the 9 fields using the B<24 galaxy sample. The errors are model fits are calculated in the our usual way.

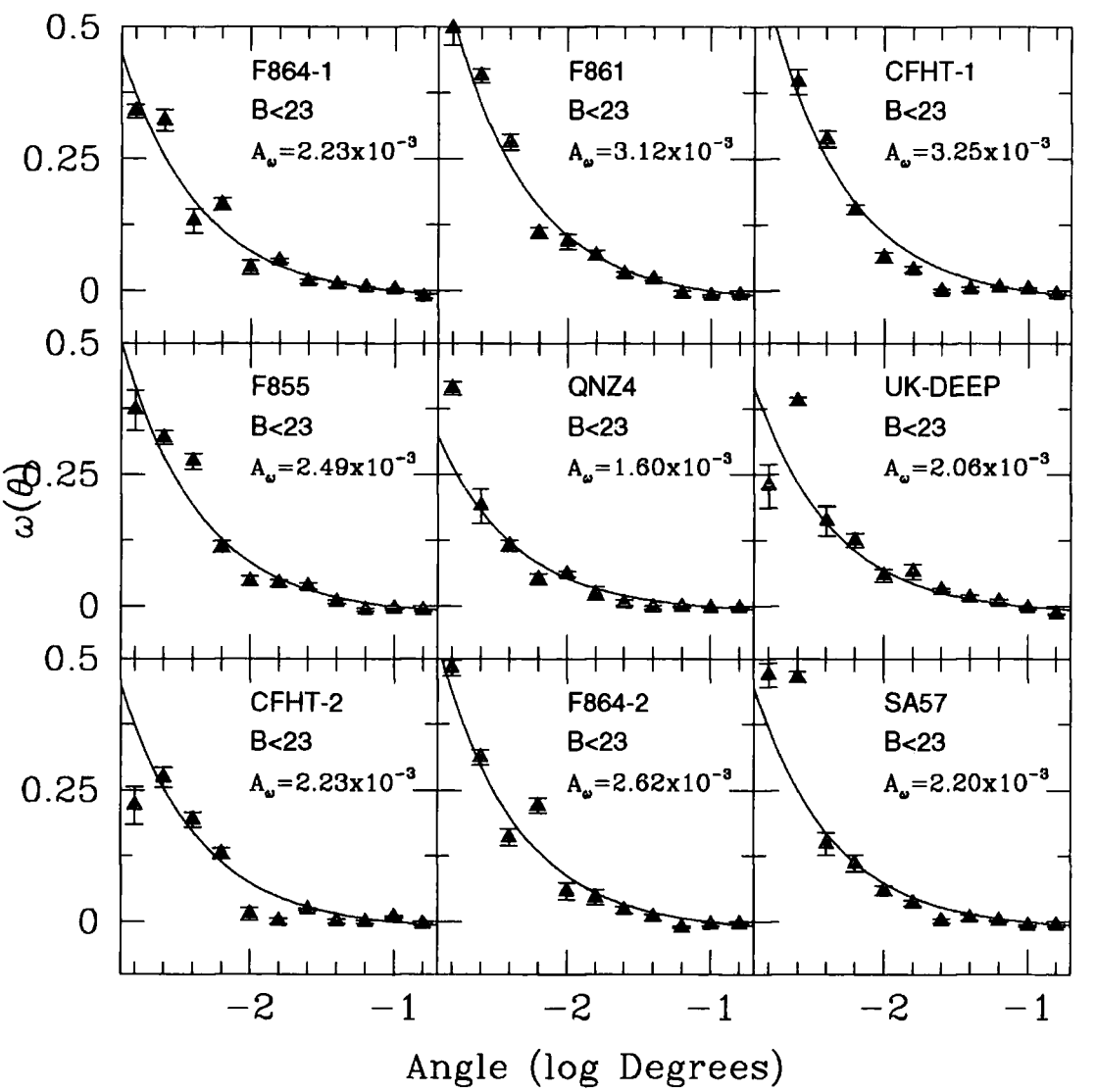

Figure 5.7: This plot shows the two point correlation function for each of the 9 fields using the B<23 galaxy sample. The errors are model fits are calculated in the our usual way.

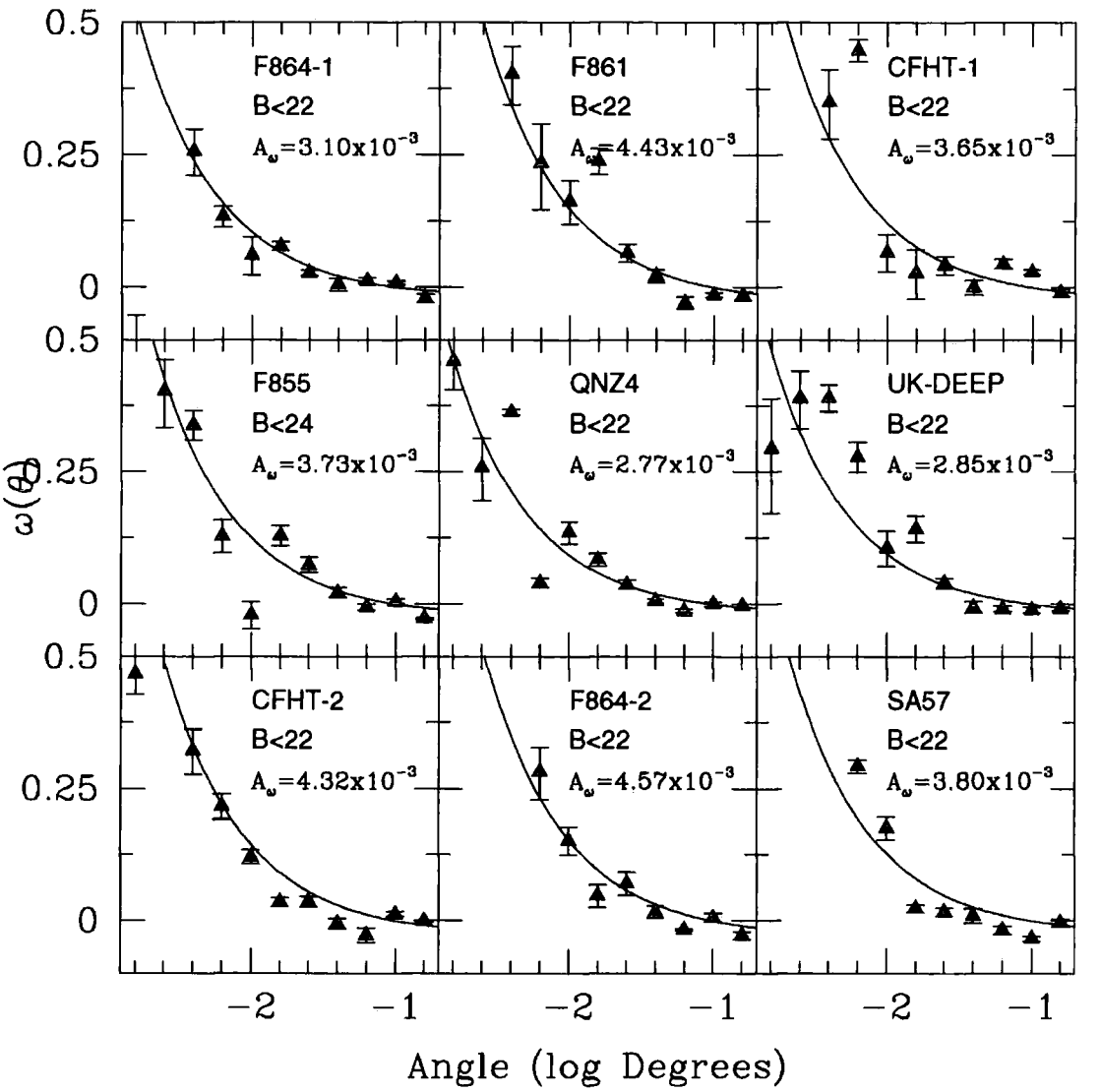

Figure 5.8: This plot shows the two point correlation function for each of the 9 fields using the B<22 galaxy sample. The errors are model fits are calculated in the our usual way.

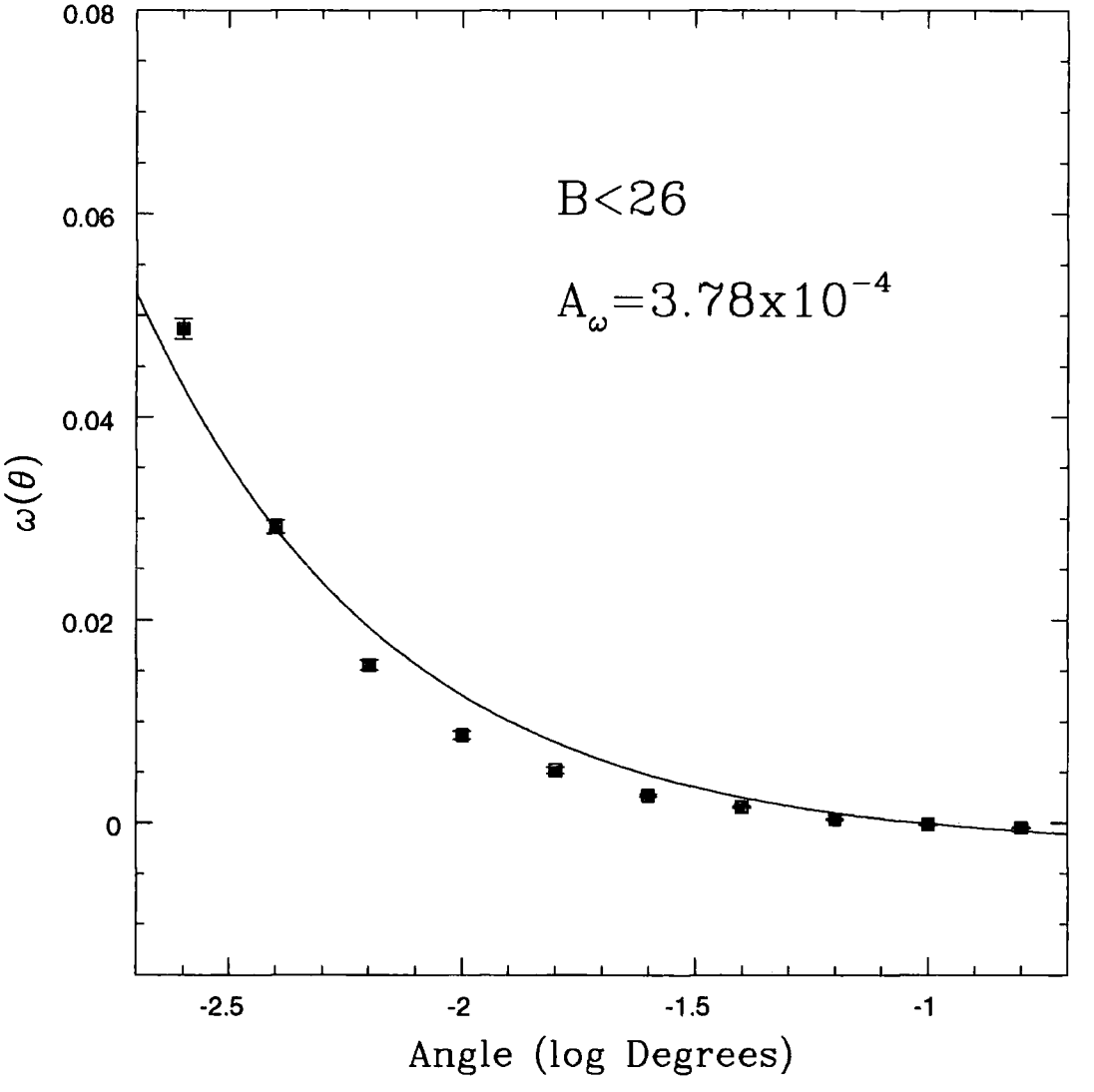

Figure 5.9: Here, we show the resultant two-point correlation function for the B<26 galaxy sample, obtained by calculating the mean in each angular bin over all the individual correlation functions from each of the 9 fields. The errors have been computed by averaging the data in each angular bin over all the fields and then dividing by a factor equal to the square root of the number of fields ie 3. The curve is a best fit of equation 5.15 to the data and the optimum value of A_ω is shown.

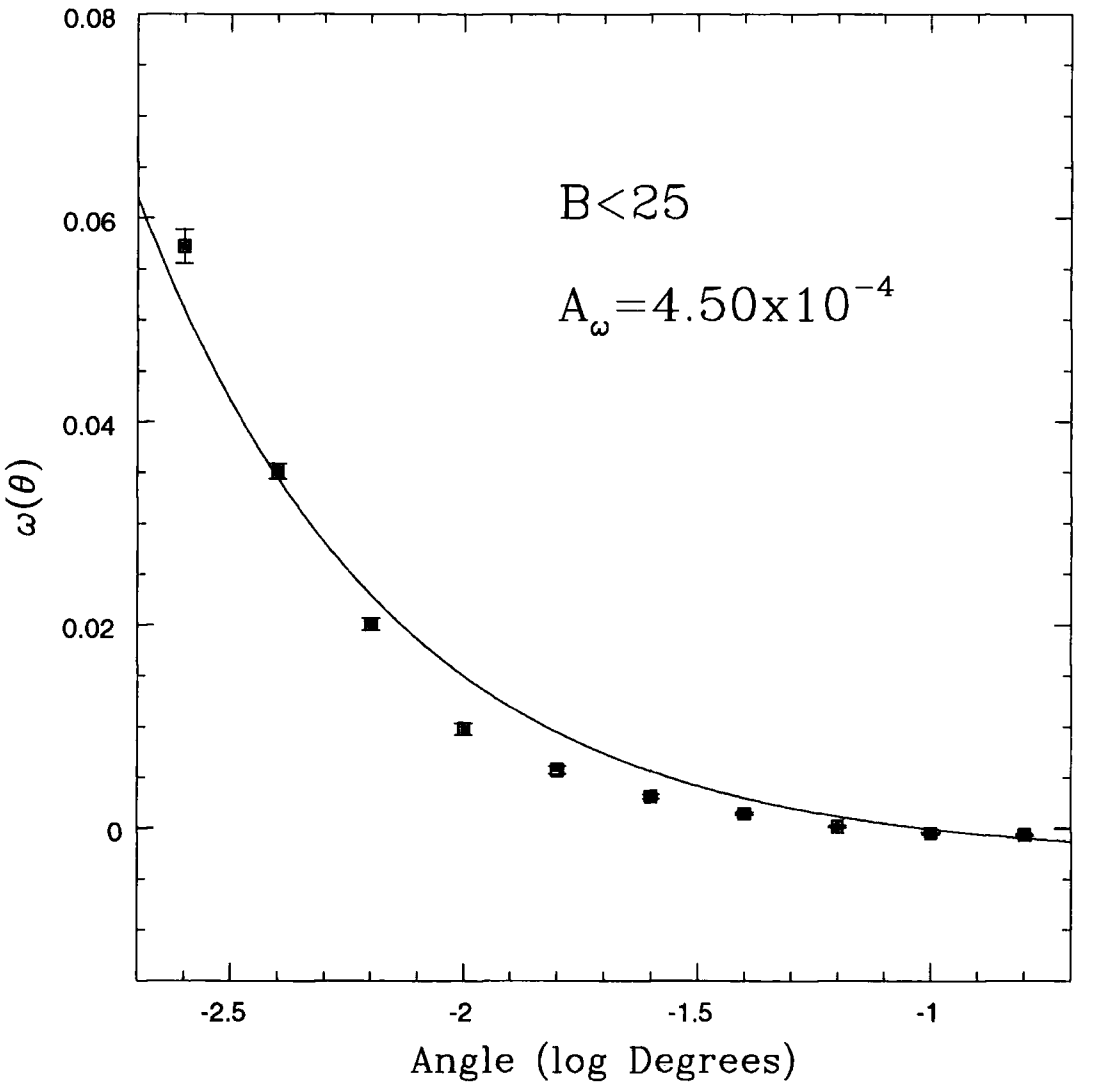

Figure 5.10: Here, we show the resultant two-point correlation function for the B<25 galaxy sample, obtained by calculating the mean in each angular bin over all the individual correlation functions from each of the 9 fields. The errors have been computed by averaging in each angular bin over all the fields and then dividing by a factor equal to the square root of the number of fields ie 3. The curve is a best fit of equation 5.15 to the data and the optimum value of A_ω is shown.

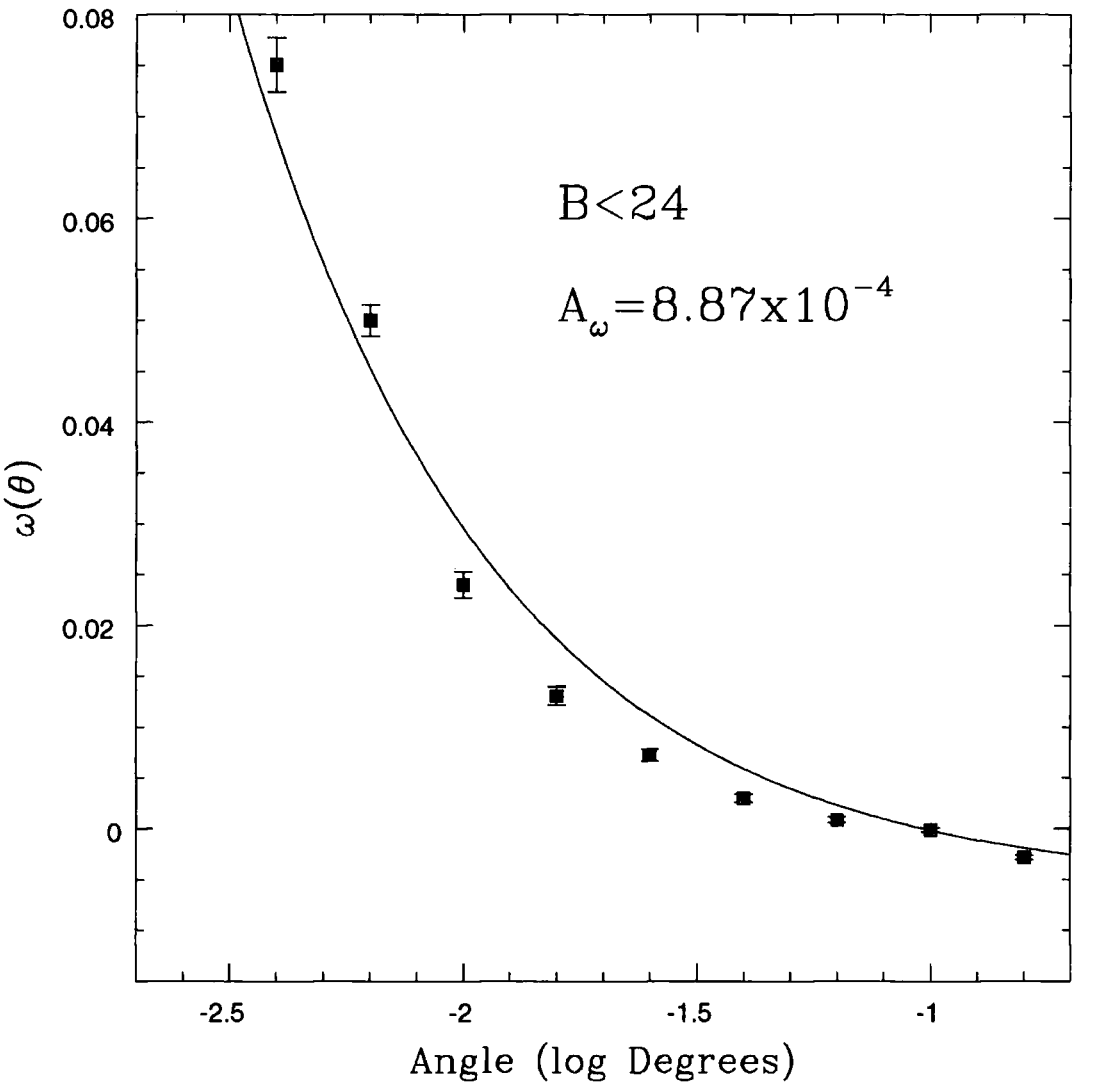

Figure 5.11: Here, we show the resultant two-point correlation function for the B<24 galaxy sample, obtained by calculating the mean in each angular bin over all the individual correlation functions from each of the 9 fields. The errors and model fits are calculated in the usual way.

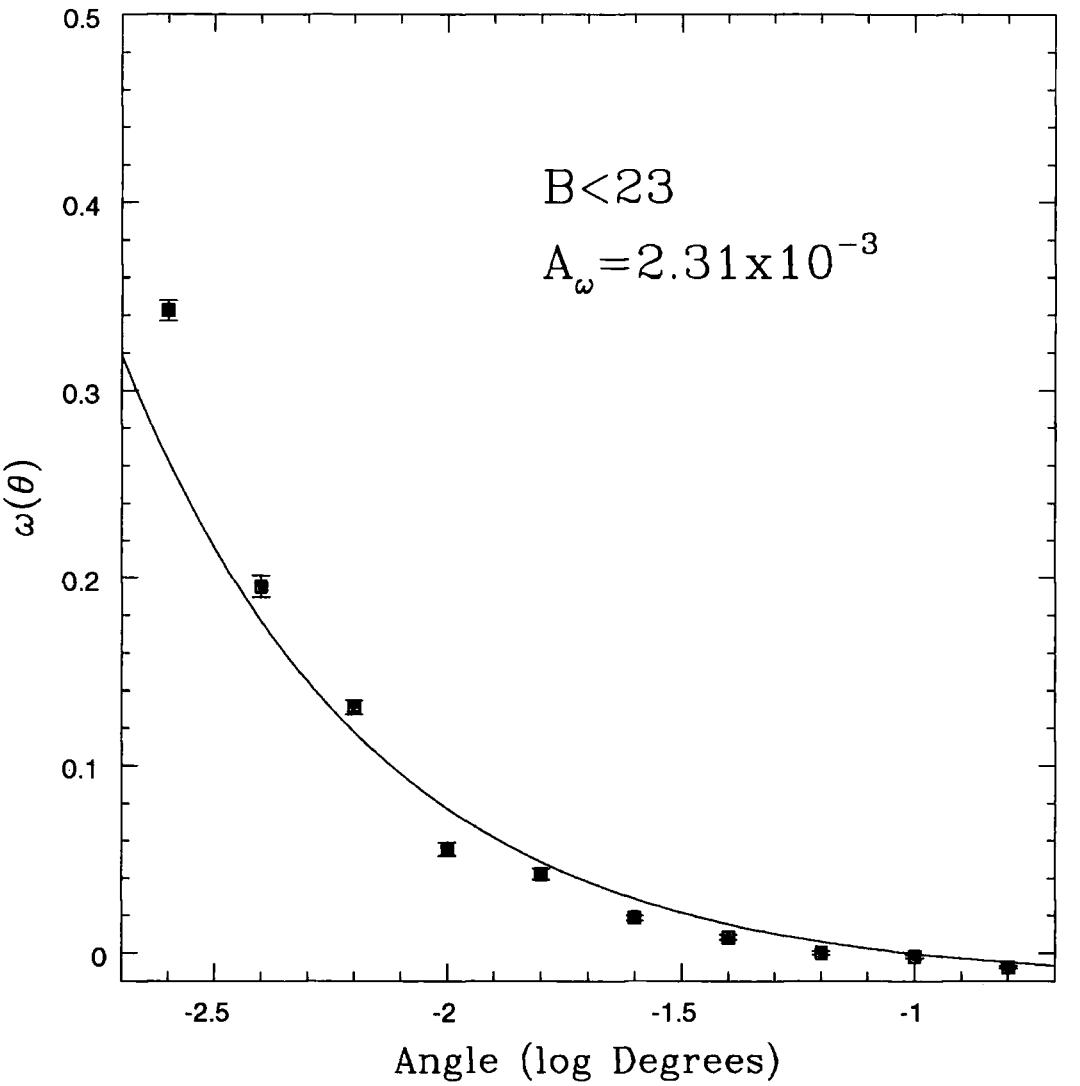

Figure 5.12: Here, we show the resultant two-point correlation function for the B<23 galaxy sample, obtained by calculating the mean in each angular bin over all the individual correlation functions from each of the 9 fields. The errors and model fits are calculated in the usual way. Note the scale change in the y-axis relative to the previous 3 figures, due to the larger clustering amplitudes we are measuring here.

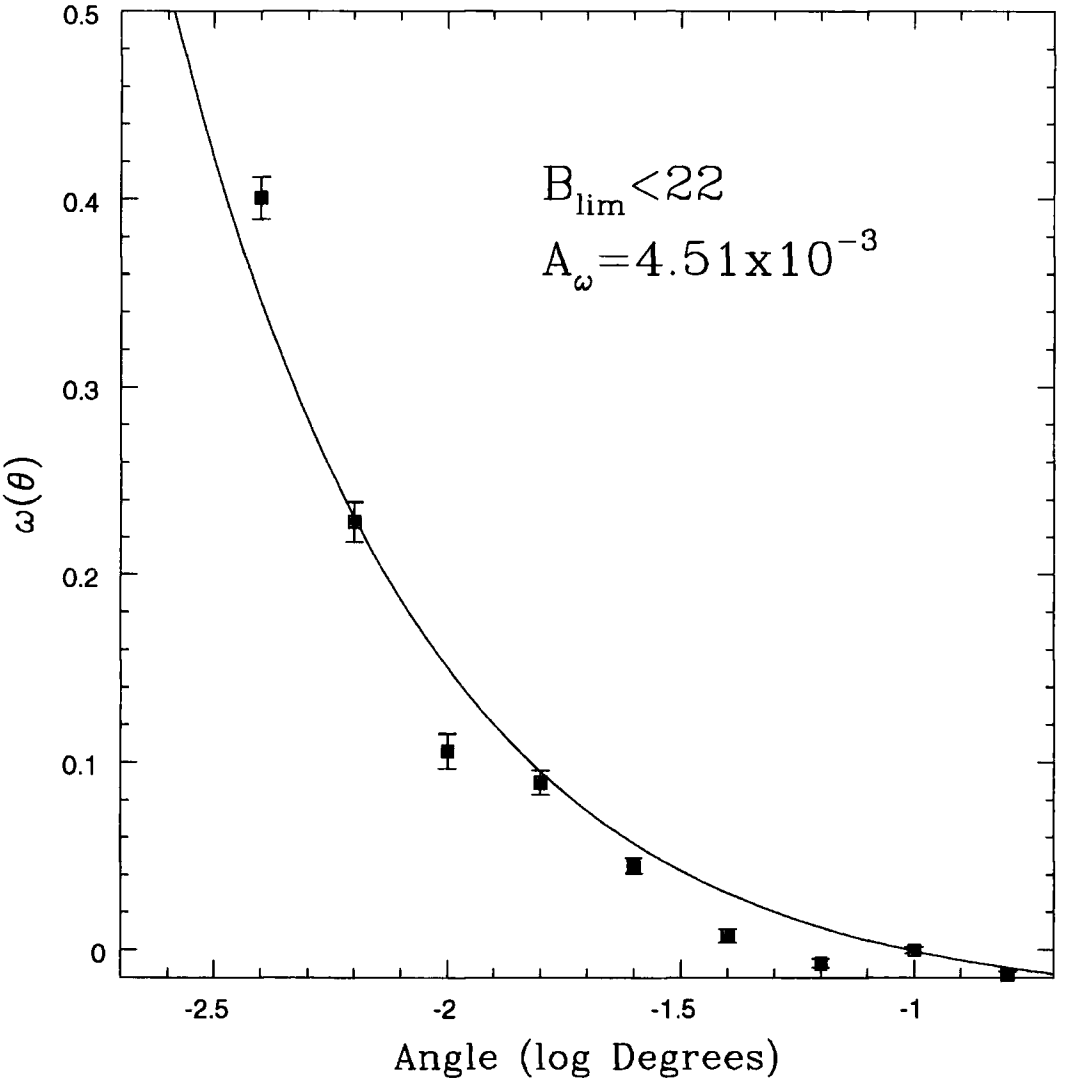

Figure 5.13: Here, we show the resultant two-point correlation function for the B<22 galaxy sample, obtained by calculating the mean in each angular bin over all the individual correlation functions from each of the 9 fields. The errors and model fits are calculated in the usual way. As in the previous figure we have used larger scale range on the y-axis due to the large clustering amplitudes we are measuring here.

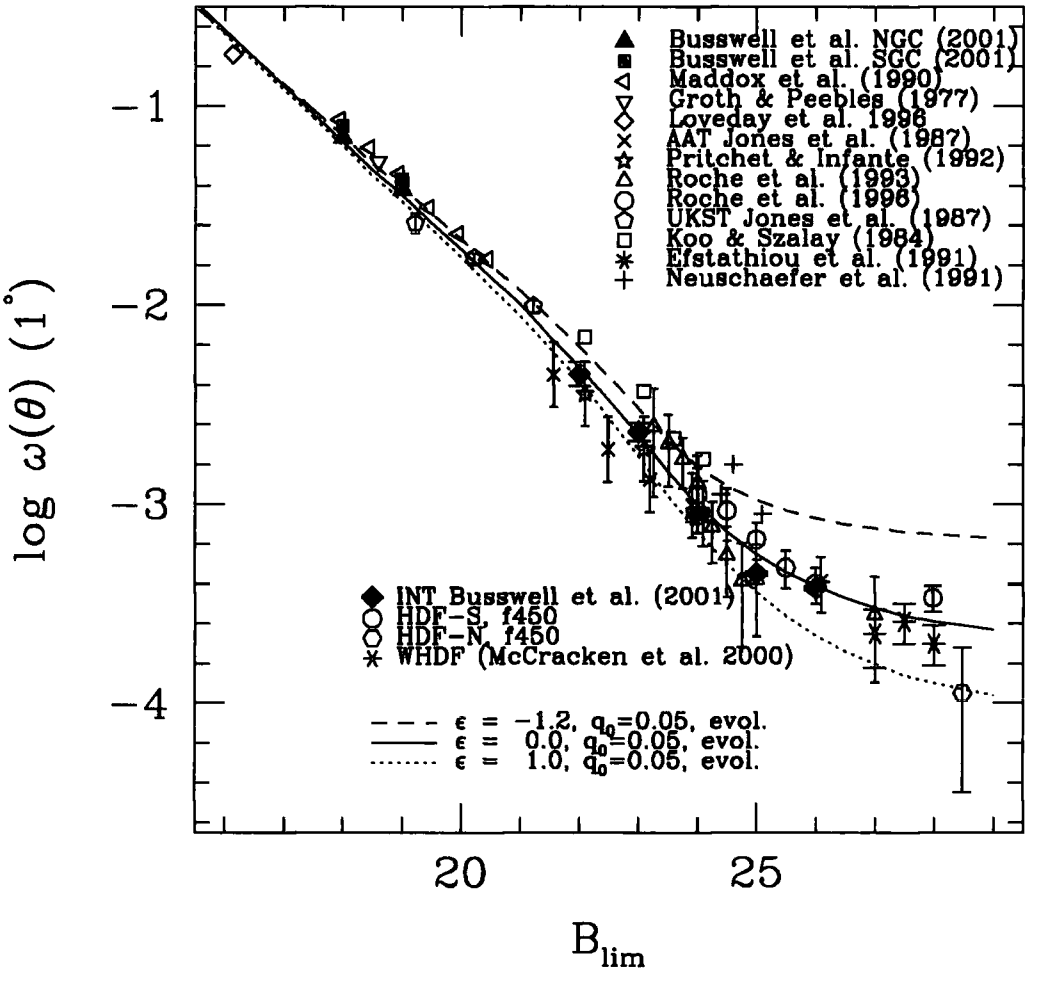

Figure 5.14: The amplitude of the two-point correlation function at 1° plotted against limiting magnitude, B_{lim}. Our INT Busswell et al. (2001) results our shown by the filled diamonds along with our CTIO clustering results from chapter 4 and a compilation of other data from the literature. The amplitude at 1° of our CTIO data as well as the APM and Lick data was calculated assuming a δ=0.72 slope. The Loveday et al. (1996) point shows the clustering amplitude at 1° of the APM-Stromlo Redshift Survey, where we have applied our photometry correction derived in Chapter 3 of 0.31 mag. For all the other data from the literature a slope with δ=0.8 was used in order to extrapolate to 1°. The curves show evolution models for different values of the clustering growth parameter, ϵ: ϵ=0 (solid line), ϵ=1.0 (dotted line) and ϵ=-1.2 (short dashed line).

and 5.13. The errors in each of these plots are computed by taking the mean in each angular bin over all 9 fields and then dividing by $\sqrt{9}$.

It can be seen in these figures that the assumed $A_\omega\theta^{-0.8}$ power law is not a good fit to the observed angular correlation function data. We could have assumed a more general $A_\omega\theta^{-x}$, with $x > 0$, power law and derived the optimum value for x as well as A_ω. However, extensive data is available in the literature where the $A_\omega\theta^{-0.8}$ power law has been assumed by the relevant authors in order to extrapolate the amplitude of the angular correlation function to 1°. By following in this trend it is straightforward for us to fairly compare our amplitudes at 1° as a function of limiting apparent magnitude. A possible alternative would have been to fit for the power law index, x, but in order to ensure a fair comparison to the literature when performing the extrapolation, we could have imposed a constraint on our chosen power law fit. This constraint would ensure that the integral of the two-point function over all $\theta < 1°$ is the same as it would have been if the $\theta^{-0.8}$ power law had been used so that:

$$\int_{\theta=0°}^{\theta=1°} A_{\omega_{0.8}}\theta^{-0.8}d\theta = \int_{\theta=0°}^{\theta=1°} A_{\omega_x}\theta^{-x}d\theta \tag{5.16}$$

where $A_{\omega_{0.8}}$ and A_{ω_x} are the amplitudes at 1° for the $\theta^{-0.8}$ and θ^{-x} power laws respectively.

Now that we have computed A_ω, the amplitude of the correlation function at 1° for each of our galaxy samples, to compare to other work in the literature we plot A_ω as a function of limiting magnitude, B_{lim}, which is shown in Fig. 5.14. This is the same as Fig. 4.10 in chapter 4, but here we include our new Busswell et al. (2001) faint blue galaxy clustering results shown by the filled diamonds. The curves are evolving models for 3 different values of the clustering growth parameter, ϵ, and they are explained in section 5.5.

5.6 Modelling the Clustering Evolution

In order to compare our data to model predictions we parametrise the evolution of the correlation function using simple ϵ models which have been commonly used in the literature (Efstathiou et al. 1991; Roche et al. 1993; Brainerd et al. 1994; Brainerd et al. 1998). These models assume that the amplitude of the *spatial* correlation function scales with redshift in accordance with the relation:

$$\xi(r,z) = \left(\frac{r_0}{r}\right)^{\gamma} (1+z)^{-(3+\epsilon)} \tag{5.17}$$

where r_0 is the correlation length at z=0, r is the proper distance and the parameter ϵ controls the growth of clustering as a function of redshift. This assumes that the spatial correlation function can be approximated by $\xi(r) = (r_0/r)^{\gamma}$ at z=0 which has been found for large galaxy surveys on scales $<10h^{-1}$Mpc and was an assumption used for our bright galaxy clustering analysis in chapter 4. The angular correlation function $\omega(\theta)$ can then by predicted by assuming a galaxy redshift distribution and integrating over $\xi(r,z)$ using Limber's equation (equation 4.13 in Chapter 4). Our redshift distribution is calculated using the galaxy evolution model of Metcalfe et al. (2001), which are described in detail in Chapter 3. We assume that r_0=$4.7h^{-1}$Mpc, γ=1.8 and q_0=0.05. We use three values of the parameter ϵ in Fig. 5.14, which measures the growth of clustering as function of redshift. ϵ=-1.2 corresponds to a Universe where clustering is fixed in co-moving co-ordinates i.e. constant relative to the expanding Universe, ϵ=0 means that clustering is fixed in proper co-ordinates and ϵ=1.0 approximately corresponds to the predictions of linear theory in an unbiased Ω=1 Universe.

5.7 Discussion

We have presented results in Fig. 5.14 for 5 galaxy samples, defined by the magnitude limits of B=22, 23, 24, 25 and 26. The size of the B<26 sample from all 9 fields is extremely large, containing over 200,000 galaxies and so we can minimize the statistical errors associated with measuring our correlation functions. The number of galaxies detected on a typical CCD chip for a B<22 sample is ~500 -

compared to ~5000 for the B<26 sample, and these relative sizes of galaxy numbers are reflected in the larger errors for the samples defined by the brighter magnitude limits. Our new Busswell et al. (2001) data shown in Fig. 5.14 agrees well with results from other authors, particularly with the results of Roche et al (1993, 1996) who also used the INT to collect their observations.

The completeness limit of our data is B=25.5 but our star/galaxy separation is only reliable as faint as B=24. However, Fig. 5.15 shows the that the ratio of galaxies to stars in terms of number density is a factor of ~20 at B=24 and ~60 at B=26 - and so the vast majority of sources fainter than B=24 are in fact galaxies. Our star/galaxy separation method was to class all B<24 sources as galaxies provided that CLASS_STAR<0.97. If B≥24 then a source was classed as a galaxy. Therefore in our B<26 galaxy sample, although the SExtractor software can no longer differentiate between stars and galaxies, we expect only 2% of these sources to be stars, which will not significantly suppress the intrinsic clustering amplitude of the correlation function we measure.

The other feature of these results is the apparent flattening of our clustering amplitudes as B_{lim} increases. We have 5 points on Fig. 5.14 with the B=26 point higher than expected if it were to follow the same trend shown by our B=22, B=23, B=24 and B=25 points, where the clustering amplitude is inversely proportional to the magnitude limit of our galaxy samples. This is an important effect and has been observed to occur in the B-band by McCracken et al. (2000) at B=27-28 and in the I-band by Brainerd & Smail (1998) at I=24. The completeness of our B<26 galaxy sample may also be an issue in terms of the observed flattening of the clustering amplitudes as the completeness limit of the Croom et al. galaxy sample is at B=25.5. The B<26 galaxy is about 60% complete and therefore the effective magnitude limit of the sample may be slightly less than B=26, exaggerating this apparent flattening. We are confident that this effect is real though since A_ω=3.8x10^{-4} deg$^{0.8}$ for the B<26 galaxy sample which is almost as large as the amplitude at 1° for the B<25 sample, where A_ω=4.5x10^{-4} deg$^{0.8}$. This means the effective completeness limit of the B<26 sample would have to be ~25.1, which is

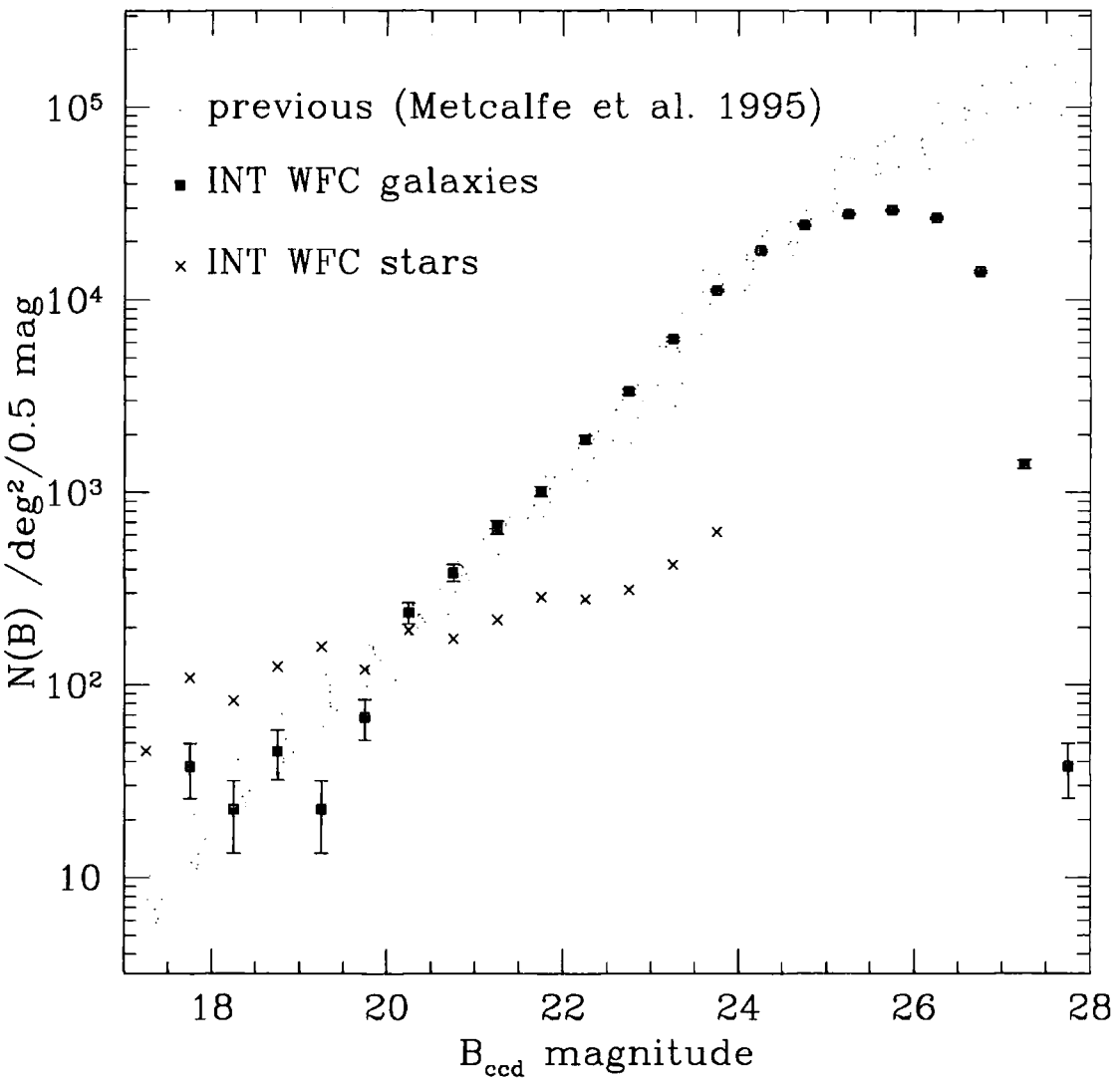

Figure 5.15: The number counts of galaxies in the SA57 field (filled squares) compared to a compilation of previous galaxy counts (Metcalfe et al. 1996) (small points). The errors on the SA57 data use Poisson statistics. At bright magnitudes there is some disagreement between the current data and previous work, as is expected due to excess variance over Poisson from large-scale structure. At intermediate magnitudes, B_{ccd}=21-25, there is good agreement. Fainter than B_{ccd}=25, the current counts start to fall below previous measurements as we reach our completeness limit at B_{ccd}=25.5. Also shown are the star counts to B_{ccd}=24 (crosses). This demonstrates that at the limit of reliable star/galaxy seperation, B_{ccd}=24, the galaxy counts clearly dominate the total numbers.

certainly not the case, in order that this flattening would not appear to occur.

In fact, the models of Metcalfe et al. (2001) predict a flattening effect which can clearly be seen in 5.14. The curves are seen to depart from the inverse proportionality trend at about B=25, in agreement with our data, where they flatten off to varying degrees depending on the value of the clustering growth parameter, ϵ. In fact this effect is most pronounced in the B-band because it is dominated by spiral galaxies, where a steep faint end slope to the luminosity function is assumed by Metcalfe et al. This steep slope means that, for B>25, our observations are dominated by galaxies that are intrinsically fainter than M* rather than more distant. Also the effect of a rapidly decreasing cosmological volume element contributes to this flattening.

All the derived clustering results in this thesis are shown by the filled symbols in Fig. 5.14. Our bright CTIO clustering results, along with other clustering results from the literature, can be used to constrain the value of r_0 in the local Universe. We can then use our clustering evolution models to find the value of ϵ which is most consistent with our INT results in the relatively distant Universe. When we do this we find that the clustering correlation length in proper co-ordinates, $r_0=4.7h^{-1}$Mpc and that our data is most consistent with a clustering growth parameter, $\epsilon=0.1$.

McCracken et al. (2000), who use an $r_0=4.3h^{-1}$Mpc which is close to our value of $4.7h^{-1}$Mpc, find that predictions from the simulations of Kravtsov & Klypin (1999) agree well with the $\epsilon=0$ model for B< 26, which would be consistent with our data. However, the simulation results used by McCracken et al. (2000) who are sampling galaxies much fainter than M*, only consider dark matter halos with v>120kms^{-1}. Our B<25 data is dominated by M* galaxies where typical halo velocities are $\gtrsim$200kms^{-1}. In fact these simulations find higher clustering amplitudes for such dark matter halo's than in the v>120kms^{-1} case, which makes sense since we expect brighter galaxies to show stronger clustering properties in accordance with bias. However, this then means that our data shows lower clustering amplitudes than the predictions of the simulations for v>200kms^{-1} halos, which may

mean that galaxies are less biased tracers of the underlying mass distribution than assumed in the simulations of Kravtsov & Klypin (1999).

Our INT data is consistent with an ϵ=0.1 model, but the LBG's at z$\sim$3 observed by Steidel et al. show much higher clustering amplitudes and are consistent with the ϵ=-1.2 model shown in Fig. 5.14. This can be explained by the fact that the selection effects are different. The crucial difference is that Steidel et al. use their Lyman Break technique which defines a sample of galaxies at a roughly constant redshift of z$\sim$3. This means that galaxies *brighter* than M* will be preferentially selected. In the case of our B<26 galaxy sample, as with the WHDF data of McCracken et al. (2000), we are sampling galaxies that are instrinsically *fainter* than M* and if galaxies are biased tracers of mass, then one would expect the very luminous LBG population to show relatively strong clustering properties.

5.8 Conclusions

In this chapter we have outlined the data reduction techniques of Croom et al. (2001) and described how we applied a radial distortion correction to the source coordinates from the final reduced data as well as calculated the integral constraint for our CCD chips. In each of our 9 fields we calculated the two-point angular correlation function for 5 galaxy samples, defined by the magnitude limits B=26, B=25, B=24, B=23 and B=22, by averaging the two-point function obtained for each of the 4 CCD chips. A resultant two-point function could then be obtained by averaging the results over all 9 fields for each of the 5 galaxy samples. The large size of our B=26 and B=25 galaxy samples meant that we could minimize statistical errors with regard to the prediction of our clustering amplitudes at 1°, but as the magnitude limit decreases the errors on these amplitudes increase significantly, as seen for the B<22 sample.

We found that our clustering amplitudes at 1° were consistent with other data in the literature, particularly with those of Roche et al. (1993, 1996) who also used the INT for their observations. We used our CTIO clustering results from Chapter

4, along with other data from the literature, in order to constrain the value of r_0 in the local Universe and found that $r_0=4.7h^{-1}$Mpc. We then found that an ϵ=0.1 model provided the best fit to our high redshift INT clustering results, which have been derived in this chapter and our data rejects the ϵ=-1.2 model prediction, which is consistent with the clustering properties of the Steidel et al. LBG's. This can be explained by the fact that Steidel et al. are preferentially selecting more instrinsically luminous galaxies than M*, which, from the idea of bias, are predicted to show relatively strong clustering properties.

All our model predictions flatten off at B_{lim}=25, in excellent agreement with our data-points, although we claim that this flattening trend in our data could be exaggerated by our B=26 point, which is beyond our completeness limit of B=25.5. Our INT results predict lower clustering amplitudes than the biased ΛCDM simulations of Kravtsov & Klypin (1999), when dark matter halo are used with $v \gtrsim 200 \mathrm{kms}^{-1}$. This may mean that galaxies are a less biased tracer of the underlying mass distribution than is assumed in these simulations.

Chapter 6

The Contribution of Faint Blue Galaxies to the Sub-mm Number Counts and Background

6.1 The Distant Universe in the Sub-mm

This chapter is devoted to the nature of the newly-discovered population of sources in the sub-mm (Ivison et al. 1997). In particular, our aim is to investigate whether dust assumed in normal spiral galaxies in the models of Metcalfe et al. (2001) could have implications for the faint (<2mJy) sub-mm population in the high red-shift (z> 1) Universe. We will first review the situation regarding the optical galaxy counts, focusing in particular on these models of Metcalfe et al. These simple models, which use a τ = 9Gyr SFR for spirals and include the effects of dust, give good fits to galaxy counts and colours from U to K. The idea is then to see whether this combination of exponential SFR and relatively small amounts of dust in the first instance (A_B = 0.3 mag. for the $1/\lambda$ law), which would re-radiate the spiral ultra-violet (UV) radiation into the FIR, could cause a significant contribution to the sub-mm galaxy number counts and background at 850μm. Our modelling will be described in section 6.3 and then in section 6.4 our predicted contribution to the 850μm and 60μm galaxy counts and the extra-galactic background in the sub-mm will be shown. Also in this section we demonstrate how to get a fit to the background in the 100 – 300μm range by using warmer, optically-thicker dust in line with that typically seen in ULIRG's. We will then discuss the implications of

our predictions in section 6.5 and conclude in section 6.6.

6.2 The Optical Counts

It is well known that non-evolving galaxy count models, where number density and luminosity of galaxies remain constant with look-back time, do not fit the optical number counts e.g. (Shanks et al. 1984), as there is always a large excess of galaxies faint-wards of $B \sim 22^m$. One way to account for this excess of 'faint blue galaxies' is to investigate the way galaxy evolution will influence the optical number counts.

Metcalfe et al. (2001) showed that by assuming that the number density of galaxies remains constant, the Bruzual and Charlot(1993) evolutionary models of spiral galaxies with a $\tau = 9$Gyr SFR give excellent fits to the optical counts. The galaxy number counts are normalised at $B \sim 18^m$ so that the non-evolving models give good fits to the B band data and red-shift distributions in the magnitude range 18<B<22. With this high normalisation, the models of the galaxy counts represent both spiral and early-type galaxies extremely well for 17^m <I<22^m (Glazebrook et al. 1995a, Driver et al. 1995) and also the less steep H/K counts out to $K \sim 20^m$. The evolution model then produces a reasonable fit to the fainter counts to $B \sim 27^m$, $I \sim 26^m$, $H \sim 28^m$.

Metcalfe et al. (2001) included a $1/\lambda$ internal dust absorption law with $A_B = 0.3$ for spirals to prevent the $\tau = 9$ Gyr SFR from over-predicting the numbers of high red-shift galaxies detected in faint B< 24 red-shift surveys (Cowie et al 1995). This $1/\lambda$ dust law differs from the Calzetti (1997) dust law derived for star-burst galaxies, in that for a given A_B, more radiation is absorbed in the UV. The Calzetti dust law is used by Steidel et al. (1999) to model their 'Lyman Break' galaxies; they find an average E(B-V)=0.15 which gives $A_B = 0.87$mag and $A_{1500} = 1.7$mag. This compares to our $A_{1500} = 0.9$mag with $A_B = 0.3$mag. Both models also fail to predict as red colours as observed for the U-B colours of spirals in the Herschel Deep Field (Metcalfe et al 1996). However, if we assumed E(B-V)=0.15 for our z=0 spirals, as compared to our E(B-V)=0.05, then the rest colours of spirals as predicted by

the Bruzual & Charlot model might start to look too red as compared to what is observed. Otherwise, the main difference between these two dust laws is that the Calzetti law would produce more overall absorption and hence a higher FIR flux from the faint blue galaxies. Thus in some ways our first use of the $1/\lambda$ law appears conservative in terms of the predicting the faint blue galaxy FIR flux. Later, we shall experiment by replacing the $1/\lambda$ law with the Calzetti (1997) law in our model.

So this pure luminosity evolution (PLE) model with $1/\lambda$ dust and $q_0 = 0.05$ then slightly under-estimates the faintest optical counts but otherwise fits the data well, whereas for $q_0 = 0.5$ the underestimate (with or without dust) is far more striking. An extra population of galaxies has to be invoked at high red-shift to attempt to explain this more serious discrepancy for the high q_0 model. This new population was postulated to have a constant SFR from their formation red-shift until $z \sim 1$ and then the Bruzual & Charlot models predict a dimming of $\sim 5^m$ in B to form a red dwarf elliptical (dE) by the present day and therefore has the form of a 'disappearing dwarf' model (Babul & Rees 1992). No dust was previously assumed in the dE population but this assumption is somewhat arbitrary.

The $\tau = 9$Gyr SFR was inconsistent with the early observations at low red-shift from Gallego et al. (1996) and this is partly accounted for by the high normalisation of the optical number counts at $B \sim 18^m$. There is still a problem with the UV estimates from the Canada-France Red-Shift Survey (CFRS) UV data of Lilly et al. (1996) at z=0.2. More recent estimates of the global SFR at low red-shift based on the [OII] line (Gronwall et al. 1998; Tresse & Maddox 1998) indicates that the decline from z=1 to the present day may not be as sharp as first thought and that the $\tau = 9$Gyr SFR in fact provides a better fit to this low red-shift data. Metcalfe et al. (2001) have further found that this model also agrees well with recent estimates of the luminosity function of the z=3 Lyman break galaxies detected by Steidel et al. (1999).

The main question then that we will address in this chapter is whether the small amount of internal spiral dust absorption assumed in these models, which give an

excellent fit to the optical galaxy counts, could cause a significant contribution to the sub-mm number counts and background at 850μm.

6.3 Modelling

Using the optical B band parameters for spiral galaxies, we attempt to predict the contribution to the sub-mm galaxy counts and background at $850\mu m$ by using a $1/\lambda$ absorption law for the dust and re-radiating the spiral UV radiation into the FIR. We use the Bruzual & Charlot (1993) galaxy evolution models with H_0 = 50kms^{-1}Mpc^{-1} and a τ=9 Gyr SFR - with a galaxy age of 16 Gyr in the low q_0 case, and 12.7 Gyr in the high q_0 case to produce our 1M$\odot$ galactic spectral energy distribution (SED) as a function of red-shift. We then use the equation:

$$G_{abs}(z) = \int F_\lambda(z)(1 - 10^{-0.4*A_B*(4500/\lambda)})d\lambda \tag{6.1}$$

as used by Metcalfe et al. (1996), which is used to calculate the radiation absorbed by the dust, $G_{abs}(ergss^{-1})$, for our 1M$_\odot$ model spiral galaxy as a function of z, using our $1/\lambda$ absorption law with A$_B$ = 0.3. Since Bruzual & Charlot provides us with a 1M$\odot$ SED at each red-shift increment, we need to calculate the factor required to scale this SED (after the effect of absorption from the dust) to obtain that of a galaxy with absolute magnitude M_B at zero red-shift, and this factor will then remain constant for M_B galaxies at all other redshifts. This then provides a zero point from which to calculate scaling factors for all the other galaxies in our luminosity functions. We find the scaling factor for an M_B galaxy by making use of a relation from Allen (1995):

$$m_B = -2.5log(\int B_\lambda f_\lambda d\lambda) - 12.97 \tag{6.2}$$

where f_λ is the received flux$(ergs^{-1}\AA^{-1}cm^{-2})$ and B_λ is the B band filter function. By re-arranging, setting m_B=M_B and then multiplying by $4\pi(10pc)^2$ we obtain the total emitted power, $L_B(ergs^{-1})$ in the B band from an M_B galaxy:

$$L_B = 4\pi(10pc)^2.10^{[-0.4(M_B+12.97)]} \tag{6.3}$$

The intensity emitted in the B band, after absorption by the dust from our $1M_{\odot}$ galaxy, $L_{B_{M_{\odot}}}$ is then calculated by integrating the SED, assuming a flat B band filter, between $4000\mathring{A}$ and $5000\mathring{A}$.

$$L_{B_{M_{\odot}}} = \int F_{\lambda}(z) 10^{-0.4 * A_B * (4500/\lambda)} B_{\lambda} d\lambda \tag{6.4}$$

The scaling factor to scale a Bruzual & Charlot $1M_{\odot}$spectral energy distribution for a particular galaxy of absolute magnitude, M_B, at red-shift z, is therefore defined by the ratio $L_B/L_{B_{M_{\odot}}}$. The total energy absorbed by the dust for this galaxy is then given by $G_{abs}L_B/L_{B_{M_{\odot}}}$.

The way the dust will re-radiate this absorbed flux depends on its temperature, particle size and chemical composition. We will adopt a simple model by assuming a mean inter-stellar dust temperature of 15K, (Bianchi et al. 2000) and also a modest warmer component of 45K, (the actual luminosity ratio we use is $L_{45K}/L_{15K} = 0.162$), which would come from circum-stellar dust (Domingue et al. 2000) and is needed in order to fit counts at shorter wavelengths eg. 60μm. The effect of varying the dust parameters is explored in section 4. We then use the fact that the rate the dust absorbs energy must equal the rate at which it emits, and therefore we simply scale integral of the Planck function over all wavelengths so that:

$$C(z, M_B) \int_{-\infty}^{\infty} \beta(\lambda, T) d\lambda = G_{abs} L_B / L_{B_{M_{\odot}}} \tag{6.5}$$

where C(z,M_B) is the scaling factor, which is a function of z and M_B, $\beta(\lambda, T)$ is the Planck function (in this case a sum of two Planck functions) and $\kappa_d(\lambda) \propto \lambda^{-\beta}$, where $\kappa_d(\lambda)$ is an opacity law (we use $\beta = 2.0$ for each Planck function to model optically thin dust).

We then calculate the received $850\mu m$ flux, S(z,M_B), from a galaxy with absolute magnitude M_B and red-shift z using the equation:

$$S(z, M_B) = \frac{C(z, M_B) \lambda_e^{-\beta} \beta(\lambda_e, T)}{4\pi(1+z) d_L^2} \tag{6.6}$$

where C(z,M_B) is defined from equation 6.5 and λ_e is equal to $850\mu m/(1+z)$. We can then obtain the number count of galaxies with absolute magnitude between M_B and $M_B + dM_B$ and red-shift between z and z+dz for which we measure the same flux density S(z,M_B) at $850\mu m$ (see equation 6.6).

$$dN(z, M_B) = \phi(M_B)\frac{dV}{dz}dM_B dz \tag{6.7}$$

where $\phi(M_B)$ is the optical Schechter function and $\frac{dV}{dz}$ is the cosmological volume element. Then the integral source counts N(>S_{lim}) are obtained, for each value of S_{lim}, by integrating over the range of values of M_B and z such that S(z,M_B) > S_{lim}, where S(z,M_B) is defined in equation 6.6.

$$N(> S_{lim}) = \int_{M_B}\int_z \phi(M_B)\frac{dV}{dz}dM_B dz \tag{6.8}$$

It is straightforward to then obtain model predictions of the FIR background for a given wavelength. The intensity, dI, at $850\mu m$ from galaxies with absolute magnitudes between M_B and $M_B + dM_B$ and redshifts between z and z+dz is given by multiplying the number of galaxies with these z's and M_B's by the flux density which we would measure from each

$$dI_{850} = S(z, M_B)\phi(M_B)\frac{dV}{dz}dM_B dz \tag{6.9}$$

and then we simply integrate over all absolute magnitudes and all redshifts ($0 < z < 4$ in this case)

$$I_{850} = \int_{M_B}\int_z S(z, M_B)\phi(M_B)\frac{dV}{dz}dM_B dz \tag{6.10}$$

6.4 Predictions

Fig. 6.1 shows our model predictions for the $60\mu m$ differential number counts of IRAS galaxies (Saunders et al. 1990). This was an all sky local survey carried out with the IRAS satellite down to a flux limit of 0.6Jy. It therefore provides an important test of our model since spiral galaxies contribute significantly to IRAS counts

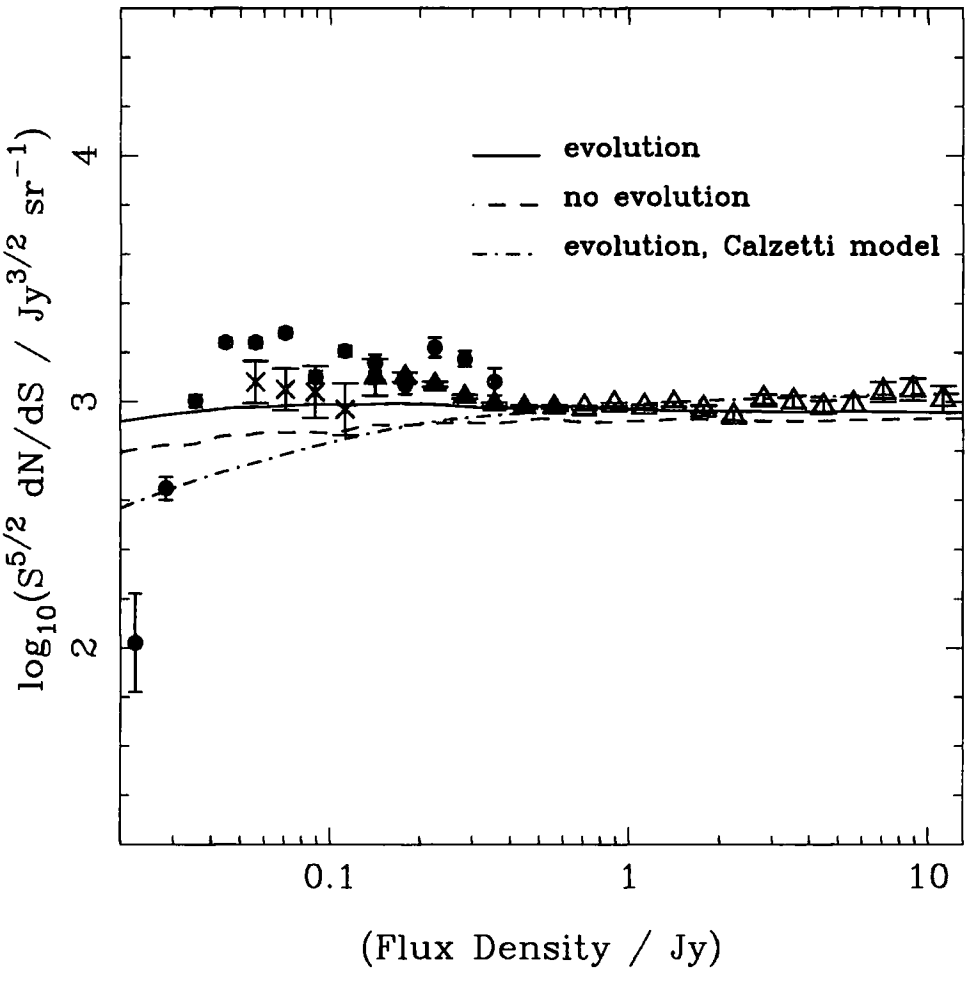

Figure 6.1: The $60\mu m$ differential number counts. The graph shows the evolution and no-evolution models for a low q_0 Universe(the corresponding high q_0 models are indistinguishable) along with the observed $60\mu m$ counts of IRAS galaxies down to a flux limit of 0.6Jy, plotted in the format used by Oliver et al. (1992). The crosses are from Hacking & Houck (1987), the empty triangles from Rowan-Robinson et al. (1990), Saunders et al.(1990) are the filled triangles and the circles are Gregorich et al. (1995) and Bertin et al. (1997). We use a two-component dust temperature of 15K and 45K to model both inter-stellar and circum-stellar dust respectively. Other parameters used are $\beta = 2.0$, $H_0 = 50$ and a red-shift of formation of $z = 4$. The dot-dashed line shows the same evolution model using the Calzetti dust law with three dust temperature components of 15, 25, and 32K. This fits the IRAS counts less well at < 0.2mJy, and this is because of the lack of a 45K dust component meaning that there is much less thermal emission from the dust at 60μm

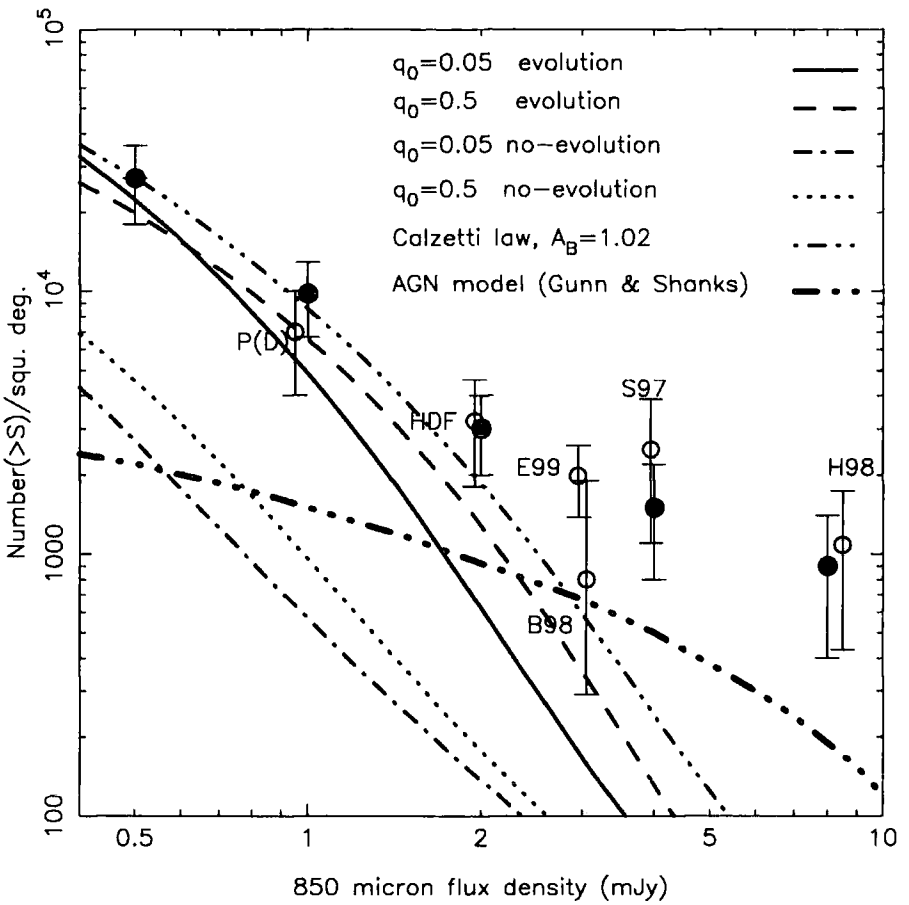

Figure 6.2: The 850μm integral number counts. The filled circles show the results of the SCUBA Lens Survey (Blain et al. 1999); the open circles are as labelled: S97 - Smail, Ivison & Blain (1997); B98 - Barger et al. (1998); H98 - Holland et al. (1998); E99 - Eales et al. (1999); HDF, P(D) - Hughes et al. (1998). Also shown are our predictions for $q = 0.05$ and $q = 0.5$ models with and without Bruzual & Charlot evolution, using the parameters from Fig. 6.1. Both the high and low q_0 models, with evolution (dashed and solid curves), do very well with the faint counts but fail the most luminous sources. In the no evolution cases(dotted and dot-dashed) the high q_0 model again predicts more galaxies then the low q_0 model, but they both under-predict the faint 850μm counts by about an order of magnitude and then again fall away again at the higher flux densities. The graph also shows a predicted contribution from AGN (Gunn & Shanks 1999) and a model using the Calzetti dust law (the two dot-dot-dot-dashed curves). The AGN model (the steeper of the curves) predicts that, at most, QSO's could contribute 30 percent of the background at 850μm, and these models do much better in the number counts at brighter fluxes, but they fail to contribute at the 0.5mJy level where we predict that faint blue galaxies are dominant.

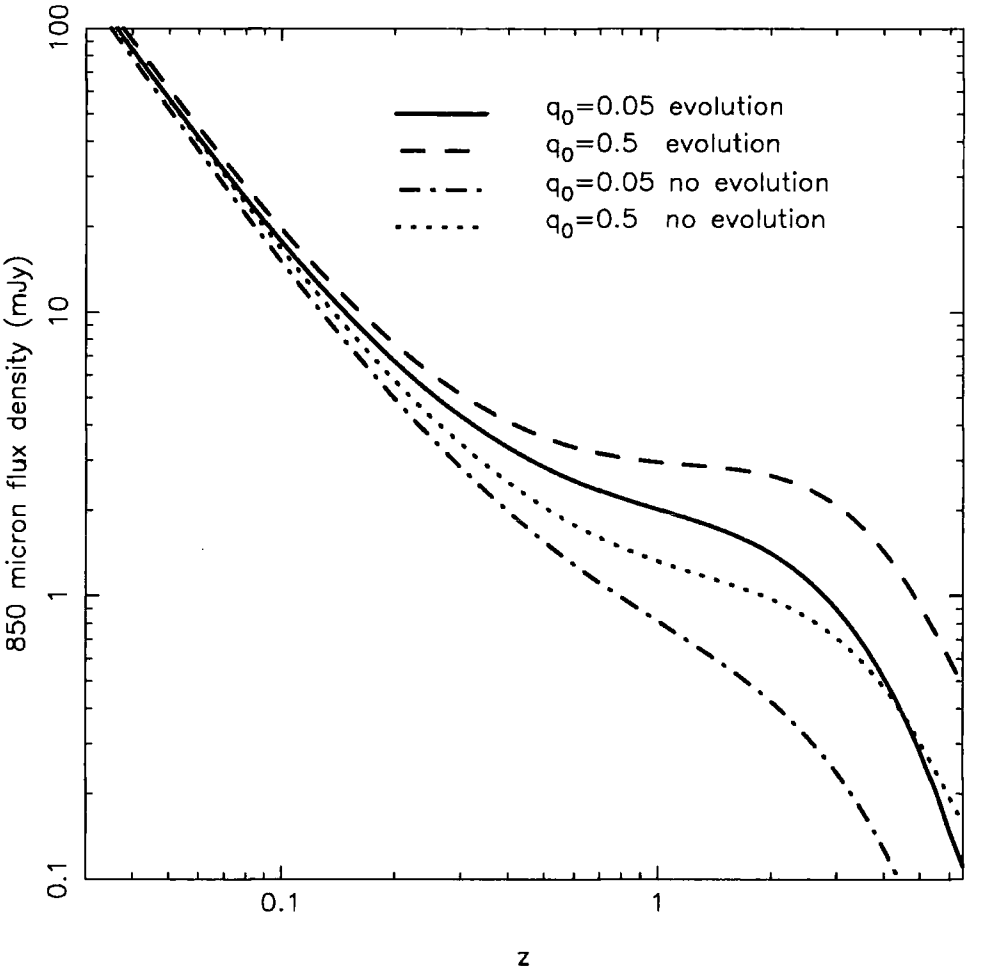

Figure 6.3: If a galaxy has an absolute magnitude $M_B = -22.5$ at the present day then these graphs show how the received flux from such a galaxy would vary as a function of red-shift using our model with the parameters described in the previous figure (Fig. 6.2). The solid line is for a $q_0 = 0.05$ Universe with Bruzual & Charlot evolution, the dashed line for $q_0 = 0.5$ with evolution, the dot-dashed line for $q_0 = 0.05$ without evolution and the dotted line for $q_0 = 0.5$ without evolution.

(Neugebauer et al. 1984) and so if we are going to assume PLE out to redshifts of 4 then our local galaxy count predictions at $60\mu m$ need to be reasonably consistent with the data. The figure shows our evolution and no evolution model(the q_0 makes no difference) and because the IRAS survey was probing redshifts out to z=0.2 we can see that there is very little difference between the two models and that they both fit the data reasonably well. The IRAS counts below 0.2Jy are slightly under-predicted using both dust laws, which could possibly be due to the fact our model doesn't include any fast-evolving AGN/ULIRG population. We use the Calzetti dust law with three dust components of 15, 25, and 32K and this failure of the fainter IRAS counts is greater than when the $1/\lambda$ law is used because of the absence of the 45K dust component, which dominates the thermal emission at 60μm.

We then go on to show in Fig. 6.2 our sub-mm predictions using the Bruzual & Charlot evolution model with low and high q_0 ($q_0 = 0.05, q = 0.5$) and also for the corresponding no-evolution models where we use the Bruzual & Charlot SED at $z = 0$ for all redshifts. We have used a two-component dust temperature, as described in the previous section and a galaxy formation red-shift, $z_f = 4$. The low q_0 model reproduces the faint counts well, but fails the very bright counts. This makes sense since these very luminous sources would require ULIRG's, having SFR's of order $\approx$ 100-1000$M_\odot yr^{-1}$, and/or AGN, in order to produce these huge FIR luminosities. Indeed, the $850\mu m$ integral log N:log S appears flat between 2-10mJy before rising again at fainter fluxes, suggesting that 2 populations may be contributing to the counts.

The high q_0 model contains a dwarf elliptical population in order to fit the optical counts, as already explained, but no dust was invoked in these galaxies in the optical models and so they do not contribute to our $850\mu m$ predictions. Contrary to the optical number counts, the high q_0 models predict more galaxies greater than a given flux limit than low q_0 models. The reason for this is illustrated in Fig. 6.3, which shows how the received flux density from a $M_B = -22.5$ galaxy would vary with red-shift in the high and low q_0 case, with and without τ=9Gyr. Bruzual & Charlot evolution. In the no-evolution cases the two factors involved

are the cosmological dimming and the effect of the negative k-correction, since we are effectively looking up the black body curve as we look out to higher red-shift. The high q_0 model(dotted line) predicts greater flux densities for a given red-shift than with low q_0, explaining why the integral number counts are higher for a given flux density. When the Bruzual & Charlot evolution is invoked (solid and dashed lines), we predict more flux than in the corresponding no-evolution cases at high red-shift, because a galaxy is significantly brighter than at the present day. The high q_0 model(with evolution) is virtually flat in the red-shift range $0.5 < z < 2$ and the low q_0 model again predicts slightly lower flux densities for a given red-shift compared to high q_0. It may be noted that the no-evolution models in this plot differ slightly from that of Hughes et al. (1998). This discrepancy is a result of the different assumed dust temperature and beta parameter. The colder temperature means that the peak of the thermal emission from the dust is probed at lower red-shifts and so we lose the benefit of the negative k-correction at $z\approx$2-3 instead of at $z\approx$7-9 as in Hughes & Dunlop (1998).

Fig. 6.4 shows the effect of altering the inter-stellar dust temperature (where we have used the low q_0 evolving model) and Fig. 6.5 shows our predicted number-red-shift distributions for varying flux limits.. The inter-stellar dust temperature, T_{int} makes a big difference to our $850\mu m$ number count predictions and the variation is perhaps contrary to what one may expect in that the lower T_{int} means that we expect to see more galaxies above a given flux limit S_{lim}. This is because, as we lower the dust temperature, although the integrated energy i.e. the area under the Planck curve goes down, the flux density at $850\mu m$ goes up slightly because we are seeing the majority of radiation at much longer wavelengths. Now recall from the previous section that the normalisation of the Planck emission curve is already defined from the amount of flux absorbed by the dust and the Planck curve is simply scaled accordingly. So because the normalisation is fixed, when we lower the dust temperature, we have to scale the Planck curve up by a much larger factor and therefore find that we obtain much larger flux densities at $850\mu m$, explaining why our models are very sensitive to T_{int}.

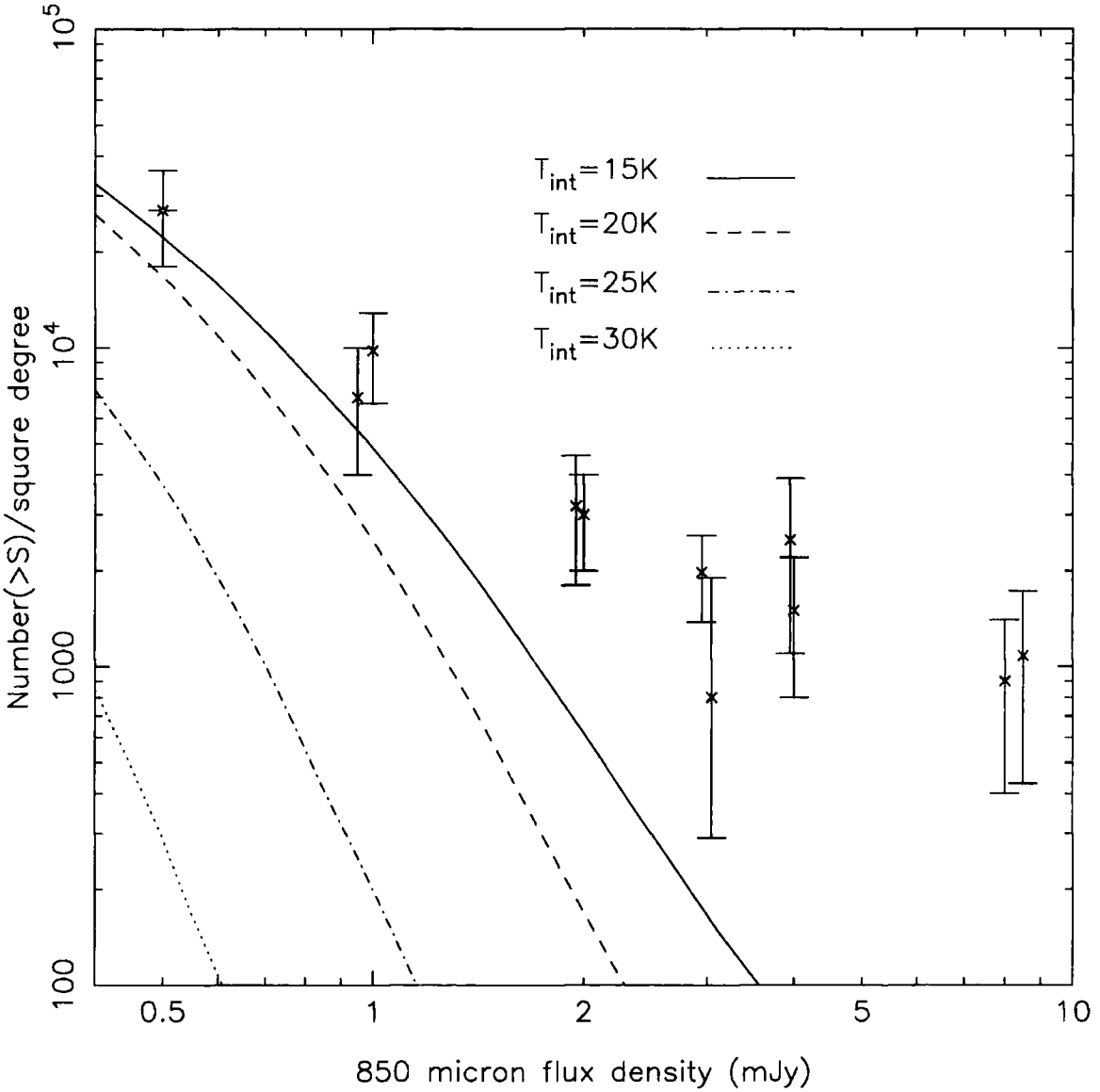

Figure 6.4: The effect of varying the inter-stellar dust temperature, T_{int} The graph shows the low q_0 model with $T_{circ} = 45K(\beta = 2.0)$ and $z_f = 4$. The modest warmer dust component is included in each plot and the inter-stellar dust temperature, which is dominant for the $850\mu m$ counts, is varied from $15K$(solid curve) to $30K$(dotted curve), again with $\beta = 2.0$. Our model predictions are sensitive to this variation and increasing the inter-stellar dust temperature in fact means we see less galaxies above a given flux limit. Typical inter-stellar dust temperatures are $\approx 15K$. This trend is perhaps the opposite of what you would expect when varying dust temperatures and the reasons are explained in Section 5.

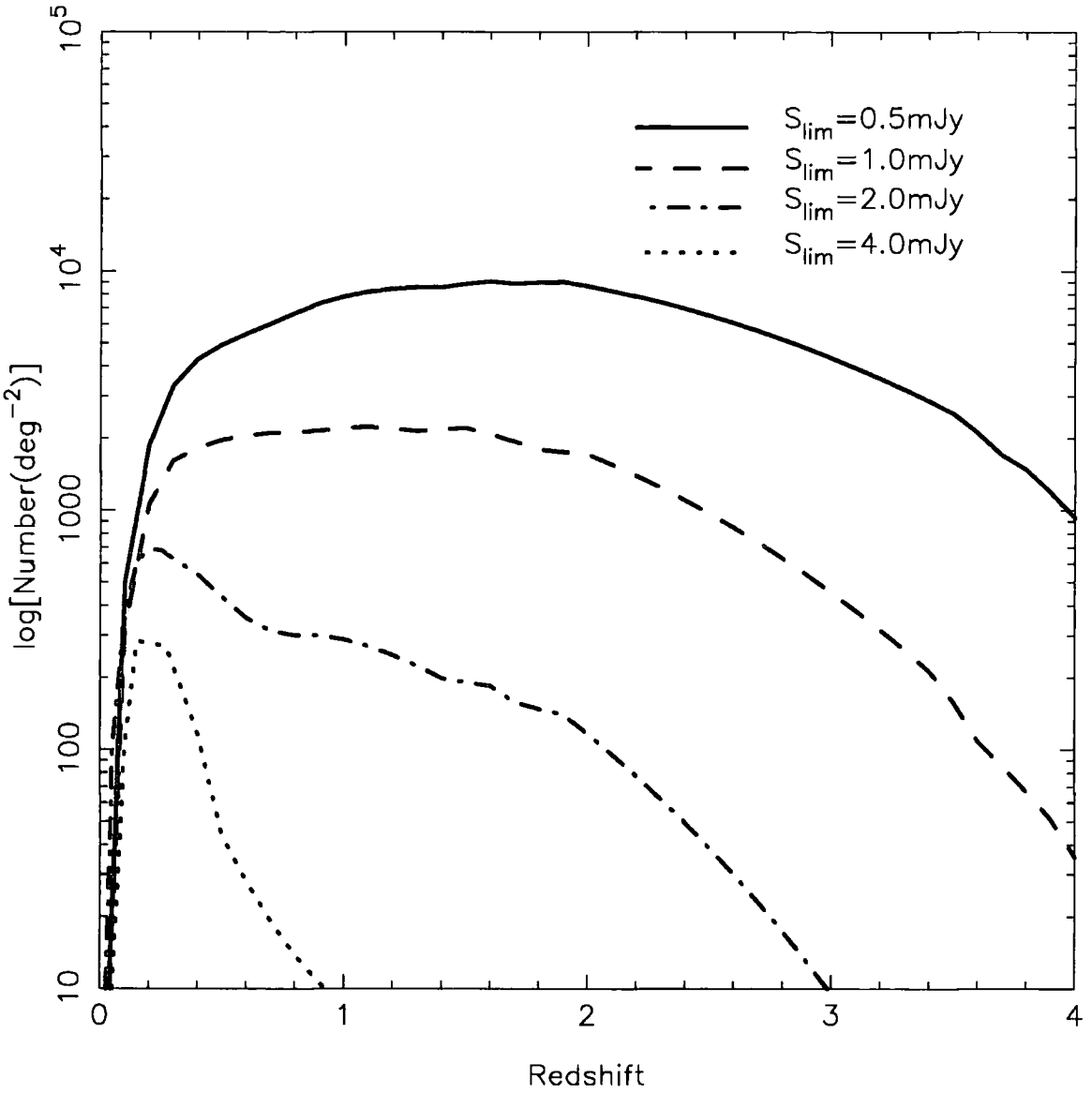

Figure 6.5: The predicted number-red-shift distribution of sub-mm selected faint blue galaxies down to flux limits, S_{lim} of 4.0, 2.0, 1.0 and 0.5mJy. The graph shows the low-q_0 model using the $1/\lambda$ dust law with the parameters described in Fig. 6.1 As the flux limit is increased, the peak in the n(z) distribution shifts from around z=1.8 at S_{lim}=0.5mJy to much lower redshifts, reaching z$\approx$ 0.2 for S_{lim}=4.0mJy.

We have used a galaxy formation red-shift, $z_f = 4$ which is reasonable since sub-mm sources seem to exist out to at least that, but we do in fact find that adopting $z_f = 4$ or $z_f = 6$ or indeed $z_f = 10$ does not make any difference to the number counts. Fig. 6.3 illustrates this, since at $z > 4$ we are observing radiation that was emitted beyond the peak of the black-body curve, and so cosmological dimming is no longer compensated for and all the curves begin to fall away very quickly explaining why increasing z_f beyond about z=4 makes essentially no difference to the $850\mu m$ number counts. Of course, a higher assumed T_{int} would extend this red-shift range to beyond z=4.

Fig. 6.6 shows what sort of contribution we get to the extra-galactic background, simply by integrating over the number counts in each wavelength bin. The plot shows the low and high q_0 models with and without evolution, and with our standard parameters of $T_{int} = 15K$, $T_{circ} = 45K$, $\beta = 2.0$ and $z_f = 4$. All the models predict the same intensity at short wavelengths($\lambda = 60\mu$m), as low red-shift objects would dominate making the evolution and q_0 dependence less significant. The low q_0 model is able to account for all of the background at $850\mu m$, the high q_0 model in fact over-predicts it by about a factor of 2 and the no evolution models, although under-predicting it, are still well within an order of magnitude. Although we can fit the background at $850\mu m$, we noticeably fail the data between about 100 and $300\mu m$. We find that the only way to fit these observations using our model is to use higher values of A_B and higher dust temperatures, as this means dust is absorbing more energy from each galaxy and so the contribution to the background in the wavelength range where warmer dust emission dominates($100\mu m < \lambda < 500\mu m$) is much greater. The solid curve in Fig. 6.6 shows a prediction where we have tried the Calzetti dust model which gives more overall absorption with similar amounts of reddening; this model might also be expected to fit the B optical counts. We see that its larger amount of absorbed flux allows more flexibility in terms of using more dust components. By using three dust temperature components results we obtain a better (though still not perfect) fit to Fig. 6.6 in the $100\mu m < \lambda < 300\mu m$ range, while still giving fits to the IRAS $60\mu m$ (Fig. 6.1) and faint $850\mu m$ number counts (Fig. 6.2).

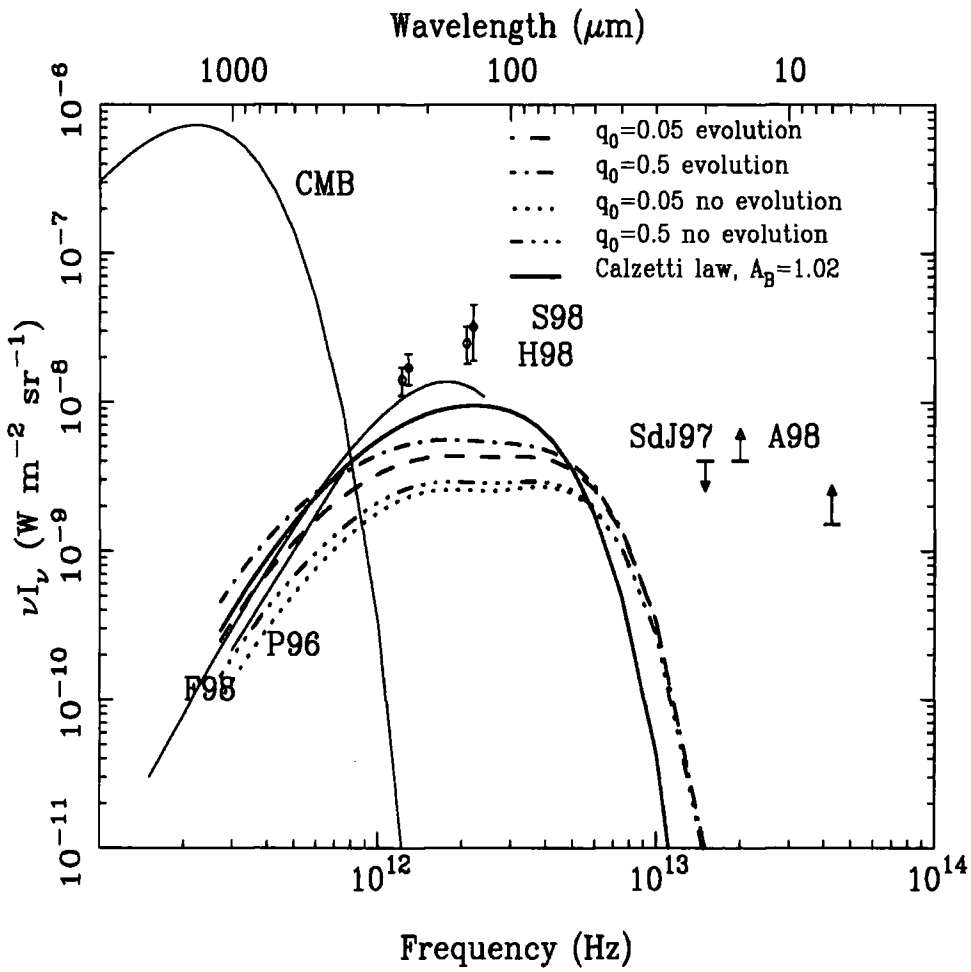

Figure 6.6: The predicted contribution to the FIR background from our models. The latest measurements of the extragalactic FIRB, compared with the COBE measurement of the cosmic microwave background (Mather et al. 1994). F98 - Fixsen et al. (1998)(upper solid line) and P96 - Puget et al. (1996)(lower solid line); H98 - Hauser et al. (1998); S98 - Schlegel et al. (1998). Both the Hauser and Schlegel data each have points at 240μm and 130μm. Low and high q_0 models are shown with and without evolution, where we have used our standard parameters of $T_{int} = 15K$, $T_{circ} = 45K$, $\beta = 2.0$ and $z_f = 4.0$ The evolution model, in the low q_0 case can account for all of the FIR background at 850μm, whereas the high q_0 one in fact over-predicts by about a factor of 2. The solid curve shows a model where we have used the Calzetti dust law using $A_B = 1.02$ (equivalent to E(B-V)=0.18 and close to the value 0.15 used by Steidel et al. (1999) for their Lyman Break Galaxies) for the dust obscuration with a three-component dust temperature of 15K, 25K and 32K. It fits the background and faint number counts at 850μm, the IRAS 60μm counts and also does much better in the wavelength range $100\mu m < \lambda < 500\mu m$.

6.5 Discussion

We have taken a different approach from the standard way in which sub-mm flux's are estimated using UV luminosities (Meurer et al. 1999). Instead of assuming a relationship between the UV slope β and the ratio L_{FIR}/L_{UV}, we proceed directly from the spiral galaxy UV luminosity functions and simply re-radiate into the FIR by assuming a simple dust law constrained from the optical counts. A direct result of this, as has already been illustrated in the previous section, is that decreasing the inter-stellar dust temperature actually increases the received flux density at $850\mu m$, firstly because the peak in the Planck emission curve moves towards longer wavelengths and secondly because (as the absorbed flux from the dust is fixed) the normalisation scaling factor goes up. The fact then that we model the dust using a dominant inter-stellar component of 15K, which is significantly colder than that used in models of star-burst galaxies (typically 30-50K), means that we are able to show that the evolution of normal spiral galaxies like our own Milky Way, using the Bruzual model with an exponential SFR of τ = 9Gyr, could make a very significant contribution to the sub-mm number counts in the $S_{850} < 2$mJy range. Indeed this sort of temperature for spirals has been given recent support from observations of ISO at $200\mu m$ (Alton et al. 1998a) where, for a sample of 7 spirals, a mean temperature of 20K was found, about 10K lower than previous estimates from IRAS at shorter wavelengths. They found that 90 percent of the FIR emission came from very cold dust at temperatures of 15K. Sub-mm observations of spirals (Alton et al. 1998b; Bianchi et al. 2000) and observations of dust in our own galaxy (Sodroski et al. 1994; Reach et al. 1995; Boulanger et al. 1996; Sodroski et al. 1997) also support the claims of these sorts of dust temperatures. Of course, at z=4 our assumed inter-stellar dust temperature of 15K is comparable to that of the microwave background.

Our models show that normal spiral galaxies (ie those that evolve into galaxies like our own Milky Way assuming the Bruzual model) fail to provide the necessary FIR flux of the most luminous sources(> 2mJy) and this is not surprising since the τ = 9Gyr SFR at high red-shift($z > 1$), which is consistent with the UV data, is lower than that inferred by other models which fit the sub-mm counts by a factor of

about 5 or so (Blain et al. 1998a). The LBG galaxies at high red-shift are predicted to be evolved spirals by the Bruzual models and the dust we invoke (A_B=0.3 implies an attenuation factor at 1500Åof 2.3) is enough to make them low luminosity sub-mm sources at flux levels of around 0.5mJy. This amount of dust, though, is not enough to account for the factor of 5 discrepancy and there are several possible reasons for this.

The first is the possible additional contribution to the sub-mm counts from AGN. Modelling of the obscured QSO population has shown that they could contribute, at most, about 30% of the background at 850μm but they can get much closer to the bright end of the sub-mm number counts (Gunn & Shanks 1999). This is shown in Fig. 6.2 where we also show the q_0=0.5 model of Gunn & Shanks. Although the slope of the QSO count at the faintest limits is too flat, at brighter fluxes the QSO model fits better than the faint blue galaxy model and the combination of the two gives a better fit overall.

It is also possible that the optical and sub-mm observations are sampling a completely different population of galaxies as the obscured galaxies sampled by the sub-mm observations may well just be too red or too faint to be detected in the UV at the current flux limits (Smail et al. 1999, 2000; Dey et al. 1999). That may mean that the most luminous sub-mm sources or ULIRG's($> 10^{13} L_{\odot}$) are not the LBG galaxies (which the Bruzual model predicts as evolved spirals) and so then it would not be surprising if the current sub-mm and UV derived star-formation histories at high red-shift were different. However, the evidence is growing that the faint blue galaxies *are* significant contributors to the faint sub-mm counts. Chapman et al. (2000) carried out sub-mm observations of 16 LBG's and found, with one exception, null detections down to their flux limit of 0.5mJy. But their one detection may suggest that with enough SCUBA integration time it might be possible to detect LBG's that are particularly luminous in the FIR and indeed work from Peacock et al (2000) suggests that faint blue galaxies may be detected at 850μm at around the 0.2mJy level. This is below the SCUBA confusion limit of $\approx$ 2mJy (Hughes et al. 1998; Blain et al. 1998b) and highlights the problem faced by Chapman et al.

(1999) in performing targeted sub-mm observations of LBG's. The conclusions of Peacock et al. (2000) suggest that the LBG population (the faint blue galaxies in our model) contribute at least 25 percent of the background at $850\mu m$ and Adelberger et al. (2000) also come to similar conclusions, namely that the UV-selected galaxy population could account for all the 850μm background and the shape of the number counts at 850μm. However, the conclusions of Adelberger et al. (2000) are based on the fact that the SED of SMM J14011+0252 is representative of both the LBG and sub-mm population. At present, they are only assumptions, but nevertheless the conclusions of all these authors seem to suggest that ULIRG's may not contribute to the faint sub-mm number counts and background as much as was first thought.

The spectral slope of the UV continuum and the strength of the Hβ emission line in Lyman Break Galaxies support the fact that inter-stellar dust is present (Chapman et al. 1999), but the physics of galactic dust and the way it obscures the optical radiation from a source is still very poorly understood. We started by adopting a very simplistic model for the dust, treating it as a spherical screen around our model spiral galaxy. The dust might, in reality, be concentrated in the plane of the disk for spiral galaxies and may also tend to clump around massive stars. This would make the extinction law effectively grayer as suggested by observations of local star-burst galaxies (Calzetti, 1997). Indeed, we have investigated the effect of the grayer Calzetti extinction law and found that it would produce a larger sub-mm count contribution due to the higher overall absorption it would imply. Metcalfe et al. (2001) have also suggested that there may be evidence for evolution of the extinction law from the U-B:B-R diagram of faint blue galaxies in the Herschel Deep Field.

We have assumed pure luminosity evolution (PLE) throughout this chapter. The assumption that the number density of spiral galaxies remains constant might certainly not be the case if dynamical galaxy merging is important for galaxy formation. However, as we have seen it is relatively easy to fit the sub-mm number counts with PLE models whereas it is in fact impossible to fit the counts using pure

density evolution models without hugely over-predicting the background by 50 or 100 times (Blain et al. 1998a). So, if existing sub-mm observations are correct then although density evolution may also occur, luminosity evolution may be dominant. It is also striking how well the PLE models do in the optical number counts and colour-magnitude diagrams and together with the fact that we observe highly luminous objects in the sub-mm out to at least $z = 3$, this could indicate that the biggest galaxies could have formed relatively quickly, on time-scales of about 1Gyr or so. If this were true, then the PLE models may be a fair approximation to the galaxy number density and evolution in the Universe out to $z \approx 3$ in both the optical/near-IR and FIR.

We have not taken into account early-type galaxies as no dust was invoked in these in the optical galaxy count models. In particular, we have not included any contribution from dust in the dE population which is invoked to fit the faint optical counts in the $q_0 = 0.5$ model (Metcalfe et al. 1996). If we were to include their possible contribution this would increase our $850\mu m$ counts predictions at the faint end since in our models both early-type and dE star formation occurs at high red-shift which is the region of greatest sensitivity for the sub-mm counts. At brighter fluxes though, where, in our models, low red-shift galaxies are the only possible influence, the inclusion of early-type galaxies would be negligible.

6.6 Conclusions

The aim of this chapter was to investigate whether, by re-radiating the absorbed spiral galaxy UV flux into the FIR, the dust invoked in the faint blue spirals at high z from the optical galaxy count models of Metcalfe et al. (1996) could have a significant contribution to the sub-mm galaxy counts and also the FIR background at 850μm. We have found that, using a inter-stellar dust temperature of 15K, a modest circum-stellar component of 45K, a beta parameter of 2.0 and a galaxy formation red-shift of $z_f \sim 4$ we can account for a very significant fraction of the faint 850μm source counts, both in the low and high q_0 cases when we invoke Bruzual & Charlot evolution (see Fig. 6.2). These evolutionary models give 5-10

times more contribution to the faint sub-mm counts than the corresponding no-evolution models. At brighter fluxes, we find that the SFR and dust assumed in our normal spiral model are too low to produce the FIR fluxes of the most luminous sources. In the no-evolution cases, we under-predict the number counts, even at the faint end. Our predicted red-shift distribution of sub-mm selected faint blue galaxies suggests that the main contribution to the faint counts is in the range $0.5<z<3$, peaking at $z \sim 1.8$. We have shown that our model fits the $60\mu m$ IRAS data well, an important local test if we want to assume PLE and extrapolate our optical spiral galaxy luminosity functions out to higher red-shift. With the evolution models we can easily account for 50-100% of the FIR background at $850\mu m$ but fail the data by nearly an order of magnitude in the $100 - 300\mu$m range. We have shown that the only way to fit these observations using this optically based model is to use assume more dust obscuration (A_B=0.6) and much warmer dust (T=30K). Effectively grey extinction laws such as that of Calzetti et al. (1997) may also provide more overall absorption and hence allow more dust temperature components to allow the flexibility to fit the FIR background from 60-850μm. However, the bright sub-mm counts will still require a further contribution from QSO's or ULIRGs to complement the contribution of the faint blue galaxies at fainter fluxes.

Chapter 7 | *Conclusions*

7.1 Summary of Thesis Outline

The aim of this thesis was to investigate the clustering and number counts of the fundamental visual tracers of mass in the Universe - galaxies. Chapter 1 introduced the two main tools we have used in the analysis of our CTIO CCD data, galaxy number counts and the two-point correlation function. We also saw how the fusion of exponential growth in computing power with technological breakthroughs in astronomical instrumentation, e.g. the 2dF instrument, has paved the way for a new generation of galaxy surveys. In Chapter 2 we outlined the reduction processes involved for our CTIO B and R-band CCD data and at the beginning of Chapter 3 we presented the galaxy number counts from this reduced data. The rest of Chapter 3 was then devoted to investigating the possibile existence of a large void in the local distribution of galaxies in the South Galactic Cap. In order to do this we used the results of our CTIO data in conjunction with data from the APM Galaxy Survey, the Durham/UKST, the 2-Degree Field Galaxy Red-Shift Survey and the 2-Micron All Sky Survey.

In Chapter 4 we developed the technical tools involved in calculating the two-point correlation function, which we then used to quantify the clustering of galaxies observed in the North and South Galactic Caps in our CTIO observations. In Chapter 5 we moved to the more distant Universe at z$\sim$1-2 where we used high quality galaxy B-band photometry, obtained from the Isaac Newton Telescope in La Palma, to analyse the clustering of the faint blue galaxy population. Chapter 6 was devoted to the relatively new field of sub-mm astronomy. We investigated the possibility that the presence of dust assumed in faint blue galaxies, which are predicted to be

evolved late-type spirals in the models of Metcalfe et al. (2001), could open up the possibility of these sources being observed in the sub-mm wave-band. The principle idea is that the dust absorbs radiation from stars in the ultra-violet and then re-emits this energy in the far infra-red region of the electromagnetic spectrum, which we then detect here on Earth.

7.2 Main Results

Our analysis of the galaxies in the local ($z<0.2$) Universe was motivated by the results of galaxy counts which were calculated from our reduced CTIO CCD data, observed in the North and South Galactic Caps. This data covered 255 deg^2 in the NGC, where about two thirds of our fields overlapped with those of the 2dFGRS, and 297 deg^2 in the SGC, which was entirely contained within the 2dFGRS area. We also showed that the galaxy catalogue obtained via our star/galaxy separation technique was 90-95% complete and contaminated by stars at the 5-10% level relative to data from the Millennium Galaxy Catalogue and Sloan Digital Sky Survey. Our number counts showed that our B and R-band data in the NGC agreed extremely well with the model predictions of Metcalfe et al. (2001), but that our SGC data showed a significant deficiency of galaxies. The deficiency was 30.7% for the B-band in the range $14<B<18$ and 22.2% for the R-band in the range $13<R<17$.

The idea was then to use preliminary data from the next generation galaxy surveys of 2dFGRS, SDSS and 2MASS, as well as the completed surveys of APM and DUKST, to investigate the angular extent and depth of this apparent hole in the distribution of galaxies in the SGC. The first step was to use our CCD data, covering large areas of sky in the NGC and SGC, to perform photometric checks of the APM Bright Galaxy Catalogue (APMBGC), the DUKST and the 2dFGRS data. In the case of the APMBGC, the DUKST and the 2dFGRS SGC field, the unique nature of our CTIO CCD data meant that this was the *first ever* time such stringent tests could be done. After comparing our CTIO CCD photometry to that of the APMBGC and DUKST data we found that our galaxies were, on average, brighter by 0.31 and 0.24 mag. respectively. This implied a scale error in the DUKST

Heydon-Dumbledon photometry of 0.1 mags/mag in the range $17<b_J<19.5$. For the 2dF NGC field we found good agreement of the zero-point at $b_J=16$ but our galaxies are, on average, 0.13 magnitudes brighter at $b_J=18$ implying a scale error of 0.065 mags/mag. The mean of the zero-point difference in the range $16<b_J<18$ was 0.1 mags. In the SGC we found no significant zero-point or scale errors relative to our galaxy magnitudes.

These photometric corrections were then used, in conjunction with the models of Metcalfe et al. (2001), to predict the expected galaxy n(z) distribution for the 2dF and DUKST surveys. In the case of the 2dF NGC we found no evidence of any significant galaxy deficiency at any observed redshift but it was interesting that our 0.1 mag. correction was essential in order that the Metcalfe et al. (2001) model agreed with the data. The 2dF SGC n(z) distribution was characterised by two distinct holes in the redshift ranges $0.03<z<0.05$ and $0.06<z<0.09$, with galaxy deficiencies of 35% and 25% .

The DUKST n(z) showed even more significant large-scale structure with four holes in the redshift ranges $0.005<z<0.025$, $0.03<z<0.055$, $0.06<z<0.09$ and $0.09<z<0.11$ with galaxy number discrepancies of 40% , 45% , 50% and 60% respectively. What was especially interesting was that the 2dF and DUKST n(z)'s showed striking common structure with regard to the two holes seen by 2dF. These were both clear features in the DUKST n(z) with the first 2dF hole appearing in the redshift range $0.03<z<0.05$ in both surveys and being almost the same size in each. The second 2dF hole was also a feature in the DUKST survey where it was much larger in size, but generally we found that the DUKST survey found much larger galaxy number deficiencies over all our measured redshifts. We present evidence that this is probably due to bias.

These holes in the galaxy redshift distributions of the two surveys were then used in conjunction with the Metcalfe et al. (2001) luminosity function to calculate variable ϕ^* models for each survey. We found that the counts of the original APM survey and those of the APM Bright Galaxy Catalogue were consistent with a hole

which extends to z=0.1 over the whole 4300 deg^2 APM. We also calculated K-band number counts in the SGC where we were able to argue that the angular extent of this hole extended even further north than the APM area. Combining the 2MASS and APM results we argue that there is a galaxy number deficiency of 30% in the SGC distribution of galaxies, which covers a very large angular area of 100°x60° or, taking into account the redshift depth of z=0.1, a huge volume of $3\text{x}10^6 h^{-3}\text{Mpc}^3$. We also show that if there is to be any reasonable chance of such a hole existing then there must be power in the two-point correlation function on very large scales of 100-200h^{-1}Mpc.

In Chapter 4 we analysed the clustering of galaxies observed in our CTIO NGC and SGC fields. We found that our angular correlation functions, in both the B and R bands, followed a power law behaviour with slopes of $\delta\sim0.70$ in the angular range $-1.8<\log(\theta)<0$, but departed from this trend at smaller and larger angular scales where steeper slopes are observed. We assumed a power law behaviour for the spatial two-point correlation function in order that we could use Limber's equation to de-project our angular functions. When we did this we found characteristic clustering lengths of $r_0=4.7h^{-1}$Mpc and $r_0=5.2h^{-1}$Mpc with the break, r_1, occurring on scales of $10h^{-1}$Mpc and $33.5h^{-1}$Mpc in the NGC and SGC fields respectively. The fact that our SGC data showed a slightly higher value of r_0, coupled with the break occurring on much larger scales, relative to the NGC, meant that our SGC correlation functions showed significant large scale power on angular scales of $\theta > 2°$ or length scales of $r>30h^{-1}$ Mpc. Our B-band correlation functions also agreed extremely well with the APM and Lick data on scales $< 1°$.

The de-projection technique performed on our B-band angular correlation functions was also carried out on our R-band functions. In the NGC we found $r_0=6.0h^{-1}$Mpc, $\gamma=1.68$, $r_1=25.0h^{-1}$Mpc and in the SGC $r_0=5.7h^{-1}$Mpc, $\gamma=1.77$, $r_1=31.0h^{-1}$Mpc. The slightly higher value of r_0 found in the NGC was the opposite trend to that found in our B-band data, but we again found the break in the SGC function to occur on larger scales. The correlation function of the SDSS was scaled to the depth of our survey and we found good agreement on small scales of $\theta < 0.1°$ for both

our NGC and SGC functions, with our NGC angular function predicting slightly more power on larger scales. Scaling tests were performed on our B-band angular correlation functions and we found that the clustering amplitudes decreased as the magnitude limit of the galaxy sample is increased, in good agreement with the trend expected from Limber's equation. These scaling checks show that we are measuring real clustering in the galaxy distribution rather than that induced by systematic errors.

A basic review of possible systematic biases to our correlation functions was performed and we found that our clustering amplitudes could be depressed by 10% due to stellar contamination of our galaxy sample. We also found that the integral constraint does have a small effect on angular scales of $\theta > 1°$. When we correct for the effect of the integral constraint, although it is small, we cannot rule out a pure power law form for the correlation function over all our measured angular scales. If this pure power law form of the correlation function were to extend out to much larger scales of 100-200h^{-1}Mpc then, as we showed in Chapter 3, this may help to explain the huge hole in the SGC galaxy distribution.

Chapter 5 was devoted to analysing the clustering of faint blue galaxies at z$\sim$1-2. We calculated the two-point angular correlation function for each of our 9 fields using 5 galaxy samples defined using the magnitude limits of B=26, B=25, B=24, B=23, and B=22. A resultant two-point angular correlation function for each galaxy sample could then be calculated by simply taking the mean of all the clustering amplitudes in the equivalent angular bins for each field. Our clustering amplitudes at 1° were found to follow the expected trend, where they decrease monotonically as the magnitude limit of the galaxy sample is increased, as well as agreeing extremely well with other data in the literature. Our data shows a characteristic flattening for $B_{lim} > 25$, although we claim that this flattening trend in our data could be exaggerated by our B=26 point, which is beyond our completeness limit of B=25.5. Our CTIO clustering results from Chapter 4, in conjunction with other data from the literature, were used to constrain the value of the galaxy clustering correlation length in the local Universe, and we found that $r_0 = 4.7h^{-1}$Mpc.

Using this value of r_0 with simple ϵ models, which parametrise clustering evolution as a function of redshift, we found that our data was most consistent with an ϵ=0.1 model. This corresponds to a scenario where clustering is close to being fixed in proper co-ordinates.

Our results rule out the ϵ=-1.2 model, which has been found by Steidel et al. to be consistent with the clustering properties of LBG's. This disagreement with our results can be explained by the Lyman Break selection method at z$\sim$3, which tends to sample galaxies that are instrinsically more luminous than M*. We have also found that our results show weaker clustering than predictions of the biased ΛCDM simulations of Kravtsov & Klypin (1999), where dark matter halos are used with v$\gtrsim$200kms^{-1}.

In Chapter 6 we investigated whether faint blue galaxies, which are predicted to be evolved spirals in the models of Metcalfe et al. (2001), could make a substantial contribution to the sub-mm number counts and background at 850μm. We found that, using an interstellar dust temperature of 15K, a modest circum-stellar component of 45K, a modified black body emission law with β=2, a formation redshift, z_f=4 and galaxy evolution based on the models of Bruzual & Charlot, that we could account for a significant fraction of the faint 850μm number counts. Furthermore, these evolution models gave 5-10 times more contribution to the counts than the corresponding no-evolution models, which seriously under-predict the observational data. At brighter fluxes we found that our τ=9Gyr star formation rate and assumed $1/\lambda$, A_B=0.3 dust law are too low to produce the required far infra-red fluxes to account for the bright (>2mJy) sub-mm population.

Our model also allowed us to predict the redshift distribution of sub-mm selected faint blue galaxies and we found that the main contribution came from sources in the redshift range 0.5<z<3, peaking at z$\sim$1.8. We could also predict a galaxy number count at 60μm in order to test whether our models fit the IRAS data, observed in the relatively local Universe. There was good agreement and this is an important test if want to assume pure luminosity evolution out to higher

redshifts. Our evolution models were able to account for 50-100% of the far infra-red background at 850μm but under-predict it by nearly an order of magnitude at 100-300μm. Reasonable fits were possible in this wavelength range, but only if more dust obscuration (A_B=0.6) and warmer dust (T=30K) is assumed. We also experimented with the Calzetti et al. dust law which is effectively greyer and can provide more overall absorption in the ultra-violet, allowing the flexibility to fit the far infra-red background from 60-850μm. Even using these more extreme assumptions we still find that a further contribution from QSO's or ULIRG's is required in order to provide the necessary far infra-red fluxes to fit the bright 850μm number counts.

7.3 Future Prospects

The astronomical community waits with continued excitement as some of the next generation of galaxy surveys like the 2-Degree Field Galaxy Redshift Survey and 2-Micron All Sky Survey near completion. Along with the Sloan Digital Sky Survey, due for completion in 2005, these projects will provide definite answers to some of the questions posed in this thesis. For example, the 2MASS survey will not only be able to tell us the exact angular size of the hole in the SGC distribution of galaxies, but because it will map the *entire* local Universe an accurate description of the cosmological principle can be determined i.e. on *exactly* what scales does the Universe appear homogeneous and isotropic?

The 2dFGRS, and eventually the SDSS, will enable the power spectrum and correlation function to be computed with tiny statistical errors. We have seen how results of the last decade have shown there to be power on large scales in the correlation function which is in excess of that predicted from the standard CDM model of structure formation. In the next few years we will know exactly how much power there is on large scales and whether this can account for the huge voids or holes in the galaxy distribution we have seen from the work in this thesis. If the currently favoured ΛCDM model, predicting more power on large scales than the standard model, were to survive the tightest constraints ever imposed by observations in a

few years, then perhaps we would then know that the correct framework is in place with which to accurately describe the Universe we live in.

Appendix

Appendix

8.1 Cosmological Parameters

In Chapter 1 we mentioned the Cosmological Principle. If the Cosmological Principle and the Theory of General Relativity is assumed, then the Universe is described by a metric known as the Friedmann-Robertson Walker (FRW) metric,

$$d\tau^2 = c^2dt^2 - a^2(t)\left[\frac{dr^2}{1-kr^2} + r^2(d\theta^2 + \sin^2\theta d\phi^2)\right] \tag{8.1}$$

Here r, θ and ϕ are comoving spherical polar coordinates, t is proper time, τ is the space time interval and k is known as the curvature constant and determines the geometry of the Universe. The function $a(t)$ is the expansion factor of the Universe and is determined by solving the Einstein field equations. The solutions, known as the Friedman equations, are

$$\frac{1}{a}\ddot{a} = \frac{4}{3}\pi G\left(\rho + \frac{3p}{c^2}\right) + \frac{\Lambda c^2}{3} \tag{8.2}$$

$$\left(\frac{\dot{a}}{a}\right)^2 = \frac{8}{3}\pi G\rho - \frac{kc^2}{a^2} + \frac{\Lambda}{3} \tag{8.3}$$

where Λ is the cosmological constant, which arises as a constant of integration in solving the Einstein field equations and has dimensions of length^{-2}. p is the pressure, ρ is the density, both due to the matter and radiation in the Universe, and G is the gravitational constant. The dot represents a derivative with respect to cosmological proper time t.

We know that the Hubble parameter, $H(t)$, measures the expansion rate at any particular time, t, for any model obeying the cosmological principle. It does,

however, vary with time in a way that depends on the contents of the Universe. If one expands the cosmic scale factor, $a(t)$, close to t_0 in a power series

$$a(t) = a_0 \left[1 + H_0(t - t_0) - \frac{1}{2} q_0 H_0^2 (t - t_0)^2 + ...\right] \tag{8.4}$$

where H_0 is Hubbles parameter defined at time t=0 then the deceleration parameter is then defined

$$q_0 = \frac{\ddot{a}(t_0) a_0}{\dot{a}(t_0)^2} \tag{8.5}$$

and is dimensionless. The suffix "0" refers to the fact that q_0=$q(t_0)$.

The critical density of a flat Λ=0 Universe, is given by

$$\rho_c = \frac{3}{8\pi G} \left(\frac{\dot{a}}{a}\right)^2 \tag{8.6}$$

and this allows the important quantity, Ω_m, to be defined as

$$\Omega_m = \frac{\rho}{\rho_c}. \tag{8.7}$$

Ω_Λ is defined as

$$\Omega_\Lambda = \frac{\Lambda c^2}{3H^2}. \tag{8.8}$$

Rearranging equation 8.3 and applying equation 8.6, we can derive

$$\Omega_m + \Omega_\Lambda = 1 + \frac{kc^2}{H^2 a^2}, \tag{8.9}$$

where H is the Hubble parameter, defined as $H(t) = \dot{a}(t)/a(t)$. If we assume Λ=0, then if k=0 we have a flat Universe, who's rate of expansion will converge to zero as t$\rightarrow\infty$. If $k > 0$ then the Universe will at some point stop expanding and start to collapse back onto itself, possibly resulting in the 'Big Crunch', the opposite of the 'Big Bang'. If $k < 0$ then the Universe is open and will expand forever. Observational evidence, such as the latest results analysis of the Cosmic Microwave Background, seem to suggest $\Omega = \Omega_m + \frac{\Lambda c^2}{3H^2} \sim 1$. The currently favoured ΛCDM model of structure formation assumes Ω_Λ=0.7, Ω_m=0.3.

8.2 Galaxy Distance Relations

Using the relations of the previous section we can derive expressions for the distance of a galaxy as a function of cosmological red-shift. Consider photons emitted at times t_e and $t_e + \delta t_e$ from a galaxy at co-moving distance r away. For a photon $d\tau$=0, and if we assume that motions are radial, integrating equation 8.1 gives

$$\int_{t_e}^{t_0} \frac{cdt}{a(t)} = \int_0^r \frac{dr}{\sqrt{1-kr^2}} = \int_{t_e+\delta t_e}^{t_0+\delta t_0} \frac{cdt}{a(t)} \tag{8.10}$$

For small δt (i.e. $\delta t << H(t)$) we can rewrite this as

$$0 = \int_{t_e}^{t_0} \frac{cdt}{a(t)} + \left(\frac{c}{a(t_0)}\delta t_0 - \frac{c}{a(t_e)}\delta t_e\right) - \int_{t_e}^{t_0} \frac{cdt}{a(t)} \tag{8.11}$$

The first and last terms cancel leaving

$$\frac{\delta t_0}{a(t_0)} = \frac{\delta t_e}{a(t_e)} \tag{8.12}$$

If we now identify δt_e and δt_0 with the period of a light wave then $\delta t_e = 1/\nu = \lambda_e/c$ and similar for δt_0, where ν and λ are the frequency and wavelength of the wave. Therefore

$$\frac{\lambda_0}{a(t_0)} = \frac{\lambda_e}{a(t_e)}. \tag{8.13}$$

and the cosmological red-shift, z, is by definition

$$1 + z = \frac{\lambda_0}{\lambda_e} = \frac{a(t_0)}{a(t_e)}. \tag{8.14}$$

The FRW metric, equation 8.1, then allows the distance of a galaxy to be determined from its redshift. For a photon, $d\tau$=0 and if the photon is moving in a purely radial direction then $d\theta$=0 and $d\phi$=0 so that

$$cdt = \pm a(t)\frac{dr}{\sqrt{1-kr^2}} \tag{8.15}$$

by integrating from t_e to the present day we find

$$\int_{t_e}^{t_0} \frac{cdt}{a(t)} = -\int_r^0 \frac{dr}{\sqrt{1-kr^2}} \tag{8.16}$$

where t_e is the time at which the photon is emitted from the galaxy and t_0 is the time at which the photon is received by the observer. The negative sign is normally taken as we consider a photon which is moving towards us.

Now replacing $dt = \frac{da}{\dot{a}}$

$$\int_{a_e}^{a_o} \frac{cda}{a(t)\dot{a}} = -\int_r^0 \frac{dr}{\sqrt{1-kr^2}} = \begin{cases} \sin(r) & \text{if } k > 0 \\ r & \text{if } k = 0 \\ \sinh(r) & \text{if } k < 0 \end{cases} \tag{8.17}$$

where $a_e = a(t_e)$ and $a_o = a(t_0)$. Let us call this f(a_e).

Now consider the co-moving distance to a galaxy at the present day. $dt = 0$ in this case so

$$\int(-d\tau^2)^{1/2} = \int_0^r a_0 \frac{dr}{\sqrt{1-kr^2}} = a_0 f(a_e). \tag{8.18}$$

Therefore the co-moving distance, $D(z)$, is given by

$$D(z) = a_0 \int_{a_e}^{a_0} \frac{cda}{a^2 H(a)} \tag{8.19}$$

where Hubble's parameter ($= \dot{a}/a$) has been introduced. Finally the co-moving distance can be written in its usual form, replacing a_0/a by $1 + z$ in equation 8.19 so that

$$D(z) = \int_0^z \frac{cdz}{H(z)}. \tag{8.20}$$

Hubble's parameter is dependent on the cosmology. Substituting the expressions for ρ_{crit} and Ω_Λ at present day we obtain

$$\left(\frac{\dot{a}}{a}\right)^2 = \frac{H_o^2 \rho}{\rho_{\text{crit}}} + \frac{kc^2}{a^2} + \Omega_\Lambda H_o^2. \tag{8.21}$$

Multiply the top and bottom of the ρ_{crit} term by ρ_o and replace ρ_{crit} and use the fact that $\rho \propto a^{-3}$ to obtain

$$\left(\frac{\dot{a}}{a}\right)^2 = H_o^2 \left(\frac{a_o}{a}\right)^3 \Omega_m + \frac{kc^2}{a^2} + \Omega_\Lambda H_o^2. \tag{8.22}$$

We now need to consider the term kc^2/a^2. At present day, we can rewrite equation 8.22 as

$$\left(\frac{\dot{a}}{a_o}\right)^2 = H_o^2 \left(\frac{a_o}{a_o}\right)^3 \Omega_m + \frac{kc^2}{a_o^2} + \Omega_\Lambda H_o^2 \tag{8.23}$$

therefore

$$kc^2 = a_o^2 H_o^2 (1 - \Omega_m - \Omega_\Lambda) \tag{8.24}$$

and equation 8.23 becomes

$$\left(\frac{\dot{a}}{a}\right)^2 = H_\circ^2 \left(\frac{a_\circ}{a}\right)^3 \Omega_\mathrm{m} + H_\circ^2(1 - \Omega_\mathrm{m} - \Omega_\Lambda)\left(\frac{a_\circ}{a}\right)^2 + \Omega_\Lambda H_\circ^2 \tag{8.25}$$

and as $a \propto (1+z)^{-1}$ we finally obtain

$$H(z)^2 = H_0^2 \left\{(1-\Omega)(1+z)^2 + \Omega_\Lambda + \Omega_\mathrm{m}(1+z)^3\right\} \tag{8.26}$$

with $\Omega = \Omega_\mathrm{m} + \Omega_\Lambda$.

If $\Omega = \Omega_\mathrm{m} = 1$ then equation 8.22 simplifies to

$$D(z) = \frac{2c}{H_0}\left(1 - \frac{1}{\sqrt{1+z}}\right) \tag{8.27}$$

Alternatively if $\Omega = \Omega_\mathrm{m} + \Omega_\Lambda = 1$ then equation 8.22 simplifies to

$$D(z) = \frac{c}{H_0}\int_0^z \frac{dz'}{\sqrt{(1-\Omega_\mathrm{m}) + \Omega_\mathrm{m}(1+z')^3}} \tag{8.28}$$

8.3 The Power Spectrum

The power spectrum, $P(k)$, measures perturbations as a function of scale in a density field. Assuming that the density field is a Gaussian Random Field, then the structure or "power" at a given length scale is defined as follows. Consider the density contrast

$$\delta(x) = \frac{\rho(\mathbf{x}) - \bar{\rho}}{\bar{\rho}} \tag{8.29}$$

where $\rho(\mathbf{x})$ is the density field as a function of position, $\mathbf{x}$, and $\bar{\rho}$ is the mean density. One can fourier expand this field

$$\delta(\mathbf{x}) = \frac{1}{8\pi^3}\int \delta_k exp[-i\mathbf{k}.\mathbf{x}]d^3k \tag{8.30}$$

such that its Fourier transform is

$$\delta_k = \int \delta(\mathbf{x}) exp[i\mathbf{k}.\mathbf{x}]d^3x \tag{8.31}$$

The power spectrum of the density fluctuations is simply the mean square modulus of these Fourier coefficients

$$P(k) = \langle |\delta_k|^2 \rangle \tag{8.32}$$

where the angular brackets denote averaging over different regions of space.

Bibliography

The following abbreviations are used in this bibliography:

A&A: Astronomy and Astrophysics

AJ: The Astronomical Journal

ApJ: The Astrophysical Journal

ApJL: The Astrophysical Journal Letters

ApJS: The Astrophysical Journal Supplement

Ap&SS: Astrophysics & Space Science

ARA&A: Annual Reviews of Astronomy and Astrophysics

JRASC: Journal of the Royal Astronomical Society of Canada

MNRAS: Monthly Notices of the Royal Astronomical Society

PASP: Publication of the Astronomical Society of the Pacific

PhRvD: Physical Review D

RA: Ricerche Astronomiche Specola Vaticana

Sci : Science

SPIE: The International Society for Optical Engineering

VA: Vistas in Astronomy

Adelberger K. L., Steidel C. C., Givalisco M., Dickinson M., Pettini M. & Kellogg M., 1998, ApJ, 505, 18

Adelberger K. L., Steidel C. C., 2000, ApJ, 544, 218

Allen C. W., 1973, Astrophysical Quantities, 3rd Edition, The Athlone Press

Alton P. B. et al., 1998a, A&A, 335, 807

Alton, P.B., Davies, J.I., Trewhella, M., 1998b, ApJ, 507, 125

Babul A. & Rees M. J., 1992, MNRAS, 255, 346

Bagla J. S., MNRAS, 299, 417

Bahcall N. A., 1977, ARA&A, 15, 505

Bahcall N. A. & Soneira R., 1980, ApJS, 44, 73

Balbi A. et al., 2000, ApJ, 545, 1

Barger A. J. Cowie L. L., Sanders D. B. Fulton E., Taniguchi Y., Sato Y., Kawara K., Okuda H., 1998, Nature, 394, 248

Barger A. J., Cowie L. L., Smail I., Ivison R. J., Blain A. W., Kneib J-P., 1999, AJ, 117, 2656

Baugh C. M., 1996, MNRAS, 280, 267

Baugh C. M., Cole S., Frenk C. S., Lacey C. G., 1998, ApJ, 498, 504

Baugh C. M., Benson A. J., Cole S., Frenk C. S., Lacey C. G., 1999, MNRAS, 305, 21

Bertin E. & Arnouts S., 1996, A&AS, 117, 393

Bertin E. & Dennefield M., 1997, A&A, 317, 43

Bertin E., Dennefield M., Moshir M., 1997, A&A, 323, 685

Bianchi S., Alton P. B., Davies J.I., 2000, ESASP, 455, 149

Blain A. W., Kneib J. P., Ivison R. J., Smail I., 1999, ApJ, 512, 87

Blain A. W., Smail I., Ivison R. J., & Kneib J-P 1998, MNRAS, 302, 632

Blain A.W., Ivison R.I., & Smail I., 1998, MNRAS, 296, 29

Boulanger F., Abergel A., Bernard J.-P., Burton W.B., Desert F.-X., Hartmann D., Lagache G., Puget J.-L., 1996, A&A, 312, 256

Brainerd T. G. & Villumsen J. V., 1994, ApJ, 431, 477

Brainerd T. G., Smail I., Mould J., 1995, MNRAS, 275, 781

Brainerd T. G., Smail I., 1998, ApJ, 494, 137

Brown G. S. & Tinsley B. M., 1974, ApJ, 194, 555

Bruzual A. G. & Charlot S. 1993, ApJ, 405, 538

Busswell G. S. & Shanks T., 2001, MNRAS, 323, 67

Busswell G. S., Shanks T., Outram P.J., Croom S., in prep.

Calzetti D., Meurer G.R., Bohlin R. C., Garnett D. R., Kinney A. L., Leitherer C., Storchi-Bergmann T., 1997, AJ, 114, 1834

Campos A. & Shanks T., 1997, MNRAS, 291, 383

Chapman S. C. et al., 2000, MNRAS, 319, 318

Coles P. & Lucchin F., 1995, Cosmlogy, John Wiley & Sons Ltd, Chichester, UK

Coles P., Lucchin F., Matarrese S. & Moscardini L., 1998, MNRAS, 300, 183

Coln P., Klypin A. A., Kravtsov A. V., Khokhlov A. M., 1999, ApJ, 523, 32

Colless M., Ellis R. S., Broadhurst T. J., Taylor K., Peterson B. A., 1993, MNRAS, 261, 19

Colless M., et al., 2001, astro-ph/0106498

Collins C. A., Heydon-Dumbledon N. H. & MacGillivray H. T., 1988, MNRAS, 236, 7

Couch W.J., Jurcevic J. S., Boyle B. J., 1993, MNRAS, 260, 241

Cowie L. L., Hu E. M., Songaila A. 1995, AJ, 110, 1576

Croom S. M., et al, 2001, in preparation

Dalton G. B., Efstathiou G., Maddox S. J., Sutherland W. J., 1995, MNRAS, 269, 151

Davis M.,Efstathiou G., Frenk C. S., & White S. D. M., 1985, ApJ, 292, 371

Dey, A., Graham, J.R., Ivison, R.J., Smail, I., Wright G.S., Liu, M.C., 1999, ApJ, 519, 610

Domingue D. L., Keel W. C., Ryder S. D., White R. E., 2000, ApJ, 545, 171

Driver S. P., Windhorst R. A., Ostrander E. J., Keel W. C., Griffiths R. E. & Ratnatunga K. U. 1995, AJ, 449, 23

Eales S., Lilly S., Gear W., Dunne L., Bond J. R., Hammer F., Le Fvre O., Crampton D., 1999, ApJ, 515, 518

Efstathiou G., Kaiser N., Saunders W., Lawrence A., Rowan-Robinson R. S., Frenk C. S., 1990a, MNRAS, 247, 10

Efstathiou G., Bernstein G., Katz N., Tyson J., Guhathakurta P., 1991, ApJ, 380, 47

Efstathiou G., Bond J. R. & White S. D. M., 1992, MNRAS 258, 1

Fixsen D. J., Dwek E., Mather J. C., Bennett C. L., Shafer R. A., 1998, ApJ, 508, 123

Flores H., et al., 1999, ApJ, 517, 148

Folkes S., 1999, MNRAS, 308, 459

Fong R., Hale-Sutton D., Shanks T., 1992, MNRAS, 257, 650

Frayer D. T., Ivison R. J., Scoville N. Z., Yun M., Evans A. S., Smail I., Blain A. W., Kneib J.-P., 1998, ApJ, 506, 7

99frayer99 Frayer D. T. et al., 1999, ApJ, 514, 13

Frith W. J., Busswell G. S., Fong R., Metcalfe N., Norberg P., Shanks T., 2001, in prep.

Gallego J., Zamorano J., Aragon-Salamanca A., Rego M., 1996, ApJ, 459, 43

Gardner J. P., Cowie L. L., Wainscoat R. J., 1993, ApJ, 415, 9

Gaztanaga E., 2001, astro-ph/0110126

Glazebrook K., Ellis R., Santiago B., Griffiths R., 1995, MNRAS, 275, 19

Governato F. et al., 1998, Nature, 392, 359

Gregorich D. T., Neugebauer G., Soifer B. T., Gunn J. E., Hertler T. L., 1995, AJ, 110, 259

Gronwall C., Salzer J. J., McKinstry K., 1998, AAS, 193, 7606

Groth E. J., Peebles P. J. E., 1977, ApJ, 217, 385

Guiderdoni B. & Rocca-Volmerange B. 1990, A&A 227, 362

Gunn K. F., Shanks T., 1999, astro-ph/9909089

Guth A. H., 1981, PhRvD, 23, 347

Hacking P. B., Houck J. R., 1987, ApJS, 63, 311

Hall P. & Mackay C. D., 1984, MNRAS, 210, 979

Hamilton A. J. S., 1993, ApJ, 417, 19

Hauser M. G. et al., 1998, ApJ, 508, 25

Hawking S. W., 1982, Astrophysical Cosmology, Proceedings of the Study Week on Cosmology and Fundamental Physics, page 563

Holland W. S., Cunningham C. R., Gear W. K., Jenness T., Laidlaw K., Lightfoot J. F., Robson E. I., 1998, SPIE, 3357, 305

Holland W. S. et al., 1999, MNRAS, 303, 659

Hu W., Dodelson S., 2001, astro-ph/0110414

Hubble E. P., 1926, ApJ, 64, 321

Hudon J. D., Lilly S. J., 1996, ApJ, 469, 519

Hughes D. et al. 1998, Nature, 394, 241

Hughes D. H. & Dunlop J. S., 1999, High Red-Shift Radio Lines, 99

Hurt R. L., Jarrett T. H., Kirkpatrick J. D., Cutri R. M., Schneider S. E., Skrutskie M., Van Driel W., 2000, AJ, 120, 1876

Infante L., 1987, A&A, 183, 177

Ivison R. J., Smail I., Le Borgne J.-F., Blain A. W., Kneib J.-P., Bezecourt J., Kerr T. H., Davies J. K., 1998, MNRAS, 298, 583

Ivison R. J., Smail I., Barger A. J., Kneib J-P., Blain A.W., Owen F. N., Kerr T. H., Cowie L. L. 2000, MNRAS, 315, 209

Jarrett T. H., Chester T., Cutri R., Schneider S., Skrutskie M., Huchra J. P., 2000, AJ, 119, 2498

Jones L. R., Shanks T., Fong R. F., 1987, in High Redshift and Primeval Galaxies, eds Bergeron J., Kunth D., Rocca-Volmerange B., Tran Thanh Van J., Editions Frontieres, Gif-sur-Yvette, p.29

Jones L. R., Fong R., Shanks T., Ellis R. S., Peterson B. A., 1991, MNRAS, 249, 481

Kauffmann G., Colberg J. M., Diaferio A., White S. D. M., 1999, MNRAS, 307, 529

Kibblewhite E. J., Bridgeland M. T., Bunclark P. S., Irwin M. J., 1984, Astronomical Microdensity Conference, NASA Conf. Pub., 2317, p.277

Koo S. D. & Szalay A. S., 1984, ApJ, 282, 390

Kochanek C. S., 2001, ApJ, 560, 566

Kravtsov A. V. & Klypin A. A., 1999, ApJ, 520, 437

Kron G. E., 1980, RA, 10, 1

Landolt A. U., 1992, AJ, 104, 372

Landy S. D. & Szalay A. S., 1993, ApJ, 412, 64

Lilly S. J., Le Fevre O., Hammer F., Crampton D., 1996, ApJ, 460, 1

Lilly S. J., Eales S. A., Gear W. K. P., Hammer F. L-F. O., Crampton D., Bond J. R., Dunne L., 1999, ApJ, 518, 641

Loveday J., 1996, MNRAS, 278, 1025

Loveday J., Peterson B. A., Maddox S. J., Efstathiou G., 1996, ApJS, 107, 201

MacGillivray H. T., Stobie R. S., 1984, VA, 27, 433

Maddox S. J., Efstathiou G., Sutherland W. J., & Loveday J., 1990, MNRAS, 243, 692

Maddox S. J., Sutherland W. J., Efstathiou G. & Loveday J., 1990, MNRAS, 243, 692

Maddox S. J., Sutherland W. J., Efstathiou G., Loveday J., Peterson B. A., 1990, MNRAS, 247, 1

Mather J. C. et al., 1994, ApJ, 420, 439

McCracken H. J., Shanks T., Metcalfe N., Fong R., Campos A., 2000, MNRAS, 318, 913

Metcalfe N., Shanks T., Fong R., Jones L. R., 1991, MNRAS, 249, 498

Metcalfe N., Fong R., Shanks T., 1995, MNRAS, 274, 769

Metcalfe N., Shanks T., Campos A., Gardner J. P. & Fong R., 1996, Nature, 21, 10

Metcalfe N., Ratcliffe A., Shanks T., Fong R., 1998, MNRAS, 294, 147

Metcalfe N., Shanks T., Campos A., McCracken H.J., Fong R., 2001, MNRAS, 323, 795

Meurer G. R., Heckman T. M., Calzetti D., 1999, ApJ, 521, 64

Mihos, C., 1999, Ap&SS, 266, 195

Neugebauer G. et al. 1984, Sci, 224, 14

Neushaefer L. W., Windhorst R. A., Dressler A., 1991, ApJ, 382, 32

Norberg P. et al., 2001, astro-ph, 0111011

Oliver S. J., Rowan-Robinson M., Saunders W., 1992, MNRAS, 256, 15O

Peacock J. A & Dodds S. J., 1994, MNRAS, 267, 1020

Peacock J. A. et al. 2000, MNRAS, 318, 535

Peacock J. A. et al., 2001, Nature, 410, 169

Peebles P. J. E., in The Large Scale Structure of the Universe, Princeton University Press.

Percival W. J., et al., 2001, MNRAS, 327, 1297

Picard A., 1991, AJ, 102, 445

Pimbblet K. A., Smail I., Edge A. C., Couch W. J., O'Hely E., Zabludoff A. I., 2001, MNRAS, 327, 588

Puget J. L., Abergel A., Bernard J. P., Boulanger F., Burton W. B., Desert F. X., Hartmann D., 1996, A&A, 308, 5

Phillipps S., Fong R., Fall R. S., Ellis S. M., MacGillivray H. T., 1978, MNRAS, 182, 673

Press W. H., Flannery B. P., Teukolsky S. A., Vetterling W. T., 1989, Numerical Recipes (Fortran), Cambridge University Press, Cambridge, UK

Pritchet C. J., Infante L., 1992, ApJ, 399, 35

Ratcliffe A., 1996, PhD Thesis, University of Durham

Ratcliffe A., Shanks T., Parker Q. A. & Fong R., 1996, MNRAS, 281, L47

Ratcliffe A., Shanks T., Parker Q. A. & Fong R., 1998a, MNRAS, 293, 197

Ratcliffe A., Shanks T., Parker Q. A. & Fong R., 1998b, MNRAS, 296, 173

Ratcliffe A., Shanks T., Parker Q. A. & Fong R., 1998c, MNRAS, 296, 191

Ratcliffe A., Shanks T., Parker Q. A., Broadbent A., Watson F. G., Collins C. A. & Fong, R., 1998d, MNRAS, 300, 417

Reach W. T., et al. 1995, ApJ, 451, 188

Roche N., Shanks T., Metcalfe N., Fong R., 1993, MNRAS, 263, 360

Roche N., Shanks T., Metcalfe N., Fong R., 1993, MNRAS, 280, 397

Roche N., Eales S. A., 1999, MNRAS, 307, 703

Rowan-Robinson M., Hughes J., Vedi K., Walker D. W., 1990, MNRAS, 246, 273

Sandage A., 1961, ApJ, 134, 916

Saunders W., Rowan-Robinson M., Lawrence A., Efstathiou G., Kaiser N., Ellis R. S., Frenk C. S., 1990, MNRAS, 242, 318

Saunders W. et al., 1991, Nature, 349, 32

Schlegel D. J., Finkbeiner D. P., Davis M., 1998, ApJ, 500, 525

Scranton R., et al. 2001, astro-ph/0107416

Seldner M., Seibers B., Groth E. J. & Peebles P. J. E., 1977, AJ, 82, 249.

Shane C. D. & Wirtanen C. A.,1967, Publs Lick Obs., 22, Part 1.

Shectman S. A., Landy S. D., Oemler A., Tucker D. L., Lin H., Kirschner R. P. & Schechter P. L., 1996, ApJ, 470, 172

Schlegel D. J., Finkbeiner D. P., Davis M., 1998, ApJ, 500, 525

Shanks T., Stevenson P. R. F., Fong R. & MacGillivray H. T., 1984, MNRAS, 106 767

Shimasaku K., 2001, AJ, 122, 1238

Smail I., Ivison R. J., Blain A. W., 1997, ApJ, 490, 5

Smail I., Ivison R. J., Kneib J.-P., Cowie L. L., Blain A. W., Barger A. J., Owen F. N., Morrison G., 1999, MNRAS, 308, 1061

Smail I., Ivison R. J., Owen F. N., Blain A. W., Kneib J.-P., 2000, ApJ, 528, 612

Smoot G. F., 1992, ApJ, 396, 1

Sodroski T. J. et al., 1994, ApJ, 428, 638

Sodroski T. J., Odegard N., Arendt R. G., Dwek E., Weiland J. L., Hauser M. G., Kelsall T., 1997, ApJ, 480, 173

Steidel C. C. et al., 1996, ApJ, 462, 17

Steidel C. C. et al., 1998a, ApJ 492, 428

Steidel C. C., Adelberger K. L., Givalisco M., Dickinson M. & Pettini M., 1999, ApJ, 519, 1

Stevenson P. R. F., Shanks T., Fong R., Macgillivray H. T., 1985, MNRAS, 213, 953

Stevenson P. R. F., Shanks T., Fong R., Spectral Evolution of Galaxies, Proceedings of the Fourth Workshop, Erice, Italy, p. 439

Sugiyama N., 1995, ApJS, 100, 281

Tresse L. & Maddox S. J., 1998, ApJ, 495, 691

Vettolani G., 1998, A&AS, 130, 323

Villumsen J. V., Freudling W., Da Costa L. N., 1997, ApJ, 481, 578

Wechsler R. H. et al., 1998, ApJ, 506, 19

White S. D. M., Frenk C. S., Davis M., Efstathiou G., 1987, ApJ, 313, 505

Williams R. E., et al., 1996, MNRAS, 112, 1335

Yasuda N., et al., 2001, AJ, 122, 1104

Yoshii Y., Takahara F., 1988, ApJ, 326, 1

York D. G., et al., 2000, AJ, 120, 1579